PROCEEDINGS OF SPIE

SPIE—The International Society for Optical Engineering

Laser Optics 2000

Semiconductor Lasers and Optical Communication

Serguei A. Gurevich
Nikolay N. Rosanov
Editors

26–30 June 2000
St. Petersburg, Russia

Organized by
Institute for Laser Physics (Russia)
All-Russia Scientific Center, S.I. Vavilov State Optical Institute
General Physics Institute, Russian Academy of Sciences
P.N. Lebedev Physical Institute, Russian Academy of Sciences
A.F. Ioffe Physico-Technical Institute, Russian Academy of Sciences
Russian National Center of Laser Physics, St. Petersburg State University
St. Petersburg Institute of Fine Mechanics and Optics (Russia)
Scientific Council on Coherent and Nonlinear Optics, Russian Academy of Sciences
SPIE—The International Society for Optical Engineering
SPIE Russia Chapter
OSA—Optical Society of America
ROS—Rozhdestvensky Optical Society (Russia)
Government of St. Petersburg (Russia)
ISTC—International Scientific and Technological Center

20010927 029

Volume 4354

DISTRIBUTION STATEMENT A
Approved for Public Release
Distribution Unlimited

REPORT DOCUMENTATION PAGE

Form Approved OMB No. 0704-0188

Public reporting burden for this collection of information is estimated to average 1 hour per response, including the time for reviewing instructions, searching existing data sources, gathering and maintaining the data needed, and completing and reviewing the collection of information. Send comments regarding this burden estimate or any other aspect of this collection of information, including suggestions for reducing this burden to Washington Headquarters Services, Directorate for Information Operations and Reports, 1215 Jefferson Davis Highway, Suite 1204, Arlington, VA 22202-4302, and to the Office of Management and Budget, Paperwork Reduction Project (0704-0188), Washington, DC 20503.

1. AGENCY USE ONLY (Leave blank)	2. REPORT DATE	3. REPORT TYPE AND DATES COVERED
	14 September 2001	Conference Proceedings

4. TITLE AND SUBTITLE

Laser Optics 2000: Semiconductor Lasers and Optical Communication (Volume 4354)

5. FUNDING NUMBERS

F61775-00-WF

6. AUTHOR(S)

Conference Committee

7. PERFORMING ORGANIZATION NAME(S) AND ADDRESS(ES)

Institute for Laser Physics
12 Birzhevaya line
St. Petersburg 199034
Russia

8. Performing Organization Report Number

N/A

9. SPONSORING/MONITORING AGENCY NAME(S) AND ADDRESS(ES

EOARD
PSC 802 Box 14
FPO 09499-0200

10. SPONSORING/MONITORING AGENCY REPORT NUMBER

CSP 00-5049

11. SUPPLEMENTARY NOTES

Conference Proceedings in five volumes. Proceedings of SPIE – The International Society for Optical Engineering, 26-30 June 2000, St. Petersburg, Russia. Volumes 4350 (Solid State Lasers), 4351 (High-Power Gas Lasers), 4352 (Ultrafast Optics and Superstrong Laser Fields), 4353 (Control of Laser Beam Characteristics and Nonlinear Methods for Wavefront Control), and 4354 (Semiconductor Lasers and Optical Communication), ISSN 0277-786X

12a. DISTRIBUTION/AVAILABILITY STATEMENT

Approved for public release; distribution is unlimited.

12b. DISTRIBUTION CODE

A

ABSTRACT (Maximum 200 words)

The Final Proceedings for the Tenth Conference on Laser Optics, 26-30 June 2000. This is an interdisciplinary conference. Topics include generation of ultrashort light pulses, application of nonlinear correction techniques in adaptive optics and lasers, advanced methods of beam control and pointing; diode-pumped solid state lasers; high average power gas and solid-state lasers; and lasers in medicine and medical applications.

14. SUBJECT TERMS

EOARD, Adaptive optics, Gas lasers, Solid state lasers, Aberration correction

15. NUMBER OF PAGES

Five bound volumes

16. PRICE CODE

17. SECURITY CLASSIFICATION OF REPORT	18. SECURITY CLASSIFICATION OF THIS PAGE	19. SECURITY CLASSIFICATION OF ABSTRACT	20. LIMITATION OF ABSTRACT
UNCLASSIFIED	UNCLASSIFIED	UNCLASSIFIED	UL

PROCEEDINGS OF SPIE

SPIE—The International Society for Optical Engineering

Laser Optics 2000

Semiconductor Lasers and Optical Communication

Serguei A. Gurevich
Nikolay N. Rosanov
Editors

26–30 June 2000
St. Petersburg, Russia

Organized by
Institute for Laser Physics (Russia) • All-Russia Scientific Center, S.I. Vavilov State Optical Institute • General Physics Institute, RAS • P.N. Lebedev Physical Institute, RAS • A.F. Ioffe Physico-Technical Institute, RAS • Russian National Center of Laser Physics, St. Petersburg State University • St. Petersburg Institute of Fine Mechanics and Optics (Russia) • Scientific Council on Coherent and Nonlinear Optics, RAS • SPIE—The International Society for Optical Engineering • SPIE Russia Chapter • OSA—Optical Society of America • ROS—Rozhdestvensky Optical Society (Russia) • Government of St. Petersburg (Russia) • ISTC—International Scientific and Technological Center

Supported by
Ministry of Science and Technical Policy of the Russian Federation • Ministry for Economics of the Russian Federation • Ministry of Education of the Russian Federation • Federal Agency for Conventional Weapons (Russia) • Russian National Foundation for Basic Research • SPIE—The International Society for Optical Engineering • Lawrence Livermore National Laboratory (USA) • European Office of Aerospace Research and Development (USA) • OSA—Optical Society of America • ISTC—International Scientific and Technological Center • Amada Corporation (Japan) • Jenoptic GmbH (Germany) • Corning Inc. (USA) • IRE-Polus Group (Germany)

Volume 4354

Published by
SPIE—The International Society for Optical Engineering

SPIE is an international technical society dedicated to advancing engineering and scientific applications of optical, photonic, imaging, electronic, and optoelectronic technologies.

AQ F01-12-2762

The papers appearing in this book compose the proceedings of the technical conference cited on the cover and title page of this volume. They reflect the authors' opinions and are published as presented, in the interests of timely dissemination. Their inclusion in this publication does not necessarily constitute endorsement by the editors or by SPIE. Papers were selected by the conference program committee to be presented in oral or poster format, and were subject to review by volume editors or program committees.

Please use the following format to cite material from this book:

Author(s), "Title of paper," in *Laser Optics 2000: Semiconductor Lasers and Optical Communication*, Serguei A. Gurevich, Nikolay N. Rosanov, Editors, Proceedings of SPIE Vol. 4354, page numbers (2001).

ISSN 0277-786X
ISBN 0-8194-4044-2

Published by
SPIE—The International Society for Optical Engineering
P.O. Box 10, Bellingham, Washington 98227-0010 USA
Telephone 1 360/676-3290 (Pacific Time) • Fax 1 360/647-1445
http://www.spie.org/

Copyright© 2001, The Society of Photo-Optical Instrumentation Engineers.

Copying of material in this book for internal or personal use, or for the internal or personal use of specific clients, beyond the fair use provisions granted by the U.S. Copyright Law is authorized by SPIE subject to payment of copying fees. The Transactional Reporting Service base fee for this volume is $15.00 per article (or portion thereof), which should be paid directly to the Copyright Clearance Center (CCC), 222 Rosewood Drive, Danvers, MA 01923 USA. Payment may also be made electronically through CCC Online at http://www.directory.net/copyright/. Other copying for republication, resale, advertising or promotion, or any form of systematic or multiple reproduction of any material in this book is prohibited except with permission in writing from the publisher. The CCC fee code is 0277-786X/01/$15.00.

Printed in the United States of America.

Contents

Laser Optics 2000 Program Committee

Chair

Artur A. Mak, Institute for Laser Physics (Russia)

Vice-Chairs

Alexander A. Andreev, Institute for Laser Physics (Russia)
Vladimir Yu. Venediktov, Institute for Laser Physics (Russia)

Scientific Secretary

A. F. Vassil'yev, Institute for Laser Physics (Russia)

Members

Zhores I. Alferov, A.F. Ioffe Physico-Technical Institute (Russia)
Pavel A. Apanasevich, B.I. Stepanov Institute of Physics (Belarus)
Sergey N. Bagaev, Institute for Laser Physics (Russia)
Nikolai G. Basov, P.N. Lebedev Physical Institute (Russia)
Yuri D. Berezin, Institute for Laser Physics (Russia)
Viktor I. Bespalov, Institute of Applied Physics (Russia)
Ernest V. Boiko, Military Medical Academy (Russia)
F. V. Bunkin, General Physics Institute (Russia)
Oleg B. Danilov, Institute for Laser Physics (Russia)
Eugeni M. Dianov, General Physics Institute (Russia)
Sergei A. Dimakov, Institute for Laser Physics (Russia)
Alexander V. Dotsenko, Corning Scientific Center (Russia)
Valentin Gapontsev, IPG Laser GmbH (Germany)
Yu. D. Golyaev, Research and Development Institute Polyus (Russia)
Vyacheslav M. Gordienko, M.V. Lomonosov Moscow State University (Russia)
Serguei A. Gurevich, A.F. Ioffe Physico-Technical Institute (Russia)
Valerii P. Kandidov, M.V. Lomonosov Moscow State University (Russia)
Yakov I. Khanin, Institute of Applied Physics (Russia)
I. V. Kovsh, Laser Association (Russia)
O. N. Krohin, P.N. Lebedev Physical Institute (Russia)
Vladimir V. Lyubimov, Institute for Laser Physics (Russia)
Alexander A. Manenkov, General Physics Institute (Russia)
Yuri T. Mazurenko, S.I. Vavilov State Optical Institute (USA)
Anatoly P. Napartovich, Troitsk Institute for Innovation and Fusion Research (Russia)
Anatoly N. Oraevsky, P.N. Lebedev Physics Institute (Russia)
Vladislav Ya. Panchenko, Scientific Research Center for Technological Lasers (Russia)
Pavel P. Pashinin, General Physics Institute (Russia)
G. T. Petrovskiy, S.I. Vavilov State Optical Institute (Russia)
N. N. Rozanov, Institute for Laser Physics (Russia)
Alexander S. Rubanov, B.I. Stepanov Institute of Physics (Belarus)
Marat S. Soskin, Institute of Physics (Ukraine)

Victor A. Serebryakov, Institute for Laser Physics (Russia)
Ivan A. Shcherbakov, General Physics Institute (Russia)
Vladimir E. Sherstobitov, Institute for Laser Physics (Russia)
Leonid N. Soms, Institute for Laser Physics (Russia)
V. B. Smirnov, St. Petersburg State University (Russia)
Anatoli P. Sukhorukov, M.V. Lomonosov Moscow State University (Russia)
Vladimir I. Ustyugov, Institute for Laser Physics (Russia)
V. V. Valuev, GPO Almaz (Russia)
V. N. Vasilev, St. Petersburg State Institute of Fine Mechanics and Optics (Russia)
Evgeny A. Viktorov, Institute for Laser Physics (Russia)
Vadim P. Veiko, St. Petersburg State Institute of Fine Mechanics and Optics (Russia)
Vladimir E. Yashin, Institute for Laser Physics (Russia)
Georgii M. Zverev, Research and Development Institute Polyus (Russia)

GaN-based Violet-blue Laser Diodes

S. Hashimoto, H. Nakajima, K. Yanashima, T. Asatsuma, T. Yamaguchi, H. Yoshida, M. Ozawa, K. Funato, S. Tomiya*, T. Miyajima, T. Kobayashi, S. Uchida**, and M. Ikeda**

Semiconductor Laser Division, Semiconductor Company,
Sony Corporation Core Technology & Network Company
2-1-1 Shinsakuragaoka, Hodogaya-ku, Yokohama, 240-0036, Japan
*Environment & Analysis Technology Development, Technical Support Center, Sony Corporation
2-1-1 Shinsakuragaoka, Hodogaya-ku, Yokohama, 240-0036, Japan
**Development Center, Sony Shiroishi Semiconductor Incorporation
3-53-2 Shiratori, Shiroishi, Miyagi-ken, 989-0734, Japan

ABSTRACT

High power GaN-based laser diodes (LDs) are very desirable for various applications such as optical storage systems. We have obtained GaN films of low dislocation density using epitaxial lateral overgrowth (ELO) technique and the raised-pressure metalorganic chemical vapor deposition (RP-MOCVD) technique. Dislocation density of the improved GaN is about 10^7 cm^{-2}. Optimized GaN-based LDs fabricated on the improved GaN films have operated up to 35mW without any kink. The lifetime is more than 500 hours with a constant power of 20 mW at 25 °C under continuous wave (CW) conditions. Furthermore, we have introduced buried-ridge laser diode structure in order to control the optical transverse mode. The features of the far field patterns (FFPs) of LDs with AlGaN burying layers indicate their controllability.

Keywords: GaN, LD, optical storage, ELO, MOCVD, buried-ridge, lifetime

1. INTRODUCTION

The violet-blue laser diode is a key device for the next generation of optical storage disc systems. High-power GaN-based violet-blue LDs are very desirable for various applications. Successful operation of GaN-based LDs has been reported by several groups[1)-9)]. Recently there has been great progress in crystal growth of GaN-related materials. Using the epitaxial lateral overgrowth technique[10),11)], GaN of lower dislocation density has been obtained. Progress in GaN-based LDs has realized a lifetime of over 10,000 hours[12)]. For future applications, better controllability of optical-mode properties of GaN-based LDs is necessary.

Here we first discuss the importance of reducing of input power and the dislocation density in order to improve the reliabilities of GaN-based LDs. The optimized superlattice (SL) cladding structures of p-type layers and the Pd/Pt/Au electrode of p-type ohmic metal has made the operation more reliable. Next, we report that the introduction of the buried-ridge structure to GaN-based LDs makes it easier to control optical transverse mode of GaN-based LDs.

2. EXPERIMENTAL

We have grown GaN by RP-MOCVD using a higher pressure than a conventional growth pressure. First, a 2-μm-thick n-GaN layer was grown on a c-plane sapphire substrate using a buffer layer grown at 510 °C. The growth pressure was raised from 1 atm up to 1.6 atm. Trimethylgallium and ammonia was used as gallium and nitrogen source. The nominal growth conditions of growth temperature, V-III ratio and growth rate were 1050 °C, 7500 and 3 μm/h, respectively. Then 2μm n-GaN was periodically etched using reactive ion etching (RIE). ELO of n-GaN was carried out at 1 atm using the patterned GaN as the seed layer[13)]. We fabricated laser structures on this re-grown Si-doped GaN layer.

Figure 1 shows schematic structure of the GaN-based LDs. A 1.0-mm-thick n-AlGaN cladding layer was grown on re-grown GaN substrates, followed by a 0.1-μm-thick n-GaN optical guiding layer, GaInN multiple quantum well activating

Laser Optics 2000: Semiconductor Lasers and Optical Communication, Serguei A. Gurevich, Nikolay N. Rosanov, Editors, Proceedings of SPIE Vol. 4354 (2001) © 2001 SPIE · 0277-786X/01/$15.00

layers consisting of 3 pairs of GaInN well layers and GaInN barrier layers, a 20-nm-thick p-AlGaN layer to minimize electron overflow, a 0.1-μm-thick p-GaN optical guiding layer, 0.5-μm-thick modulation-doped AlGaN/GaN superlattice cladding p-layers, and a 0.1-μm-thick p-GaN contact layer. The modulation-doped superlattice cladding layers consisted of 100 pairs of 2.5-nm-thick undoped AlGaN layers and 2.5-nm-thick p-GaN layers. 2.0 to 3.5-μm-width ridge stripes and the n-type electrode structures were formed using RIE. The ridge stripes were aligned just above the lateral re-grown n-GaN regions to prevent coalescent regions of lateral growth. The ohmic metals were Pd/Pt/Au or Ni/Pt/Au for p-type contacts and Ti/Pt/Au for n-type contacts.

When we introduced buried-ridge structures, the ridge stripes were buried by AlGaN before forming n-type electrode structures as shown in Fig. 2. The burying growth was carried out using a patterned SiO_2 mask at a lower growth temperature than 700 °C. In order to stabilize the optical transverse mode, the lateral index step (Δn), the difference in effective refractive index between the inside and outside of the lasing area, plays an important role. The Al contents of the burying layer were varied from x = 15% to 40% to control the refractive index of the AlGaN burying layer. The relatively low-temperature growth of AlGaN was not selective growth, and therefore etching to expose the p-GaN contact layer was required[14].

The cavity mirror was fabricated by cleaving after the thickness of the LD wafers with ridge stripes or buried ridges was reduced to about 100 μm. The length of the cavities was from 500 μm to 700 μm. The rear facet was coated with high-reflection film of 96% reflectivity and the front facet was coated with anti-reflection films of 10% reflectivity.

In order to evaluate the optical quality, the threshold power density of stimulated emission from Si-doped GaN films by optical pumping was measured[15]. Optical pumping was carried out using a 337-nm N_2 laser whose pulse width was 6ns.

3. RESULTS AND DISCUSSION

Figure 3 shows the growth pressure dependence of the threshold power density of stimulated emission from Si-doped GaN. GaN films grown under the growth pressure of 1.6 atm have much lower threshold power density than those grown under the conventional growth pressure of 1 atm. This result agrees with the tendency in the etch-pit densities of GaN films to be lower with higher pressure[9]. These results suggest that the optical properties of GaN films can be improved by using RP-MOCVD. Using these improved GaN-films, ELO was performed in order to obtain GaN film regions with reduced threading dislocation density. While there are threading dislocations of about $10^9 cm^{-1}$ in the seed regions, the lateral over-growth regions have no more than a $10^7 cm^{-1}$ dislocation density (Fig. 4). These two techniques proved very effective in reducing the dislocation density of GaN grown on sapphire substrates. As for the effect of ELO, the cleaving facets of ELO-regrown GaN films were much better than that on sapphire. In fact, the slope efficiency of LDs on ELO-regrown GaN was 20% higher than those on sapphire. This means that the cleaving of GaN films is severely inhibited by the difficulty in cleaving sapphire substrates. Removing the sapphire substrates from GaN films could make the cleaved facets of GaN-based LDs much better.

GaN-based LD structures were fabricated on the improved GaN films. Through optimizations of the LD structure, we succeeded in reducing the input power[16]. Introducing SL cladding structures as p-type layers and a Pd/Pt/Au electrode as a p-type ohmic metal realized an operating voltage of 2 V at the output power of 30 mW, which required for the next generation of optical storage systems. The threshold current depends strongly on the stripe width (w), and the remaining etching depth (d), as defined in Fig. 5. Figure 6 shows typical light output power versus current (L-I) and voltage versus current (V-I) characteristics of a ridge-stripe laser with a 600-μm cavity operated under CW condition at 20 °C. The threshold current was 61.2 mA, which corresponds to a threshold current density of 3.4 kA/cm^2, and the threshold was 5.38 V. This typical LD was operated up to 35 mW without any kink, and the slope efficiency was 0.85 W/A. As shown in Fig. 7, the single-peak emission at 10-mW output power was observed. The FFP of this typical LD at an output power of 10 mW is shown in Fig. 8. Full-width-at-half-maximum (FWHM) angles parallel and perpendicular to the junction plane were 8.0 ° and 27.0 °, respectively. These properties of the emission are appropriate for an application to optical storage systems.

As regard reliability, the results of an aging test of a 500-μm-cavity LD grown on a ELO GaN film at 25 °C under CW conditions is shown in Fig. 9. The output power was maintained at 20 mW automatically through the experiment. The 20-mW emission was also obtained after 500 hours of operation. Figure 10 shows the relation between the dislocation density and the input power and lifetime. We confirmed that lower dislocation density leads to more reliable operation. Furthermore, we found that lifetime is strongly dependent on input power. Our optimization of the LD structure raises the reliability of operation at a high power of 30 mW. To achieve longer lifetime, it is important to reduce not only the dislocation density but also the input power at the operating voltage.

In the above work, both sides of the ridge stripe are covered by an insulator or metal layers. Because of this, the lateral index step (Δn) can be controlled by varying the remaining etching depth. As we have noted above, the remaining etching depth also strongly affects the threshold current. In order to tune Δn value independently from other LD properties, introducing the AlGaN burying process is one solution. Figure 11 shows the dependence of the threshold current on the Al contents of AlGaN burying layer. The threshold current of buried-ridge LDs decreases with increasing Al contents. Considering that the refractive index value of AlGaN is supposed to decrease with increasing the Al content, Fig. 11 reveals that the threshold current became lower with Δn increasing. Effective optical confinement with sufficient Δn must lead to lowering the threshold current, with less optical loss in the waveguide. The FWHM emission angles parallel to the junction plane ($\theta_{//}$) also reflect the confinement. Figure 12 shows that the dependence of $\theta_{//}$ on the Al contents changes significantly at the Al content of 30%. With lower Al contents, the properties of the gain-guided structure are dominant due to insufficient Δn. As the Al content becomes higher, the properties of the index-guided structure become more prominent. With the $Al_{0.4}Ga_{0.6}N$ burying layer, $\theta_{//}$ of the emission shows that an index-guided LD was obtained[17]. This tendency also agrees with the results shown in Fig. 11. Comparing the experimental results with calculated $\theta_{//}$ at different stripe widths, the values of Δn at the Al content of 30% and 40% are estimated as 0.007 and 0.010, respectively (Fig. 13). The experimental results at the Al contents of 15% are plotted far from the calculated lines. This indicates that buried-ridge LDs with $Al_{0.15}Ga_{0.85}N$ burying layers have gain-guiding characteristics. The optical transverse mode of GaN-based LDs is controllable when AlGaN buried-ridge structures are introduced.

4. CONCLUSION

We have grown GaN films of low dislocation density using RP-MOCVD and the ELO technique. GaN-based LD with an optimized structure grown on the improved GaN has been operated up to 35 mW without any kink. Through the optimization of the LD structure, we found the importance not only of a low dislocation density but also the low input power at the operating voltage for the reliable operation. Furthermore, we have introduced AlGaN burying process to the fabrication of GaN-based LDs. AlGaN buried-ridge structures are effective for controlling the optical transverse mode.

ACKNOWLEGEMENT

The authors would like to thank T. Hino, T. Asano, M. Takeya, S. Kijima, T. Tojyo, K. Naganuma, E. Morita and R. Minatoya for their fruitful discussions and technical support. They also thank M. Abe, M. Ohara and M. Yamazaki for their assistance in the experiments. Finally, they would like to thank K. Honda, K. Tamamura, Y. Yabuki, T. Aoki and Dr. O. Kumagai for their encouragement throughout this work.

REFERENCES

1. I. Akasaki, S. Sota, H. Sakai, T. Tanaka, M. Koike, and H. Amano, Electron. Lett. **32**, 1105 (1996).
2. S. Nakamura, M. Senoh, S. Nagahama, N. Iwasa, T. Yamada, T. Matsushita, Y. Sugimoto, and H. Kiyoku, Appl. Phys. Lett. **69**, 4056 (1996).
3. K. Itaya, M. Onomura, J. Nishio, L. Sugiura, S. Saito, M. Suzuki, J. Rennie, S. Nunoue, M. Yamamoto, H. Fujimoto, Y. Kokubun, Y. Ohba, G. Hatakoshi, and M. Ishikawa, Jpn. J. Appl. Phys. **35**, L1315 (1996).
4. J. Edmond, G. Bulman, H. S. Kong, M. Leonard, K. Doverspike, W. Weeks, J. Nicum, S. Sheppard, G. Negley, and D. Slater, *Proc. 2nd Int. Conf. Nitride Semiconductors* p.448 (1997).
5. M. P. Mack, A. Abare, M. Aizcorbe, P. Kozodoy, S. Keller, U. K. Mishra, L. Coldren, and S. DenBaars, MRS Internet J. Nitride Semiconductors. Res. 2, 41 (1997), (Available from http://nsr.mij.mrs.org/2/41/).
6. A. Kuramata, S. Kubota, R. Soejima, K. Domen, K. Horino, and T. Tanahashi, Jpn. J. Appl. Phys. **37**, L1373 (1998)
7. T. Kobayashi, F. Nakamura, K. Naganuma, T. Tojyo, H. Nakajima, T. Asatsuma, H. Kawai and M. Ikeda, Electron. Lett. **34**, 1494 (1998).
8. M. Kuramoto, C. Sasaoka, Y. Hisanaga, A. Kimura, A. Yamaguchi, H.sunakawa, N. Kuroda, M. Nido, A. Usui, and M. Mizuta, Jpn. J. Appl. Phys. **38**, L184 (1999).

9. K. Yanashima, S. Hashimoto, T. Hino, K. Funato, T. Kobayashi, K. Naganuma, T. Tojyo, T. Asano, T. Asatsuma, T. Miyajima, and M. Ikeda, J. Electronic. Mat. 28, 287 (1999).
10. A. Usui, H. Sunakawa, A. Sakai, and A. Yamaguchi, Jpn. J. Appl. Phys. **36**, L899 (1997).
11. O. H. Nam, M. D. Bremser, T. Zheleva, and R. F. Davis, Appl. Phys. Lett. **71**, 2638 (1997).
12. S. Nakamura, M. Senoh, S. Nagahama, T. Matsushita, H. Kiyoku, Y. Sugimoto, T. Kozaki, H. Umemoto, M. Sano, and T. Mukai, Jpn. J. Appl. Phys. **38**, L226 (1999).
13. M. Takeya, K. Yanashima, T. Asano, T. Hino, S. Ikeda, K. Shibuya, S. Kijima, T. Tojyo, S. Ansai, S. Uchida, Y. Yabuki, T. Aoki, T. Asatsuma, M. Ozawa, T. Kobayashi, E. Morita, and M. Ikeda, J. Crystal Growth (to be published as the special issue for IC-MOVPE Xth).
14. T. Asano, K. Yanashima, T. Asatsuma, T. Hino, T, Yamaguchi, S. Tomiya, K. Funato, T. Kobayashi, and M. Ikeda, phys. stat. sol. (a) 176, **23** (1999)
15. K. Funato, S. Hashimoto, K. Yanashima, F. Nakamura, and M. Ikeda, Appl. Phys. Lett. Vol. **75**, 1137 (1999).
16. S. Uchida, S. Kijima, T. Tojyo, S. Ansai, M. Takeya, T. Hino, K. Shibuya, S. Ikeda, T. Asano, K. Yanashima, S. Hashimoto, T. Asatsuma, M. Ozawa, T. Kobayashi, Y. Yabuki, T. Aoki, M. Ikeda, (to be published).
17. T. Asatsuma, H. Nakajima, S. Hashimoto, T. Yamaguchi, H. Yoshida, S. Tomiya, T. Asano, T. Hino, M. Ozawa, T. Miyajima, T. Kobayashi, and M. Ikeda, J. Crystal Growth (to be published as the special issue for IC-MOVPE Xth).

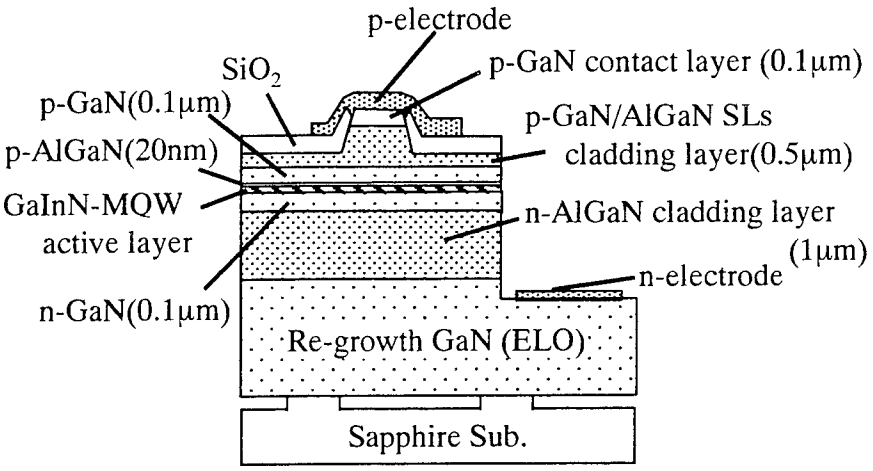

Fig.1 Schematic structure of GaN-based LDs

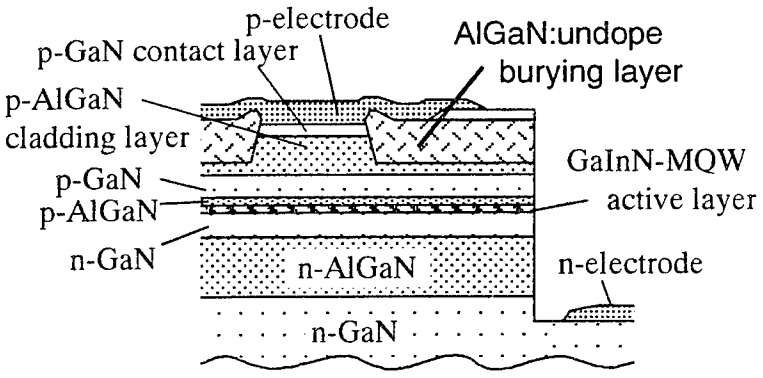

Fig.2 Schematic structure of GaN-based buried-ridge LDs.

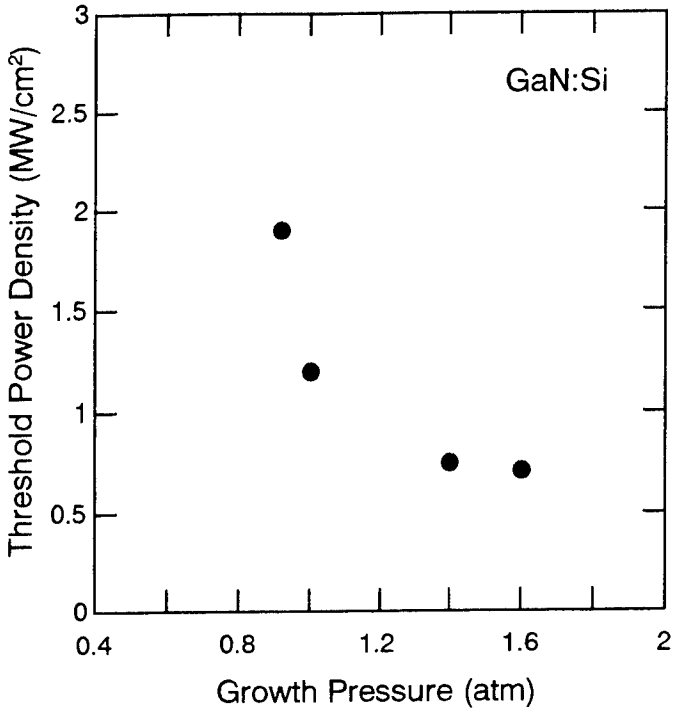

Fig. 3 Threshold power density of n-GaN as a function of growth pressure.

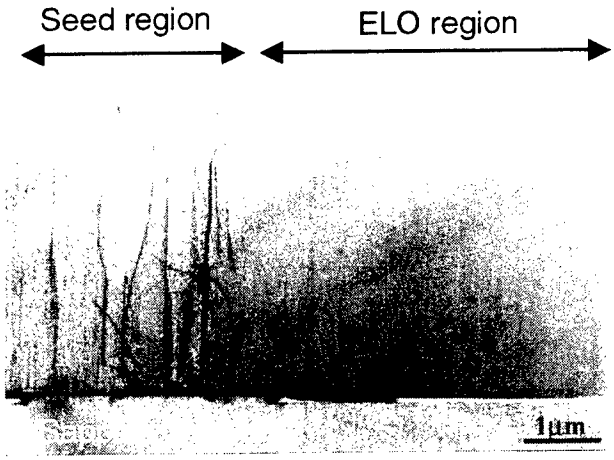

Fig.4 Cross-sectional transmission electron microscopy image of ELO-GaN.

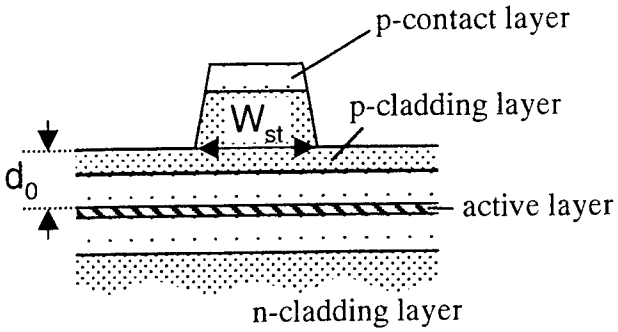

Fig.5 Definition of the stripe width W_{st} and the remaining etching depth d_0.

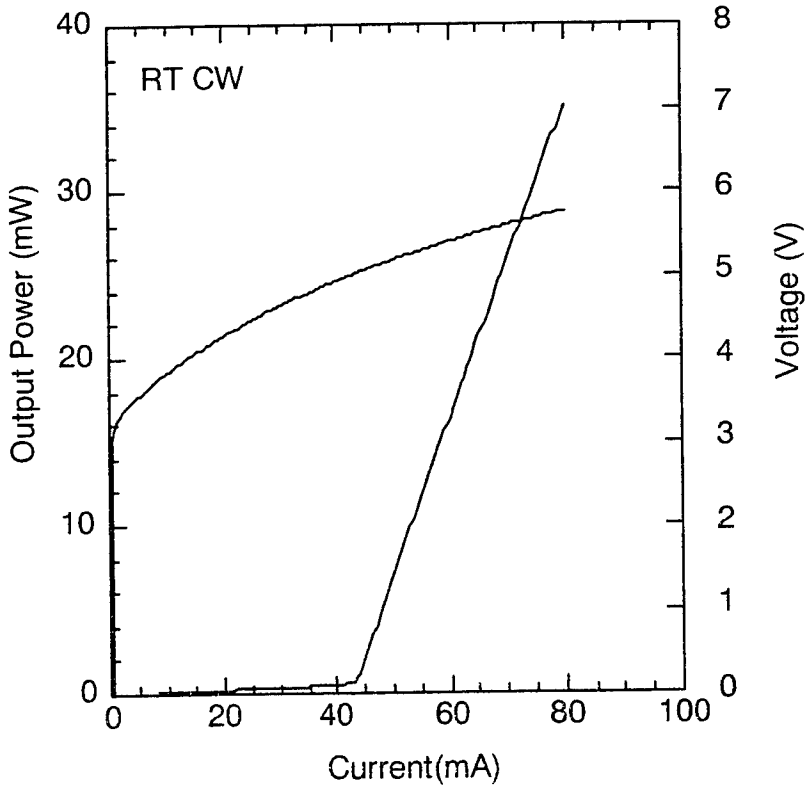

Fig.6 Typical L-I and V-I characteristics under CW operation at 20°C

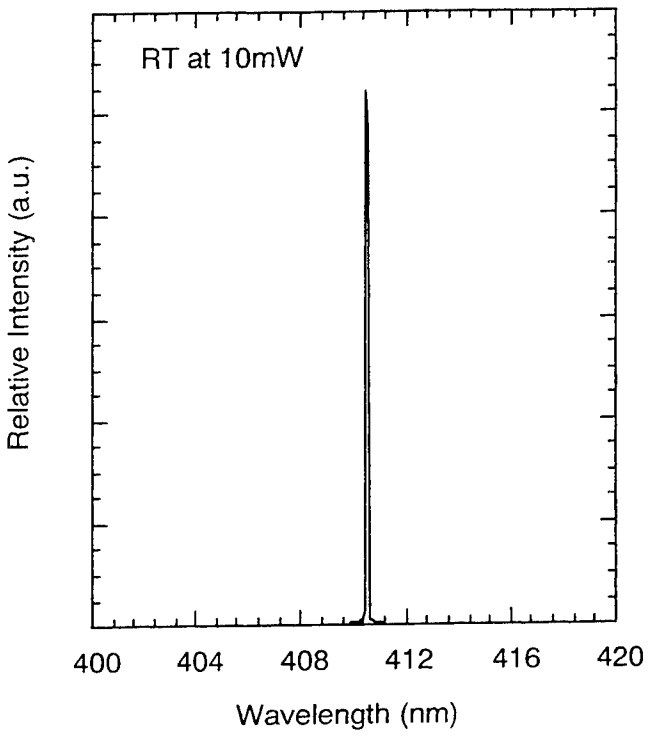

Fig.7 Laser emission spectrum measured under CW operation at output power of 10mW

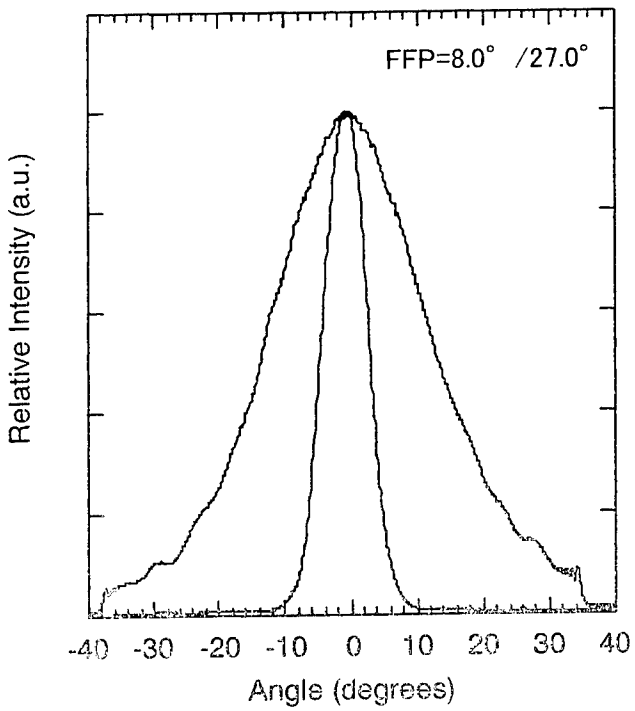

Fig.8 Far Field Patterns measured under CW operation at output power of 10mW

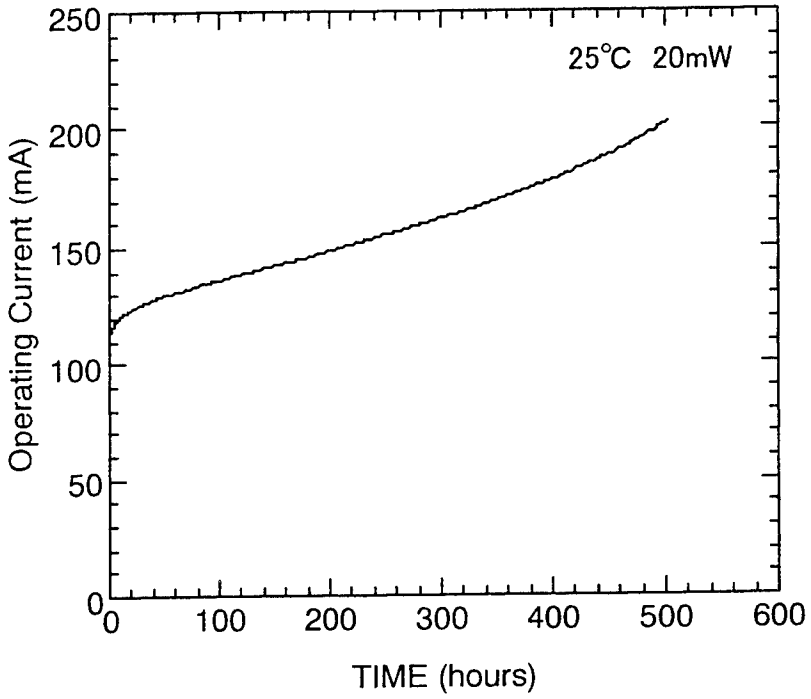

Fig.9 Lifetime test of GaInN laser under CW operation at output power of 20mW

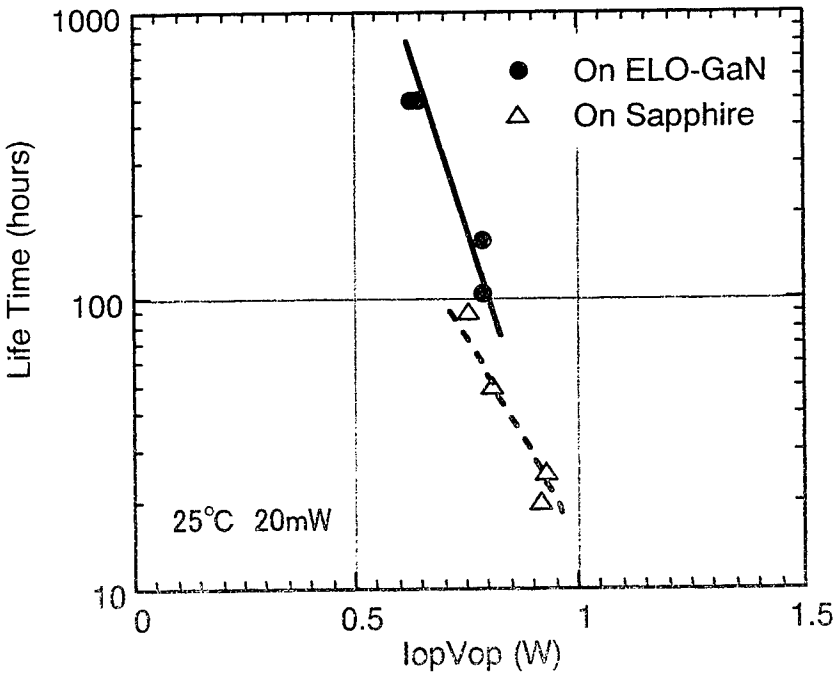

Fig.10 Lifetime vs IopxVop at the initial point.

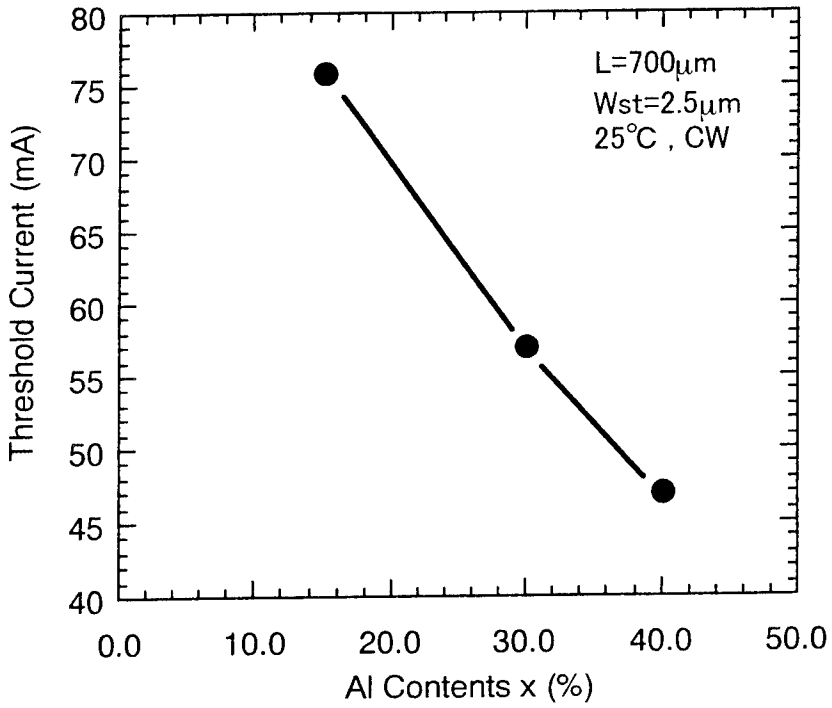

Fig.11 Reduction of Threshold Current with increaseing Al contents.

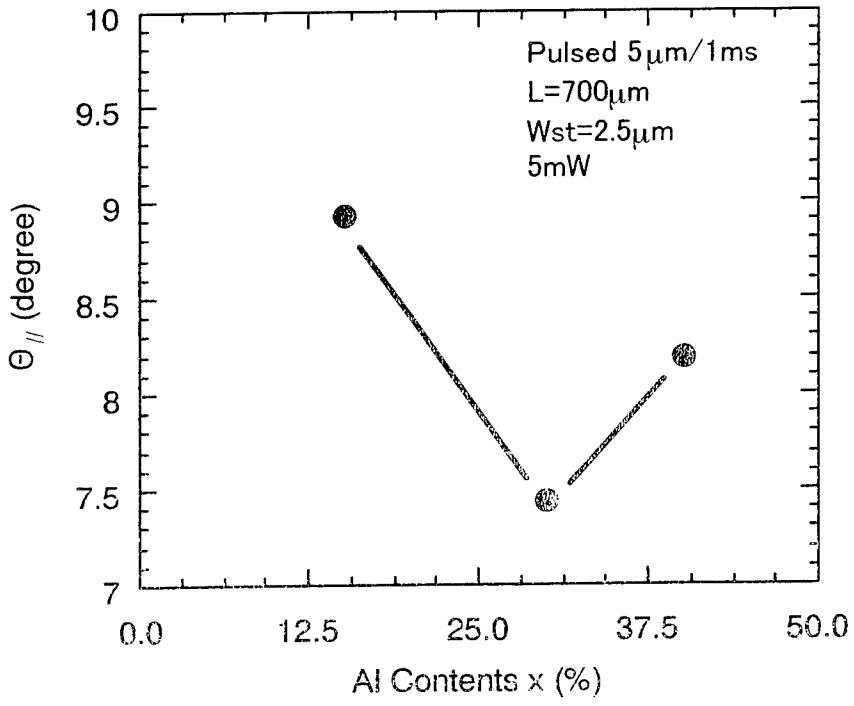

Fig.12 The Transition of $\theta_{//}$ from Gain-guided LD to Index-guided LD.

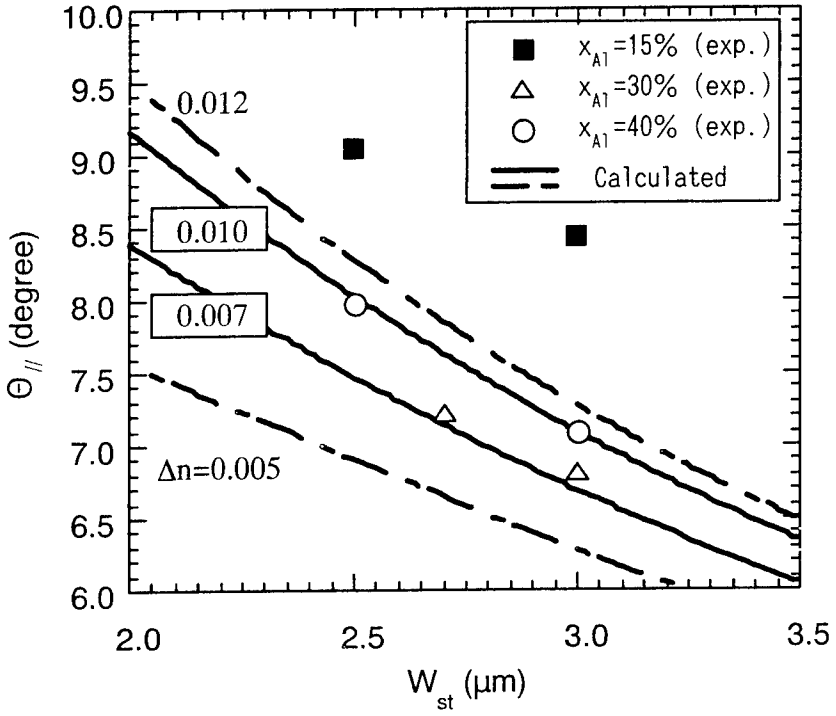

Fig.13 Estimation of Lateral Index StepΔn by comparing experimental and calculated $\theta_{//}$ values.

Waveguide optics of new short-wavelength laser diodes

P. G. Eliseev

Center for High Technology Materials, University of New Mexico
Albuquerque, NM 87106, USA
and P. N. Lebedev Physics Institute, Moscow, 117924 Russia

ABSTRACT

The optical confinement and related issues are considered of novel semiconductor laser structures based on III-group nitrides. The approach of normal modes is used in an analysis of the InGaN-based laser diode that is actually a set of coupled waveguides. Laser emission mode is found to be subjected to internal mode coupling. When phase velocities are close in coupled modes, the interaction is resonantly strong, and produces a significant modification of both the spatial mode configuration and laser threshold. Particularly, the modal gain can be quenched totally keeping the material gain at high level. Therefore such resonance is an important issue in the nitride-based laser designing. Also, the modeling of nitride-based VCSEL is performed using an effective frequency method and laser operation is simulated numerically. The thermal lens effect is shown to be important in the mode formation.

Key words: Semiconductor lasers, nitrides, optical confinement, internal mode coupling, VCSEL modeling.

1. INTRODUCTION

The III-group nitride-based semiconductor structures are active materials for laser diodes in visible and UV wavelength ranges [1-3]. The laser science is quite matured now to propose numerical models and comprehensive numerical simulation of these lasers. It allows engineers to perform effectively the laser design optimization, including those types that are not yet practically realized, like nitride-based electrically-pumped vertical-cavity surface-emitting lasers (VCSELs). In comparison with more traditional semiconductor laser materials (GaAs, InGaAs), nitride-based structures have following features:

1) they cover important short-wavelength range, including UV (practically, the range is 380-450 nm);

2) they are chemical inert and mechanically robust. This seems to be useful to provide reliability of the laser devices. The chemical stability is important especially because of short-wave emission producing active species in the environment that can attack the laser diode surfaces;

3) there is a rather low structural quality of material grown on heterogeneous substrates: the threading dislocation density of 10^8-10^{10} cm^{-2} in ordinary structures on sapphire and $\leq 10^6$ cm^{-2} in special *epitaxial lateral overgrowth* structures (ELOG, see below). Such a high defect content does not prevent efficient light emission from these materials; ELOG structures are shown to be more reliable [2];

4) there is a larger lattice mismatch in working heterojunctions AlGaN/GaN and InGaN/GaN. For a comparison, there are lattice parameter difference of ~2.5% between AlN and GaN whereas it is only 0.14% between the AlAs and GaAs. The misfit is resulted in dislocation networks, threading dislocations and residual stress in epitaxial layers. Typically the mismatched layers are grown rather thin to avoid micro-cracks and layer separation. Additional compensating layers are included sometimes in the structure for the same goal;

5) the operation current in these laser structures is typically higher than in more traditional laser diodes (the threshold is in a range of 4-10 kA/cm^2 at room temperature), and the specific resistivity of materials is higher that in GaAs-based structures. This results in a higher heat generation under the laser operation. So the temperature sensitivity of the structure is of crucial importance.

Laser Optics 2000: Semiconductor Lasers and Optical Communication, Serguei A. Gurevich, Nikolay N. Rosanov, Editors, Proceedings of SPIE Vol. 4354 (2001) © 2001 SPIE · 0277-786X/01/$15.00

6) Due to shorter wavelength the light scattering is more prominent in nitride-based lasers. The scattering occurs on geometrical imperfections and on structural defects in the active region. Therefore the requirements on the geometrical parameters and interface flatness are more rigid.

Typically, these structures include InGaN active region, namely single- or multi-quantum well, barrier layers of InGaN or GaN between active layers if any, some waveguide and cladding layers of GaN and AlGaN. Also GaN cap layer is provided at the top of the structure to reduce the diode resistance. The structure is grown on heterogeneous substrates (sapphire, silicon carbide) with some nitride buffer/substrate intermediate layers (typically, the 30-nm thick buffer layer of GaN immediately on the sapphire surface + 2-4-μm thick GaN layer). The total thickness of the nitride buffer/substrate layer is chosen to maintain optimized quality of the GaN surface that serves as a substrate for the multilayer laser structure. The ELOG technique is elaborated [4] to eliminate a majority of threading dislocations and to increase the thickness of the nitride buffer/substrate up to tens or even hundred micrometers. It is based on a possibility to restrict the heritage of large amount of threading dislocations that generated at the mismatched interface by an introducing the insulator mask. The mask allows the single crystal growth whereas the dislocations can enter above only through the windows in a mask. Thus some parts of the overgrown layer appear to be almost free from inherited dislocations.

One of important issues of the laser design is the waveguiding optics in the multilayer epitaxial structures of both versions of diodes, namely, edge-emitting ones and vertical-cavity ones. The guiding is provided in edge-emitting lasers by the index steps at heterojunction interfaces (index-guiding). In vertical-cavity device, the heterojunction interfaces are normal to the optical flux and guiding is provided by profile of gain and absorption (gain-guiding). In this paper we consider the optical modeling of InGaN-based laser structures and analyze the optical confinement and resonant effects of *internal mode coupling* [5,6]. The effective index of coupled modes and modal gain is calculated in dependence of the size parameters of waveguides and of optical barriers (AlGaN cladding layers). It is found that the internal mode coupling can modify mode configuration and, if resonance occurs, it can depress substantially the modal gain and even stop laser action at all. These data are important for the laser designing as they give rules to control resonance behavior.

2. REFRACTIVE INDEX

The optical confinement in nitride-based structures is provided by a strong dispersion of the refractive index in vicinity of the intrinsic absorption edge. The refractive index of GaN is used from Sellmeier approximation of experimental data given in Ref. [7]:

$$n^2(\lambda) = A + B/[1 - (C/\lambda)^2], \qquad (1)$$

with fitting parameters $A = 4.37$; $B = 1.0$; $C = 0.3$ μm (the normal dispersion branch below the absorption edge was fitted between 370 and 600 nm). We also calculated the group index which is important for the interpretation of longitudinal mode spectrum:

$$n^*(\lambda) = n + B/(nS), \qquad (2)$$

where $S = (\lambda/C) - (C/\lambda)$. Results are shown in Fig. 1. Calculations for AlGaN are made using data for $Al_{0.1}Ga_{0.9}As$ in the same Ref. [7] with linear interpolation of Sellmeier parameters. There are several other publications on refractive index of GaN and AlGaN [8-10], but no direct measurements are found for InGaN. We assume that the InGaN alloy of the active region at the laser wavelength 400 nm is characterized the same index as GaN at its laser wavelength of ~370 nm. We understand, that the index dispersion curve in narrower-bandgap InGaN is shifted as compared with one of GaN into longer wavelength side. On the other hand, the spectral operation point of the laser is placed at about the same distance from the index peak in both materials. The peak (as it is seen in Fig.1, by experimental points) is explained by Kramers-Kroenig dispersion relationship in a vicinity of the sharp intrinsic absorption edge. The index dispersion changes a sign somewhat above the edge. Usually the laser operates also above the

edge and rather close to this peak but at the *normal* dispersion edge ($dn/d\lambda < 0$). This is typical for GaAs and other materials where group index is regularly larger than phase one, $n^* = n - \lambda dn/d\lambda > n$. The group index rules the longitudinal intermode spacing, $\delta\lambda = \lambda^2/(2n^*L)$, where L is the cavity length. In InGaN-based laser diode, according to Ref. [11] the intermode spacing of 0.042 nm in the 550-μm long cavity at wavelength of 405 nm corresponds to $n^* = 3.6$. Such a value in bulk GaN is expected at $\lambda = 365$ nm where the phase index is ~2.75 (see Fig. 1). This wavelength is corresponding very closely to the energy bandgap of GaN (3.39 eV at room temperature), therefore, these parameters could be characteristic for laser action in GaN. When InGaN is used, the spectral point is shifted into longer wavelength, but using analogue to GaN one can expect the optical parameters of InGaN at this point rather close to that in GaN. This gives a reasonable estimation for parameters of InGaN active region at the laser wavelength ($n = 2.75$, $n^* = 3.6$ near $\lambda = 400$ nm), certainly, for small amount (<20%) of indium in the alloy.

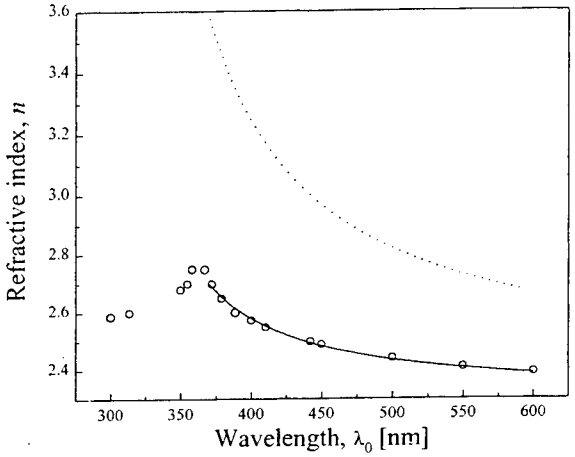

Fig. 1. Refractive index of GaN: circles are for experimental data [7] that are fitted by solid curve according to the Sellmeier approximation (1); dotted curve is for calculated group index (2). The group index at 365 nm is about 3.6 which is ~31% larger than phase index. The group index in InGaN-based laser diode is ~3.6 from experimental study of longitudinal mode spacing [11].

In general, the refractive index of InGaN quantum well material is different from the bulk value. Particularly, in stressed quantum well, the intrinsic absorption edge is substantially splitted by the stress giving a rise for three peaks of the index (due to three valence bands involved), and the individual magnitude is lowered by this splitting as compared to the bulk material. Theoretical calculation are performed in Ref. [12].

An important issue is a sensitivity of the refractive index to temperature T and carrier density N. Both these factors are involved in the operation regime because of some thermal lens effect and strong optical nonlinearity effects (including the line broadening). The temperature coefficient is reported in GaN to be $(1/n)dn/dT = 3.81\times10^{-5}$ K^{-1} (see [13] and references there). Carrier density effect is known in terms of the linewidth enhancement factor $\alpha = (d\mathrm{Re}\varepsilon/dN)/(d\mathrm{Im}\varepsilon/dN)$ where ε is the relative dielectric constant. Theoretical calculations of α in bulk GaN are given in Ref. [14]. The results have been obtained using the model accounting for the Coulomb interaction of carriers. At room temperature, it is found the α factor in the range of 1.7-1.9 in the spectral peak of the gain and in the range of N between 10^{19} and 1.4×10^{19} cm^{-3}. This means relatively weak anti-guiding effect caused by free carriers in the active region of the lasers. An estimation can be given for $dn/dN \approx 2.4\times10^{-20}$ cm^3. We see that reliable data on optical characteristics is available for GaN, but not for InGaN, and one has to get them by extrapolation from GaN to InGaN. The extrapolation is acceptable for small amount of indium in the alloy. A difficulty to measure the refractive index in InGaN is associated with a fact that InGaN exists only in thin layers and typically contains many defects and substantial deviations from composition homogeneity. The alloy is known to be subjected to the phase separation, therefore the composition homogeneity is not an easy problem. Therefore real InGaN samples are thin and ultra-thin layers with strong misfit stress (partially relaxed by dislocation formation) and with composition variations (depending on the thermal history of each sample).

3. OPTICAL CONFINEMENT

Interface between InGaN active layer and GaN (both bulk material) can provide an estimated refractive index step of ~0.17 at the laser wavelength of 400 nm. This means that the double-heterostructure can be made in this basis (with no adding aluminum containing layers). The first order cutoff thickness for corresponding InGaN layer should be ~200 nm. Actually the InGaN-based laser structure are consisted with a single- or multi-wuantum-well active region whereas the waveguide region is formed by transparent GaN layers sandwiched between AlGaN claddings. For an design orientation, the cutoff thickness for AlGaN/GaN/AlGaN waveguide is expected to be ~230 nm at 400 nm - wavelength and at aluminum content of ~10%. Therefore 100-nm thick GaN waveguiding layers at both sides of the active region are suitable for a single-mode index-guiding in the vertical plane. The typical laser structure is presented in Table 1 and optical parameters have been assumed in our calculation of the optical confinement factor in dependence on various size parameters of the laser structure.

Table 1. Assumed optical parameters of materials consisting the InGaN-based laser diode structure; n is real refractive index, k is extinction coefficient [6].

Material	n	k	Thickness, nm	Comments
Au	1.5	1.7	∞	Electrode material: data at 400 nm
p-GaN	2.55	0.000032	100-2000	p-cap
p-$Al_{0.07}Ga_{0.93}N$	2.50	0.000032	300-800	p-cladding (optical barrier)
p-GaN	2.55	0.000032	100	p-waveguide
$4\times In_{0.15}Ga_{0.85}N$ + $3\times In_{0.02}Ga_{0.98}N$	2.75 2.63	-0.0032 0.000032	4×3.5 3×7	MQW active region: g_{mat} = 1000 cm^{-1} barriers between active wells
n-GaN	2.55	0.000032	100	n-waveguide
n-$Al_{0.07}Ga_{0.93}N$	2.50	0.000032	300-800	n-cladding (optical barrier)
n-GaN	2.55	0.000032	100-4000	n-substrate
α-Al_2O_3	1.77	0	∞	sapphire substrate

We assume the active region contains 4 quantum-well layers of $In_{0.15}Ga_{0.85}N$, providing a gain for the laser action at 400 nm. Active quantum wells are separated by $In_{0.02}Ga_{0.98}N$ layers by 7 nm each. These seven layers with n- and p-waveguide layers of GaN forms 235-nm thick active waveguide (see Fig. 2).

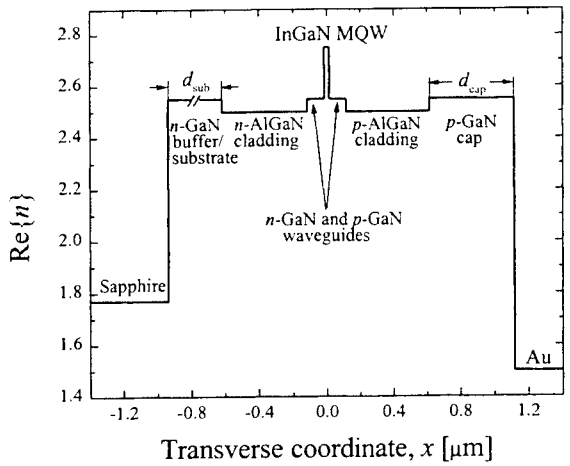

Fig. 2. Profile of refractive index across the typical edge-emitting InGaN-AlGaN-GaN diode laser grown on the sapphire substrate (left end). Material of the metal electrode is Au (right end). AlGaN cladding layers at both sides of the active region provide optical barriers for photons. GaN buffer/substrate layer and GaN cap layer are both the parasitic waveguides for photons tunneling through the optical barriers.

4. RESONANT PHENOMENA AND GHOST MODE CONCEPT

The nitride materials are formed as a multi-layer films on the sapphire or other heterogeneous substrate. The optical isolation between structure layers and between nitride film and substrate is usually not perfect,

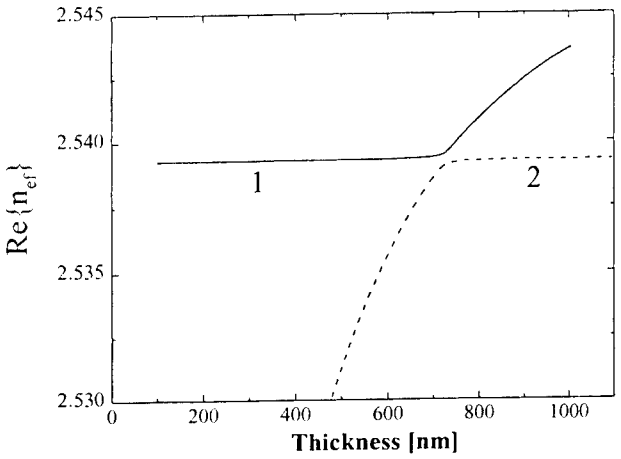

Fig. 3. Dispersion curves of two normal modes near the resonant point. Dependence of the effective index on the thickness of the GaN cap layer is shown. The anti-crossing occurs at the synchronism point, and mode 1 is substituted by mode 2 as a dominant mode for the laser emission.

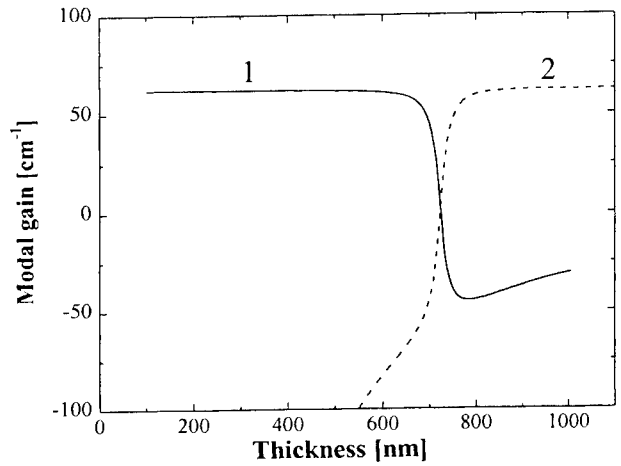

Fig. 4. Dependence of the modal gain on the GaN cap layer thickness of the same normal modes as shown in Fig. 3. Mode 1 is substituted by mode 2 after the resonant point, and model gain of ~60 cm^{-1} is sufficient to maintain the laser oscillations in mode 1 before the resonance and in mode 2 after the resonance. However at very resonance the modal gain drops down to about zero. Therefore, no laser oscillation is expected under resonant conditions.

particularly due to small thickness of confining layers. As a result, the laser emission penetrates into layers outside the active region and into substrate. It can be accumulated in guiding layers of the diode chip and reflected by remote surfaces, particularly, by the bottom surface of the substrate. An important property of the chip structure is the transparency of all layers for the laser emission. This property is the same as in InGaAs QW lasers grown at GaAs substrate. In Ref. [5], the model of coupled waveguides (active and passive) was developed and applied to InGaAs lasers. There are transparent dielectric waveguides for laser emission ("parasitic" waveguides: cap layer, stop-etch layers, substrate). Each waveguide contains a system of modes ("ghost" modes) which generally are rather different from excited mode (or modes) of active

region ("active mode"). However, ghost modes can interact with active mode and can consume energy from active mode. Such an interaction was called *mode internal coupling* [5]. The essence is that there are passive waveduides in the diode chip with own systems of guided (ghost) modes, which can interact with the mode of laser emission. The chip of these laser diodes is almost entirely transparent to the emission of InGaAs active region. The *internal mode coupling* is shown to modify the spatial profile of the emitted mode (including modification of near- and far-field patterns), to modify the spectral distribution (producing some spectral waving in the intensity of superluminescent modes), and to modify the modal gain even to prevent laser action at all. Similar situation is in InGaN/AlGaN laser diodes where laser emission easily penetrates into all layers of the chip due to diffraction and scattering. It can be accumulated in the layers having guiding properties (GaN cap layer, etch-stop layers, GaN substrate, some auxiliary layers introduced to stabilize the epitaxial structure). The approach of normal modes of coupled waveguides (see, for example, [6]) allow us to understand the complex behavior of these modes which includes very strong effects at resonant conditions (see Figs. 3-5). Also, in spectral studies of blue laser diodes [1,15], it was found the waving in superluminescent spectrum resembling that in InGaAs lasers. It seems, the concept of ghost mode will be of practical importance in InGaN-based lasers. In the modeling of the waveguiding properties of InGaN-based lasers, it was noticed some resonant-like penetration of laser mode into passive regions [16]. Also in Ref. [17], it was also noticed that there are some resonant peaks of losses and minima of confinement factor in the laser emission mode along with variation of the parameters of the active waveguide region. These phenomena are of the same nature as above mentioned.

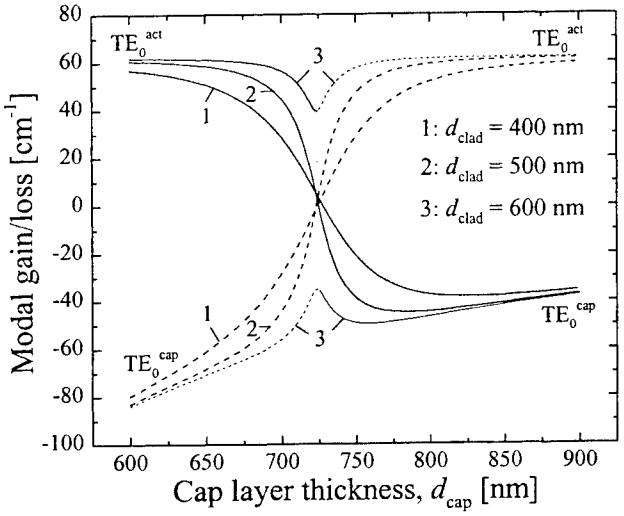

Fig. 5. Modal gain of two normal modes in vicinity of the substitution point against the cap layer thickness. Three different values of the cladding layer thickness are assumed in calculations as shown (curves 1-3). The normal mode substitution occurs at cap layer thickness of 724 nm. A deep minimum of the modal gain leads to stopping of laser action when the cladding thickness is 400 or 500 nm. Increase of the cladding thickness leads to narrowing and reducing of the gain dip.

There are a few reports on spatial distribution of the emission from InGaN-based laser diodes [18-20] and a complex character of the light directionality has been indicated. The coupled mode emission seems to be involved with a some portion of power coming from passive GaN parts.

We can formulate our results as rules that is suitable to remember when the system under consideration is coupled waveguides. We associate these conclusions with the modal behavior along with an increase of the thickness d of parasitic waveguide.

1) The effective index of normal modes $n_{eff}(d)$ follows almost the same curves as those of uncoupled modes except regions near crossing points: instead of crossing the *anti-crossing* occurs. As a result, there are no spatial mode degeneracy even if both uncoupled mode have the same phase velocity.
2) According to anti-crossing behavior, mode of the active region (*laser* mode) is not a single normal mode, but it corresponds to different normal modes. Thus the "mode of laser emission" is actually one of a set of normal modes: they substitute each other and this occurs at every anti-crossing point.

3) Out of the *anti-crossing* vicinity, the modal profile of normal mode is close to the corresponding uncoupled mode, but it contains certain additional bumps at tails coming to other waveguide layers. In terms of *supermodes*, there are in-phase or anti-phase combinations of main mode and modes of parasitic waveguides. In-phase combination means that nearest bumps of partial (uncoupled) modes are of the same sign; anti-phase combination means opposite signs with a field node between.
4) As an most important case, the *laser* mode contains in-phase components at wings corresponding to uncoupled modes with larger effective index and anti-phase components corresponding to uncoupled modes with smaller effective index.
5) When phase velocities of uncoupled modes coincide, the resonant coupling takes place with a power flow shared between interacting components evenly. In such a case, the modal gain in both normal modes can be substantially depressed.

5. VCSEL MODELING: GAIN BALANCE

The vertical-cavity surface-emitting laser (VCSEL) is another important version of the diode lasers that is under intense researches as applied to nitride-based structures. There is report on optically-pumped vertical-cavity AlGaN/GaN/InGaN structure with Bragg reflectors [21], but not yet data on corresponding electrically-pumped nitride-based VCSEL. Usual problem of VCSEL design is to supply sufficient modal gain in the vertical direction that is much lower than that in horizontal direction of edge-emitting devices. This leads to a necessity to provide higher quality factor of the vertical cavity, usually using high-reflectivity Bragg reflectors. The active region in above-mentioned Ref. [21] has been consisted by 26 InGaN quantum wells 3-nm thick each. There the spectral narrowing has been demonstrated to ~0.1 nm at wavelength of 399 nm. In previous papers claiming observation of vertical-cavity lasing under optical pumping the results are less convincing for quantitative analysis. The issue is that there is an intense superluminescence along the active layer under strong pumping. It can be observed in the surface-emitted beam due to optical scattering in the active region. Sometimes such a scattering is produced by microcracks that can provide simultaneously some cavities for in-plane lasing. However, in a short-wavelength structures the geometrical irregularities of the in-plane waveguide can give a rise for a stronger scattering than one in more traditinal GaAs-based lasers. So even in absence of microcracks, the in-plane lasing would be seen in the surface-emitting geometry as a result of light scattering. Thus, in some publications the claimed surface-emitting lasing could be simply a result of scattering by non-flat interfaces of the in-plane superluminescence or in-plane lasing. In Ref. [22], a spectral narrowing is observed (to about 25 meV at 16 K) of surface-emitted radiation with an estimate of the gain in InGaN of $\sim 2\times10^5$ cm^{-1}. The gain seems to be overestimated as available gain in InGaN under pumping of 1 MW/cm^2 is typically by 2-3 orders lower. The overestimation follows from the assumption that the lasing threshold condition is fulfilled for a 150-nm thick InGaN active region of the vertical cavity. There are rather low reflectivity at both ends of supposed vertical cavity, namely 2.4% at the GaN/sapphire interface and 17% at the GaN/air interface. So the Q-factor seems to be much lower than in Bragg-reflector confined cavity in Ref. [21] where the reflectivity is at the level of 98 and 99.8% at the cavity ends, respectively. The narrowing observed in Ref. [22] do not indicate unambiguously the laser action: spectral bandwidth is more than the thermal energy kT. It can be, but not necessarily, the result of in-plane superluminescence that reaches the vertically-oriented photodetector by scattering under ~90°. If one assume the gain in the active region as large as $\sim 2\times10^5$ cm^{-1} and the optical confinement factor of ~0.1 for horizontal propagation in 150-nm thick active waveguide, the single-pass gain of the amplified spontaneous emission (ASE) along the illuminated spot (400-μm wide) would be $\exp(800) \approx 10^{347}$. Obviously, this huge gain would be undergone to strong saturation, so actual material gain should be much less than assumed value. The realistic magnitude is about $(2\text{-}5)\times10^3$ cm^{-1}, that gives in-plane single-pass amplification of $\geq 10^3$. This material gain is not enough for vertical cavity lasing, but it provides in-plane ASE that is ≥1000 times stronger than vertical ASE. So scattered 0.1% of the in-plane ASE would be comparable with the direct vertical emission. The achievement of the vertical cavity lasing seems to be not easy task and requires rather high cavity-end reflectivity. According to Ref. [21], 98%-reflectivity is achievable with 43 pairs of quarter-lambda layers (each pair includes 38-nm thick GaN and 40-nm thick $Al_{0.34}Ga_{0.66}N$). Such a structure is placed on the buffer/substrate side and at top of the laser structure, the dielectric Bragg reflector is placed, namely 15-pair SiO_2/ZrO_2 structure providing reflectivity of 99.8% at 400 nm wavelength.

For the 1-μm long vertical cavity with 78-nm total thickness of active region and geometric-mean reflectivity ≥98.5% (we assume internal attenuation coefficient of 10 cm^{-1}) a sufficient material gain is ~ 2×10^3 cm^{-1} that seems to be quite realistic. The material gain as estimated in Ref. [21] is 890 cm^{-1} at room temperature. An estimated pumping rate (optical power absorbed in the active region) was about 250 kW/cm^2 at wavelength of 367 nm, and it corresponds to the injection current of 74 kA/cm^2 in short pulses.

6. VCSEL MODELING: 3-D NUMERICAL SIMULATOR

We developed a computer program solving a 3-D boundary problem for following coupled systems: electrical system (electrical potential and vector of current density over whole semiconductor chip), electronic system (generation, diffusion and recombination of excess carriers in the actirve region), thermal system (temperature distribution and profiles of temperature sensitive refractive index over whole mode volume), optical system (distribution of electromagnetic field across the cavity according to light amplification, absorption and diffraction over whole vertical cavity). Some details of the numerical simulation are given in Refs. [23]. For this particular case of the nitride-based VCSEL modeling we use the cylindrical geometry with dielectric aperture of the current window. Because of the poor conductivity in Bragg reflectors, the intra-cavity contacted version of the VCSEL is treated (see Fig. 6). The optical output is designed through the bottom of the structure (through the sapphire substrate), and the bottom of the sapphire substrate is assumed to be maintained at constant (room) temperature. The temperature dependencies are included for resistivity in all conducting layers, for optical bandgap, refractive index, heat conductivity, recombination coefficients and material gain. The optical model is based on the effective frequency method (EFM) [24] combined with the rate equations in the active region. The model of the optical gain is also developed for InGaN taking into account the band tails. The EFM is extended for the realistic situation of optical cavity parameters continuously dependent on the radius. The requirement of the EFM applicability is the change of parameters in the radial direction should be slow. On this basis, we include in the consideration following features: continuous radial dependence of the gain/absorption in active plane according to the distribution of excess carriers, continuous profile of refractive index across the vertical cavity according to the variation of temperature, presence of ring metal contacts outside the cavity aperture, non-uniform profile of the pumping current (strong current crowding at the periphery of the cavity aperture), non-uniform temperature-induced detuning of Bragg reflectors, radiation transport in the lateral direction, etc.

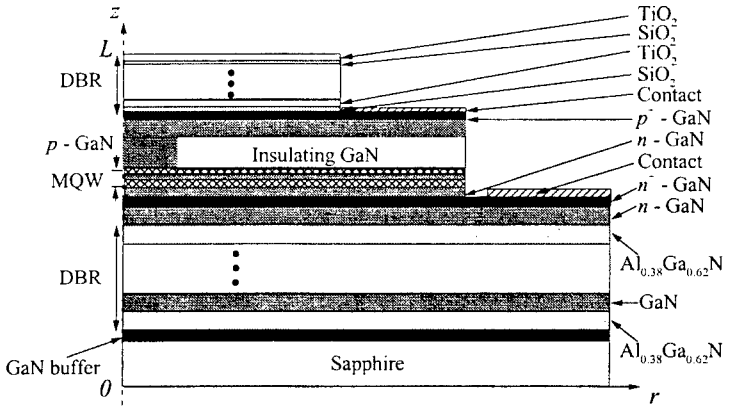

Fig. 6. Structure of intra-cavity-contact VCSEL diode considered in this paper. A half of cross-section is shown of the cylindrically symmetric chip.

Combining the optical modeling with electrical and thermal modeling over whole diode chip, and with diffusion/recombination model for the active plane, we obtain effective numerical simulator of nitride-based VCSEL, that seems to be most complicated semiconductor device ever subjected to a comprehensive simulation. Below we demonstrate particular results of optical modeling for VCSEL with multi-quantum-well active region of 10 mm in diameter. The 3- or 4-λ long cavity is placed between Bragg reflectors, one (bottom one) composed by 43 pairs AlGaN/GaN layers and another (top one) composed by 7 pairs of TiO_2/SiO_2 layers. The emission comes outside through the bottom Bragg reflector and sapphire substrate (see Fig. 6). The current is assumed to be confined by dielectric (oxide) aperture and both electrodes are designed at the same side of the substrate. The current does not pass Bragg structures due to the intra-cavity-contact configuration used. Preliminary optimization of the design allows us to simulate CW laser action in the VCSEL and to analyze the influence of different parameters on the laser performance.

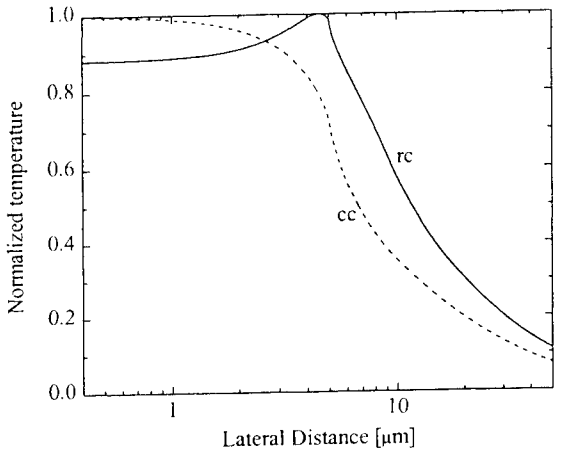

Fig. 7. Radial temperature profiles in CW regime of two versions of nitride-based VCSEL. Solid line is for ring-contact diode that give a rise for a strong current crowding at the peripheral part of the current window (radis of 5 μm). This leads to a rise of the temperature peak near the edge of window. Dashed line is given for circular-contact diode. It differs by a metal semitransparent layer inserted on top surface of diode. The circular contact remove the lateral temperature peak.

The lowest lasing threshold is expected at about 12 kA/cm^2 and the output power is followed up to a thermal roll down at about 25 mW with rather high external efficiency. The predominant mode is a fundamental one LP_{01} in the isothermal approach, whereas under CW operation the lasing occurs at LP_{11} mode. This change of the mode order is a result of the thermal lens effect that provides an enhancement of the index guiding whereas a weak initial lateral confinement has been provided by a gain guiding. The temperature profiles in a normalized scale are shown in Fig. 7. Two cases are shown: ring-contact is labeled by **rc**, circular contact is labeled **cc**.

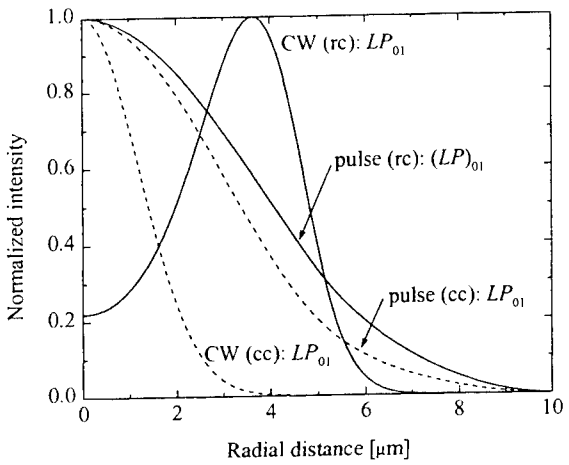

Fig. 8. Radial profiles of optical modes in ring-contact (rc) and circular-contact (cc) diodes. A comparison is given for a fundamental mode LP_{01} that is influenced by the thermal lens. In pulse regime (isothermal condition) there is no thermal lense and mode is bell-shaped (quasi- Gaussian), whereas in CW regime the profile is distorted by the thermal lens: it is peaked at the edge of the current window in rc-case and narrowed to the center in cc-case.

The thermal lens formed under CW condition is complicated: it has a temperature (and index) peak at the aperture edges in the **rc**-case, therefore, the central part of the aperture is undergone to thermal anti-guiding which acts to suppress the fundamental mode. Its profile can be simulated by special numerical experiment with exclusion of the LP_{11} mode. It is seen that the profile of the fundamental mode becomes non-Gaussian, with out-of-axis peaks (see Fig. 8). In order to modify the heat sources distribution, we simulated an insertion of the semitransparent metal layer on the top of the diode chip (**cc**-case) to provide more uniform current distribution. In this case the cavity losses increases due to absorption in the metal, and the lasing threshold increases. However the selection of the fundamental mode is not easy at fixed aperture. If the aperture is decreased, the fundamental mode lasing is expected in 4-μm wide cavity.

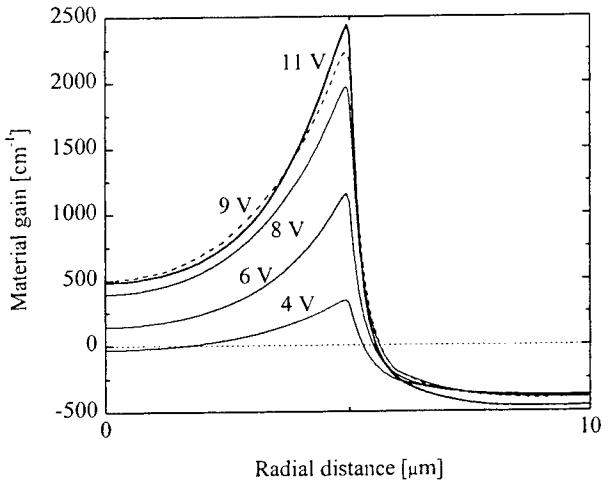

Fig. 9. Radial profile of material gain at different diode voltage (ring-contact case). Peak of the gain is placed at the edge of active region, and it is depressed in the center due to a strong current crowding. Above the threshold (~9 V) the gain profile is distorted due to the spatial hole burning. Peak continues to grow but in central part there is some additional depression of gain to maintain almost constant modal gein.

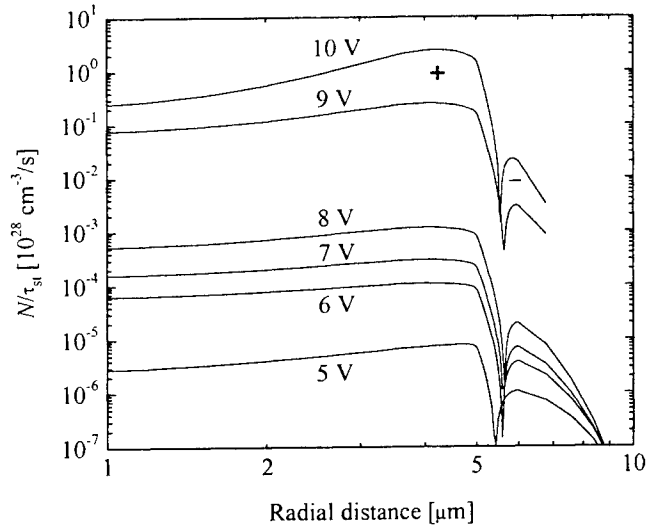

Fig. 10. Radial profile of stimulated recombination rate (ring-contact case). Notice the value changes a sign beyond the edge of the current window (at radius of 5 μm). Inside the active region the rate is positive providing generation of photons of laser radiation. Outside the active region the rate is negative, the photons of the laser radiation are consumed to generate electron-hole pairs. Therefore, the mode of the laser oscillation provides certain radiation transport in the radial direction.

Current crowding in the case of ring-contact configuration leads to nonuniformity of material gain as it is seen in Fig. 9. The lasing threshold is about 9 V. It is seen that the gain curve above the threshold goes in such a manner that the gain drops down near the center while it continues to grow near the edge. As a result, a curve for 11 V crosses one for 9 V. This behavior corresponds to a spatial hole burning when a overlapping of the gain and mode profiles is not optimal. Obviously, the increase of the gain near the edge of the current window makes possible excitation of higher-order modes. Therefore the suppression of the current crowding is desirable to get a stable single-mode laser operation.

In Fig. 10 we show the calculated distribution of the stimulated recombination rate at different diode voltage. This rate can not be directly measured in lasers, but can be easily obtained in numerical simulation. The distribution indicates what parts of the active region gives a contribution into laser radiation. The rate grows significantly as the pumping rate approaches the laser oscillation threshold. It is seen that main contribution goes from peripheral parts of the active region, and there is a depression in the center. Also, the electron-hole pair generation occurs outside the active region. This is an illustration of the fact that vertical optical flow is accompanied with a lateral transport of the pumping power.

7. DISCUSSION AND CONCLUSIONS

The optical modeling of the nitride-based lasers is presented for both main laser configuration, edge- and surface-emitting ones. A normal mode approach is used for edge-emitting lasers, and most important finding is a complicated behavior of the emission mode when the size parameters are changes continuously. The laser emission goes by different normal modes that are modes of coupled system of waveguiding layers. Typical normal mode evolution along with an increase of the parasitic waveguide thickness is as follows. The "dark" mode appears in the parasitic waveguide above its cutoff; it has a small bump in the active region. When its propagation constant approaches one of the mode of laser emission, its intensity grows by consuming the gain in active region. So the mode becomes "bright" and competitive to lasing one. It substitutes the latter and serves as the lasing mode until another ghost mode replaces it. Then it goes again into a "dark" state. Substitution occurs in resonance points, and these points are characterized by a depression of the modal gain. There are several ways to avoid the resonant gain depression: 1) increase of the optical barriers (increase of AlGaN cladding-layer thickness and/or amount of Al in it); 2) increase of the effective index of the active mode above index of GaN; 3) choice of not-resonant thickness of all parasitic waveguides. Notice, that the resonance can occur due to change of the propagation constant of the active mode as a result of the free-carrier effect and temperature effect on the refractive index. This would lead to a negative differential gain or even to a stopping of the laser action. The detailed numerical modeling allows us to predict resonance behavior and avoid undesirable parameters of the structure.

In VCSEL devices, we propose a most detailed numerical modeling that allows us to simulate the device that is not yet practically realized. The mode pattern and *L-I* curves are obtained along with distributions of all important parameters mapped over whole diode chip. This gives a tool for a prediction of behavior of various diode modification under different operation regimes and for an optimization of the laser design. A promising version of intra-cavity-contact VCSEL is considered in details. The laser threshold of ~12 kA/cm^2 is predicted in a 10-μm-in-diameter diode. Further wide scale numerical experiments are planned.

8. ACKNOWLEDGMENTS

Author express acknowledgments to colleagues M. Osinski, G. A. Smolyakov, V. A. Smagley of the Center for High Technology, UNM, Albuquerque, NM, for taking valuable parts in presented researches.

9. REFERENCES

1. S. Nakamura and G. Fasol, *The Blue Laser Diode*, Springer-Verlag, Berlin, 1997.
2. S. Nakamura, "InGaN-based laser diodes with an estimated lifetime of longer than 10,000 hours", *Proc. SPIE*, 3283 (I) 2-13 (1998).

3. I. Akasaki, S. Sota, H. Sakai, T. Tanaka, M. Koike, and H. Amano, "Shortest wavelength semiconductor laser diode". *Electron. Lett.*, **32** (12), 1105 (1996).
4. S. Nakamura, M. Senoh, S. Nagahama, N. Iwasa, T. Yamada, T. Matsushita, H. Kiyoku, Y. Sugimato, T. Kozaki, H. Umemeto, M. Sano, and K. Chocho, *Appl. Phys. Lett.*, 72, 211 (1998).
5. P. G. Eliseev and A. E. Drakin, "Analysis of the mode internal coupling in InGaAs/GaAs laser diodes", *Laser Physics*, 4 (3), 485-492 (1994).
6. P. G. Eliseev, G. A. Smolyakov, and M. Osinski, "Ghost modes and resonant effects in AlGaN-InGaN-GaN lasers", *IEEE J. Select. Topics Quant. Electron.*, 5 (3) 771-779 (1999).
7. H. Amano, N. Watanabe, N. Koide, I. Akasaki, "Room-temperature low-threshold surface stimulated emission by optical pumping from $Al_{0.1}Ga_{0.9}N$/GaN double heterostructure", *Jpn. J. Appl. Phys.*, v. 32, part 2, no 7b, pp. L1000-L1002 (1993).
8. M. E. Lin, B. N. Sverdlov, S. Strite, H. Morkoc, A. E. Drakin, Refractive indices of wurtzite and zinc-blende GaN, *Electron. Lett.*, v. 29, no 20, pp. 1759-1761 (1993).
9. O. Ambacher, M. Arzberger, D. Brunner, H. Angerer, F. Freudenberg, N. Esser, T. Wethkamp, K. Wilmers, W. Richter, M. Stutzmann, "AlGaN-based Bragg reflectors", *MRS Internet J. Nitr. Semicond. Res.*, 2, Art. 22 (1998).
10. T. Peng and J. Piprek, "Refractive index of AlGaInN alloys", *Electron. Lett.*, 32 (24) (1996).
11. S. Nakamura, "Characteristics of room temperature-CW operated InGaN multi-quantum-well-structure laser diodes", *MRS Internet J. Nitride Semicond. Res.*, 2, Art. 5 (1997).
12. M. M. Y. Leung, A. B. Djurisic, and E. H. Li, "Refractive index of InGaN/GaN quantum well", *J. Appl. Phys.*, 84 (11), 6312-6317 (1998).
13. P. Mackowiak and W. Nakwaski, "Designing guidelines for possible continuous-wave-operating nitride vertical-cavity surface-emitting lasers", *J. Phys. D: Appl. Phys.*, 33, 642-653 (2000).
14. F. Renzoni, J. F. Donegan, and C. H. Petterson, "Optical gain and linewidth enhancement factor in bulk GaN", *Semicond. Sci. Technol.*, 14, 517-520 (1999).
15. S. Nakamura, M. Senoh, S. Nagahama, N. Iwasa, T. Yamada, T. Matsushita, Y. Sugimoto, and H. Kiyoku, "Subband emissions of InGaN multi-quantum-well laser diodes under room-temperature continuous wave operation", *Appl. Phys. Lett.*, 70 (20), 2753-2755 (1997).
16. V. E. Bougrov and A. S, Zubrilov, "Optical confinement and threshold currents in III-V nitride heterostructures: Simulation", *J. Appl. Phys.*, 81 (7), 2952-2956 (1997).
17. M. J. Bergmann and H. C. Casey, Jr., "Optical-field calculations for lossy multiple-layer $Al_xGa_{1-x}N/In_xGa_{1-x}N$ laser diodes", *J. Appl. Phys.*, 84 (3), 1196-1203 (1998).
18. S. Heppel, J. Off, F. Scholz, and A. Hangleiter, "Complex spectral behavior of the waveguide modes in InGaN/GaN laser structures", *Conf. Dig., 16th IEEE Int. Conf. Semicond. Lasers*, Nara, Japan, Oct. 1998, 11-12, pap. MB3 (1999).
19. D. K. Young, M. P. Mack, A. C.Abara, M. Hansen, L. A. Coldren, S. P. DenBaars, E. L. Hu, and D. D. Awschalom, "Near-field scanning optical microscopy of indium-gallium nitride multiple-quantum-well laser diodes", *Appl. Phys. Lett.*, 74 (16), 2349-2351 (1999).
20. M. Onomura, S. Saito, K. Sasanuma, G. Hatakoshi, M. Nakasuji, J. Rennie, L. Sugiura, S. Nunoue, J. Nishio, and K. Itaya, "Analysis of transverse modes of nitride-based laser diodes", *IEEE J. Select. Topics Quant. Electron.*, 5 (3) 765-770 (1999).
21. T. Someya, R. Werner, A. Forchel, M. Catalano, R. Cingolani, and Y. Arakawa, "Lasing emission from an $In_{0.1}Ga_{0.9}N$ vertical cavity surface emitting laser", *Science*, 285 (5435), 1905-1906, (1999).
22. A. V. Sakharov, W. V. Lundin, V. A. Semenov, A. S. Usikov, N. N. Ledentsov, A. F. Tsatsul'nikov, Zh. I. Alferov, A. Hoffmann, and D. Bimberg, "Surface-mode lasing from optically pumped InGaN/GaN heterostructures", *7th Int. Symp. "Nanostructures: Physics and Technology"*, St. Petersburg, Russia, June 14-18, 1999, 124-127 (1999).
23. M. Osinski, V. A. Smagley, C. Fu, G. A. Smolyakov, and P. G. Eliseev, "Design of InGaN/GaN/AlGaN vertical-cavity surface-emitting lasers using electrical-thermal-optical simulation", *Proc. SPIE*, 3944 (2000).
24. H. Wenzel and H.-J. Wuensche, "The effective frequency method in the analysis of vertical-cavity surface emitting lasers", *IEEE J. Quant. Electron.*, 33 (7) 1156-1162 (1997, July).

Generation of pico- and femtosecond-wavelength tunable optical pulses with self-seeded laser diodes

D. Huhse, O. Reimann, E.H. Böttcher, and D. Bimberg

Institut für Festkörperphysik I, Technische Universität Berlin, Hardenbergstraße 36, D-10623 Berlin, Germany

ABSTRACT

A simple way to generate wavelength tunable ($\Delta\lambda > 50$ nm) semiconductor laser pulses with a width (FWHM) of a few hundred femtoseconds and a timing jitter well below 1 ps is self-seeding of a gain-switched Fabry-Perot laser diode with subsequent chirp compensation and soliton compression. The low timing jitter of the single mode laser pulses allows self-seeding to be used e.g. in high temporal resolution electro-optic sampling systems. Additionally, by controlling the electrical phase delay between two self seeded laser diodes femtosecond pulses with electrically adjustable time delay can be generated.

Keywords: self-seeding, wavelength tuning, semiconductor laser pulses, ultra short laser pulses, soliton compression

1. INTRODUCTION

Ultrashort, wavelength tunable laser pulses find an increasing range of quite different applications, like measurement techniques of ultrafast physical phenomena (e.g. electro-optical sampling), analysis of environmental data, and telecommunications. A fundamental and at the same time low cost technique to generate wavelength tunable semiconductor laser pulses having a width (FWHM) of a few tens of picoseconds is self-seeding (SeSe) of a gain-switched Fabry-Perot (FP) laser diode. It was first demonstrated by Andersson et al. [1] and has been investigated in a number of different experimental configurations by several groups [2, 3, 4]. This technique is particularly simple and low-cost. Neither highly sophisticated laser structures like, e.g. Tunable Twin Guide (TTG) or multi-section DBR lasers, nor anti-reflection coating of the facet, as required for mode-locking, is needed.

2. PRINCIPLE OF SELF-SEEDING

2.1 Experimental Set-up

A lot of different experimental self-seeding set-ups have been investigated. In Fig. 1 the commonly used set-up is shown. A Fabry-Perot laser diode is gain-switched by short electrical pulses (FWHM 200-400 ps). The laser pulses emitted by the diode are coupled into a single mode fiber coupler. Part of the light is wavelength selectively reflected by a grating and feed back into the laser diode. If the repetition rate of the electrical pulses equals an integer multiple of the fundamental frequency of the external cavity, then the laser switches from multi mode to single mode operation. Typical spectra with and without self-seeding are shown in Fig. 2.

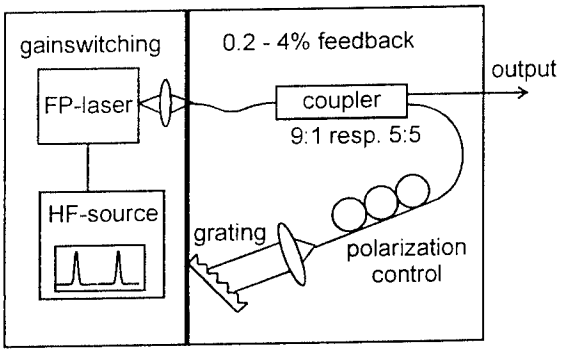

Fig. 1: The common self-seeding set-up

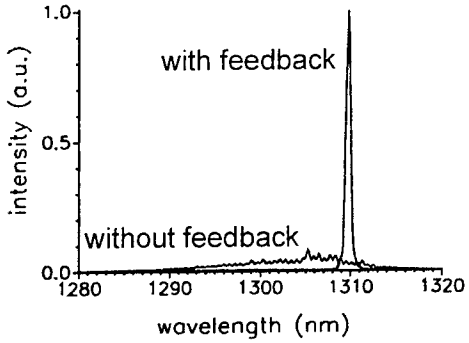

Fig. 2: Typical spectra of a gain-switched laser diode with and without self-seeding

Laser Optics 2000: Semiconductor Lasers and Optical Communication, Serguei A. Gurevich, Nikolay N. Rosanov, Editors, Proceedings of SPIE Vol. 4354 (2001) © 2001 SPIE · 0277-786X/01/$15.00

2.2 Numerical Model

The self-seeding process can be described by the well-known multi-mode rate equations with an additional feedback term,

$$\frac{dN}{dt} = \frac{I}{q} - \frac{N}{\tau_S} - \sum_{i=-M}^{M} \Gamma v_g g_i S_i \tag{1}$$

$$\frac{dS_i}{dt} = \Gamma v_g g_i \left(1 - \varepsilon \frac{\Gamma}{V} \sum_{i=-M}^{M} S_i\right) S_i + \frac{\beta N}{\tau_S} - \frac{S_i}{\tau_P} + P_{fb,i}(t) \tag{2}$$

Here N denotes the carrier number, S_i the photon number of mode i, τ_s the carrier lifetime, 2M+1 the total number of modes, Γ the mode confinement factor, v_g the group velocity, ε the gain compression parameter, V the active layer volume, β the spontaneous emission factor, and τ_p the photon lifetime. For the input current I normally a gaussian pulse is assumed. The optical input term $P_{fb,i}$ in Equ. 2 is zero for all modes except for the selected one (index k), where

$$P_{fb,k} = \kappa \cdot 0.5 \cdot \alpha_m v_g S'_k (t - \tau_k) \tag{3}$$

with S'_k the emitted power in the k^{th} mode of the last pulse, α_m the mirror loss, and κ the feedback efficiency. The time delay τ_k is chosen such as to result in a maximum side mode suppression. For the wavelength dependent gain a parabolic profile

$$g_i(\lambda) = \frac{A_0 (N - N_0)}{V} \left(1 - \frac{\left[\lambda - \lambda_0 + \lambda'(N - N_0)\right]^2}{2 \cdot G_0^{\,2}}\right) \tag{4}$$

is assumed, where A_0 is the differential gain, N_0 the carrier number for transparency, λ_0 the peak wavelength, and G_0 the modal gain factor. λ' accounts for the shift of the gain peak to higher photon energies with increasing carrier concentrations. All numerical simulations presented in this paper are based on these set of equations.

3. DYNAMICS OF SELF-SEEDING

After switch-on of the self-seeding, the first pulse generated in such a scheme still shows the broad spectrum peculiar to gain-switched FP laser diodes, because it is not yet 'seeded' by a previous pulse. When the first pulse is fed back into the laser diode (after spectral filtering), the spectral output power of the next pulse increases in the selected longitudinal mode and decreases in the other modes. The accumulation of the spectral power in the selected mode continues until a stable state is reached. For a number of applications it is important to know how fast the stable state is reached. In mode locking schemes, the most commonly used wavelength tunable pulse generating set-up, stable pulse emission appears after about hundreds to thousands of roundtrips [5, 6], which is far too slow for some applications. In self-seeding set-ups the stable state is reached much faster [7]. The results of time-resolved measurements of the evolution of the optical spectra during the switch-on of the self-seeding set-up are shown in Fig. 3 and Fig. 4.

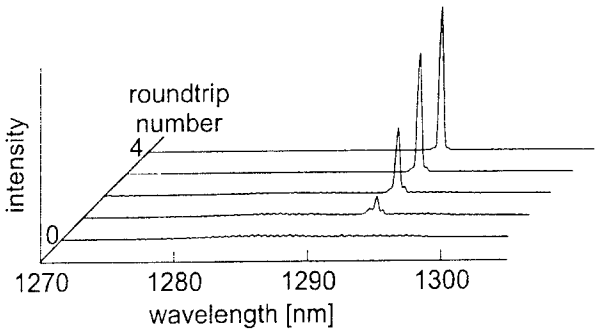

Fig. 3: Evolution of the spectrum during the switch-on of a self-seeded FP laser diode

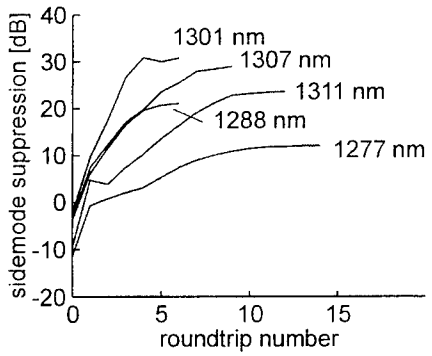

Fig. 4: Evolution of the sidemode suppression ratio for different feedback wavelengths

As can be seen, for wavelengths near the gain peak of the laser diode (in this case 1300 nm) the stable state is reached within about 5 roundtrips. A side mode suppression ration of more than 10 dB within the first 5 roundtrips can be reached within tuning range of about 30 nm. At the outer borders of the more than 40 nm wide tuning range 10 to 15 roundtrips are needed until the stable state is reached. These results show the potential of self-seeding for fast wavelength tuning, which will be discussed in the next section.

4. FAST WAVELENGTH SWITCHING

One of the most important advantages of self-seeding is the very simple way the wavelength can be tuned electrically. In a completely fiber-optical cavity without any wavelength selective elements a tuning range of 43 nm with a side mode suppression ratio better than 20 dB was obtained [8]. Further improvement of this set-up using a number of discrete fiber Bragg gratings [9] or a chirped fiber Bragg grating [10] allows extremely fast wavelength switching with switching times between two wavelengths of less than 100 ns.

The key component in all switching set-ups is a virtual multifold external cavity where different FP modes of the laser diode are reflected at different distances from the laser diode, leading to different round trip times for each wavelength. Here the distance between the different reflecting parts of the external cavity is the most critical parameter of the system. If the distance is too small, parts of both feedback pulses arrive back at the laser diode within the sensitive time window for the self-seeding process, and therefore emission in both modes will occur, leading to a decreased competing mode suppression ratio (CMSR). Therefore the influence of the grating distance on the competing mode suppression ratio and the switching behavior has been investigated [11]. The used experimental set-up is shown in Fig. 5 and is described in detail in [11].

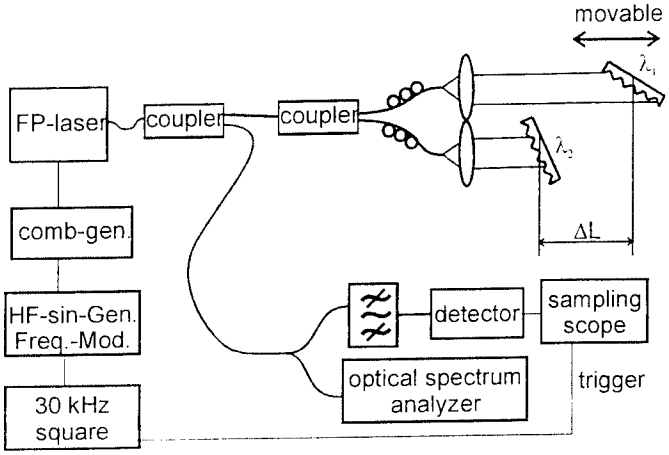

Fig. 5: Experimental set-up fast wavelength switching

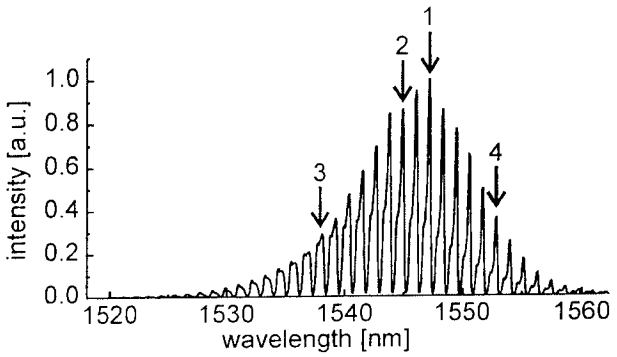

Fig. 6: Gain-switching spectrum of the laser diode with the laser modes chosen for the experiments indicated by arrows

The laser switches to single mode operation defined by the feedback wavelength of one of the gratings, if the repetition frequency equals an integer multiple of one of the two feedback frequencies. Otherwise, the laser shows the free running multi mode spectrum peculiar to gain-switched FP laser diodes. To switch between the two wavelengths set by the gratings one only have to change the repetition frequency of the electrical pulses.

A spectrum of the pulsed laser diode without feedback is shown in Fig. 6. The arrows indicate the modes which were later on selected for the wavelength switching experiments.

Fig. 7 shows the competing mode suppression ratio (CMSR) between the desired mode and the mode excited by the second grating for the 4 modes of Fig. 6. The influence of the second grating increases with decreasing difference between the lengths of the two cavities. When the spacing between the two gratings is too small it can happen that the laser emits pulses with more power in the undesired mode, and the desired mode is more or less suppressed, leading to a negative CMSR. The length difference range in which a second strong mode significantly influences the output of a weaker 'preselected one' is larger for larger gain differences. But a grating distance of about 10 mm is still large enough to ensure that no influence of the second grating can be seen, even in the worst cases like Fig. 7b. These results are independent of the average cavity length, because the only significant parameter is the absolute time difference between the two feedback modes arriving back at the laser diode, and this time difference is directly related to the cavity length difference and is independent of the total length of the cavity.

Fig. 8 shows the required roundtrip numbers during the switching process, until 99 % of the maximum power of the selected mode is reached. It can be seen that for cavity length differences of more than 10 mm switching occurs within less than 6 round trips for the center wavelengths. Even for the wavelengths at the border of the gain curve switching takes less than 10 round trips. For the case that the two modes show a large gain difference (as e.g. in Fig. 8b) the switching in the high gain mode occurs faster (4 round trips) than in the lower gain mode (10 round trips).

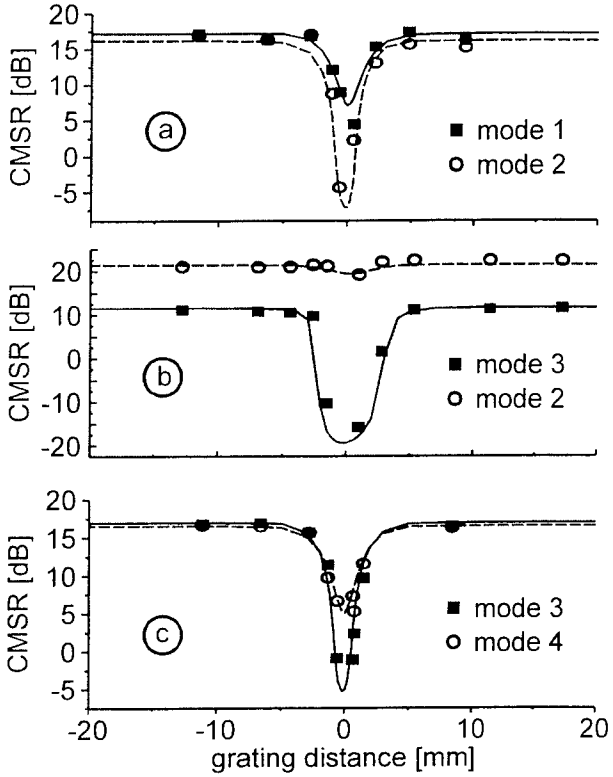

Fig. 7: Measured (data points) and numerical simulated (lines) competing mode suppression ratio for different cavity length differences. a) Both excited modes are near the gain peak, b) One mode near the gain peak and one mode at the border of the gain, c) both modes at each border of the gain curve. (see also Fig. 6)

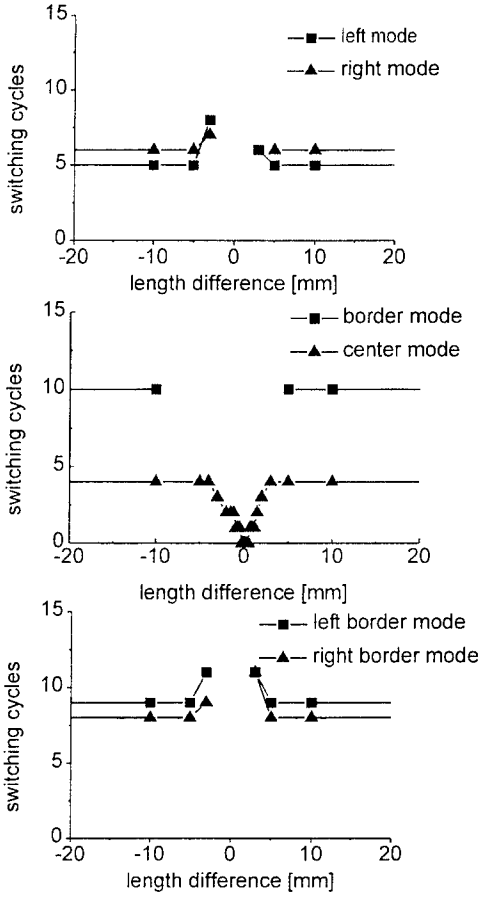

Fig. 8: Simulated switching time until 99 % of the maximum power of the selected mode is reached

5. PULSE COMPRESSION BY CHIRP COMPENSATION

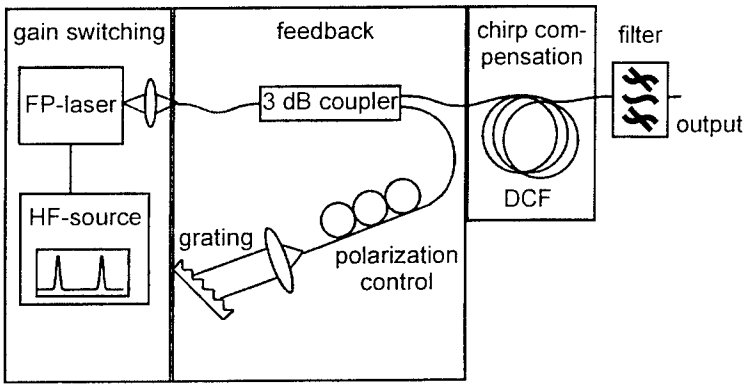

Fig. 9: Set-up for chirp compensation

The self-seeding set-up is based on gain-switching a semiconductor laser diode and thus the generated pulses are red chirped. Therefore pulse compression by chirp compensation in an optical fiber, similar to the well known compression of single mode DFB laser pulses, is possible [12]. A typical experimental set-up for the compression of self-seeded laser pulses by chirp compensation is shown in Fig. 9. In this example the laser emits at 1.55 µm and a dispersion compensating fiber (DCF) is used for chirp compensation. An example for a spectrum of a self-seeded laser pulse is shown in Fig. 10, the spectral width is 3.2 nm. The autocorrelation trace of the pulses is shown in Fig. 11.

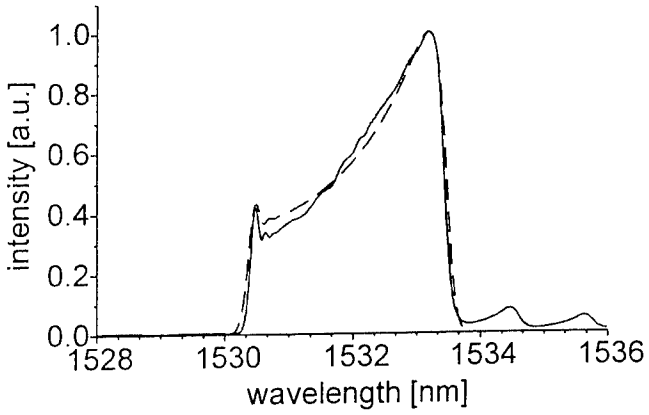

Fig. 10: Measured (—) and simulated (- - -)spectrum

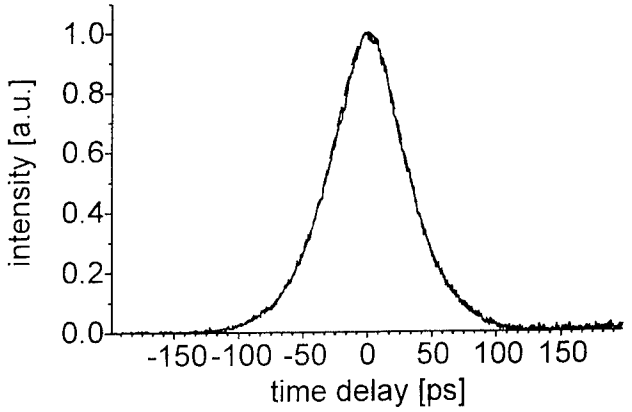

Fig. 11: Measured (—) and simulated (- - -)autocorrelation

Using the multi mode rate equations, the measured spectrum and autocorrelation trace are fitted by varying the numerical values of the parameters of the laser diode. The numerical calculated spectrum and autocorrelation trace are also shown in Fig. 10 and Fig. 11. The temporal width (FWHM) of the pulse is about 45 ps.
With the information about the amplitude and phase of the optical pulses derived by the fitting procedure one can calculate the propagation (and pulse compression due to chirp compensation) of the pulses in a dispersive optical fiber by [13]

$$A(z,T) = FT^{-1}\left[\exp\left(\frac{i}{2}\beta_2\omega^2 z\right)\cdot FT(A(0,T))\right] \tag{5}$$

where A(0,T) is the complex amplitude of the optical pulse at the fiber position z, FT denotes the Fourier transformation, and β_2 is the fiber dispersion. The calculated pulse shapes (with and without the additional filter) and the autocorrelation traces after chirp compensation are shown in Fig. 12 and Fig. 13, respectively. It can clearly be seen that the pulse structure improves significantly after filtering the pulse. The sub-pulses decrease and the large, slow tail of the pulse nearly vanishes.

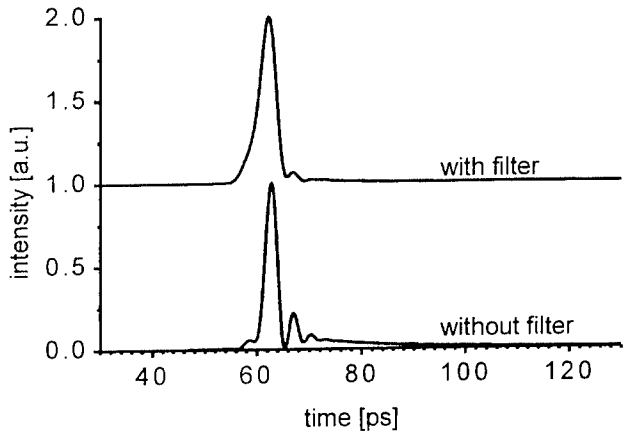

Fig. 12: Calculated pulse shape traces of the chirp compensated self-seeded laser pulses after total fiber dispersion of D = -16 ps/nm

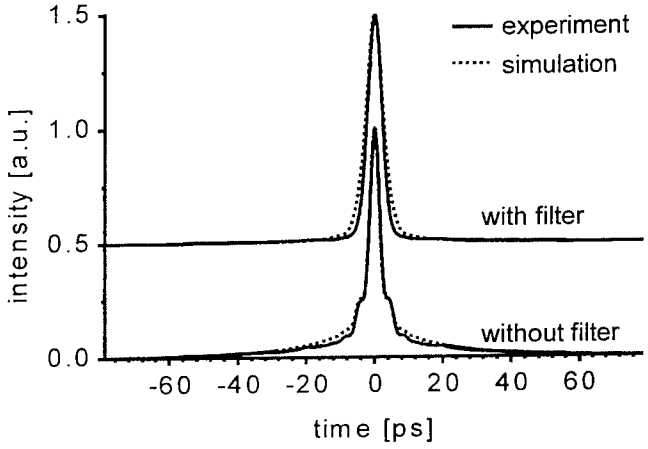

Fig. 13: Calculated (- - -) and measured (—) autocorrelation traces of the chirp compensated self-seeded laser pulses after total fiber dispersion of D = -16 ps/nm

The pulse widths assuming a sech²-fit are 2.9 ps without filter and 3.1 ps with filter, respectively. The small increase in the pulse width after the filter is due to the small bandwidth of the used filter. The time-bandwidth-product of the pulses after the filter is 1.3 times the Fourier-limit.

6. JITTER OF SELF-SEEDED LASER PULSES

The timing jitter of gain switched laser diodes is caused by statistical fluctuations of the number of photons in the active area at the time when the carrier density in the laser diode reaches the threshold value. These fluctuations are, due to the statistical nature of the photon number, inverse proportional to the square root of the total number of photons. Due to the small number of photons in the mode of gain switched DFB laser diodes the pulses of these lasers show a large jitter of about 2 to 6 ps [14]. This is of the order of the pulse width of the compressed laser pulses and therefore significantly decreases the potential time resolution of possible measurements.

Using self-seeding the jitter of single mode laser pulses could decisively be decreased. Here the photons in the active area of the laser diode when the carrier density reaches threshold is no longer determined by the spontaneous emitted photons but by the much larger number of photons fed back from the previously emitted pulse. Therefore the relative fluctuations and hence the timing jitter of the laser pulses should be smaller. In deed it has been shown in previous experiments that the jitter of single mode laser pulses generated by self-seeded laser diodes is about one order of magnitude smaller than the jitter of laser pulses generated by DFB laser diodes [15].

7. SET-UP FOR PUMP-AND-PROBE EXPERIMENTS

For optical measurements which require a high time resolution very often a so-called pump-and-probe configuration is used. In these set-ups normally a ultra-short laser pulse is split into two pulses. One of these pulses is delayed via a variable delay line, mostly a mechanically movable retroreflector. Because the time delay between the two pulses can be controlled precisely, the time resolution is determined by the temporal width of the used optical pulses and the stability of the set-up. A drawback of these set-ups is the used mechanical delay line. Small shocks caused e.g. by sonic distortions can lead to small vibrations of the retroreflector which will change the time delay between the pulses. Although this effect can be minimized, another drawback can hardly be removed. The mechanical movement of the retroreflector is inherently slow and limits the minimal time needed to scan a certain time range.

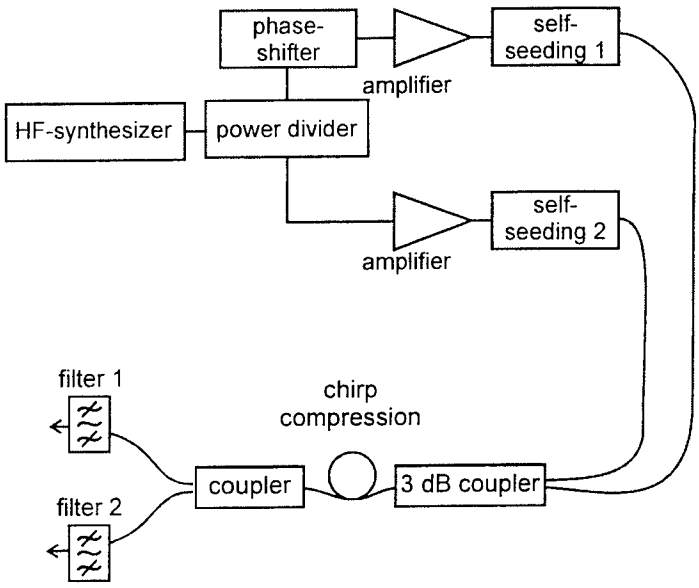

Fig. 14: Set-up of a laser source for pump-and-probe experiments

An electrically controllable time delay between the pump and the probe pulse will overcome all the mentioned problems. A previously demonstrated set-up consists of a mode-locked laser diode and a gain-switched DFB laser [16]. Here the time delay between the optical pulses can easily be adjusted by controlling the phase difference between the electrical HF signals applied to the two laser diodes. This simple and reliable set-up suffers from the high timing jitter of the DFB laser pulses. Because the pump and the probe pulse are taken from two different sources, the timing jitter plays a significant role and, if the jitter is of the order or larger than the optical pulse width, could limit the possible time resolution.

Self-seeded laser diodes are ideally suited for such a set-up due to their small timing jitter. A possible realization of such a configuration is shown in Fig. 14. The sinusoidal HF signal, which is used to generate the short electrical pulses for the gain switching process, is split by a power divider. The phase of one of the two signals can be changed electrically by a phase shifter. By controlling the electrical phase in branch 1 in respect to the one in branch 2, the time delay between the two optical pulses emitted by the laser diodes can be controlled. Both laser diodes operate in self-seeding mode to ensure a small timing jitter of well below 1 ps. The optical output of the two laser diodes is combined by a fiber coupler. The pulses are subsequently compressed by chirp compensation in a dispersive optical fiber. Because both pulses are compressed together in the same fiber, small length fluctuations of the optical fiber (caused e.g. by temperature changes) do not lead to time delay changes.

The measured optical intensities at the end of the compression fiber are shown in Fig. 15. Here the output of self-seeding set-up number 1 is artificially damped to distinguish the two laser pulse sources. As expected the time delay between the two laser pulses can be controlled. Because this delay is controlled electrically and not mechanically, a high stability and a

high scanning rate are possible. Despite the low timing jitter another advantage of using self-seeded laser diodes is the ability to tune the wavelength. Therefore it causes no problem to adjust the two output wavelengths of the self-seeding set-ups in a way that the pulses can easily be separated by spectral filters at the output, as shown in Fig. 14. The spectra and the time-resolved intensity behind one of the filters are shown in Fig. 16 and Fig. 17, resp. With this set-up a high reliable and easy to use source for pump-and-probe experiments is made available. In first experiments this set-up has proven its suitability as a source in an electro-optical sampling system [17].

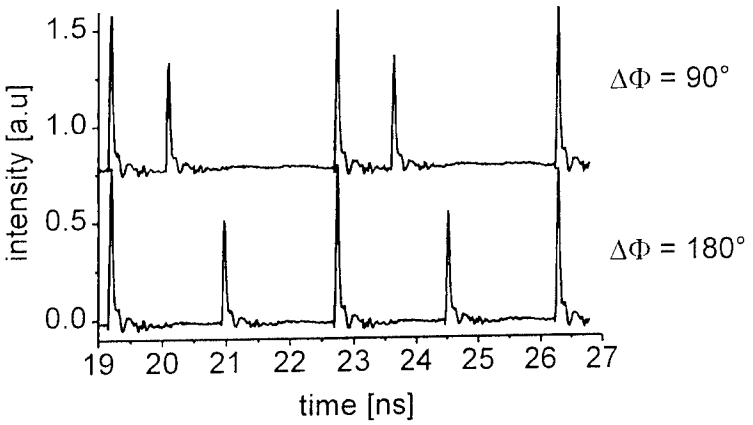

Fig. 15: Example for electrically controllable time delay between the two laser pulses

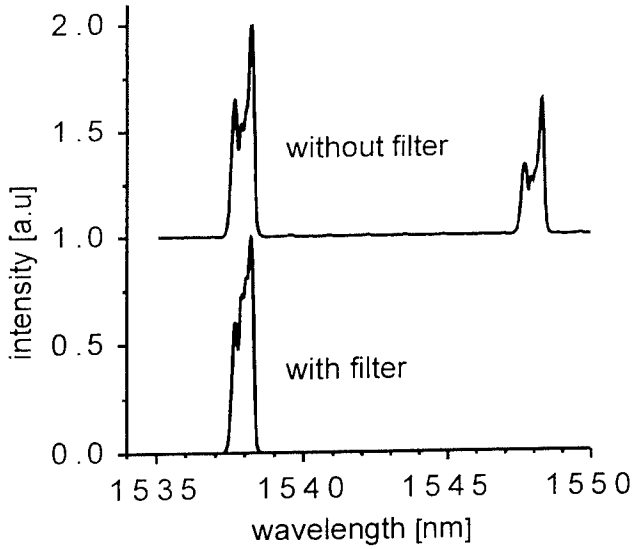

Fig. 16: Measured spectra of the pump-and-probe set-up with and without filter

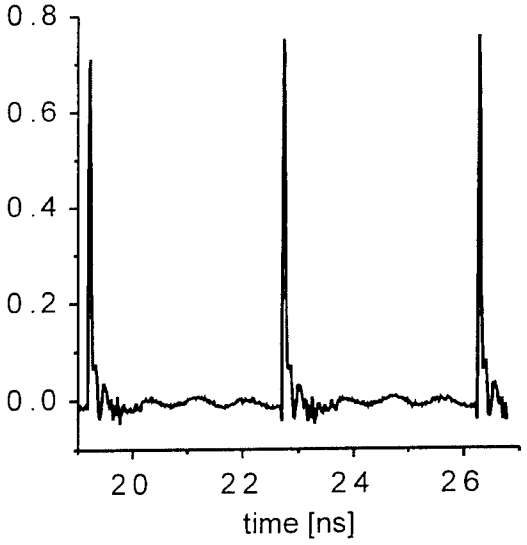

Fig. 17: Measured output of the pump-and-probe set-up behind one of the filters

8. ULTRA-SHORT PULSE GENERATION

The laser pulses after chirp compensation have a pulse width of about 3 ps. These pulses could be further compressed using higher order soliton compression in standard single mode fibers [18]. The used experimental set-up is shown in Fig. 18.

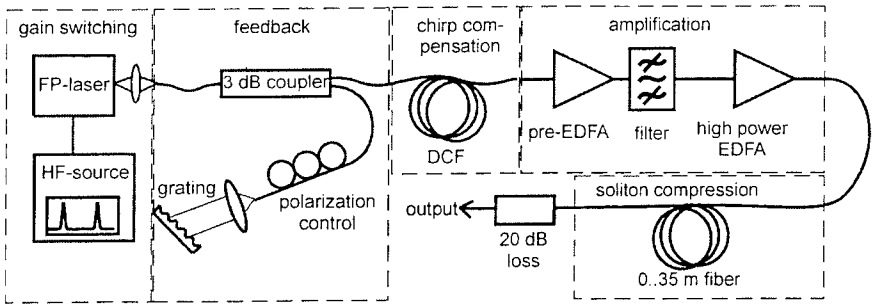

Fig. 18: Experimental set-up for soliton compression

After amplification in the EDFA the average output power is 50 mW. The pulse width is not significantly changed by the EDFAs. The actually measured autocorrelation pulse width as a function of the fiber length is shown in Fig. 19. The shortest achieved pulse width is 290 fs ($sech^2$) for a fiber length of 25 m. From the initial pulse width of 3.1 ps and the repetition rate of 269 MHz one can calculate an input pulse peak power of 53 W. Therefore the generated soliton is of order N = 4, and the expected compression factor for optimized fiber length is about 12 for idealized fibers [19]. This leads to an expected pulse width of 260 fs in good agreement with the experimental result. The autocorrelation trace of the shortest pulse, which shows the typical wings associated with higher order soliton compression, is shown in Fig. 20.

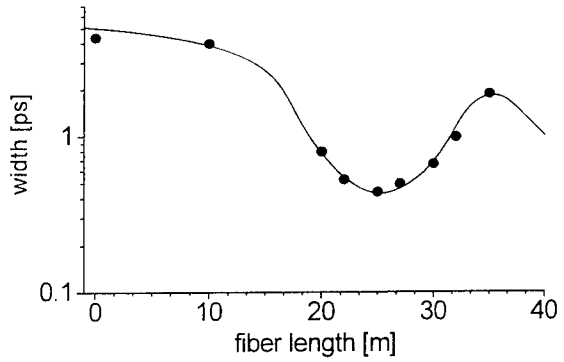

Fig. 19: Calculated (—) and measured (•) autocorrelation pulse width during the propagation through the optical fiber.

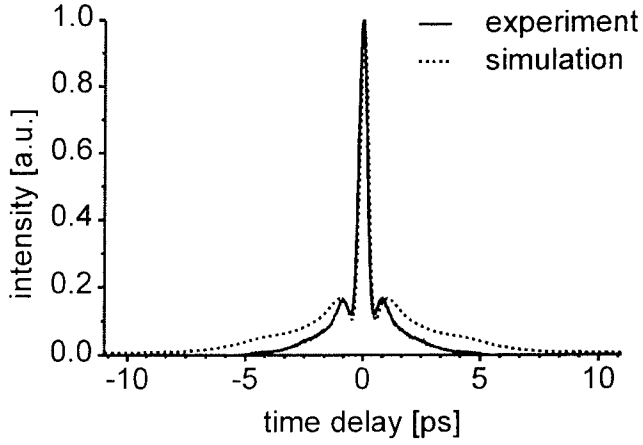

Fig. 20: Calculated (- - -) and measured (—) auto-correlation trace of the shortest pulses (after 25 m fiber).

We also simulated the soliton propagation and narrowing with the equation

$$\frac{\partial A}{\partial z}+\frac{i}{2}\beta_2\frac{\partial^2 A}{\partial T^2}-\frac{1}{6}\beta_3\frac{\partial^3 A}{\partial T^3}+\frac{\alpha}{2}A=i\gamma|A|^2A-i\gamma T_R A\frac{\partial|A|^2}{\partial T}-\frac{2\gamma}{\omega_0}\frac{\partial}{\partial T}\left(|A|^2A\right) \tag{6}$$

describing the pulse propagation in real fibers, taking into account also the nonlinear effects [13]. This equation was solved numerically using the split-step Fourier method described in [13]. As input pulse we used the calculated complex amplitude function from section 5 with a pulse energy of 3.36 pJ, as measured after the filter. For the simulation of the amplification in the 2nd EDFA a total fiber length of 24 m with a fiber diameter of 6 µm was assumed. Following the experiments a constant amplification of 0.725 dB/m was chosen. The calculated width of the autocorrelation trace is shown in Fig. 19, together with the experimentally retrieved data, and shows an excellent agreement. The measured and calculated autocorrelation traces for the point of optimal compression are shown in Fig. 20, which shows also a good agreement in the main part of the pulse.

9. APPLICATIONS OF SELF-SEEDING ELECTRO-OPTICAL SAMPLING

The ultra short laser pulses after pulse compression are ideally suited for use in optical sampling systems, like Electro-Optical Sampling (EOS) [20]. The ultra short laser pulses after higher order soliton compression were used in an EOS system for the characterization of high speed MSM photo detectors. Details of the EOS set-up are given in [20]. A measured impulse response of the photo detector, together with the accessory frequency response, are presented in Fig. 21 and Fig. 22, respectively. Please note that the frequency response is directly calculated from the impulse response without any deconvolution of the measurement system or the optical pulses. These results show that low jitter ultra short self-seeded laser pulses provide the possibility for ultrahigh frequency measurements up into the THz range.

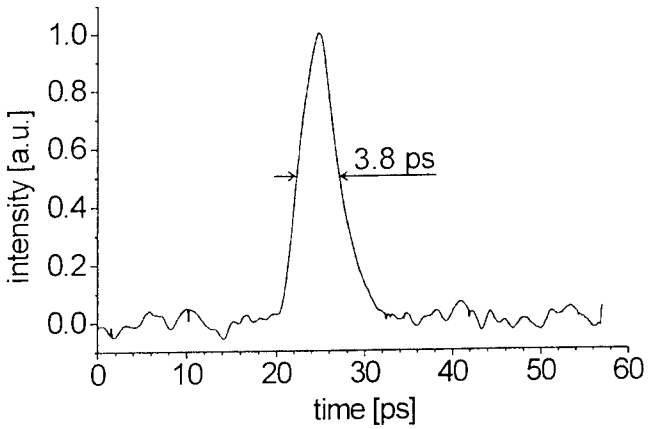

Fig. 21: Measured response of a fast photo detector measured with an EOS system using ultra short optical pulses generated by self-seeding and soliton compression

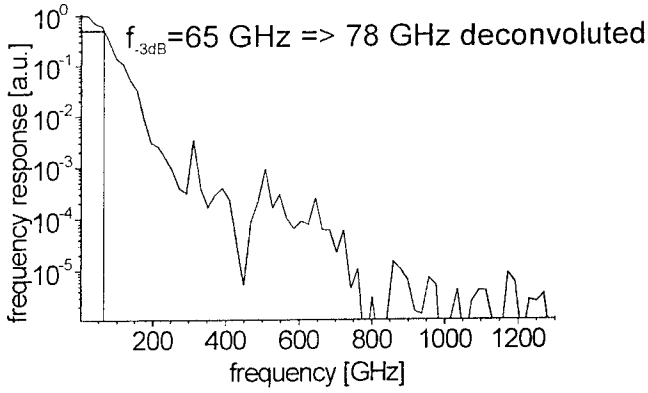

Fig. 22: Frequency response of the photo detector. The frequency response is calculated without any deconvolution

10. CONCLUSION

Self-seeding of a gain-switched FP laser diodes is a simple and reliable concept for the generation of short, wavelength tunable laser pulses. Without any further compression, laser pulses with a width of 20 to 40 ps (FWHM) and a tuning range of more than 50 nm can easily be generated. With subsequent chirp compensation the pulses can be compressed to a width of a few picoseconds only. Further compression of these laser pulses exploiting nonlinear effects in optical fibers (soliton compression) allows the generation of laser pulses with a width (FWHM) of less than 300 fs. Due to the low timing jitter of the self-seeded laser pulses (less than 500 fs), self-seeding can be used in optical sampling systems with high temporal resolution. First results of electro-optical sampling system measurements using these laser system as a pulse source show the capability of these system for measurements up to the THz range. In a set-up consisting of two similar self-seeded laser diodes operating of slightly different wavelengths short laser pulses with electrically adjustable time delay and low jitter can be generated by controlling the electrical phase delay between two self seeded laser diodes.

11. ACKNOWLEDGEMENTS

Parts of this work are supported by the German Ministry of Education, Research and Technology (BMBF) under contract number 13 N 7159 and by the German Research Foundation (DFG).

12. REFERENCES

1. T. Anderson, S. Lundquist, and S. T. Eng, "Generation of single-mode pulses by injection locking of an AlGaAs semiconductor laser," *Appl. Phys. Lett.* **41**, pp. 14-16, 1982
2. M. Schell, D. Huhse, A.G. Weber, G. Fischbeck, D. Bimberg, D.S. Tarasov, A.V. Gorbachov, and D.Z. Garbuzov, "20 nm Wavelength Tunable Single Mode Picosecond Pulse Generation at 1.3 μm by a Self-Seeded Gain-Switched Semiconductor Laser," *Electron. Lett.* **28**, pp. 2154-2155, 1992
3. S. Bouchoule, N. Stelmakh, M. Cavelier, and J.-M. Lourtioz, "Highly Attenuating External Cavity for picosecond tunable pulse generation from gain/Q-switched laser diodes," *IEEE J. Quantum Electron.* **25**, pp. 1693-1699, 1993
4. Y. Uchiyama, M. Tsuchiya, H.-F. Liu, and T. Kamiya, "Spectrally Narrowed Operation of a gain-Switched 690 nm GaInP/AlGaInP Fabry-Perot Laser by Self-Seeding Technique," *Jpn. J. Appl. Phys. Pt. 2* **35**, pp. 637-639,1996

5. P.A. Morton, R.J. Helkey, and J.E. Bowers, "Dynamic detuning in actively mode-locked semiconductor lasers," *IEEE J. Quantum Electron.*, **QE-25**, pp. 2621-2633, 1989
6. A.G. Weber, M. Schell, G. Fischbeck, and D. Bimberg, "Generation of single femtosecond pulses by hybrid mode locking of a semiconductor laser," *IEEE J. Quantum Electron.*, **QE-28**, pp. 2220-2229, 1992
7. D. Huhse, M. Schell, W. Utz, J. Kaessner, and D. Bimberg, "Dynamics of Single Mode Formation in Self-Seeded Fabry Perot Laser Diodes," *IEEE Photon. Technol. Lett.* **7**, pp. 351-353, 1995
8. D. Huhse, M. Schell, J. Kaessner, D. Bimberg, D. S. Tarasov, A. V. Gorbachov, and D. Z. Garbuzov, "Generation of Electrically Wavelength Tuneable ($\Delta\lambda$ = 40 nm) Single Mode Laser Pulses from a 1.3 μm Fabry-Perot Laser by Self-Seeding in a Fiberoptical Configuration," *Electron. Lett.* **30**, pp. 157-158, 1994
9. D. Huhse, M. Schell, W. Utz, D. Bimberg, J.A.R. Williams, L. Zhang, and I. Bennion, "Fast wavelength switching of semiconductor laser pulses by self-seeding," *Appl. Phys. Lett.* **69**, pp. 2018-2020, 1996
10. H. Ding, S. Li, Z. fang, and K.T. Chan, "Wavelength Switching of Semiconductor Laser Pulses by Self-Seeding from a Chirped Fiber Bragg Grating," *IEEE Photon. Technol. Lett.* **9**, pp. 901-903, 1997
11. D. Huhse and D. Bimberg, "Competing Mode Suppression Ratio of Electrically Wavelength Tunable Self-Seeded Lasers," *IEEE Photon. Technol. Lett.* **11**, pp. 167-169, 1999
12. M. Schell, D. Huhse, and D. Bimberg, "Generation of 2.5 ps Light Pulses with 15 nm Wavelength Tunability at 1.3 μm by a Self-Seeded Gain-Switched Semiconductor Laser", IEEE Photon. Technol. Lett. **5**, 1267-1269, 1993
13. G.P. Agrawal, *Nonlinear Fiber Optics* Academic Press, Inc., Boston, 1989
14. M. Jinno, "Correlated and uncorrelated timing jitter in gain-switched laser diodes," *IEEE Photon. Technol. Lett.* **5**, pp. 1140-1143, 1993
15. M. Schell, D. Huhse, W. Utz, J. Kaessner, D. Bimberg, and I.S. Tarasov, "Jitter and Dynamics of Self-Seeded Fabry-Perot Laser Diodes", IEEE J. Sel. Top. Quantum Electron. **1**, 528, 1995
16. T. Kanada and D.L. Franzen, "Optical waveform measurement by optical sampling with a mode-locked laser diode," *Opt. Lett.* **11**, pp. 4-6, 1986
17. O. Reimann, D. Huhse, E. Dröge, E.H. Böttcher, D. Bimberg, "Low jitter dual semiconductor laser system using electrical phase shift for fast temporal scanning in time-resolved pump and probe experiments," *Proceedings of the Pacific Rim Conference on Lasers and Electro-Optics CLEO/PACIFIC RIM '99*, Paper WI3, pp. 203-204, 1999
18. D. Huhse, O. Reimann, E.H. Böttcher, D. Bimberg, "Generation of 290 fs Laser Pulses by Self-Seeding and Soliton Compression", Appl. Phys. Lett. **75**, S. 2530-2532, 1999
19. L.F.Mollenauer, R.H. Stolen, J.P. Gordon, and W.J. Tomlinson, "Extreme picosecond pulse narrowing by means of soliton effect in single-mode optical fibres," *Opt. Lett.* **8**, pp. 289-291, 1983
20. O. Reimann, D. Huhse, E. Dröge, E.H. Böttcher, and D. Bimberg, "Advanced Semiconductor Laser Based Electro-Optical Sampling System Using Soliton Pulse Compression for Direct Probing at 1.55-μm Wavelength," *Proceedings of the 1998 IEEE Lasers and Electro-Optical Society Annual Meeting LEOS'98*, paper WJ1, 1998

Dynamic Operation of Laser Diode Accompanied by Hot-Carrier Effects

Boris E. Golubev, Vladimir M. Chistyakov and Serguei A. Gurevich

Ioffe Physical Technical Institute, Polytechnicheskaya, 29, St. Petersburg, Russia

ABSTRACT

We propose a relatively simple dynamic laser model based upon continuity equations for electron and hole concentrations, energy balance equation and a set of rate equations describing spectrally dependent photon density. These equations are solved in a self-consistent way together with Poisson equation. The model assumes that characteristic times of establishing the carrier temperature are shorter than those of carrier-to-phonon interaction. Using this model, the dynamic response of *AlGaAs/GaAs* double heterostructure laser is analyzed at current densities up to $\sim 6 \times 10^4$ A/cm^2. It is shown that the reaction of carrier temperature to the appearance of optical pulse is spatially nonuniform and is determined by the balance of the heating induced by the stimulated emission and the cooling associated with carrier and heat transfer across the active layer.

Keywords: heterostructure laser, dynamic model, hot carrier effects

1. INTRODUCTION

Hot carrier effects in laser diodes have been extensively studied in a large number of experimental and theoretical works. In general, in heterostructure lasers there are several sources of carrier heating, such as hot carrier injection from heterobarriers,[1,2] stimulated emission,[3] Auger recombination and free carrier absorption of emitted photons.[4] These effects have been shown to have strong impact on laser dynamic behavior via considerable temperature dependence of the optical gain. In some cases, carrier heating can be enhanced by external electric field[5] or by optical pulse injection into the laser cavity.[6] Since carrier heating and cooling are very fast processes, these techniques are promising for high-speed output modulation. On the other hand, the intrinsic carrier heating may be an adverse factor limiting the modulation response. Carrier heating associated with stimulated emission can suppress the gain dynamically, which is known to be an important contribution to nonlinear gain.[3] Enhanced gain nonlinearity leads to excess damping of laser modulation response thus decreasing the modulation bandwidth.[7] Several propositions were made in a way to design specific laser structures containing tunnelling barriers in order to control either the energy of injected carriers[8] or the energy-dependent carrier capture rate into the quantum well.[9] In these structures hot carrier effects are employed for more effective gain switching operation and for substantional expansion of the modulation bandwidth.

Several approaches to simulation of laser dynamics accounting for carrier heating were suggested. Some of them deal with carrier density and temperature averaged over the width of the active layer.[3] Other, more sophisticated, models consider spatially nonuniform carrier concentration and temperature[10] or employ Monte-Carlo technique.[11] However, the complexity of these models limits their use and often is unjustified for the description of experimental results.

In this paper we propose a relatively simple dynamic model based upon continuity equations for electron and hole concentrations, energy balance equation and a set of rate equations describing spectrally dependent photon density. These equations are solved in a self-consistent way together with Poisson equation. The use of Poisson equation rather than employing charge neutrality assumption makes the model applicable to the analysis of heterostructure lasers with bulk active layer of arbitrary thickness and even of more complicated structures with variable doping profile in the active layer. The model assumes that characteristic times of establishing the carrier temperature are much shorter than those of carrier-to-phonon interaction, the condition which is satisfied for any practical concentrations in laser structures. Alongside with known temperature effects, this model enables to treat coordinate-dependent carrier heating as well as dynamic multimode laser behavior.

Further author information: E-mail: gurevich@quantel.ioffe.rssi.ru

Laser Optics 2000: Semiconductor Lasers and Optical Communication, Serguei A. Gurevich, Nikolay N. Rosanov, Editors, Proceedings of SPIE Vol. 4354 (2001) © 2001 SPIE · 0277-786X/01/$15.00

2. DERIVATION OF THE MODEL

2.1. Basic Equations

The structure under analysis is a double heterostructure laser consisting of a weakly doped $GaAs$ active layer sandwiched between N^+ and P^+ $AlGaAs$ emitters. In equilibrium, the whole active layer is located within the space-charge region, and almost all the carriers are wiped. After the pumping current starts, the carrier accumulation can be seen as two successive processes. First, the barrier capacity of the p-n junction is charged. The majority of the carriers are involved in this process, and the current through the active layer is low. After all capacitances are charged, and the band bending disappears, carrier injection to the active layer comes to be significant. Disregarding the initial period of capacitance charging, high injection level approximation can be used to describe the device behavior.

In lasers with Fabry-Perot resonator, the emission consists of several longitudinal modes with the energy of quanta $\hbar\omega_m$ separated by energy $\delta(\hbar\omega) = \pi\hbar v_g/L$, where $v_g = c/n$ is the light group velocity, and L the cavity length. The model employs a number of spectral windows extending from the bandgap energy to an energy well exceeding the expected range of stimulated emission (1.424–1.45 eV). Each of the windows encloses one longitudinal mode. In each mode, the deviation of photon intensity along the cavity is neglected, while photon distribution $\Psi^2(x)$ across the active layer is determined by solving the TE-modes equation. This distribution is assumed independent of time and carrier concentrations.

Let the x-axis be directed across the laser active layer of thickness d, $x = 0$ corresponding to the heterobarrier at the p-emitter Let n, p denote electron and hole concentrations, respectively; T the temperature of the electron-hole plasma measured in energy units, j_n and j_p electron and hole current densities. Then, the continuity equations are as follows:

$$\frac{\partial n}{\partial t} = \frac{1}{e}\frac{\partial j_n}{\partial x} - B_{sp}np - v_g\int d(\hbar\omega)\,\mathcal{G}(n,p,T,\hbar\omega)N_{ph}(\hbar\omega)\Psi^2(x), \tag{1}$$

$$\frac{\partial p}{\partial t} = -\frac{1}{e}\frac{\partial j_p}{\partial x} - B_{sp}np - v_g\int d(\hbar\omega)\,\mathcal{G}(n,p,T,\hbar\omega)N_{ph}(\hbar\omega)\Psi^2(x). \tag{2}$$

Here B_{sp} is the spontaneous emission factor, $N_{ph}(\hbar\omega)$ is the number of photons in the laser mode with energy $\hbar\omega$. $\Psi^2(x)$ is the photon distribution function along the x-axis. The fraction of photons within the active layer

$$\Gamma = \int\limits_{\text{(Act. Layer)}} dx\,\Psi^2(x) \Big/ \int\limits_{-\infty}^{\infty} dx\,\Psi^2(x)$$

is the confinement factor. The local optical gain is of the following form:

$$\mathcal{G}(n,p,T,\hbar\omega) \propto \rho(\hbar\omega)\Big(f_c(E') + f_v(E'') - 1\Big), \tag{3}$$

where

$$E' = \frac{\hbar\omega - E_g}{T}\frac{m_r}{m_c}, \qquad E'' = \frac{\hbar\omega - E_g}{T}\frac{m_r}{m_v}$$

are energies of electrons and holes recombining with emission of photon of the energy $\hbar\omega$, f_c and f_v are the Fermi functions, m_c and m_v the effective masses, m_r the reduced mass, ρ is the reduced density of states.

Note that in the continuity equations (1, 2) nonradiative recombination processes are not included. It is because Auger recombination in $GaAs$ is still negligible at concentrations typical of generation. The linear mechanism, on the other hand, is important only at low concentrations. Consequently, all types of recombination can be neglected except for the radiative spontaneous recombinations which starts the stimulated recombination.

Dividing the whole spectral range into narrow windows, the following equation is obtained for each spectral mode:

$$\frac{\partial}{\partial t}N_{ph}(\hbar\omega) = -\frac{N_{ph}(\hbar\omega)}{\tau_{ph}} + v_g N_{ph}(\hbar\omega)\int d\,x\,\mathcal{G}(n,p,T,\hbar\omega)\Psi^2(x) + \; + \beta(\hbar\omega)\int d\,x\,B_{sp}np, \tag{4}$$

where τ_{ph} is photon lifetime determined by the sum of the distributed and radiation optical losses. The second term in (4) corresponds to stimulated emission. It is a convolution of the local material gain with spatial photon density

distribution. $\beta(\hbar\omega)$ describes the fraction of spontaneously emitted photons that contribute to the lasing mode. It is a product of two factors: one is connected with energy distribution of spontaneous photons and is proportional to $\sqrt{\hbar\omega - E_g} f_c(E') f_v(E'')$, while the second is the energy-independent probability that the emitted photon matches the cavity mode.

To be able to write the energy balance equation one needs to ensure that the carrier distribution function is nearly isotropic. This condition holds since the characteristic electron-electron scattering time is very low (about 10^{-14} s) at concentrations necessary for lasing. Since electron-hole interaction time is also low, it is possible to describe the electron-hole plasma with temperature T equal for all types of carriers. This temperature, however, differs from the lattice temperature T_L due to the fact that interaction with phonons is much weaker. The characteristic distance at which distribution function is established can be estimated as $L \approx \tau_{ee} v_{max} < 10^{-7}$ cm, so temperature can be expressed as coordinate function.

With these assumptions, the equation of energy balance can be written down as follows:

$$\frac{\partial W}{\partial t} = (j_n + j_p)E - \frac{\partial Q}{\partial x} - P(n, p, T). \tag{5}$$

Here the energy density W is given by

$$W = \frac{3}{2} T \left[\aleph_c(T) \Phi_{3/2}\left(\frac{\zeta_n}{T}\right) + \aleph_v(T) \Phi_{3/2}\left(\frac{\zeta_p}{T}\right) \right] \tag{6}$$

which is a general expression applicable to the case of degeneracy, $\aleph_c$, $\aleph_v$ are densities of states in conduction and valence bands, respectively. Entering this expression, the Fermi integrals are

$$\Phi_k(\xi) = \frac{1}{\Gamma(k+1)} \int_0^\infty \frac{d\varepsilon\, \varepsilon^k}{1 + \exp(\varepsilon - \xi)}.$$

The parameters ζ_n and ζ_p are the Fermi quasi-levels for carriers.

In Eq. 5, Q is energy flux density whose form will be considered in the next section; P describes energy variation due to interaction with LO-phonons, and owing to spontaneous and stimulated emission:

$$P = P_{\hbar\Omega} + P_{sp} + P_{stim}. \tag{7}$$

For stimulated emission, we sum up the contributions from each spectral window:

$$P_{stim} = v_g \int d(\hbar\omega)\, [\hbar\omega - E_g] \mathcal{G}(n, p, T, \hbar\omega) N_{ph}(\hbar\omega) \Psi^2(x). \tag{8}$$

For the two remaining terms in (7) we use the formulas derived in Ref. 3:

$$P_{sp} = \frac{3}{2} T B_{sp} \left(\frac{\sqrt{m_c m_v}}{m_r}\right)^{3/2} \aleph_c(T) \aleph_v(T) \frac{4}{3\sqrt{\pi}} \int_0^\infty \frac{du\, u^{3/2}}{\left[1 + \exp(u\sqrt{m_v/m_c} - \zeta_c/T)\right] \left[1 + \exp(u\sqrt{m_c/m_v} - \zeta_v/T)\right]} \tag{9}$$

and

$$P_{\hbar\Omega} = \sum_{j=c,v} P_{\hbar\Omega j}, \qquad P_{\hbar\Omega j} = \frac{\hbar\Omega}{\tau_{\Omega j}} (f_{\Omega e} - f_{\Omega 0}) \left(\frac{\hbar\Omega}{\pi T}\right)^{1/2} \aleph_j \int_0^\infty \frac{du\, u}{(u + u_{sj})^2} \ln\left[1 + \frac{f_e(\varepsilon_\Omega)}{f_{\Omega e}}\right] \frac{\nu_{\Omega D}}{\nu_{\Omega D} + \nu_{\Omega E}}. \tag{10}$$

Here $\tau_{\Omega j}$ are the characteristic carrier-phonon interaction times, u_{sj} are the plasma screening parameters, $f_e(\varepsilon_\Omega)$ is the electron distribution function at energy $\varepsilon_\Omega = \hbar\Omega(u+1)^2/(4u)$; $f_{\Omega e}$ and $f_{\Omega 0}$ are phonon distribution functions at carrier and lattice temperatures, respectively. Frequencies $\nu_{\Omega D}$ and $\nu_{\Omega E}$ describe decay and birth rates of LO-phonons.

In our case, both P_{sp} and $P_{\hbar\Omega}$ are considered as functions of coordinate. When using (10), interaction of electron-hole plasma with LO-phonons is described accounting for the bottleneck effects. The interaction is considered a two-step process. First, hot carriers transfer energy to the lattice by emitting a phonon. Since LO-phonons have

weak dispersion, and their decay time is relatively long, there occurs a local lattice heating which inhibits further carrier-to-lattice energy transfer. It can be proven from (10) that the widely used dependence $P = n(T - T_0)/\tau$ is not obeyed for practical concentrations. In particular, with concentrations increasing, the energy transfer rate can even decrease.

To complete the system of equations, it should be supplemented with the Poisson equation:

$$\frac{\partial^2 \varphi}{\partial x^2} = -\frac{e}{\varepsilon \varepsilon_0}(p - n + N_D - N_A), \tag{11}$$

where N_D and N_A are donor and acceptor concentrations, respectively.

2.2. Current Density and Energy Flux

In general, current densities and energy flux only depend on gradients of two dynamic characteristics: electrochemical potential and temperature, the latter being dependent on energy density. The current densities and energy flux can be written down as

$$j_n = \sigma_n \frac{\partial}{\partial x}\left(\frac{\zeta_n}{e} - \varphi\right) + \beta_n \frac{\partial T}{\partial x}, \tag{12}$$

$$j_p = \sigma_p \frac{\partial}{\partial x}\left(\frac{\zeta_p}{e} - \varphi\right) - \beta_p \frac{\partial T}{\partial x}, \tag{13}$$

$$Q = Q_n + Q_p, \tag{14}$$

$$Q_n = -\chi_n \frac{\partial}{\partial x}\left(\frac{\zeta_n}{e} - \varphi\right) - \kappa_n \frac{\partial T}{\partial x}, \tag{15}$$

$$Q_p = \chi_p \frac{\partial}{\partial x}\left(\frac{\zeta_p}{e} - \varphi\right) - \kappa_p \frac{\partial T}{\partial x}. \tag{16}$$

Coefficients σ, β, χ and κ strongly depend on the type of carrier interaction with the lattice. For the case of LO-phonons, the following expressions are obtained[12] (presented here for electrons only):

$$\sigma_n = e\mu_n \aleph_c(T)\Phi_{1/2}\left(\frac{\zeta}{T}\right) = e\mu_n n, \tag{17}$$

$$\beta_n = \mu_n \aleph_c(T)\left[\frac{5}{2}\Phi_{3/2}\left(\frac{\zeta}{T}\right) - \frac{\zeta}{T}\Phi_{1/2}\left(\frac{\zeta}{T}\right)\right], \tag{18}$$

$$\chi_n = \mu_n \aleph_c(T) T\left[\frac{5}{2}\Phi_{3/2}\left(\frac{\zeta}{T}\right) - \frac{\zeta}{T}\Phi_{1/2}\left(\frac{\zeta}{T}\right)\right], \tag{19}$$

$$\kappa_n = \frac{\mu_n}{e} \aleph_c(T) T\left[\frac{35}{4}\Phi_{5/2}\left(\frac{\zeta}{T}\right) - 5\frac{\zeta}{T}\Phi_{3/2}\left(\frac{\zeta}{T}\right) + \left(\frac{\zeta}{T}\right)^2 \Phi_{1/2}\left(\frac{\zeta}{T}\right)\right]. \tag{20}$$

The term proportional to gradient of electrochemical potential can then be transformed by extracting diffusion and drift components explicitly:

$$\sigma_n \frac{\partial}{\partial x}\left(\frac{\zeta_n}{e} - \varphi\right) = e\mu_n n E + D_n \frac{\partial n}{\partial x}, \tag{21}$$

with the diffusion coefficient D_n related to mobility by the generalized Einstein relation:

$$\frac{\mu_n}{D_n} = \frac{e}{T}\frac{d \ln n}{d \zeta_n}.$$

2.3. Initial and Boundary Conditions

To solve this system of equations, it is also necessary to establish initial and boundary conditions. As was previously mentioned, initial conditions for carrier concentrations are

$$n = p = 0. \tag{22}$$

Within the high injection level approximation, currents flowing through heterobarriers are equal to the external current density j_{ext} which is supposed to be a given function of time. The leakage currents are neglected since they are small compared to j_{ext} owing to the extra factor of $\exp(-\Delta E_j/kT)$ where ΔE_j, $j = c, v$ are discontinuities of conduction and valence bands, respectively. Thus,

$$j_p\Big|_{x=0} = j_n\Big|_{x=d} = j_{ext}, \qquad j_n\Big|_{x=0} = j_p\Big|_{x=d} = 0. \tag{23}$$

Disregarding leakage currents also leads to vanishing of the electron and hole energy flux at the p- and n-sides of the active layer:

$$Q_n\Big|_{x=0} = 0, \qquad Q_p\Big|_{x=d} = 0. \tag{24}$$

At the same time,

$$Q_p\Big|_{x=0} = j_{ext}\varepsilon_{eff\,p}, \qquad Q_n\Big|_{x=d} = -j_{ext}\varepsilon_{eff\,n}, \tag{25}$$

where $\varepsilon_{eff\,j}$ is the effective energy passed over by the injected carriers counted per one carrier. To calculate this energy input, we consider the rate of carrier cooling during their "fall" from the heterobarrier as

$$\frac{d\varepsilon}{dt} = \left(\frac{d\varepsilon}{dt}\right)_{ee} + \left(\frac{d\varepsilon}{dt}\right)_{\hbar\Omega}. \tag{26}$$

This rate consists of two terms: the first is the energy transfer to the plasma, and the other is associated with emission of LO-phonons. Integration of (26) over the time interval of carrier thermalization yields

$$\varepsilon_0 - \zeta = -\int \left(\frac{d\varepsilon}{dt}\right)_{ee} dt - \int \left(\frac{d\varepsilon}{dt}\right)_{\hbar\Omega} dt,$$

which can be rewritten in terms of energy losses:

$$\varepsilon_0 - \zeta = -\int_{\zeta}^{\varepsilon_0} \frac{\left(\frac{d\varepsilon}{dt}\right)_{ee}}{\left(\frac{d\varepsilon}{dt}\right)_{ee} + \left(\frac{d\varepsilon}{dt}\right)_{\hbar\Omega}} d\varepsilon - \int_{\zeta}^{\varepsilon_0} \frac{\left(\frac{d\varepsilon}{dt}\right)_{\hbar\Omega}}{\left(\frac{d\varepsilon}{dt}\right)_{ee} + \left(\frac{d\varepsilon}{dt}\right)_{\hbar\Omega}} d\varepsilon, \tag{27}$$

where ε_0 is the height of the heterobarrier. In this expression, the first integral is ε_{eff}. The rate of cooling due to interaction with carriers $\left(\frac{d\varepsilon}{dt}\right)_{ee}$ is as follows:

$$\left(\frac{d\varepsilon}{dt}\right)_{ee} = \frac{4\pi n e^4}{\kappa_\infty^2 \sqrt{2m\varepsilon}} \left[1 + \ln\left(\frac{\varepsilon\sqrt{m}}{2\hbar\sqrt{2\pi n e^2/\kappa_\infty}}\right)\right], \tag{28}$$

while $\left(\frac{d\varepsilon}{dt}\right)_{\hbar\Omega}$ is calculated using the procedure similar to that given by (10).

The boundary conditions for Poisson equation are established under the assumption that electric field at heteroboundaries is a linear function of the pumping current. Neglecting the difference in permittivities of the active layer and the emitters leads to

$$E\Big|_{x=0} = \frac{j_{ext}(t)}{\mu_p p|_{x=0}}, \qquad E\Big|_{x=d} = \frac{j_{ext}(t)}{\mu_n n|_{x=d}}. \tag{29}$$

To make the initial and boundary conditions compatible, the integral concentration of donors and acceptors in the active layer should be equal:

$$\frac{e}{\varepsilon\varepsilon_0}\int (N_D - N_A)\, dx = 0. \tag{30}$$

Note that after the initial point, the carriers are injected and recombine in pairs, so the integral charge neutrality will hold.

3. RESULTS AND DISCUSSION

The developed model has been applied to analyze the transient response of double heterostructure laser pumped by current pulse with short leading front. Simulations were performed for $Al_{0.3}Ga_{0.7}As/GaAs$ laser with undoped active layer 0.58 μm thick. The cavity length was taken 400 μm, and the stripe width 20 μm. The leading front of the pumping current was 100 ps, whereas the amplitude of current was varied in the range of 1–5 A which corresponds to current density of $1.25 \times 10^4 - 6.25 \times 10^4$ A/cm^2.

Shown in Fig. 1 are the laser output responses simulated at the pumping current amplitude of 1 A and 5 A. At each current, the responses were simulated both with carrier temperature taken into account and disregarding temperature effects. Quite naturally, increasing the current amplitude results in shortening of the switching-on delay and in suppression of relaxation oscillations after the optical pulse. However, as it is clearly seen in this figure, carrier heating results in longer delay times and considerably increased relaxation oscillation damping. The former effect is related to gain suppression by temperature so that a higher concentration is required to reach the threshold. The dynamic temperature rise associated with the onset of generation (which will be discussed below) is equivalent to additional contribution to nonlinear gain which is known to suppress the relaxation oscillations.

The temporal evolution of laser emission spectrum simulated at current amplitude of 1 A is presented in Fig. 2. As one can see from this figure, the first optical spike has the maximum spectral width and in this spike the envelope of the emission spectrum is asymmetric. Following this spike, the total power oscillates, its spectrum shifting towards lower energy of quanta. This behavior is explained by depletion of population inversion during the first optical pulse, which leads to further shift of the gain spectrum to longer wavelengths.

Alongside the appreciable difference in optical power, the laser behavior under low and high pumping levels is different in terms of the temperature of recombining carriers. The simulated temporal evolution of carrier temperature is shown in Fig. 3. It is readily seen that both at low and high pumping levels, the carrier temperature is enhanced in respect to the lattice temperature. Except for the short starting period when the carrier density is low and local charge neutrality condition has not been reached, at any time of interest the only source of carrier heating is their injection from the heterobarrier. When carriers fall down from the heterobarriers, a fraction of their excess energy is, as was discussed in previous section, transferred to the electron-hole plasma. Carrier heating is more intensive in the vicinity of heterojunctions and is proportional to the current density. Due to heat conduction, the energy introduced to the system of carriers spreads over the whole active layer, which leads to flattening of temperature profile. Since the number of carriers comprising the system rises in time, a gradual decrease of average temperature accompanies carrier accumulation in the active layer. As it is clear in these figures, the carrier temperature profile is inhomogeneous across the active area. The temperature is higher near the n-emitter because the conduction band discontinuity is greater than that of the valence band. Besides, the fractions of the energy transferred to the carrier system and to the lattice differ for electrons and holes: electrons offer a more pronounced heating.

Another interesting feature of the temperature profiles is connected with appearance of laser generation. As one can see in Fig. 3a, while the optical pulse is developing at $t \approx 1300$ ps, the carrier temperature increases at the side of p-emitter and slightly drops at the opposite side. This behavior is explained as follows. Stimulated emission takes place mostly at the maximum of gain spectrum the energy of which is less than Fermi levels separation. Thus stimulated emission removes carriers whose energies are lower than the average one, and the heating/cooling balance is shifted towards carrier heating (see Eqs. 5, 8). However, the energy balance is also determined by energy flux gradient. At the development of laser generation the carrier density starts to diminish most rapidly in the center of the active layer where the mode shape $\Psi^2(x)$ has its maximum. This changes dramatically diffusion currents and energy fluxes at both sides of the active layer. As detailed analysis shows, the most pronounced effect is that energy flux gradient changes its sign at the side of n-emitter*.

The comparison of Figs. 3a,b indicates that at higher current the carriers are more hot, and the temperature variation across the structure is more distinct. At the pumping current of 5 A (Fig. 3b), carrier temperature undergoes a sharp change at the onset of laser generation as well. At this current, however, the temperature rise is observed throughout the whole active layer. This shows that it is merely a quantitative effect that temperature response to the optical pulse may change its sign along the x-axis as was discussed above for the case of lower pumping.

Fig. 4 displays carrier concentration vs. time and coordinate simulated at the pumping current of 5 A. As it is seen, there is a strong inhomogeneity in the carrier concentration which persists with time. The carrier density is

*No such effect occurs at the side of p-emitter, apparently because of lower hole mobility.

higher at the side of p-emitter due to difference in mobilities. An interesting manifestation of such inhomogeneity is that the carrier density relaxation peak preceding the optical spike is somewhat delayed at the n-side with respect to that at the p-side.

4. CONCLUSION

In this paper we have presented a model which allows to simulate dynamic response of heterostructure laser with bulk active layer under high pumping level, when carrier heating effects are important. An attractive feature if this model is that it deals with coordinate-dependent carrier density and temperature. We believe the model provides a reasonable balance between relative simplicity of its approach and the possibility to describe various laser operation regimes. In particular, it can be applied to the analysis of gain-switching and (with subtle modifications) Q-switching operation modes. It can also be used in optimization of laser structure design aimed at the enhancement of optical pulse power.

ACKNOWLEDGMENTS

The authors are grateful to Prof. I. N. Yassievich for her essential help in the development of the model. This work was supported by INTAS grant 97-OPEN-1609.

REFERENCES

1. O. Wada, S. Yamakoshi, and T. Sakurai, "Band-gap enhanced carrier heating in InGaAsP/InP double heterostructure light-emitting diodes," *Appl. Phys. Lett.* **41**(10), pp. 981–983, 1982.
2. J. Shah, R. F. Leheny, R. E. Nahory, and H. Temkin, "Hot carrier effects in 1.3-μ $In_{1-x}Ga_xAs_yP_{1-y}$ light emitting diodes," *Appl. Phys. Lett.* **39**(8), pp. 618–620, 1981.
3. V. I. Tolstikhin and M. Willander, "Carrier heating effects in dynamic-single-frequency GaInAsP-InP laser diodes," *IEEE J. of Quantum Electron.*, **31**(5), pp. 814–833, 1995.
4. A. Mozer, K. M. Romanek, W. Schmidt, and M. Pilkuhn, "Evidence for Auger and free-carrier losses in GaInAsP/InP lasers: Spectroscopy of a short wavelength emission," *Appl. Phys. Lett.*, **41**(10), pp. 964–966, 1982.
5. V. B. Gorfinkel, B. M. Gorbovitsky, and I. I. Filatov, "Hight frequency modulation of light output power in double-heterojunction laser," *Int. J. Infrared Millim. Waves*, **12**, pp. 649–658, 1991.
6. M. Elsässer, S. G. Hense, and M. Wegener, "Subpicosecond switch-off and switch-on of a semiconductor laser due to transient hot carrier effects," *Appl. Phys. Lett.*, **70**(7), pp. 853–855, 1997.
7. J. D. Ralston, S. Weisser, I. Esquivias, E. C. Larkins, J. Rosenzweig, P. J. Tasker, and J. Fleissner, "Control of differential gain, nonlinear gain, and damping factor for high-speed application of GaAs-based MQW lasers," *IEEE J. of Quantum Electron.*, **29**(6), pp. 1648–1659, 1993.
8. V. I. Tolstikhin and M. Willander, "Resonant-tunneling injection hot electron laser: An approach to picosecond gain-switching and pulse generation," *Appl. Phys. Lett.*, **67**(18), pp.2684–2686, 1995.
9. L. Davis, H. C. Sun, H. Yoon, and P. K. Bhattacharya, "Small-signal modulation and temperature dependence of the tunneling injection laser," *Appl. Phys. Lett.*, **64**(24), pp. 3222–3224, 1994.
10. M. Grupen and K. Hess, "Severe gain suppression due to dynamic carrier heating in quantum well lasers," **70**(7), pp. 808–810, 1997
11. V. I. Tolstikhin and G. Yu. Khrenov, "Mechanisms of carrier and energy injection in three-terminal laser structures," *Appl. Phys. Lett.*, **69**(15), pp. 2157–2159, 1996.
12. I. N. Yassievich, Doctoral thesis, Ioffe Institute, 1975.

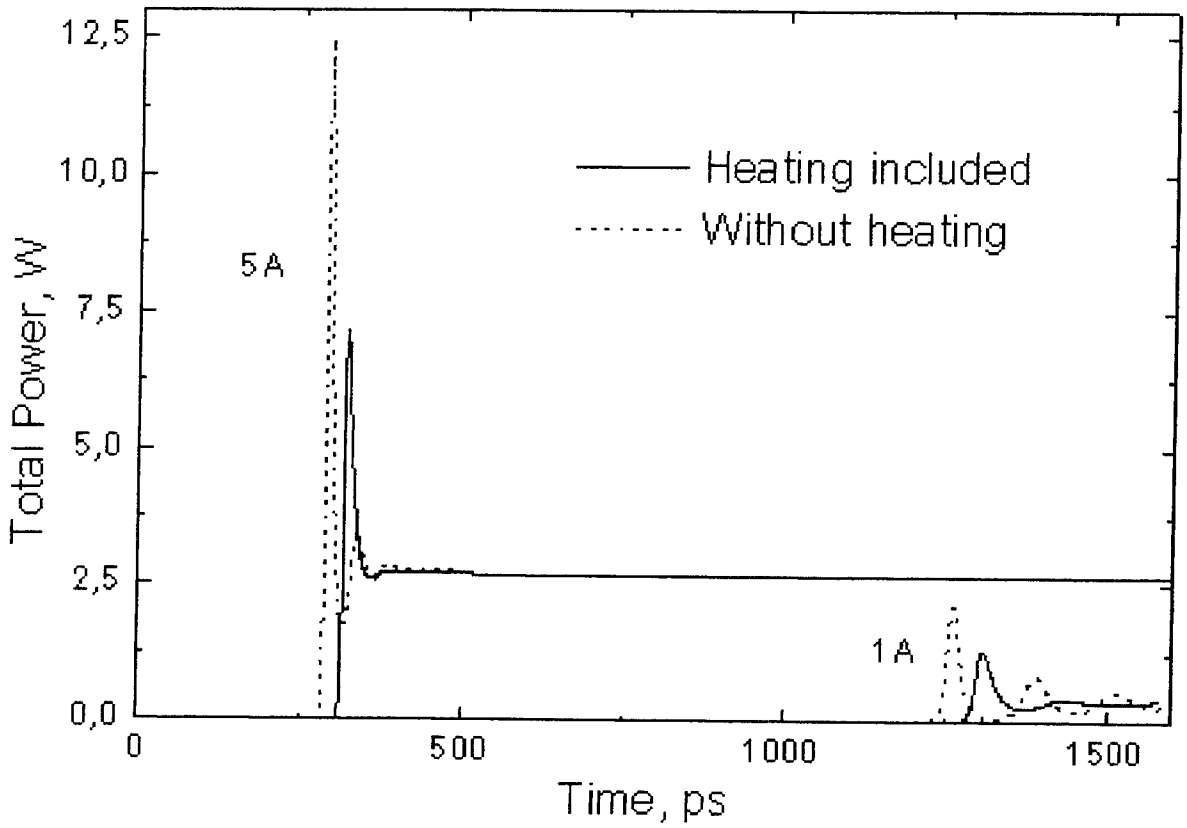

Figure 1. Laser output responses simulated at the pumping current amplitude of 1 A and 5 A. Solid lines — carrier heating effects are taken into account, dashed lines — carrier and lattice temperatures are taken to be equal.

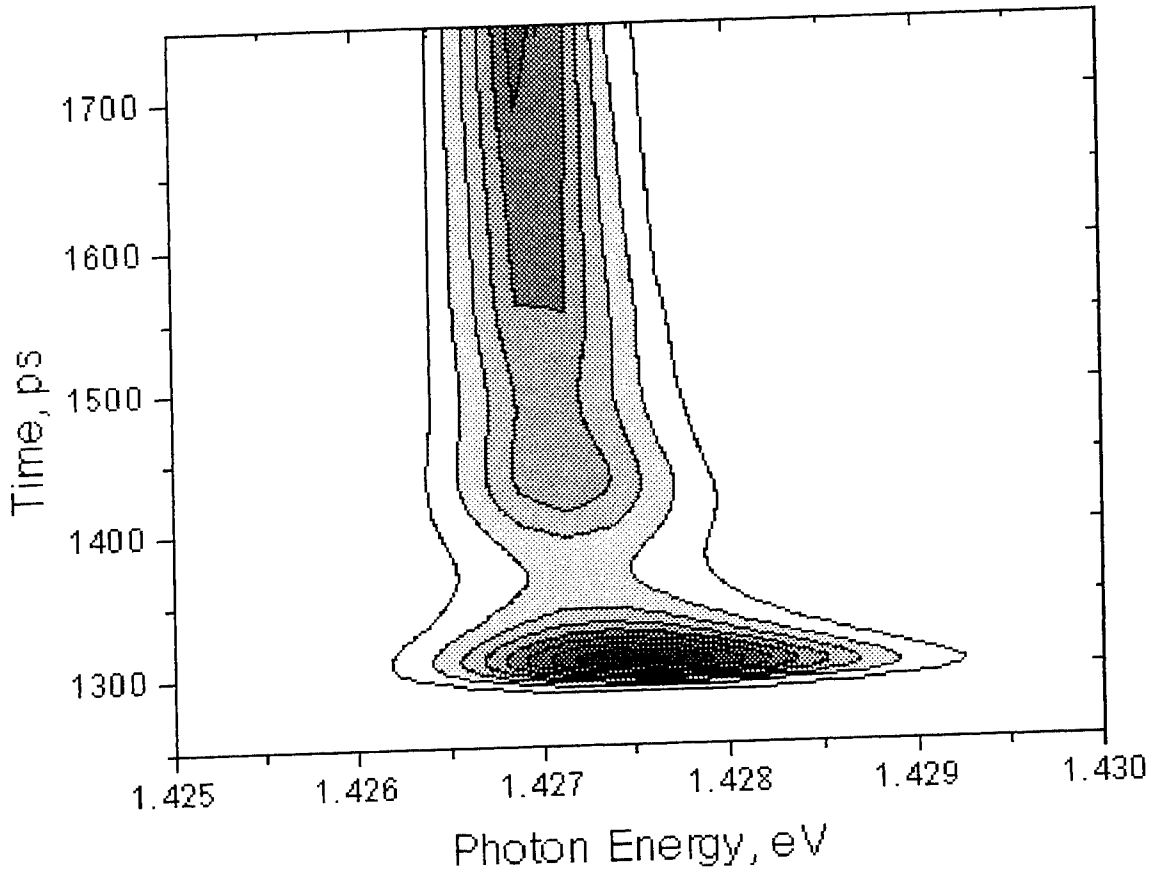

Figure 2. Temporal evolution of laser emission spectrum.

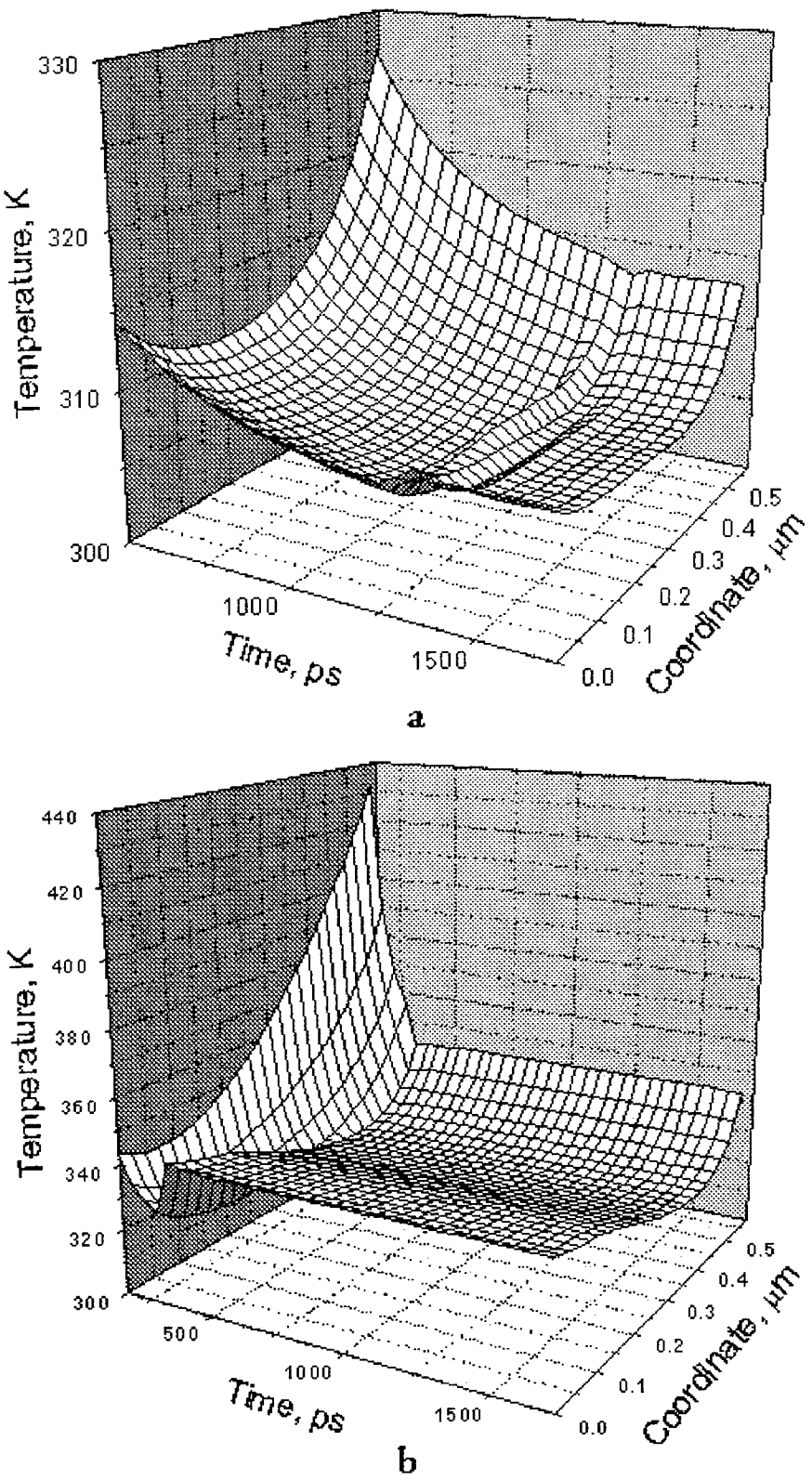

Figure 3. Simulated carrier temperature as a function of time and coordinate for pumping currents of: **a** — 1 A, **b** — 5 A. Note different temperature scales.

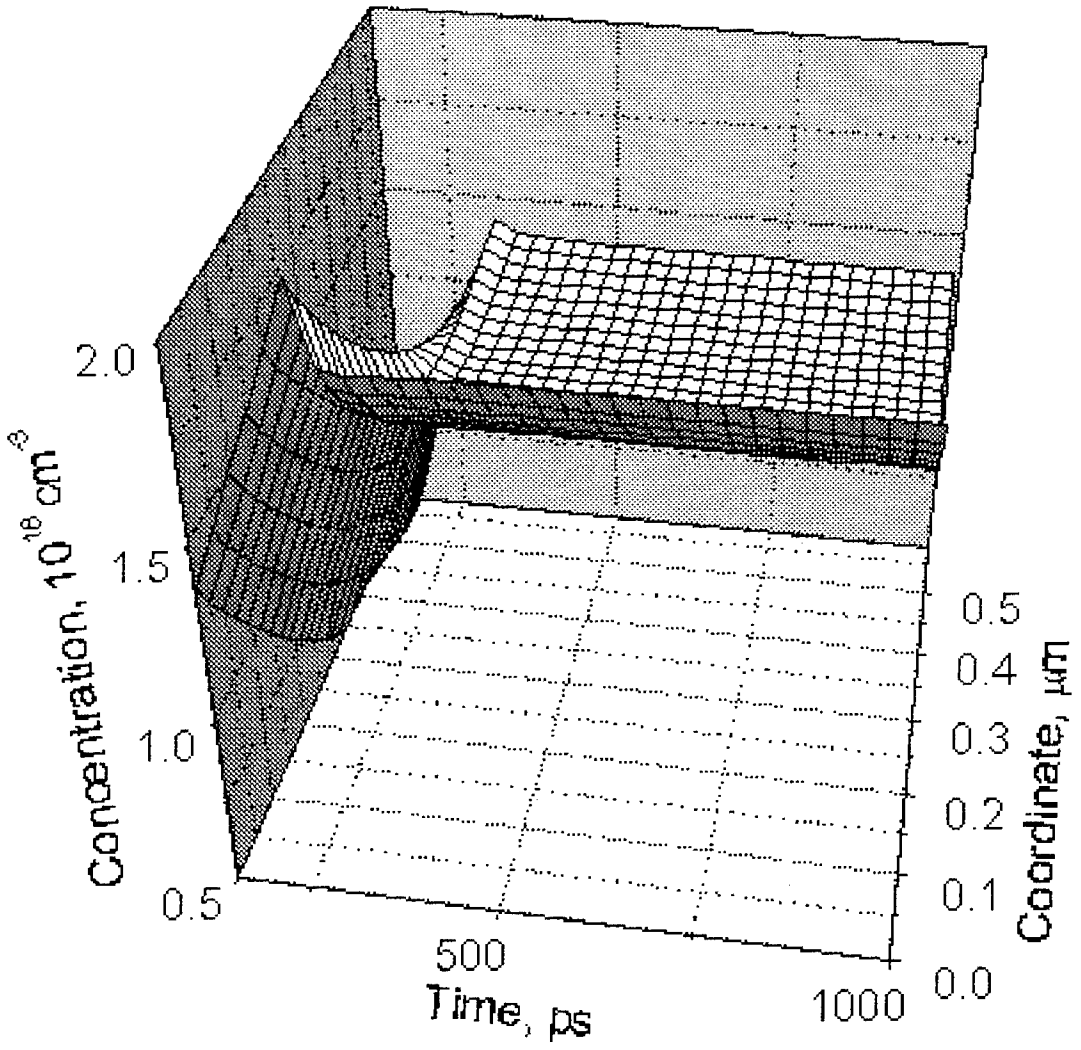

Figure 4. Temporal evolution of electron density at the pumping current of 5 A.

Internal Q-switching in single-heterostructure lasers: one term for two phenomena.

S.N. Vainshtein*), J.T. Kostamovaara

University of Oulu/ Dept. of El. Eng. / El. lab. / Linnanmaa PL 4500 FIN-90401, Oulu, FINLAND, Fax: +358 - 8 -5532700, e-mail: vais@ee.oulu.fi

*) S. Vainshtein is on leave from the A.F. Ioffe Institute of the Russian Academy of Science / 194021 / Politechnicheskaya Ul. 26 / St. Petersburg, RUSSIA, e-mail: vais@seva.stoic.spb.su

ABSTRACT

Great differences were found between the spectral and power responses for two modes of a single-heterostructure laser operation, with the dynamic behaviour of each mode fitted to the traditional definition of the internal Q-switching phenomenon. The first mode is interpreted in terms of the most popular diffraction losses theory, while the other one is related to the practically important method of high-power picosecond optical pulse generation and interpreted in terms of a recent carrier heating and cooling model. This finding could obviate confusion in the interpretation of mechanisms of high-power picosecond pulse generation in the Q-switching mode.

The generation of clean single 200W / 23ps pulses is demonstrated in the second Q-switching mode. An important role of the intrinsic tail-state absorption is shown for this operating regime. A mechanism of an intrinsic positive feedback is discussed which allows picosecond synchronisation in the absorber saturation instant to be achieved for the entire laser volume. This causes strong gain overshoot over the losses and the picosecond pulse generation by this means.

Keywords: Semiconductor laser, picosecond pulses, Q-switching, carrier heating, saturable absorption.

I. INTRODUCTION

Generation of high-power (10-10^3 W) single picosecond optical pulses by laser diodes, which fills the existing gap between ordinary nanosecond and the novel femtosecond range for semiconductor lasers[1], is important for a number of practical applications. A method of transient mode filtering from a high-power (45 W) gain-switched laser[2] allows a 16W / 25ps pulse to be generated. This method seems to be applicable for any type of laser diode, but the achievable peak power is only moderate. Another method which is makes use of Q-switched single-heterostructure (SH) lasers seems to be more effective[3-6]. Normalised to the emitting area, the optical power is higher by a factor of 20-100 than that achieved in Ref.[2]. Diodes of the same type were used in all these experiments[3-6] (LD-62, Laser Diode Inc.), with standard peak power of 5W, and the operating mode was ascribed to an internal Q-switching effect. An exception may be made for the experiments[6] where ion implantation was additionally used in order to form an ultra-fast saturable absorber within the diode mirrors.

Two approaches were adopted to physical interpretation of the observed laser behaviour. The authors of papers[3,4,6] followed the ideas of the most popular theory of the internal Q-switching phenomenon[7], which consider the complicated dependence of the refractive index step within the homojunction on carrier concentration, gain and Joule heating in the active region. The refractive index step, in turn, dramatically affects the diffraction losses. Alternatively, the model[5,8] considers saturable absorption via the tail states in heavily doped and compensated semiconductor materials, and also current-induced carrier heating.

We report here on time-resolved spectral measurements corresponding to both conditions realised in Ref.[7] and for high-power picosecond pulse generation. We aim to show the existence of two phenomena which fit the formal definition of internal Q-switching in SH laser diodes.

Let us briefly discuss the formal definition of the phenomenon. Internal Q-switching in homojunction and SH lasers was first observed in the early 1960s and has been studied extensively for many years[9]. It consists of the appearance of stimulated emission immediately after the current pulse stops, which means that the current pulse reduction stimulates the lasing. A closely related phenomenon is the effect of a long lasing delay, which means that the onset of the stimulated emission takes much longer than is needed for population inversion to be achieved. Both phenomena have always been observed together for a laser diode within the same lattice temperature range at different amplitudes of the pumping current. A characteristic shape for the Q-switching region in the current-temperature plane, as measured for a homojunction laser in Ref.[10], is shown in Fig.1(a). This shape is similar for various homo and SH laser diodes, but the minimal (transition) lattice temperature at which the phenomenon appears varies from ~ 100 to ~ 350°K depending on the fabrication process[9], and the

Laser Optics 2000: Semiconductor Lasers and Optical Communication, Serguei A. Gurevich, Nikolay N. Rosanov, Editors, Proceedings of SPIE Vol. 4354 (2001) © 2001 SPIE · 0277-786X/01/$15.00

current range varies as well. Delayed lasing occurs at a high current, and the Q-switching mode manifests itself when the current is reduced, provided that the lattice temperature is higher than the transition value.

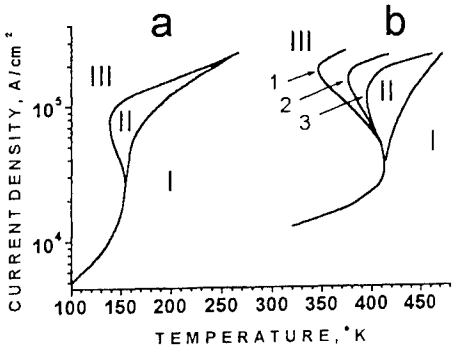

Fig.1. Regions of spontaneous emission (I), internal Q-switching (II) and normal lasing (III). The right-hand boundaries in both graphs define the dependence of the threshold current on temperature.
(a): reproduced from work [9] for a 84 ns current pulse, (b): curves 1-3 define the left-hand boundary of the Q-switching region for laser LD-62,[4] depending on the minimal current pulse duration used in the experiment: 1-1.2 ns, 2-2.5 ns, 3-7 ns.

We will thus regard the following criteria as constituting a traditional definition of Q-switching: stimulated emission occurs only within the end of the current pulse, and the Q-switching region has a characteristic shape in the current-lattice temperature plane similar to that shown in Fig.1(a). We also show in Fig.1(b), for the sake of comparison, the Q-switching region for SH laser LD-62 from Ref.[5], corresponding to a high-power, short pulsing mode. The region shapes in Fig.1(a,b) are qualitatively similar in appearance despite the significant differences in laser structure, current pulse duration and actual operating mode (as we will see in our further discussions). Together with the specific dynamic behaviour mentioned earlier, this creates a strong impression that one is dealing with the same physical phenomenon in both cases.

II. EXPERIMENTAL RESULTS

II. 1. Two different types of the Internal Q-switching

Two SH laser structures and two sets of pumping conditions were selected for our experiments in order to show the differences between the two types of Q-switching phenomena. Both types of laser diode had a structure *AlGaAs(P^+)-GaAs(p)-GaAs(n^+)*. The active p-region of the first type was relatively narrow *(~1 μm)* with a moderate *(~ 10^{17} cm^{-3})* total doping concentration. These lasers were pumped with relatively long-duration current pulses (40-100 ns) in order to reproduce conditions typical of those used in earlier publications[7,9,10]. The second type was a LD-62 laser with a wider *(~2 μm)*, heavily doped and compensated active region[3]. The total doping concentration in the active region can roughly be evaluated [11-12] as being over *1·10^{18} cm^{-3}* from a spectrum for a quasi-steady-state lasing mode (curve1, Fig.3(b)). This huge doping level is not particularly surprising for old-style technology, in which the active region was formed by acceptor compensation during the growing process of n^+- material with an initial donor concentration of *(2-4)·10^{18} cm^{-3}*. The current pulses with a duration of a few nanoseconds pumped this laser in order to fit the experimental conditions of high-power picosecond pulse generation[2-5,8].
The pumping current pulses and optical responses are presented in Fig.2. Curves related to the first type of laser structure are shown in Fig.2(a,b), and those presented in Fig.2(c,d) correspond to the second type. The optical responses in Fig.2(b,d) are normalised in both cases with reference to the nominal power of the corresponding laser diode. The nominal power of the first laser type was ~ 4 W for a stripe *150 μm* wide and *200 μm* long with a pumping current density of *30 kA/cm^2* at room temperature. For the second laser type the nominal power was ~ 5W for a stripe *150 μm* wide and *380 μm* long with the same current density.
One can see that the laser behaviour satisfies the formal definition for internal Q-switching in both cases despite the significant differences. The current pulse duration is an order of magnitude longer for the first laser type. If the pulse duration was reduced to under 30 ns, no Q-switching was observed at current densities of up to *150 kA/cm^2* at any lattice temperature. Namely, laser emission disappeared at a high temperature. When the lattice temperature was reduced smoothly, lasing appeared within the leading and trailing edges simultaneously and then spread over the whole current pulse duration at an even lower lattice temperature. Spikes appeared within the leading edge of the optical response when short current pulses (of a few nanoseconds) were used for pumping this first laser type with an amplitude of up to *250 kA/cm^2*, but no Q-switching behaviour was observed at any lattice temperature.
The laser diodes of the second type showed a much more intensive spike in the gain-switching mode when high-current pulses of a few nanoseconds were used. An increase in the lattice temperature caused a jump-like increase in both the lasing delay (which became equal to the current pulse duration), and the spike intensity [4, 8]. Q-switching behaviour was observed

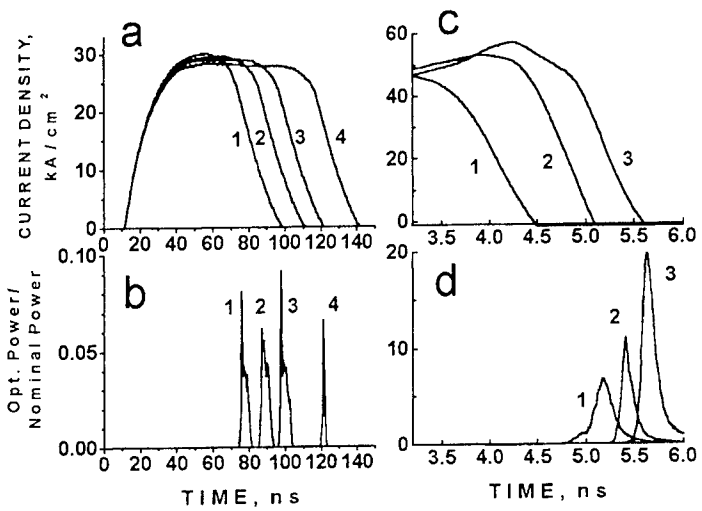

Fig. 2. Pumping current and optical pulse waveforms for lasers of the first (a,b) and second (c,d) types. The responses shown in (b) and (d) were measured at diode lattice temperatures of 372 °K and 413 °K respectively. The position of the leading edge of the current pulse corresponds to 0 ns in (c).

at this lattice temperature, (or higher), as illustrated for relatively low currents in Fig.2(c,d). For higher currents, the behaviour is qualitatively the same except that the optical spikes have a much higher intensity and shorter duration.
Time-resolved spectra are shown in Fig.3, which presents the difference between quasi-steady-state lasing modes and Q-switching modes for both types of laser diode. All the transient spectra were measured by means of a streak-camera equipped with a spectrograph, so that only the spectrum of the mode under investigation was recorded. Curve 1 in Fig.3(a) shows the spectrum of the quasi-steady-state lasing mode for the first laser type. The spectrum was measured at a lattice temperature T_L=*364 °K* at the end of a 100 ns current pulse immediately before the current decreased. The laser pulse duration was comparable to the current pulse duration at this temperature. The Q-switching mode was achieved when the temperature was increased to T_L=*372 °K* (curve 4 in Fig.2(b)). The corresponding spectrum is represented by curve 2 in Fig.3(a). A trivial spectral shift caused by the temperature band-gap dependence is automatically corrected by the selection of the type of horizontal scale, and the resulting Q-switching mode shift towards low photon energy can be seen. It is worth noting that the spectral band in the experiment did not just shift towards the longer wavelength when the temperature was growing, but the emission band shown by curve 1 decreased in intensity and disappeared and that shown by curve 2 appeared at the same time.

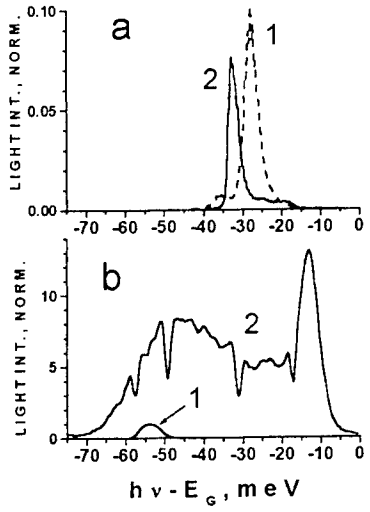

Fig.3. Transient spectra for quasi-steady-state modes (curves 1) and Q-switching modes (curves 2) for laser diodes of the first (a) and second types (b). The horizontal axis presents the difference between the photon energy and band-gap of pure GaAs for a given lattice temperature.

A completely different spectral transformation was found for the second type of laser structure when changing to the Q-switching mode. Curve 1 in Fig.3(b) represents the lasing spectrum for a 10 ns optical pulse at a *30 kA/cm²* current pulse amplitude and a lattice temperature T_L = *297 °K*. The transient spectrum for a ~30 ps high-power Q-switching pulse is represented by curve 2 in Fig.3(b), which corresponds to a *140 kA/cm² / 2.2 ns* (FWHM) pumping current pulse and a lattice temperature T_L = *381 °K*. The local signal oscillations in spectrum 2 (Fig.3(b)) are caused by the features of the photo-cathode of the streak-camera. The signal is normalised for all the spectra by relating the integral under curve 1 in Fig.3(b) to the 5 W peak power of the optical pulse and other integrals over the spectra to the peak power of the corresponding optical pulses.

II. 2. Role of the saturable absorption in the second type of the Q-switching.
We still have not answered the questions of when precisely lasing will occur around the trailing edge of the current pulse in the case of the second type of Q-switching, when picosecond optical pulse generation occurs and how short the trailing edge

of the current pulse should be in that case for the phenomenon to be observed. The answers will drastically affect the optical pulse intensity that can be achieved, as will follow from the discussion below.
Considering quasi-steady-state conditions in the case of the first Q-switching type, when the current pulse is relatively long (Fig.2(a,b)), lasing occurs when the carrier concentration reduces to a level which allows diffraction losses to be reduced sufficiently. The situation is more complicated in the case of the second Q-switching type, when the intensive optical pulse can be observed either within the trailing edge of the current pulse or a few nanoseconds after the current pulse stop.
An investigation of transient spectrum relaxation undertaken to clarify this problem showed that the exact moment of lasing onset depends on the lattice temperature in the active region. Lasing delay with respect to the trailing edge of the current pulse grows as the lattice temperature rises (left column in Fig.4) and the amplitude of the optical spike diminishes at the same time (Fig.4(b1-b4)) and the transient spectrum narrows (Fig.4(c1-c4)). This spectrum is measured by means of a spectrograph-equipped streak-camera and corresponds to the optical spike only in the laser response, thus ignoring the emission "tail" of low-intensity which appears after the picosecond pulse[5]. A correlation can be seen between the intensity of the picosecond optical pulse and its spectrum width together with the spectrum amplitude.

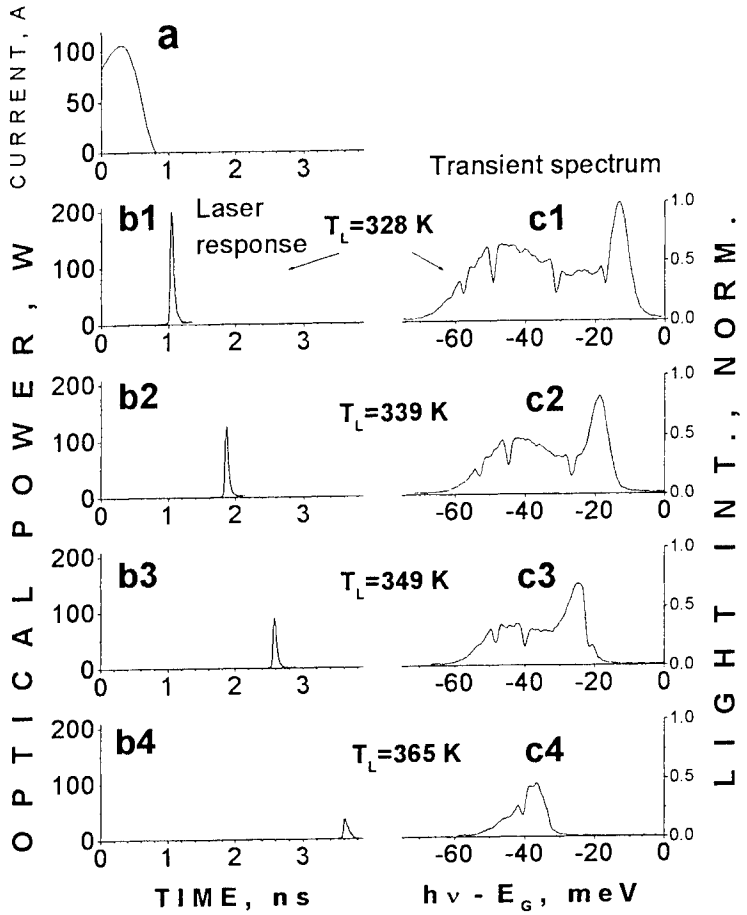

Fig.4. Trailing edge of the pumping current pulse (a), the optical response for the laser diode LD-62 (b1-b4), and corresponding transient spectra for the short optical spike (c1-c4) measured for different lattice temperatures.

We ascribe the observed behaviour to the simultaneous effects of absorber saturation, carrier energy relaxation and carrier recombination, and assume that carrier cooling takes place within the trailing edge of the current pulse, following the quantitative explanation for the second type of internal Q-switching[5,8]. The characteristic time for energy relaxation of the hot carriers in the band is very short (< 1 ps) [13], as compared with the current pulse fall time (~1 ns). Investigations into energy relaxation within localised states in heavily doped GaAs[14] have shown that the thermally activated multiple trapping mechanism is responsible for the relaxation in this case.

The characteristic time required for carrier relaxation in the tails is very sensitive to the lattice temperature, but for high lattice temperatures (of over 200 °K) the relaxation time is very short as well (< 0.5 ps)[14]. The question thus arises of why the lasing delay with respect to the trailing edge of the current pulse can be as long as a few nanoseconds (Fig.4 (a,b1-b4)). We believe that this is caused by the saturable absorption via the tail states. The distribution of the injected carriers across the active region is not homogeneous, the concentrations of both electrons and holes being high near the emitters and significantly lower in the centre of the base due to low carrier mobility. The exact moment when lasing occurs is defined by the competition between the gain for the optical transitions between the free carrier states and the absorption via the tail states in the centre of the base region. The gain becomes very high when the current pulse is stopped, but the absorption is also high, since the tail states are essentially depopulated at a high lattice temperature. This absorption decreases in time due

to spontaneous emission re-absorption, which leads to a tail state population (absorber saturation) in the center of the active region. Lasing occurs after the tail states are filled. The corresponding delay rises as the lattice temperature increases. One should now take into account the fact that there is no pumping current during the delay time, and that carrier recombination reduces the carrier density and thus the width of the carrier energy distribution. Accordingly, both the gain amplitude and the gain spectrum width should decrease as the lattice temperature rises. This is the case shown in Fig.4. The characteristic time required for carrier recombination can now be evaluated. Radiative recombination obviously predominates in the process and the recombination lifetime $\tau \sim 1/(n_0 \cdot B)$, where n_0 is the carrier concentration in the active region within the end of the current pulse, and B is the radiative recombination coefficient (for heavily doped GaAs $B \sim 2.5 \cdot 10^{-10}$ cm^3 / s) [12]. The value n_0 was evaluated to be $n_0 \sim 2 \cdot 10^{18}$ cm^{-3} from the width of the dynamic spectrum of spontaneous emission within the trailing edge of the current pulse. The resulting recombination lifetime value $\tau \sim 2$ *ns* agrees well with a characteristic time of both amplitude and spectrum relaxation for the short optical pulse (Fig.4).

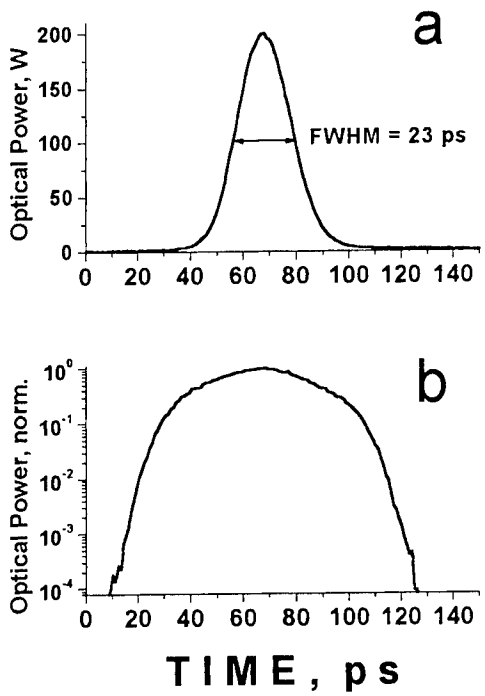

Fig. 5. Single optical pulse with linear (a) and logarithmic (b) intensity scales, derived by spectral filtering from the Q-switched LD-62 laser. The photon counting mode of a streak-camera was used in (b) in order to achieve a wide dynamic range. The optical signal is normalised to a 200 W peak value in this case.

Optimal pumping and temperature conditions for the generation of highly intensive picosecond optical pulses can be formulated on the basic of this consideration. First, the current pulse amplitude must be sufficient for carrier heating. Then the lattice temperature should be so high that the localised tail states are efficiently depopulated by thermal activation. The pumping current pulse should be longer than the carrier lifetime (a few nanoseconds), so that a thick active region is efficiently optically pumped. The trailing edge of the current pulse should be shorter than the recombination time for a given carrier density at the end of current pumping ($\tau \sim 2$ *ns* in the case of LD-62 laser). Finally, the lattice temperature must be accurately adjusted in such a way that the delay in the optical pulse with respect to the trailing edge of the current pulse has its minimal value not longer than τ .

The optical pulse presented in Fig.5 was achieved following these requirements, and making use of the transient spectrum filtering method [5] to suppress long-term emission after the pulse. Single pulses of 200 W / 23 ps were achieved with no pre-pulsing or after-pulsing signal with respect to the 20 mW level. The measurements were performed using a streak-camera (Hamamatsu C4742-95). The peak power was estimated from the measured average optical power after the band-pass filter.[4]

III. DISCUSSION

III.1 Physical reasons for two types of the Q-switching behaviour.

We interpret the Q-switching mode observed for the first type of laser diode (Fig.2(a,b), Fig.3(a)) in terms of the diffraction losses theory[7], which considers the very sharp dependence of the diffraction losses on the value of a small refractive index step in the homojunction side of the diode wave-guide. This index step decreases as the carrier concentration increases, thus destroying the wave guiding effect at a high current (but not so high that gain guiding confinement can compensate for the reduction in the refractive index). Such assumption provides a means for understanding the situation when lasing does not occur during the whole duration of the current pulse except for its leading and trailing edges, i.e. when the current level is not high enough for strong diffraction losses to be induced.

Furthermore, the time-dependent contribution to the refractive index step, considered in Ref.[7], is caused by Joule heating due to the passage of a current through the active region. The band gap of the active region material decreases relative to the value in the adjoining regions, since all the heat generation is limited to the active region for a ~100 ns pulse. Fairly insignificant Joule heating in the active region (~a few °K) can compensate for the current-associated decrease in the refractive index step.

Theory[7] allows both a long lasing delay and the Q-switching phenomena to be explained for long-duration current pulses (~100 ns). The long lasing delay can be interpreted as follows. Lasing does not occur when optical losses exceed the gain for a high current amplitude. Joule heating in the active region can reduce the diffraction losses after an interval of several dozens of nanoseconds, which causes the onset of delayed laser generation. Otherwise, lasing may occur within both the leading and trailing edges of the current pulse due to lower diffraction losses at a low current, as we observed for the first laser type with a pulse duration less than ~30 ns (Chapter II). Some increase in the losses with respect to gain, e.g. through the increase in lattice temperature in the whole laser structure, suppresses this emission, but it is still possible to achieve lasing at the end of the current pulse by increasing the current pulse duration. The diffraction losses become time-dependent in this case, and local Joule heating of the active area causes Q-switching behaviour (Fig.2(a,b)).

The spectral features shown in Fig.3(a) can be easily understood in the framework of this model. The spectral maximum of the gain in the semiconductor lasers shifts towards low photon energies when the current is reduced[11]. The Q-switching spectral band should thus be shifted towards lower photon energy with respect to the stationary lasing, since the current value decreases in the trailing edge. The spectral shift of ~10 meV can be expected [11] when the current is reduced to about a half of its nominal value, which is in reasonable accordance with the experimental data (Fig.3(a)). Note finally that the Joule heating of the active region was evaluated by the spectral shift in the emission band maximum during a $100\,ns / 30\,A / cm^2$ current pulse. The emission band maximum shifted by 1.1 nm towards a long wavelength from the beginning to the end of the optical pulse, which corresponds to an increase of ~ 3 °K in the temperature of the active region.

An alternative qualitative model[5,8] is used here to interpret Q-switching behaviour in the second laser type with pumping pulses of a few nanoseconds. Two basic assumptions are used in this model, which should be intrinsically inherent for a heavily doped and compensated active region. These are strong light absorption with the tail states involved and very low carrier mobility, which allows a strong electric field, causing carrier heating to be achieved in a thick active region at high currents. The first assumption seems to have been well proved experimentally long ago as a reason for the long lasing delays in SH laser diodes[13-15].

The carrier heating hypothesis[8] has not been directly proved so far, but it did allowed the time-resolved spectra observed in recent years to be explained[5,8]. The operation of the laser can be described in the framework of this model as follows. The distribution of the injected carriers across the active region is not homogeneous after the pumping current pulse is applied, the concentration of both electrons and holes being high near the emitters and significantly lower in the centre of the base due to the low carrier mobility. Lasing should in principle not occur in this structure, since light absorption predominates in the central part of the active region. Specific optical pumping nevertheless allows lasing to be achieved. Indeed, a certain fraction of the spontaneous photons generated near the emitters are absorbed in the whole active region of the diode, leading to a population of tail states. No carrier activation from the localised tail states occurs at a low temperature, and the gain at a given moment will exceed the optical losses for the photons, whose energy is significantly lower than the semiconductor band gap (curve1 in Fig.3(b)). Abnormally long lasing delays can be expected for these lasers, since only a small fraction of the spontaneous photons which are generated around the emitters should be absorbed in the active region. Thermal activation from localised to delocalised states becomes possible at a higher lattice temperature, which leads to a widening of the carrier distribution towards higher energies and to a decrease in the population of lower energy states. This will increase the lasing delays, which will become very sensitive to the lattice temperature[8] due to widening of the carrier energy distribution[5] and corresponding gain suppression. Unlike the low temperature case, the high-energy transitions are involved in lasing at a high lattice temperature. The corresponding energy states are delocalised, and the carriers which occupy these states participate in the conductivity. This makes it possible for the carrier energy distribution to be dependent on the current for a high current density, and this may cause Q-switching behaviour.

The strong electric field in the central part of the active region (caused by low mobility) heats the carriers, thus broadening the carrier distribution and suppressing the gain. This causes an additional increase in the lasing delay and at the same time allows an increase in carrier concentration in the active region before lasing occurs. Instantaneous carrier relaxation to the bottom of the energy band should be expected when the current pulse is broken off, which causes a very marked gain in the spectral range, corresponding to the transitions between the band edges. The exact moment when lasing occurs is defined by the competition between the gain for the optical transitions between the free carrier states and the absorption via the tail states. The gain becomes very high when the current pulse is stopped, but the absorption is also high, since the tail states are essentially depopulated at a high lattice temperature. This absorption decreases in time due to spontaneous emission re-absorption, which also leads to a tail state population. When, after a certain delay, the tail states are filled, the optical peak

can be expected at the front of lasing (Section II.2) with the intensity dependent on the falltime of the current pulse and the lattice temperature.

An alternative explanation for short-pulse generation by LD-62 lasers[3,4,6] accounts for the same idea of wave guide destruction by a high carrier concentration as in Ref.[7]. Although this approach can explain the long delays and carrier accumulation in the active region before the gain-guiding effect[7] leads to lasing, the explanation of Q-switching behaviour may encounter difficulties in this case since the Joule heating for short current pulses is negligible. Furthermore, this model should be able to explain the spectral peculiarities[5,8] of the phenomenon. Finally, it is worth noting that Q-switching in the first laser type was not observed with short high-amplitude current pulses in our experiments (Chapter II), despite the effect of the carrier density on the refraction index step should play an even more important role in the case of a SH laser diode with a thin, low-doped active region. It is otherwise clear from the alternative model[5,8] that Q-switching of the second type should not be observed in a laser diode with a moderate doping level in a relatively thin active region.
We would further assume that certain contradictions in publications on the internal Q-switching effect from the 1960s and 1970s might be associated with the investigation of different physical phenomena by different authors. This evidently concerns the physical nature of long lasing delays caused by diffraction losses, or alternatively by saturable absorption. We would assume, for example, that it was the first type of Q-switching that was investigated in Ref.[10] and the second one in Ref.[15-17].

III.2. Automatic synchronisation of the absorber saturation in the second Q-switching mode.
An important question which remains still open is: why the switching instant can be so well synchronised for entire active region of the laser diode that a high gain overshoot takes place? Indeed, a high local gain should take place when the absorber in a certain area of the laser diode has been saturated. This saturation is caused by the spontaneous photon generation near emitters and their absorption within the central part of the active region, and a characteristic time for this process lies in the nanosecond range. Natural structure inhomogeneities should cause different instants of the absorber saturation for different parts of the laser structure. A synchronisation in these instants should not be as good as some picoseconds, which will reduce significantly the overshoot in the integral gain and should not allow the high-power picosecond generation to be achieved in a real structure.

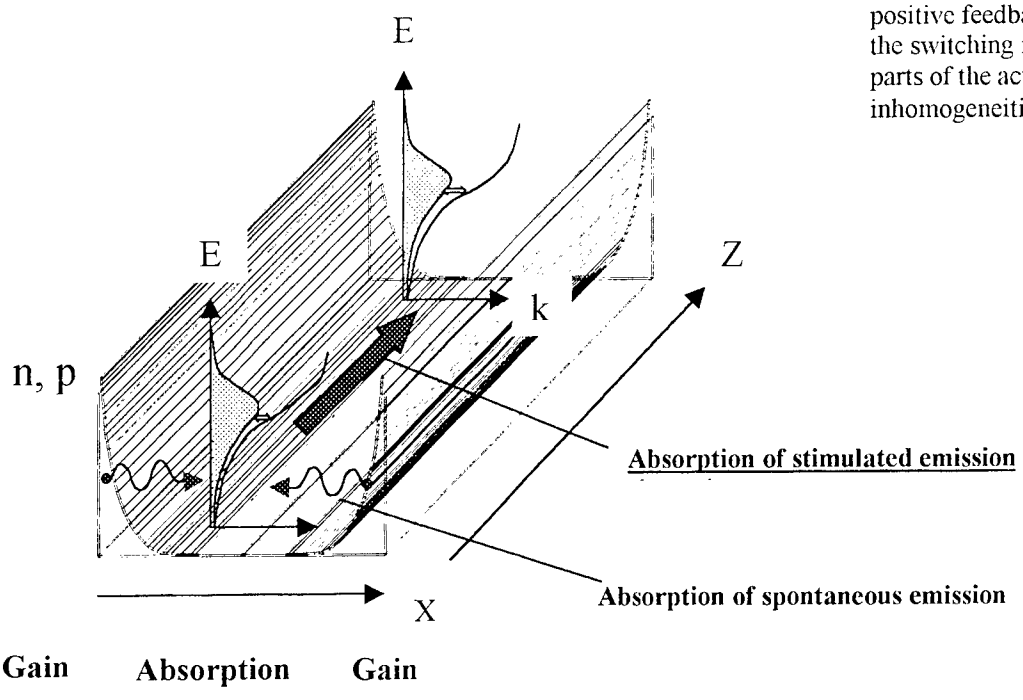

Fig.6. Illustration of an idea of the positive feedback which synchronizes the switching instants for different parts of the active region with inhomogeneities .

A simple idea of an intrinsic positive feedback could explain this contradiction (see illustration in Fig.6). Imagine that the absorber is saturated in a small region of the laser structure. This region becomes a source of superluminescent emission,

which will be limited within the waveguide, and will provide the means for the absorber saturation in the adjacent areas of the diode. These new regions with the saturated absorber will provide further increase in the stimulated emission intensity, and finally whole the active region will have the absorber saturated within a picosecond time range. This avalanche-like process, which is an intrinsic property of the distributed absorber, will case a prompt increase in the integral gain over whole inhomogeneous active region.

IV. CONCLUSIONS

Two forms of spectral and power response behaviour were demonstrated experimentally for SH laser diodes operating in internal Q-switching mode. Both regimes fit the formal definition for the Q-switching phenomenon, but they can be attributed to different physical processes in the laser structure. The Q-switching observed for long current pulses (~100 ns) in a SH laser with a lightly doped thin active region is interpreted in terms of the diffraction losses theory[7]. High-power picosecond pulse generation by a SH laser with a heavily doped thick active region pumped with short current pulses (~ a few nanosecond) is interpreted in terms of the carrier heating and cooling model[5,8], accounting for the intrinsic saturable absorption in the structure. This intrinsic absorber should play very important role in the switching synchronisation in a real laser diode with structure inhomogeneities.

ACKNOWLEDGEMENTS

This work was supported by INTAS grant 97 -OPEN- 1609 and by the Academy of Finland. The authors are grateful to all the participants in the project for their assistance. The authors would also like to express their deep gratitude to Grigoriy Simin for fruitful discussions.

REFERENCES

1. Special issue on ultrashort optical pulse technologies and their applications. IEICE Trans. Electron., vol. E81-C, No.2, 1998.
2. S.N. Vainshtein, G.S. Simin, and J.T. Kostamovaara, "Deriving of single intensive picosecond optical pulses from a high-power gain-switched laser diode by spectral filtering", *J. Appl. Phys.* **84**, pp. 4109-4113, 1998.
3. A. Biernat and G. Kompa " Powerful picosecond laser pulses enabling high-resolution pulsed laser radar", *J. Optics*, **29**, pp.225-228, 1998.
4. F. P. Vople, V. Gorfinkel, J. Sola, G. Kompa, "140/40 ps single optical pulses for laser sensor application.", *Conf. Lasers & Electr.-Opt. (CLEO-9)* , Anaheim, CA, 1994.
5. S.N. Vainshtein and J.T. Kostamovaara, "Spectral filtering for time isolation of intensive picosecond optical pulses from a Q-switched laser diode", *J. Appl. Phys.* **84**, pp. 1843-1847, 1998.
6. E.L. Portnoi, G.B. Venus, A.A. Khazan, I.M. Gadjiev, A.Yu. Shmarcev, J. Frahm, D. Kuhl. "Superhigh-power picosecond optical pulses from Q-switched diode laser". *IEEE J. Select. Topics Quant. Electr.* **3**, p. 256-260, 1997.
7. F. D. Nunes, N. B. Patel, Jose E. Ripper. "A theory on long time delays and internal Q switching in GaAs junction lasers." *IEEE J.Quant. Electr.* **13**, pp.675-681, 1977.
8. S. Vainshtein, V. Rossin, A. Kilpela, J. Kostamovaara, R. Myllyla, K. Maatta "Internal Q switching in semiconductor lasers: high intensity pulses in the picosecond range and spectral peculiarities." , *IEEE J.Quant. Electr.* **31,** pp. 1015 - 1021, 1995.
9. J.E.Ripper and J.A.Rossi. "Delays and Q switching in Semiconductor lasers -still open question," *IEEE J.Quant. Electr.* **10**, pp. 435 - 441,1974,
10. J. C. Dyment and J. E. Ripper " Internal Q switching in GaAs junction lasers, " *Appl. Phys. Lett.* **12**, pp.365 - 367, 1968.
11. F. Stern. "Calculated spectral dependence of gain in excited GaAs." *J.Appl. Phys.* **47**, pp. 5382-5386, 1976.
12. H.C. Cassey, F. Stern. "Concentration-dependent absorption and spontaneous emission of heavily doped GaAs." *J.Appl. Phys.* **47**, pp. 631-643, 1976.
13. J.Shah "Hot carriers in quasi-2-D polar semiconductors." *IEEE J. Quant. Electr.* **22**, pp. 1728-1743, 1986.
14. E.O.Gobel and W.Graudszus "Optical detection of multiple-trapping relaxation in disordered crystalline semiconductors," *Phys. Rev. Lett.*, **48**, pp.1277-1280, 1982.
15. J. I. Pankove, "Optical filling of delay - inducing traps in injection lasers," *IEEE J.Quant. Electr.* **4**, pp. 427 - 429, 1968.
16. G.E. Fenner. "Delay of the stimulated emission in GaAs laser diodes near room temperature." *Sol.- State Electr.* **10**, pp. 753-764, 1967.
17. M.J.Adams, S.Grundorfer, B.Thomas, C.F.L.Davies and D.Mistry "Time delays and Q switching in homostructure and heterostructure injection lasers". *IEEE J.Quant. Electr.* **9**, pp. 328 - 337, 1973.

High power picosecond laser transmitter with highly stable switching delay.

Sergey N. Vainshtein [a]), Andrey V. Maslevtsov [b]), Juha T. Kostamovaara

University of Oulu/ Dept. of El. Eng. / El. lab. / Linnanmaa PL 4500 FIN-90401, Oulu, FINLAND, Fax: +358 - 8 -5532700, e-mail: vais@ee.oulu.fi

[a]) S. Vainshtein is on leave from the A.F. Ioffe Institute of the Russian Academy of Science / 194021 / Politechnicheskaya Ul. 26 / St. Petersburg, RUSSIA, e-mail: vais@seva.stoic.spb.su

[b]) A. Maslevtsov is with the State Technical University / 194021 / Politechnicheskaya Ul. 29 / St. Petersburg, RUSSIA, e-mail: andronov@twonet.stu.neva.ru

A compact laser diode based transmitter was designed and tested for laser radar and various laboratory applications. Single optical pulses with a peak power of up to 200 W, 23-65 ps pulse duration and a repetition rate of up to 50 kHz were measured. Transient mode spectral filtering suppressed afterpulsing modes by a factor of 10^4-10^5 with respect to the peak power. A control module was developed which provided a jitter value between electrical triggering and the optical pulses as low as 14 ps. Averaging of 10^3 events allows 1.5 ps stability between the triggering and the optical pulses to be achieved within a delay range from 5 to 250 ns.

I. INTRODUCTION

A stable high-power picosecond light source is useful for a number of laboratory tests and for practical applications such as high resolution optical radars, precise 3 D imaging, lidars, laser tomography, time imaging spectroscopy, lifetime studies, etc. Low cost compact transmitters may find further industrial applications.

We report here on a transmitter based on the Q-switching operation regime of a commercial single-heterostructure (SH) laser diode with intrinsic absorber[1,2] . A method of transient mode spectral filtering allows a clean single pulse to be derived from the Q-switched laser response[3]. The achievement of high optical power ($\geq$ 100 W) together with short (picosecond range) pulse duration require the use of a high current (~ 100A) pulses a few nanoseconds in length for the pumping, and optimal temperature conditions [1]. Moreover, precise temperature control in the active region of the diode is necessary for achieving a highly reproducible waveform in the optical pulse, and also a stable pulse delay with respect to the triggering pulse. High stability of the current pulse amplitude and waveform are also important.

Principles for precise local temperature stabilisation and the results of tests on a prototype of the picosecond pulse transmitter are presented.

II. PUMPING AND TEMPERATURE CONDITIONS

Internal Q-switching behaviour associated with high-power picosecond optical pulse generation in laser diode LD-60 (Laser Diode Inc) is illustrated in Fig.1. This phenomenon can be observed in a single-heterostructure (SH) laser diode with a thick, heavily doped active region when a current pulse of a few nanosecond in length is used for pumping. The effect manifests itself at a sufficiently high current amplitude and lattice temperature in the laser diode. A slight increase in the current pulse amplitude or in the lattice temperature causes a jump-like increase in the lasing delay, a reduction in the duration of the gain-switching spike and a significant rise in spike intensity (Fig.1(a,b)). Fairly significant spectrum broadening (curves 2, 2' in Fig.1(c)) for the Q-switching pulse is observed in this case (curve 2 in Fig.1(b)).

This phenomenon has lately been ascribed to the simultaneous effect of carrier heating and intrinsic absorption in the diode active region [1-3]. One should not confuse the behaviour illustrated here with another internal Q-switching phenomenon in SH lasers[4-6] caused by the diffraction losses in the cavity. This concerns lasing near the trailing edge of a ~100 ns current pulse in a SH diode with a thin, lightly doped active region, and the optical pulse intensity is very low in this case.

High-power picosecond pulse generation is caused by a high gain overshoot over the losses level. These conditions can be attained in a SH laser diode with a thick, heavily doped active region due to current-induced carrier heating and intrinsic tail-

Laser Optics 2000: Semiconductor Lasers and Optical Communication, Serguei A. Gurevich, Nikolay N. Rosanov, Editors, Proceedings of SPIE Vol. 4354 (2001) © 2001 SPIE · 0277-786X/01/$15.00

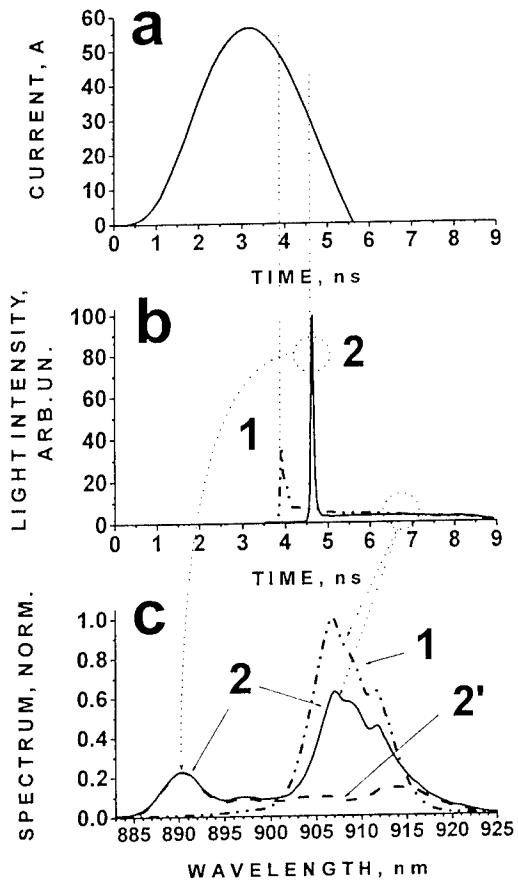

Fig.1. Pumping current (a), optical pulse waveforms (b) and optical spectra (c) measured for laser diode LD-60 operating in gain-switching (curves 1) and Q-switching (curves 2,2') modes. Curves 1 and 2 in (c) present time-integrated spectra, and curve 2' presents the transient spectrum corresponding to the Q-switching spike. Optical waveforms and spectra are measured with a spectrograph-equipped streak camera. Lattice temperature of the laser diode T_L: 1-306.27 °K; 2,2'- 308.85 °K. The absolute accuracy of temperature measurement is about 1 °K and the relative accuracy about 0.01 °K.

state absorption[1,2,7]. Very low carrier mobility causes a strong electric field in the centre of the active region at a high pumping current, carrier heating allows carrier accumulation in the energy space to be achieved in the active region prior to lasing. High gain appears when the current pulse causing the carrier heating stops. A very high rate of carrier cooling should not in principle allow high gain to be achieved when the trailing edge of the current pulse lies in the nanosecond or subnanosecond range. Intrinsic tail-state absorption in the central part of the active region nevertheless makes this possible. Lasing occurs when the absorber is saturated and the saturation time, being dependent on the lattice temperature, varies in the nanosecond range.

Carriers cool down within the trailing edge of the current pulse and create high spatially localised gain, but lasing does not occur until the absorber is saturated, and the exact instant of the generation onset can be controlled by lattice temperature adjustment. This qualitative consideration allows optimal pumping and temperature conditions to be formulated.

II.1.Pumping.

Three laser transmitters were designed and tested, so that three types of laser diode which satisfy the listed requirements were used with the same structure. These lasers differ in the size of their emitting area: 2 X 75 μm (LD-60, Laser Diode Inc., standard peak power 3 W), 2 X 150 μm (LD-62, standard peak power 5 W) and 2 X 225 μm (LD-65, standard peak power 10 W).

The following optimal (sufficient) pumping conditions can be specified for high-power picosecond optical pulse generation in the internal Q-switching mode.

First, the dI/dt rate and amplitude of the current pulse should be successfully high in order for carrier heating to prevent lasing during pumping at a moderate lattice temperature (see below).The pulse duration is then a compromise between two factors. Optical pumping of the central part of the active region[2] requires the pulse duration to be longer than the radiative recombination lifetime (~2ns)[1] at an excess carrier concentration of $2\,10^{18}$ cm^{-3}. Contrariwise, an excessively long current pulse requires the use of a high lattice temperature for the Q-switching mode to be obtained[2]. An increase in the lattice temperature reduces the efficiency of radiative recombination, thus reducing the power in the Q-switching peak. Finally, the fall time of the current pulse should be shorter than the recombination lifetime[1].

A sufficient current density was found to be $1.5\,10^5$ A/cm^2 in all cases at a current pulse rise time of 2-3 ns. The optimal duration for the current pulse was found to be 2.5-3.5 ns, while its fall time should be as short as possible (preferably less than 2 ns). The required current density would mean current amplitudes of 43 A, 85A and 130A for the laser diodes LD-60, LD-62 and LD-65 respectively. A compromise was found between these requirements and simple realisation of the pumping circuit by using an avalanche transistor based switch. The original circuit design used here requires special analyses and will

be discussed elsewhere. This has allowed the current across the laser diode to be as high as 130 A with a maximum residual voltage across the avalanche switch of 85 V and a differential resistance of 0.2 Ω in the switch. The values for the current pulse rise time were found to be 1.7, 2.0 and 2.7 ns for 43, 85 and 130A amplitudes respectively (Fig.2).
The durations (2.5, 4.3, 6.1 ns) and fall times (1.3, 2.6, 4.7 ns) of the pumping pulse were defined by the current oscillation in a circuit containing a full inductance of 3.4 nH and a capacitor C_0 (0.33, 1, 2.2nF). The capacitor that served as the voltage source was preliminarily charged to 300 V. A shunting diode was used to defend the laser diode from negative current oscillation. The second (positive) oscillation of the current was damped to the extent that the corresponding laser pulse (if this appeared) had a much narrower spectral band than the Q-switching pulse, and the spectral filtering (see below) suppressed this emission completely.

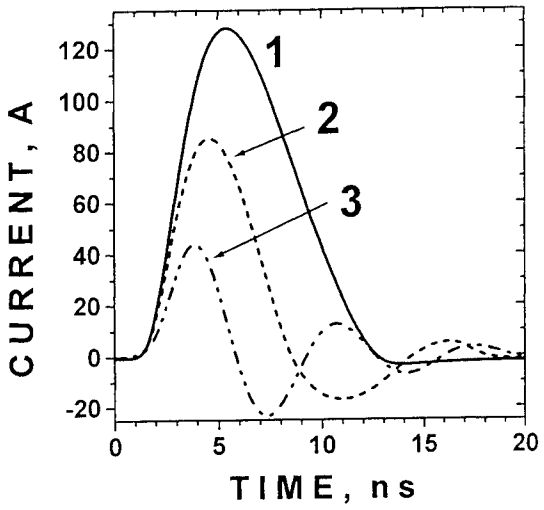

Fig.2. Current pulses generated by the avalanche transistor-based driver at various values of the voltage source capacitor C_0, nF: 1-2.2, 2-1, 3-0.33. The current pulses were obtained by replacing the laser diode chip with a 0.94 Ω load resistor with a parasitic inductance of 0.7 nH. An iteration procedure was then used for deriving the current pulses from the voltage pulse across the load resistor.

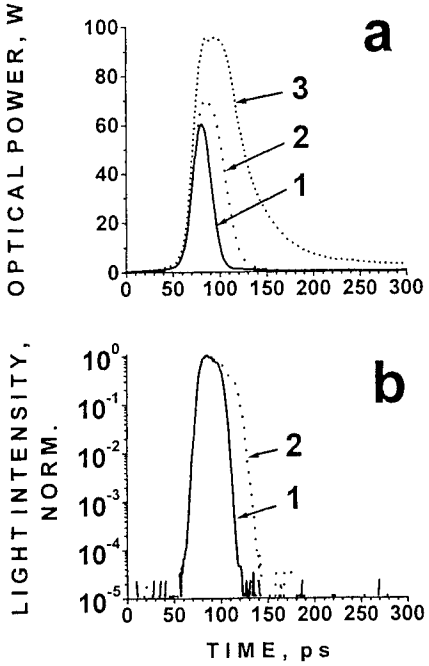

Fig.3. Illustration of the effect of spectral flittering on the optical pulse waveform of Q-switched laser diode LD-60. Waveform 3 is measured with a spectrograph-equipped streak camera without spectral filtering, and curves 1 and 2 correspond to the numerical filtering in the camera pattern with long cut-off wavelengths of 894 and 904 nm respectively (compare with Fig.1(c)). The peak power was evaluated from the optical energy measured with 904 nm interference filter[3]. The optical waveforms with a wide dynamic range (b) were obtained in photon counting mode.

II.2.Temperature conditions and spectral filtering

The highest intensity of the Q-switching peak was observed when the diode temperature exceeded the critical value corresponding to the transition from the gain switching to Q-switching mode by only a few°K. The transient spectrum width for the optical spike in this case (curve 2' in Fig.1(c)) was an order of magnitude higher than that for the normal quasi-steady state mode (~30 nm against ~3nm). Any further increase in the lattice temperature caused a gradual rise in the lasing delay, a reduction in the power and transient spectrum width of the Q-switching pulse and an increase in its duration. Precise thermal stabilisation at a level of a few °K above the transition temperature should thus be required for the optimal operating mode to be achieved under given pumping conditions.
A stimulated emission "tail" typically appears after the Q-switching spike, when the current pulse has already stopped [3]. This emission is caused by the transitions between the localised states, its intensity is lower than the Q-switching pulse by a factor of 10-50 (depending on pumping and the lattice temperature), and its duration can be as long as several dozens of

nanoseconds. Luckily this emission tail has a much narrower spectrum than the transient Q-switching mode, which allows spectral filtering to be used to derive the single picosecond pulse[3]. The interference optical filters used in the module were specially designed and fabricated by Chroma Technology Inc. and had a transparency of 75-80% and a steep spectral characteristic near cut-off (~1.5 nm/decade). Use of these filters allowed a clean single Q-switching pulse to be derived, with a reduction of 30-40% in the pulse amplitude due to the narrowing of the transient spectrum (Fig.3(a)), and an additional 20-25 % due to filter transparency.

Spectral filtering can also be used to reduce the Q-switching pulse duration from ~ 45 to ~23 ps by fine adjustment of the laser temperature. The method is based on chirping of 1.5 ps / nm as observed in the picosecond range spike[3]. An increase in the lattice temperature shifts the transient spectrum towards a longer wavelength and the filter cuts off the modes with a longer switching delay (compare curves 1-3 in (Fig.3(a)). Furthermore, spectral filtering allows the emission after Q-switching spike to be suppressed by a factor of 10^4-10^5 with respect to the peak power (Fig.3(b)).

III. TRIGGERING AND TEMPERATURE CONTROL

Block and timing diagrams which illustrate the principles of temperature, charging and triggering control are shown in Figures 4 and 5. The module is designed for operation with a streak camera and has an output for the sweep triggering (pulse "Sweep Trig.") before optical pulse generation (pulse "Laser Trig"). The timing of sweep triggering can be delayed relative to the "Ref. Trig." pulse by intervals ranging from 0 to 100 ns in 10 ns steps. The "Laser Trig." pulse used for laser driver triggering can be delayed by intervals ranging from 0 to 250 ns (in 25 ns steps) at a lowjitter FWHM value of 14 ps with respect to both "Ref. Trig." and "Sweep Trig." Tunnel diodes with precise thermocontrollers were used in fast comparators (Fig.4) in order to provide high stability between the pulses "Ref. Trig.", "Laser Trig" and "Sweep Trig." An additional facility is a "MCP Trig." pulse which serves as the preliminary (~200 ns before "Ref. Trig.") trigger for a pulse generator in the micro-channel plate of a streak-camera.

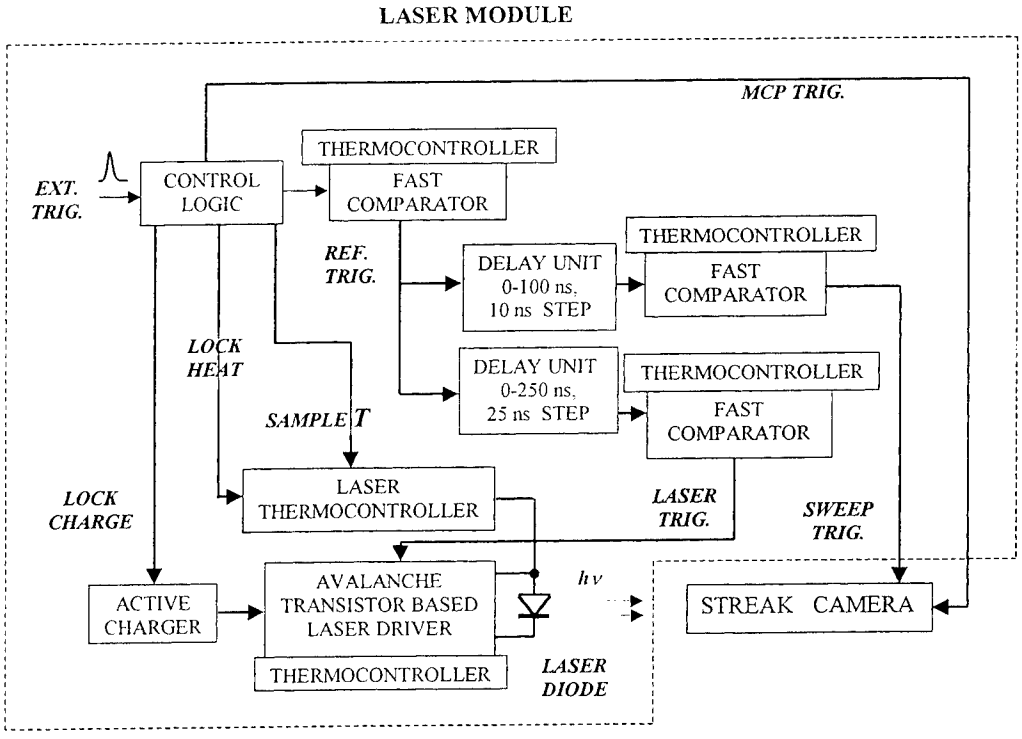

Fig.4. Block diagram of the laser module. The thermocontroller loops are shown separately in Fig.6.

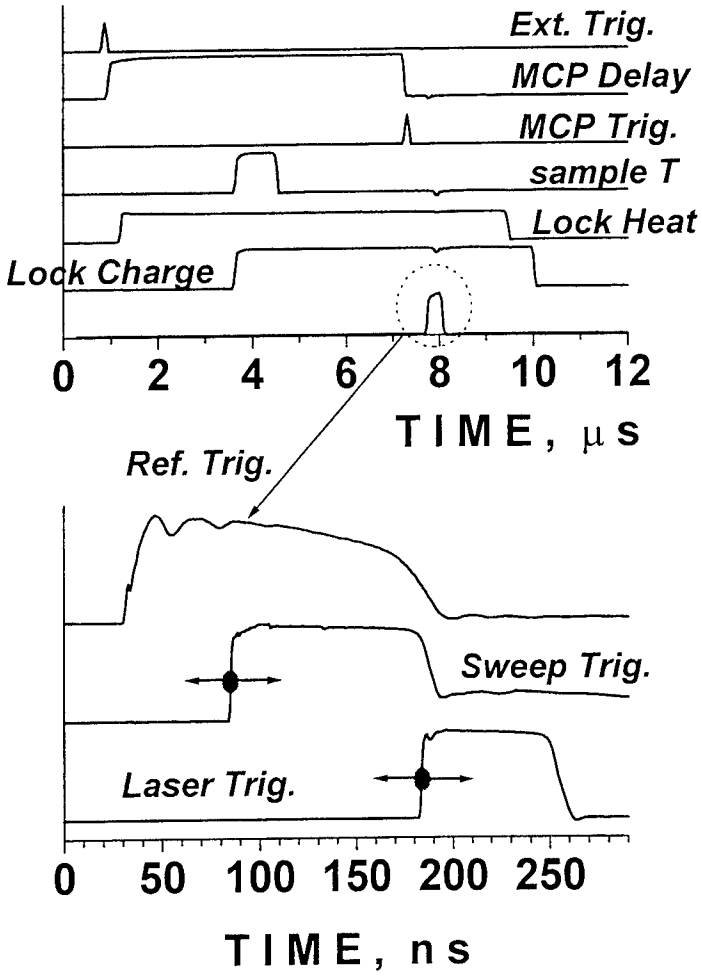

Fig.5. Diagram of the electrical pulses in the laser module. The pulses with high delay stability are shown on a nanosecond scale.

Dynamic charging of the capacitor C_0, which supplies an avalanche transistor switch, was used for stable driver operation at high repetition rates. The charging, controlled by the pulse "Lock Charge" (see diagrams), stops a few microseconds before laser pulse generation and further charging arises within ~ 2 μs after the laser pulse. A simple but effective method was used for precise thermal stabilisation of the active region of the laser diode. This method is based on the fact that the threshold current of the laser (~ 10^4 A/cm^2) is so high that moderate forward biasing (~300 A/cm^2) affects the lattice temperature in the active region rather than the laser pumping. This means for LD-62, for example, that a constant biasing current of 200 mA can heat the diode structure by a few dozens of °K and still remain lower than the threshold current by a factor of 25.

The voltage drop across the laser diode at low current forward 2 mA biasing was used as a measure of the lattice temperature in the active region (Fig.6(a)). An additional 0-500mA biasing current was heating the active region all the time except in an interval controlled by the pulse "Lock Heat". Only the probe current flows through the diode during this time, and the voltage drop across the diode is measured during the pulse "sample T" duration. Variation in this voltage has a thermal coefficient of -1.8 mV/°K, and this voltage value is used for both heating current control and laser temperature indication. A standard thermocontroller loop as used for the thermal stabilisation of all the fast comparators and avalanche transistors in the laser driver is shown in Fig.6(b). Peltier coolers were used for the thermal control, and package-free Si diodes as temperature sensors. Both the sensor diodes and the Peltier coolers had good thermal contact with the elements under stabilisation.

IV. TEST RESULTS

IV.1. Optical power and pulse duration.

As already been mentioned (curve 2 in Fig.1(b)), a Q-switching optical pulse always has an emission tail of low intensity but very long duration. This tail creates difficulties in reliable power measurement since the contribution of the emission tail to the pulse energy exceeds that for the picosecond pulse. The problem becomes even more complicated since the emission tail has a different angle diagram from the Q-switching spike. Spectral filtering allows this problem to be overcome, since no optical signal except the Q-switching pulse contributes to the measured optical energy.

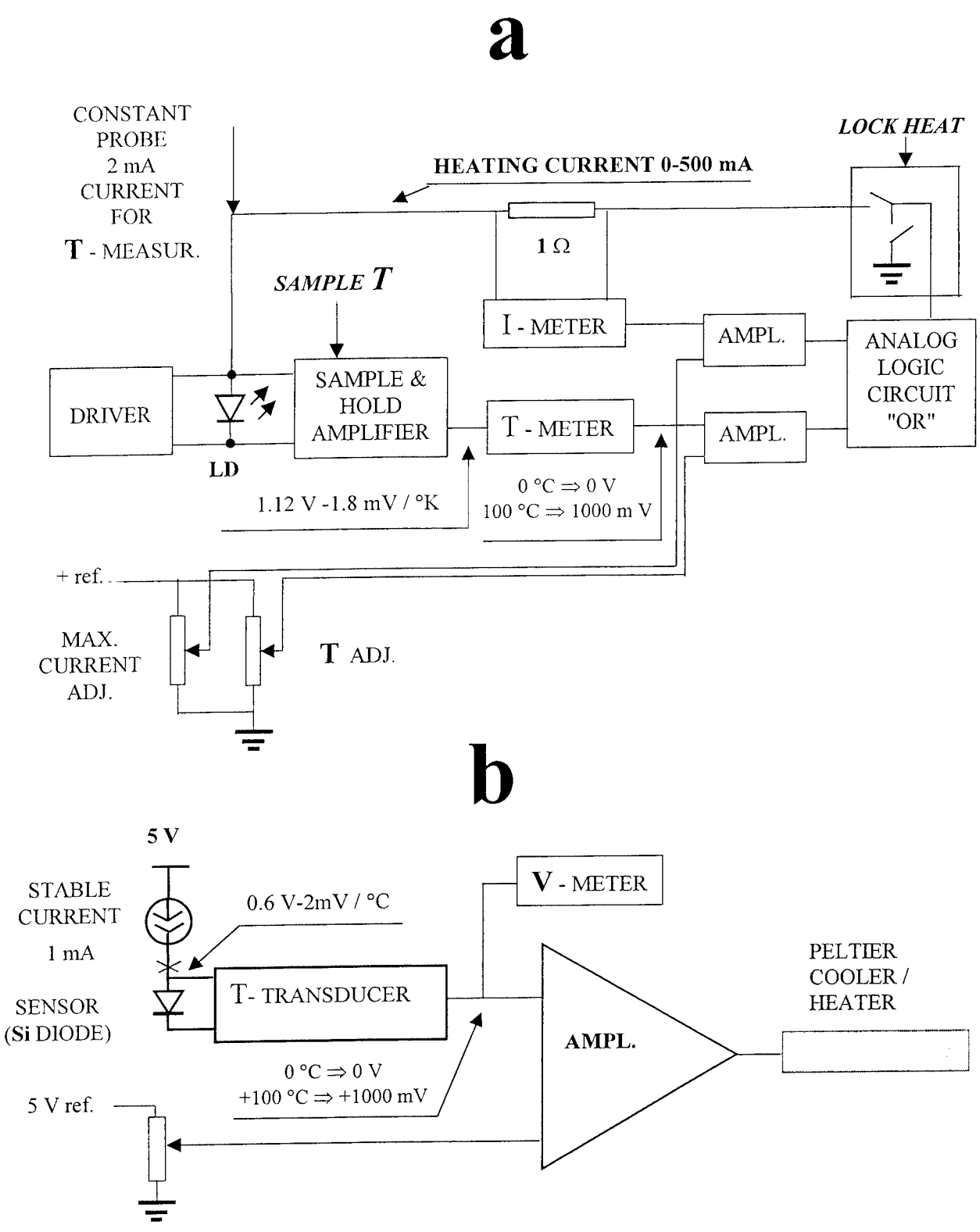

Fig.6. Thermocontroller loop for the laser diode (a), and loop for the comparators and the laser driver thermocontrollers (b).

The measured optical energies for the optical pulses after the filter are 1.5-2.5 nJ, 3.5-4.5 nJ and 5.2-6.5 nJ for LD-60, LD-62 and LD-65 respectively with various pumping pulses and lattice temperature adjustments. The current pulse amplitude was controlled by adjusting the voltage across the capacitor in the laser driver, and temperature of the laser diode was optimised for each set of pumping conditions in order to achieve the maximum Q-switching spike amplitude. An alternative criterion for temperature optimisation can be selected in order to match the transient spectrum (curve 2' in Fig.1(c)) to the spectral characteristic of the selected optical filter. An increase in the diode temperature shifts the spectrum towards a long wavelength, thus reducing the optical pulse duration (compare waveforms 1 and 2 in Fig.3(a,b)) together with a reduction in the "tail" emission and a certain decrease in peak power. Two alternative bandpass optical filters were used in our tests, both suppressing long-wavelength emission, with cut-off wavelengths of 904nm and 912 nm respectively. An appropriate filter was selected for each laser transmitter. The module allows simple, prompt adjustment of the optimal diode temperature according to the requirements of a specific application.

The shortest pulse duration was found to be 23 ps for LD-60 and 30-45 ps for the others (optical pulse waveforms measured with a streak camera for LD-60 are shown in Fig.3). The full range of the peak optical power for all the transmitters in the output of the collimating optics and the spectral filter was measured to be 50-180 W.

The peak power without spectral filtering is typically 60-80% higher, but the FWHM of the pulse ranges from 40 to 70 ps and the long emission "tail" is not suppressed in this case.

It is worth noting that use of a wider laser stripe allows a higher optical energy to be achieved in the single spike, but the pulse duration becomes longer and the eventual gain in peak power is not very significant due to structuralinhomogeneity.

IV.2. Stability of the lasing onset.

An optical "start" pulse is typically used in laser radars, and a stable delay between the electrical triggering and the optical pulse is not important in this case. It is very convenient, however, for this delay to be stable in laboratory tests and in various optical measurements when a dispersive medium is to be probed by the laser pulse. This especially concerns receiving channels with free-space optics which need triggering some dozens or hundreds of nanoseconds before the optical pulse is recorded.

The normal deviation value of the jitter between the "Sweep Trig." and "Laser Trig" outputs was found to be 7 ps (14 ps FWHM). This value does not define the long-term stability of the laser pulse with respect to the electrical triggering, however, since averaging over 1000 shoots reduces jitter to a value under 1 ps. The main problem consists of a drift in the laser switching delay,

which can be brought about by the following causes:

- fluctuation in the supply voltage of the avalanche transistor based laser driver
- variations in the temperature of the active region of the laser, associated with the instant of absorber saturation
- thermal fluctuations in various switching semiconductor devices such as avalanche transistors in the driver, tunnel diodes and RF transistors used in the fast comparators
- uncontrollable mechanical stresses in the optical construction and even in the RF cables

Some of these causes were investigated and corresponding arrangements (voltage and temperature stabilisation) were undertaken in order to reduce the delay drift. It was found that an *increase* in the lasing delay by ***1 ps*** could be caused by

- a *reduction* of *11 mV* in the 300V supply voltage (stabilised with an accuracy of *2 mV*)
- an *increase* of *0.018 °K* in the lattice temperature of the active region of the laser diode (stabilised with an accuracy of *0.01 °K*)
- an *increase* of *0.096 °K* in the temperature of the avalanche transistors (stabilised with an accuracy of *0.02 °K* at repetition rates under 5 kHz)
- a change of *0.05 °K* in the temperature of the tunnel diodes (stabilised with an accuracy of *0.01 °K*). The temperature of the RF transistors was stabilised at the same level, while the thermal coefficient for the transistors was lower than that for the tunnel diodes.

The stability of the laser pulse with respect to "sweep" triggering was found to be $\pm$ *1.5 ps* within one hour, with averaging over 1000 shoots. This instability is higher than that expected from the above estimates, which means that some other factors affecting the delay have not been taken into account. The resulting stability is still fairly good for many applications, however, and apparently this corresponds to an accuracy of $\pm$ 0.25 mm in the distance measurements.

IV.3. Maximum repetition rate

Stable, long-term operation was observed with a maximum repetition rate of 50 kHz in the modules based on the laser diodes LD-60 and LD-62, and 10 kHz in that based on LD-65. The maximum repetition rate was limited by the avalanche transistor driver. The Peltier cooler used in the module allowed 10 W of the average power from the avalanche transistors to

be dissipated. We assume, however, that the average power is not the only limit at a frequency close to 100 kHz. The repetition period becomes comparable to the characteristic time required for thermal diffusion across the transistor structure in this case, which should create a fundamental restriction. Operation of the LD-60 based module becomes unstable at 75-80 kHz, which leads to prompt degradation of the transistors.

CONCLUSIONS

A transmitter module for laser radar and various laboratory applications was designed and tested. The module generates single optical pulses of length 23-45 ps with a peak power of 50- 180 W and an emission band 10-20nm wide with its centre at about 900 nm. Operation is based on the Q-switching operation mode of low-cost commercial laser diodes. Transient mode spectral filtering is used to suppress the long emission tail and control the pulse duration. The repetition rate is limited by the driving circuit up to 50 kHz.
An original method for precise thermal control of the active region allows1.5 ps stability to be achieved between the electrical triggering and the optical pulses within a delay range from 5 to 250 ns.

ACKNOWLEDGMENTS

This work was supported by the Academy of Finland and by INTAS project 97-OPEN-1609. The authors are grateful to all the participants in the project for their assistance.

REFERENCES:

1. S.N. Vainshtein and J.T. Kostamovaara, Proceedings of SPIE, **3940**, 192, (2000).
2. S.N. Vainshtein, V. Rossin, A. Kilpela, J. Kostamovaara, R. Myllyla, K. Maatta. IEEE J. Quant. Electr., **QE-31**, 1015, (1995).
3. S.N. Vainshtein and J.T. Kostamovaara, J. Appl. Phys., **84**, 1843 (1998).
4. F. D. Nunes, N. B. Patel, Jose E. Ripper. IEEE J. Quant. Electron., **QE-13**, 675, (1977).
5. J.E.Ripper and J.A.Rossi. IEEE J. Quant. Electron., **QE - 10**, 435, (1974).
6. J. C. Dyment and J. E. Ripper. Appl. Phys. Lett., **12**, 365, (1968).
7. M.J.Adams, S.Grundorfer, B.Thomas, C.F.L.Davies and D.Mistry. IEEE J. . Quant. Electron., **QE -9**, 328, (1973).

Pattern formation in a broad-area VCSEL

N.A. Loiko, I.V. Babushkin
Institute of Physics, National Academy of Sciences of Belarus,
Skorina ave., 70, 220072, Minsk, Belarus,

ABSTRACT

We show that in addition to the dispersion mechanism of selection of tilted waves in a cavity of a broad-area VCSEL the dependence of the reflection from distributed Bragg reflectors on an incidence angle of the tilted waves leads to the mode selection and spatial periodic pattern formation. The mode competition may acquire even more diversity if the polarization of the laser field comes into play.

Keywords: periodic spatial structures, Bragg reflector, VCSEL, polarization pattern.

1. INTRODUCTION

Vertical-cavity surface emitting lasers (VCSELs) hold promise as microcavity light sources for optical parallel processing and high capacity optical fiber communications due to inherent advantages, resulting from their unique device geometry[1,2]. On the other hand, due to a designed transverse symmetry, field polarization properties in VCSELs are not so simple in comparison with conventional edge-emitting semiconductor lasers: in general the polarization of the fundamental transverse mode is free to be randomly oriented in the plane of the active layer[3-5]. The orientation of polarization can vary from one VCSEL to another, depending on the directions of the crystal axes, stresses and geometrical asymmetries. Also , as has been shown in works[6,7], the continuous wave (cw) transverse mode structure of VCSELs is relatively more dense than is typically encountered in edge-emitting devices. This impacts upon the polarization properties of the device where it has been found that the steady-state distribution of lasing power between polarization states changes markedly as higher order transverse modes are excited[3,5,8,9]. These aspects of cw properties of VCSELs can be anticipated as having a strong influence on the dynamical properties of the device. So polarization control and transverse-mode control are two linked practical problems which require a better fundamental understanding of the physical mechanisms of polarization and transverse-mode selection in VCSELs.

The most experiments in this direction display Hermite- or Laguerre- Gaussian modes[3,5,8-13] that indicates the formation of waveguide in the device due to thermal-lensing effects. An aperture of lasers used in these experiments is considerably small. Remarkable improvements in device performance have been attained in the last years using selective oxidation of high aluminum content in the VCSEL structure[14-16]. These so-called "selectively oxidized" or "native-oxide confined" VCSELs can be design as broad-area devices opening new possibilities for their application on the basis of a rich variety of dynamical behavior inherent to a broad-area lasers[17-23]. One of them is formation of transverse field periodic structures corresponding to tilted waves. This phenomenon has been demonstrated by recent experiments[24]. It has been shown that the shape of observed structures depends on the polarization of lasing field.

Theoretical predictions of periodic pattern formation in a broad-area laser are based on the scalar Maxwell-Bloch equations for two-level atoms in a single- longitudinal mode planar cavity treated in the uniform field limit[18-21]. In accordance with this theory a selection of transverse Fourier modes which correspond to tilted waves in a cavity occurs due to the gain dispersion mechanism. Nonuniform field profile is formed when the detuning $\delta=\omega_a-\omega_c$ between the atomic resonance ω_a and the cavity frequency ω_c is positive. At that there arise waves travelling in the transverse direction if a system is infinite and standing waves in the case of finite transverse sizes. Similar and even richer behavior is found in models which take into account more closely the semiconductor nonlinearty[25,26] and light polarization degrees of freedom[27].

In this report, we show that the dependence of the field reflection from distributed Bragg reflectors on an incidence angle of tilted wave leads also to the mode selection. Due to this mechanism transverse standing waves appear even in an infinite system. Direction of these waves is determined by a direction of laser field polarization. These structures are similar to structures observed in experiments[24] near the lasing threshold.

2. MODEL

Our model is a modified version of the model developed in the work[25] which takes into account the successive transmission of the lasing emission through cavity elements (the corresponding scheme is presented in figure 1). It is based on the fact that a thickness of the active layer in VCSEL is often much less than the light wavelength so we can neglect diffraction

Laser Optics 2000: Semiconductor Lasers and Optical Communication, Serguei A. Gurevich,
Nikolay N. Rosanov, Editors, Proceedings of SPIE Vol. 4354 (2001) © 2001 SPIE · 0277-786X/01/$15.00

effects within the thin layer and obtain expressions that relate the slowly varying amplitudes of the incident and transmitted fields.

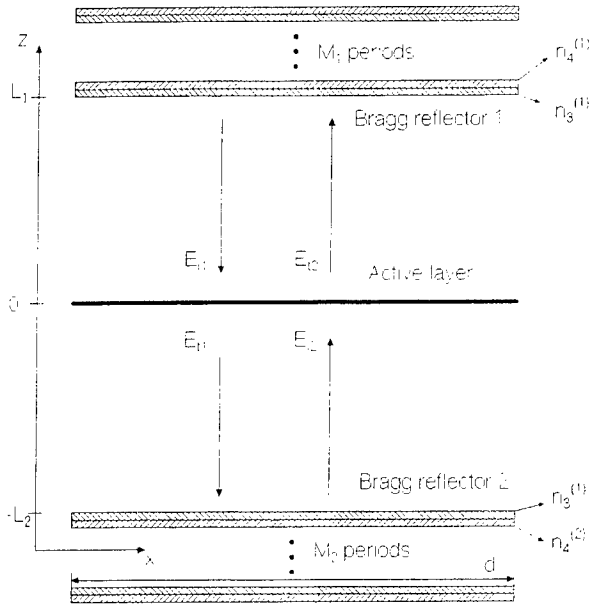

Figure 1. The model of VCSEL. The thin active layer is placed between Bragg reflectors on the distance L_1 from the first and L_2 from the second reflector. Each reflector comprises M_i $(i=1,2)$ periods, consisting in turn of quarter-wave layers $n_3^{(i)}$ and $n_4^{(i)}$. A space between Bragg reflectors and active layer is filled by media with reflection coefficients n_1 and n_2 correspondingly. $\mathbf{E}_{i1}$, $\mathbf{E}_{i2}$ are incoming waves and $\mathbf{E}_{t1}$, $\mathbf{E}_{t2}$ are waves transmitted through the active layer.

The effective field inside the layer is composed from the incident fields $\mathbf{E}_{i,1}$, $\mathbf{E}_{i,2}$ and a secondary field created by the polarization of active medium[28]:

$$\mathbf{E}(t,\mathbf{r}_\perp) = \mathbf{E}_{i1}(t,\mathbf{r}_\perp) + \mathbf{E}_{i2}(t,\mathbf{r}_\perp) + \frac{2\pi i\omega l}{c}\mathbf{P}(t,\mathbf{r}_\perp). \tag{1}$$

Here $\mathbf{E}$ ($\mathbf{E}_i$) and $\mathbf{P}$ – are slowly varying in time vector amplitudes for the fields and polarization with x- and y- polarized components; ω- is the field frequency; l is the active layer thickness; $\mathbf{r}_\perp = (x,y)$ determines a coordinate in the transverse section. Transmitted fields $\mathbf{E}_{t1}$, $\mathbf{E}_{t2}$ are related with the incident fields by the next expressions:

$$\mathbf{E}_{t1,2}(t,\mathbf{r}_\perp) = \mathbf{E}_{i1,2}(t,\mathbf{r}_\perp) + \frac{2\pi i\omega l}{c}\mathbf{P}(t,\mathbf{r}_\perp). \tag{2}$$

Propagation of the radiation in the upper and lower parts of the cavity can be described in the operator form:

$$\mathbf{E}_{i1,2}(t,\mathbf{r}_\perp) = \hat{F}_{1,2}\mathbf{E}_{t1,2}(t,\mathbf{r}_\perp) \tag{3}$$

with the propagation operator:

$$\hat{F}_{1,2} = \rho_{1,2}\exp(i2kL_{1,2})\exp(i\frac{\Delta_\perp}{k}L_{1,2})\Gamma\hat{R}_{1,2}. \tag{4}$$

Parameters $\rho_{1,2}$ determine losses in linear media between the active layer and reflectors; $\Delta_\perp$ - is the transverse part of Laplacian. The propagation operator is obtained in the paraxial wave approximation. Note that $\Delta_\perp$ acts in such way that $\Delta_\perp \propto |\mathbf{k}_\perp|^2$, where $\mathbf{k}_\perp = \begin{pmatrix} k_x \\ k_y \end{pmatrix}$ –is the transverse component of the full wave vector $\mathbf{k}$, $k = \omega/c = 2\pi/\lambda$ – is its module. Γ – is the 2x2 matrix determined by a linear anisotropies inside the cavity:

$$\Gamma = \begin{pmatrix} \exp(\gamma_a + i\gamma_p) & 0 \\ 0 & \exp(-(\gamma_a + i\gamma_p)) \end{pmatrix} \tag{5}$$

Parameters γ_a and γ_p determine an amplitude and phase anisotropy correspondingly. Operators $\hat{R}_{1,2}$ are determined in the $\mathbf{k}_\perp$ - space as 2x2 matrices $R_{1,2}$ describing the reflection of a tilted plane wave with vector $\mathbf{k}_\perp$. To determine them we use the techniques developed in[29]: at first, we decompose the vector $\mathbf{E}(\mathbf{k}_\perp)$ in TE and TM – modes for which reflection coefficients from a Bragg reflector are known[30], find the reflected TE and TM – modes, and using them compose the reflected vector field in the x-y basis. It should be noted that these matrices are not diagonal in a common case, which is due to polarization mixing by the reflectors.

In view of the expressions (1)-(3), we can get the recurrent relation connecting the field in the active layer in a two moments of time t and $t+\tau$ ($\tau = \tau_1 + \tau_2$ is the photon round-trip time in the cavity, τ_i is twice the transit time of the radiation from the active layer to one of reflectors):

$$\mathbf{E}(t, \mathbf{r}_\perp) = \hat{F}_1 \hat{F}_2 \mathbf{E}(t-\tau, \mathbf{r}_\perp) + \frac{2\pi\omega l i}{c}\left[\mathbf{P}(t, \mathbf{r}_\perp) + \hat{F}_1 \mathbf{P}(t-\tau_1, \mathbf{r}_\perp) + \hat{F}_2 \mathbf{P}(t-\tau_2, \mathbf{r}_\perp) + \hat{F}_1 \hat{F}_2 \mathbf{P}(t-\tau, \mathbf{r}_\perp)\right] \tag{6}$$

To obtain the equation (6) we have taken into account that the operators $\hat{F}_1$ и $\hat{F}_2$ are commutative. The times τ_i are determined by effective lengths of the upper and lower parts of the device with allowance for a penetration depth of the incident wave into the Bragg reflectors[31].

To find a reply of active medium on the radiation we use the model developed in the work[32]. This model is the vectorial extension of usual Bloch equations for two-level atoms. In its framework the active medium is separated in different spin classes, each interacting with circularly polarized light of one specific handedness. The two transitions are coupled by spin-flip relaxation processes. The corresponding equations describing dynamics of these coupled two two-level systems are:

$$\begin{aligned} \frac{d\mathbf{P}}{dt} &= -\left(\frac{1}{T_2} + i\delta\right)\mathbf{P} - \frac{|\mathbf{d}|^2}{3\hbar} i\mathrm{A}\mathbf{E}, \\ \frac{dN}{dt} &= -\frac{N-J}{T_1} - \frac{i}{2\hbar}(\mathbf{E}^*\mathbf{P} - c.c), \\ \frac{dn}{dt} &= -\gamma_s n + \frac{1}{2\hbar}(\mathbf{E}^*\mathbf{P}' - c.c). \end{aligned} \tag{7}$$

Here, A is 2x2 matrix:

$$\mathrm{A} = \begin{pmatrix} N - N_0 & in \\ -in & N - N_0 \end{pmatrix}. \tag{8}$$

$\mathbf{P}'$ – is vector with components $(P_y, -P_x)$, N is the total population difference between the conduction and valence bands, N_0 is its value at transparency, n is the difference of the population differences for the two allowed transitions between

magnetic sublevels, γ_s is the decay rate for difference in the populations of the different magnetic sublevels, T_1 and T_2 – are the relaxation times for the total population difference and polarization correspondingly, $|\mathbf{d}|$ – is the module of dipole momentum of transition (we suppose that it is the same for both transitions), J- is the pump parameter.

3. THRESHOLD CONDITIONS AND NUMERICAL SIMULATIONS

Evidently, with increasing the pump parameter, the trivial nonlasing solution loses its stability. For spatially uniform pumping, we seek a lasing solution in the form of a wave travelling in the transverse direction:

$$\begin{aligned}\mathbf{E}(t,\mathbf{r}_\perp) &= \mathbf{e}\exp[-i(\Omega(\mathbf{k}_\perp)t-\mathbf{k}_\perp\mathbf{r}_\perp)],\\ \mathbf{P}(t,\mathbf{r}_\perp) &= \mathbf{p}\exp[-i(\Omega(\mathbf{k}_\perp)t-\mathbf{k}_\perp\mathbf{r}_\perp)]\end{aligned} \tag{9}$$

We suppose that the amplitudes $\mathbf{e}$ and $\mathbf{p}$ do not depend on time. A value Ω describes the frequency shift in the cavity. In general, it depends on the transverse wave vector because of different conditions for propagation of different tilted waves (equation (4)).

If the linear amplitude anisotropy is very large so that only one from two orthogonally polarized components can be exited the problem is reduced to the "scalar" one. For example, if $\gamma_a >> 1$, we can leave under consideration only x-polarized components of the field $\mathbf{E}$ and polarization $\mathbf{P}$.
In this case, the reflection coefficients are:

$$R_i(\mathbf{k}_\perp) = r_{s,i}(\mathbf{k}_\perp)\varepsilon_{sx}^{\ 2} + r_{p,i}(\mathbf{k}_\perp)\varepsilon_{sy}^{\ 2}, \tag{10}$$

where $\varepsilon_{sx} = -\dfrac{k_y}{k_\perp}, \varepsilon_{sy} = \dfrac{k_x}{k_\perp}$, r_s and r_p- are the reflection coefficients for TE and TM – modes, correspondingly.
The solutions (9) can be determined from the next equations:

$$\begin{aligned}&1 = \tilde{r}_1(\mathbf{k}_\perp)\tilde{r}_2(\mathbf{k}_\perp) + \frac{2\pi\omega l\,|\mathrm{d}|^2\,T_2}{3c\hbar}L_\omega(\mathbf{k}_\perp)\{(1+i\alpha)D[1+\tilde{r}_1(\mathbf{k}_\perp)\tilde{r}_2(\mathbf{k}_\perp)+\tilde{r}_1(\mathbf{k}_\perp)+\tilde{r}_2(\mathbf{k}_\perp)-\\ &i\alpha D_0[1+r_1(0)r_2(0)+r_1(0)+r_2(0)]\},\\ &p = -\frac{|\mathrm{d}|^2\,T_2}{3\hbar}L_\omega(\mathbf{k}_\perp)(i-\alpha)De,\\ &e^2 = \frac{3\hbar^2(J-D)}{|\mathrm{d}|^2\,T_1T_2L_\omega D}.\end{aligned} \tag{11}$$

Here, $D=N-N_0$, the pump parameter J has been correspondingly changed, $L_\omega(\mathbf{k}_\perp) = 1/[1+((\delta+\Omega(\mathbf{k}_\perp))T_2)^2]$ describes the shape of gain line. The parameters $\tilde{r}_j(\mathbf{k}_\perp) = r_j(\mathbf{k}_\perp)\exp[i\theta_j(\mathbf{k}_\perp)]$, where $r_i(\mathbf{k}_\perp)$ - are modules of the reflection coefficients of Bragg reflectors, their phases $s_i(\mathbf{k}_\perp)$ enter in the expressions for the total phase: $\theta_i(\mathbf{k}_\perp) = s_i(\mathbf{k}_\perp) + 2kL_i - |\mathbf{k}_\perp|^2 L_i / k + \Omega(\mathbf{k}_\perp)\tau_i$. The parameter α describes relative changes in the index of refraction and gain accompanying changes in the population. In comparison with the two-level system in which $\alpha = \delta T_2$, this parameter for semiconductor media (so-called linewidth enhancement factor) does not depend from a sign of the detuning and is not equal to zero at $\delta = 0$. We take this fact into account in the following consideration.
The last term has been introduced into the first equation of the system (11) to exclude the frequency shift of zero harmonic ($\mathbf{k}_\perp = 0$) at its threshold ($D=D_0$) because of changes in the refractive index with changes in the population. When the active layer is in a maximum of the standing wave in the cavity the magnitude $s_i(0) + 2kL_i = j_i\pi$, where j_i – is integer numbers. Assuming also that the resonance conditions are fulfilled, i.e. $j_1 + j_2$ is an odd number and, correspondingly, $\Omega(0) = 0$, we have:

$$D_0 = \frac{3c\hbar[1 - r_1(0)r_2(0)]}{2\pi\omega l \,|\,\mathrm{d}\,|^2 \, T_2 L_\omega(0)[1 + r_1(0)r_2(0) + r_1(0) + r_2(0)]}. \tag{12}$$

Values of D found from equations (11) determine the lasing threshold for every transverse Fourier mode. If the lowest threshold corresponds to the mode with non zero transverse wave vector, a pattern formation in the system is to be expected. The same threshold characteristics can be obtained by performing a linear stability analysis of the nonlasing state assuming a perturbation of the form (9).

Using (11) we find the next relative threshold for a transverse mode excitement:

$$\frac{D}{D_0} = \frac{L_\omega(0)}{L_\omega(\mathbf{k}_\perp)} \frac{[1 - r_1(\mathbf{k}_\perp)r_2(\mathbf{k}_\perp)][1 + r_1(0)r_2(0) + r_1(0) + r_2(0)]}{[1 - r_1(0)r_2(0)][1 + r_1(\mathbf{k}_\perp)r_2(\mathbf{k}_\perp) + r_1(\mathbf{k}_\perp) + r_2(\mathbf{k}_\perp)]} \tag{13}$$

If the reflection coefficients are independent from an incidence angle the expression (13) describes the known gain dispersion mechanism of transverse mode selection[17-20]. Pattern formation takes place at $\delta>0$ because of transverse modes with $\Omega(\mathbf{k}_\perp) = \delta$ have the minimal threshold. Note that in this case, a value of threshold is determined only by a value of module $|\mathbf{k}\perp|$. An example of this is presented in figure 2a. With allowance for a dependence of the reflection coefficients on the transverse wave vector a value of threshold is determined also by a direction of $\mathbf{k}\perp$ It is clear evident in figure 2b. The threshold has a minimal value for harmonics orthogonal to the direction of the field polarization. Two symmetrical minima is shifted to k_y=0 and become deeper (compare the solid and dashed lines in figure 3).

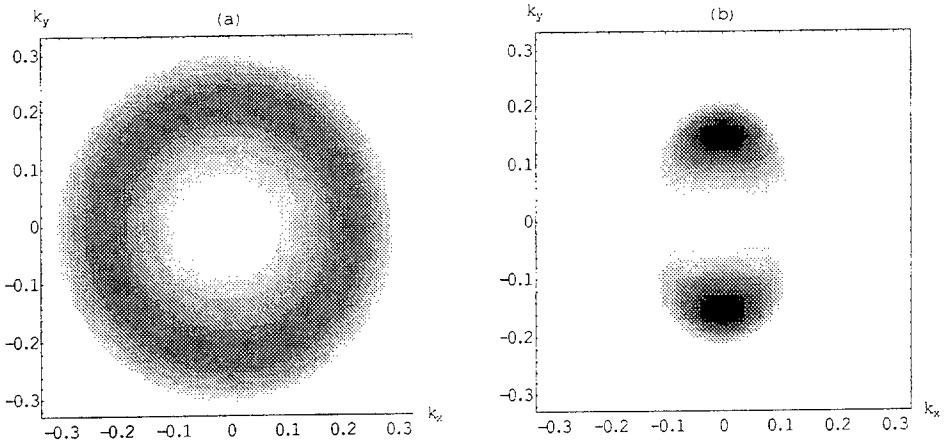

Figure 2. Dependence of lasing threshold on the spatial harmonic $\mathbf{k}_\perp$. Values of threshold are ranged between $0.75D_0$ (black) and 1.0 (white).

(a) Only gain dispersion mechanism are taking into account.

(b) Gain dispersion and loss dispersion mechanisms acting cumulatively.

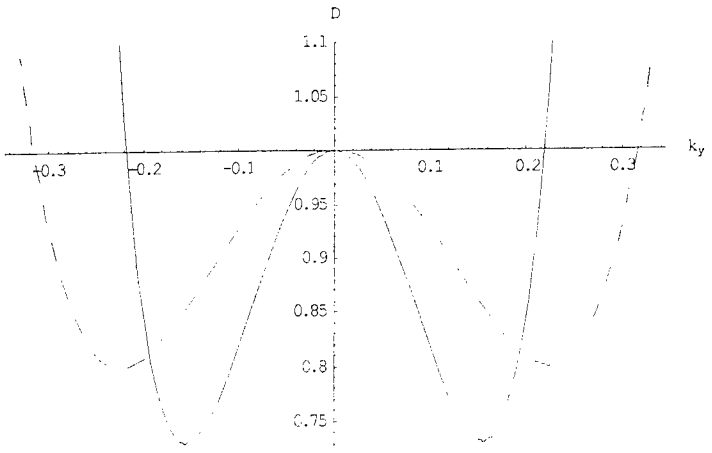

Figure 3. Cross-section (k_x=0) of figure 2b (solid line) and 2a(dashed line)

In result, periodical spatial patterns appear near the threshold. An example of a $10T_1$ time-averaged distribution of the near-field (a) and far-field (b) intensities are shown in figure 4. The far-field exhibits a double spot at $(k_x, k_y)= (0, \pm k_{y,min})$ and the near-field is the corresponding standing wave. The stripes observed in the near-field are parallel to the direction of the field polarization.

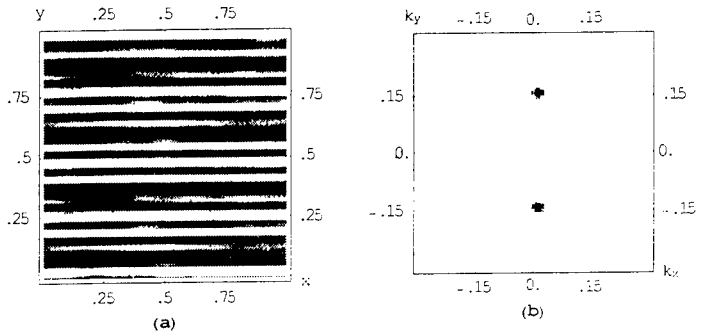

Figure 4. Stripes in near field (a) and far field (b) at J=0.8J_0 (J_0=$J(\mathbf{k}_\perp$=0))

When the amplitude anisotropy γ_a has a large negative value, only y-polarized components of the lasing field can be excited. Maximal reflection coefficients (minimal thresholds) correspond to transverse harmonics with wave vectors $(\pm k_{x,min},0)$, stripes in the near field are orthogonal to stripes presented in figure 4. This regime is stable while the pump parameter is increased in 1.5-2 times in comparison with its lasing threshold value. Further increasing of the pump leads to an excitement additional harmonics the wave vectors of which lie in the circle determined by local minima of the threshold due to the gain dispersion mechanism. Complicated transverse patterns appear in both considered above cases (see, for example figure 5). The field keeps the linearly polarized state.

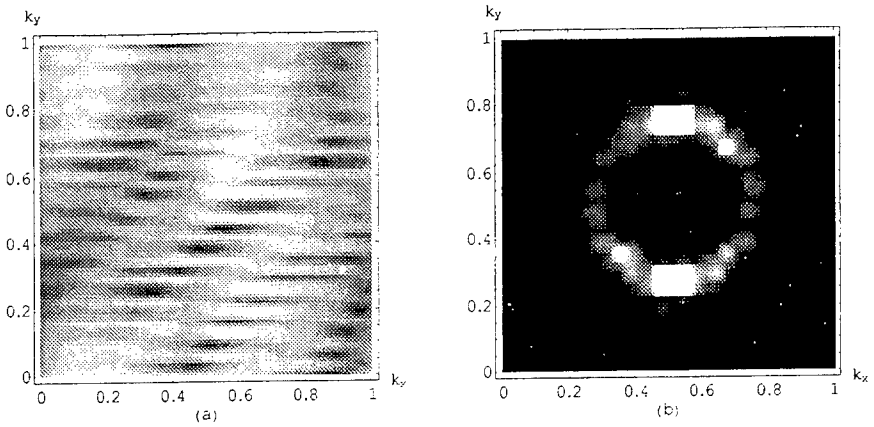

Figure 5. Spatial structure in near field (a) and far field (b) obtained at $J=2.J_0$

In a common case, it is not possible to distinguish linearly polarized solutions of equations (11) because of a continuous mixing two orthogonally polarized components E_x and E_y by the reflectors. However, the laser behavior near threshold can be like to one described above. An example of dependence of the threshold on $\mathbf{k}_\perp$ for small amplitude anisotropy is presented in figure 6. Figure 6a displays two pairs of minimal values of the threshold corresponding to two orthogonal wave vectors with k_x or k_y equal to zero. The minima are deeper for k_x=0 (figure 6b). The corresponding wave are linearly polarized with E_y=0 at pump closed to its minimal value. So, near the lasing threshold only one of the orthogonal components is excited and transverse structures are similar to the structure shown in figure 4. This state is stable when the pump is slightly increased even at the value equal to the minimal threshold for the mode with orthogonal wave vector. As result, a second pattern similar to the first after rotation through $\pi/2$ is superimposed on the near field. This phenomenon is like to the experimentally observed[24]. A frequency difference between two orthogonally polarized fields is determined by the phase anisotropy parameter γ_p.

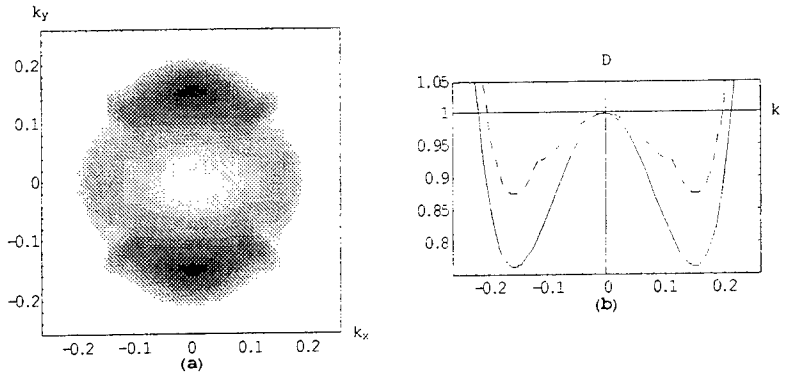

Figure 6. Dependence of threshold on $\mathbf{k}_\perp$ for vectorial case and the amplitude anisotropy parameter $\gamma_a = 0.01$.
(a) Whole spatial picture: black color corresponds to $D=0.75D_0$, whereas white corresponds to $D=1.05D_0$
(b) Cross-section through the line k_x=0 (solid line, x-polarized field) and through the line k_y=0 (dashed line, y-polarized field).

Further increasing of the pump parameter leads, at first, to a complication of two independent orthogonally polarized patterns. Then elliptically polarized harmonics enter into interplay. Regularities determining the laser behavior in this case will be considered in the future work.

4. CONCLUSIONS

On the basis of the developed thin layers model of VCSEL which takes into account the dependence of reflection from distributed Bragg reflectors on the angle of incidence (on the transverse wave vector of tilted waves), we show that this

effect leads to two consequences. At first, it introduces the influence on the transverse Fourier-mode selection of a direction of the mode wave vector in comparison to the gain dispersion mechanism. Secondly, differences in the polarization anisotropy of different tilted waves appear. Interplay of these two tendencies causes the formation of independent orthogonal linearly polarized patterns near the lasing threshold and complex elliptically polarized structures under a higher level of pump. The linearly polarized structures are the standing waves direction of which is determined by the direction of polarization. This is in accordance with experimental data[24].

ASKNOWLEDGMENTS

The work has been funded in part by the Byelorussin Republic Fund of Fundamental Researches.

REFERENCES

1. K. Iga, *IEIC Trans.* **E75-A** p. 12, 1992.
2. S.W. Koch, F. Jahnke, W.W. Chow, *Semiconductor Sci. Technol.*, **10** p. 739, 1995.
3. C.J. Chang-Hasnain, J.P. Harbison, G. Hasnain, A. Von Lehmen, L.T. Flozer, N.G. Stoffel, *IEEE J. Quantum Electron.*, **27** p. 1402, 1991.
4. K.D. Choquette, D.A. Richie, R.E. Leibenguth, *Appl. Phys. Lett.* **64** p. 2062, 1994.
5. Iga et al *Electron. Lett.*, **27** p. 163, 1991.
6. Li et al, *Chaos, Solitons, Fractals*, **4** p. 1619, 1994.
7. Vakhshoori, *Appl.Phys. Lett.*, **65** p. 259, 1994
8. Mukaihara,et al , *IEEE Photon.Technol. Lett.*, **5** p. 133, 1993
9. A. Chavez-Pirson, H. Ando, H. Saito, H. Kanbe, *Appl.Phys.Lett.*, **62** p. 3082, 1993.
10. D.B. Young, J.W. Scott, F.H. Peters, M.L. Majewski, B.J. Thibeault, S.W. Corzine, L.A. Coldren. *IEEE J. Quantum Electron.*, **29** p. 2013, 1993.
11. K. Tai, Y. Lai, K.F. Huang, T.C. Huang, T.D. Lee, C.C. Wu, *Appl. Phys. Lett.*, **64** p. 2624, 1993.
12. R.A. Morgan. G.D. Guth, M.W. Focht, M.T. Asom, K. Kojima, L.E. Rogers, S.E. Callis. *IEEE Photonics Tevhnology Letters*, **4** p. 374, 1993.
13. O. Buccafusca, J.L.A. Chilla, J.J. Rocca, S. Feld, C. Wilsmen, V. Morozov, R. Leibenguth, *Appl.Phys. Lett.*, **68** p. 590 , 1996.
14. K.L. Lear, K.D. Choquette, R.P. Schneider, Jr., S.P. Kilcoyne, K.M. Geib, *Electron Lett.*, **31** p. 208, 1995.
15. D.L. Huffaker, H. Deng, Q. Deng, D.G. Deppe, *Appl.Phys. Lett.* **69** p. 23, 1996.
16. K.D. Choquette, W.W, Chow, G.R. Hadley, H.Q. Hou, K.M. Geib, *Appl. Phys. Lett.* **70** p. 823, 1997.
17. G. Huyet, M. C. Martinoni, J. R. Tredicce, S. Rica, *Phys. Rev. Lett.*, **75** p. 4027, 1995.
18. P. Coullet, L. Gil, F. Rocca, *Opt. Commun.*, **73** p. 403, 1989.
19. L.A. Lugiato, J. R. Oppo, G.L. Tredicce, L. M. Narducci, M. A. Pernigo, *J. Opt. Soc. Am. B*, **7** p. 1019, 1990.
20. P. K. Jakobsen, J. V. Moloney, A.C. Newell, R. Indik, *Phys. Rev. A*, **45** p. 8129 1992.
21. G.K. Harkness, W.J. Firth, J.B. Geddes, J.V. Moloney, E.M. Wright, *Phys. Rev. A* **50** p. 4310, 1994.
22. K. Staliunas, C. O. Weiss, *Physica D*, **81** p. 79, 1995.
23. M Brambilla, F.A. Lugiati, F. Prati, L. Spinelli, W.J. Firth, *Phys.Rev. Lett.*, **79** p. 2042, 1997.
24. S. P. Hegarty, G. Huyet, J. G. McInerney, H. Q. Hou, K D. Choquette, *Phys.Rev. Lett.*, **82** p. 1434, 1999.
25. Yu. A. Logvin, N.A. Loiko, S.I. Turovets, P.S. Spencer, K.A. Shore, *Laser Physics*, **7** p. 1160, 1997.
26. T. Rossler, R.A. Indik, G.K. Harkness, J.V. Moloney, *Phys. Rev. A*, **58** p. 3279, 1998.
27. M. San Miguel, Q. Feng, J.V. Moloney, *Phys. Rev. A*, **52** p. 1728, 1995.
28. M.Benedict, V.A. Malyshev, E.D. Trifonov et all. *Phys.Rev. A*, **43** p. 3845, 1991.
29. D.J. Babic, Yo. Chung, N. Dagli, J.E. Bowers, *IEEE J. Quantum Electron.*, **QE-29**, p. 1950, 1993.
30. M. Born, E. Wolf, *Principles of optics*, Pergamon press, 1968.
31. K. J. Ebeling, in *Semiconductor Quantum Optoelectronics*, edited by A. Miller, M. Ebrahimzaden, D. M. Finlayson, *SUSSP Proc.*, **50** p. 295, 1998.
32. M. San Miguel, Q. Feng, J.V. Moloney, *Phys.Rev. A.*, **52** p. 1728, 1995.

GENERATION OF POLARIZATION CHAOS IN VCSEL

N.A. Loiko[a], A.V. Naumenko[a], N.B. Abraham[b]

[a]Institute of Physics, National Academy of Belarus,
Skorina ave., 68, 220072 Minsk, Belarus
[b]DePauw University, Greencastle, IN 46135-0037

ABSTRACT

We find three types of complex polarization dynamics arising in VCSELs with polarized optical feedback when axes of the intrinsic and external anisotropies are aligned. Their appearance depends on the interplay between these anisotropies which determines the stability of modes polarized along the polarizer axis with respect to perturbations with the same and orthogonal polarization. The influence on the laser behavior of a rotation of the external polarizer is considered.

Keywords: polarization chaos, VCSEL, anisotropic feedback

1. INTRODUCTION

Interest in controlling semiconductor laser nonlinear dynamics has been stimulated by the opportunity to achieve secure communication systems which exploit the properties of chaotic dynamical systems.[1] Of particular interest are studies of the control of chaotic dynamics in external cavity laser diodes exhibiting coherence collapse.[2] In the case of weakly anisotropic devices, such as vertical-cavity surface-emitting lasers (VCSELs), complex nonlinear behaviors may acquire even more diversity when the polarization of the laser field comes into play. The influence of the feedback on polarization dynamics is heightened if the optical elements that are incorporated in the laser-optical systems have their own anisotropy or polarization converting properties. Switching between orthogonal linearly polarized states was observed in experiments when external feedback enhanced one of two states and its phase was modulated.[3,4] Corresponding behavior in theoretical models has been reported.[4,5] The steady states and conditions of their stability were found in the case of polarized feedback. In our previous work,[6] we considered the more general case of a misalignment of the axes of the feedback anisotropy with the axes of the intrinsic amplitude and phase anisotropies of the VCSEL. Modifications of the stability regions by the misalignment were elucidated. The external mode structure and changes in it due to the polarizer rotation were considered.

The present work is devoted to investigations of the polarization dynamics in this system. We consider some types of complex polarization-dynamical regimes existing in the laser due to effects of the polarization-selective feedback, analyze mechanisms of their appearance, and investigate the influence of the intrinsic anisotropy parameters (the amplitude γ_a and phase γ_p linear anisotropy parameters), the relaxation rate γ_s (nonlinear anisotropy), and the external anisotropy parameters (the strength σ and phase $\omega\tau$ of the feedback, and also the misalignment angle χ between the polarizer axis and one of the intrinsic axis).

2. MODEL

The rate equations describing polarization dynamics in a quantum well VCSEL with eternal anisotropic feedback have the following form[5,6] (the axes $\hat{x}$, $\hat{y}$ are aligned with the axes of intrinsic amplitude and phase anisotropies which are diagonalized by the same axes):

$$\frac{d}{dt}\bar{E} = \hat{G}\cdot\bar{E} + \sigma\, e^{-i\omega\tau}\,\hat{\chi}\cdot\bar{E}_\tau \tag{1}$$

Further author information: (Send correspondence to N.A.L.)
N.A.L.: E-mail: nloiko@dragon.bas-net.by
A.V.N.: E-mail: anaum@dragon.bas-net.by
N.B.A.: E-mail: nabraham@depauw.edu

Laser Optics 2000: Semiconductor Lasers and Optical Communication, Serguei A. Gurevich, Nikolay N. Rosanov, Editors, Proceedings of SPIE Vol. 4354 (2001) © 2001 SPIE · 0277-786X/01/$15.00

$$\frac{d}{dt}\bar{N} = \bar{\mu} + \hat{S} \cdot \left|\bar{E}\right|^2, \tag{2}$$

where $N_{\pm} = N \pm n$, $\gamma = \gamma_a + i\,\gamma_p$, column vectors are denoted '$\bar{}$': $\bar{E} \equiv (E_+, E_-)$, $\left|\bar{E}\right|^2 \equiv \left(|E_+|^2, |E_-|^2\right)$, $\bar{N} \equiv (N, n)$, $\bar{E}_\tau = \bar{E}(t-\tau)$, $\bar{\mu} = (\mu - N, -\gamma_s n)$; while matrices are '$\hat{}$': $\hat{G} = \begin{pmatrix} \kappa(1+i\alpha)(N_+ - 1) & -\gamma \\ -\gamma & \kappa(1+i\alpha)(N_- - 1) \end{pmatrix}$, and $\hat{S} = -\begin{pmatrix} N_+ & N_- \\ N_+ & -N_- \end{pmatrix}$, and $\hat{\chi}$ is the polarization matrix for round-trip transmission through the external cavity. For the external cavity with a linear polarizer inserted in it with an angle of polarization χ with respect to the x-axis aligned with one of the intrinsic axis, $\hat{\chi} = \frac{1}{2}\begin{pmatrix} 1 & e^{2i\chi} \\ e^{-2i\chi} & 1 \end{pmatrix}$. $E_\pm = \frac{1}{\sqrt{2}}(E_x \pm i\,E_y)$, where E_x and E_y are $\hat{x}$ - and $\hat{y}$ - polarized components of the slowly varying amplitude of the electromagnetic field; ω is the solitary laser frequency; N is the total population difference between the conduction and valence bands; n is the difference of the population differences for the two allowed transitions between magnetic sublevels[7]; κ is the mean of the decay rates of the two linearly polarized components of the field; γ_a is the anisotropic field loss rate (positive γ_a gives the $\hat{y}$-polarized component a lower threshold); γ_p represents the effect of linear birefringence of the medium (which gives the different linearly polarized field of the solitary laser opposite frequency shifts) which is commonly caused by anisotropic stress; α is the linewidth enhancement factor; μ is the normalized injection current, which takes the value 1 at the lasing threshold; γ_s is the decay rate for difference in the populations of the different magnetic sublevels, which accounts for its elimination by both spontaneous emission and spin-flip relaxation processes, and σ is the feedback strength. The parameters κ, γ_a, γ_p and γ_s are normalized to the decay rate Γ of the total carrier population (we use the typical value of $\Gamma = 10^9 c^{-1}$); time t and the delay time τ are normalized to Γ^{-1}.

3. DISCUSSION OF RESULTS

Analysis of numerical results shows that three different dynamical regimes can arise in the system (1)-(2). These regimes differ in polarization, temporal and spectral characteristics. They are determined by different mechanisms and exist in various intervals of the feedback strength. These intervals are sensitive to the choice of the feedback phase.

The first type of complex dynamics exists when the intrinsic and external anisotropies are comparable. The polarization-selective feedback partially compensates the intrinsic anisotropy of two optical subsystems generating orthogonally polarized light. This leads to instability of linearly polarized modes existing in the system with respect to orthogonally polarized perturbations and appearance of polarization pulsations. The mechanism of these oscillations is a dynamic synchronization of orthogonally polarized components nonlinearly coupled due to spin-flip processes. Increasing the relaxation rate γ_s (up to the values about 300-500^{-1}) or the intrinsic phase anisotropy parameter γ_p (up to 7^{-1}) leads to the disappearance of the first zone of polarization dynamics.

In particular, for the parameters for the results shown in the figures 1, the external cavity x-mode with the maximal gain is stable with respect to static perturbations with the same polarization, but it is unstable with respect to static orthogonally polarized perturbations due to symmetry breaking (pitchfork) bifurcation. This instability depends on several factors: a small level of the intrinsic anisotropy γ_p and relative importance of the spin-flip relaxation process ($\gamma_s$is small enough). The pair of symmetrical elliptically polarized modes created due to this bifurcation are unstable at these parameters as is the single y- mode (Details of the instability analysis are presented elsewhere[5,6]). As a result, all these instabilities can lead to complex homoclinic orbits near the x- mode with maximal gain. Trajectories go away from the x- mode along the unstable (with respect to orthogonally polarized perturbations) manifold and then go back, approaching the stable (to own perturbations) manifold and then turning round it as shown in the figure 1.

Domains where the first type of pulsations exists intermix with synchronization windows of two frequencies: the frequency of the optical feedback ($1/\tau$), which is adjusted here to approximately coincide with the relaxation frequency of the x- mode, and the lower frequency of antiphased oscillations of the x- and y- polarized components appearing due to the static instability of x- mode to orthogonally polarized perturbations.

Because of the inherent symmetry of the system (1)-(2) regimes, such as those presented in the figure 1, exist in pairs with the opposite signs of η, ψ and n. As σ is decreased to 1, these two symmetrical orbits tend to the

x- polarized mode with maximal gain, and then collide, creating a total atractor with more developed chaos. The chaotic attractor exists even for $\sigma < 1$, where the y- polarized steady state is stable. With a further decrease in σ, the laser emission is constrained to the stable y- polarized mode.

The polarization distortion caused by the rotation of the polarizer in the external resonator by the misalignment angle $\chi \neq 0$ optically connects the polarization components of the solitary laser and thus can lead to strong synchronization of orthogonally polarized modes. As a consequence, misalignment of the polarizer may lead to widening of the synchronization windows or to desynchronization of periodic regimes, depending on the feedback phase.

The second type of chaotic pulsations exists at larger values of the feedback strength when several x- polarized modes of the external cavity are exited. For a linearly polarized laser, it would correspond to a conventional form of chaos that occurs in an edge-emitting semiconductor laser with optical feedback.[8] In this case the trajectory wanders in a vicinity of unstable external cavity modes. In our case, the introduction of the additional orthogonal degree of freedom destabilizeds the chaotic behavior with oscillations of only the E_x component ($E_y = 0$); perturbations of the othogonally polarized component induces oscillatoins in both components. Pecularities of this chaotic attractor can be connected with the types of instability of the $\hat{x}$-polarized modes embeded in it. In this case the main $\hat{x}$ -polarized mode is unstable only with respect to perturbation with the same polarization, while $\hat{x}$-polarized modes with a smaller gain are unstable also with respectto perturbation with orthogonal polarization.

This type of pulsations can be excited at any value of γ_s because of instabilities of the chaotic attractor with $E_y = 0$ in respect to orthogonal perturbations, which arise due to development of the structure with minimal loses. The level of intrinsic anisotropy must be small enough for this. Moreover, the appearance of the instabilities is sensitive to a choice of the external feedback phase. For instance, the chaotic attactor with $E_y = 0$ is stable with respect to orthogonally polarized perturbations at the phase $\omega\tau = 0.8\pi$. However, there are low frequency polarization oscillations with a long period of their decay (metastable polarization chaos) in the interval of σ from 3.5 up to 5.1.

Examples of this kind behavior are presented in figure 2(left column). The corresponding spectrum (right column) shows that the chaotic pulsations in this zone have a low frequency component. A trajectory is located in a vicinity of the "scalar" chaotic set with $E_y = 0$ for a long time. After this the trajectory rapidly goes away from it and there is a rapid increase in the y-polarized component of the lasing field which was about zero before. This is accompanied by a dropout in the intensity of the x-polarized component. Then the intensity of y- component disappears abruptly and the trajectory returns in the domain of "scalar" chaotic set with $E_y = 0$. As consequence of these spikes, a low frequency component appears in the spectra of intensity fluctuations of both polarized components of the lasing field. However they are very different. So, the maximum of the x- component corresponds to the frequency equal to 0.05GHz, while the maximum of the y- component is situated near 0.012GHz. This difference is caused, obviously, by the more complex structure of low frequency pulsations of the x- polarized component in which its own low frequency fluctuations (presented in the "scalar" manifold with $E_y = 0$) make a contribution as well as dropouts connected with spikes in the y- component.

If the value of γ_s is increased (which dimishes the nonlinear connection of the two orthogonally polarized subsystems), then the low frequency peak in the spectrum tends to the zero frequency (figure 3). The spectrum in the low frequency domain becomes similar to the $1/f$ spectrum (flicker noise spectrum). The duration of the laminar phases rises. In the limit $\gamma_s \to \infty$ the equations (1)-(2) are reduced to the Lang and Kobayashi ones[9] describing dynamics of two orthogonally polarized components of a conventional semiconductor laser. However, the low frequency oscillations of the y- component in this case still exist. They are more similar to flashes consisting of a several spikes. Time intervals between these flashes can reach 300-400 ns.

Misalignment of the polarizer in the external cavity strengthens the connection of the orthogonal components. Thus, at $\chi = 0.02\pi$ (figure 4) the amplitude of the high frequency spectral component of the y- polarized field component is increased about threefold. Accordingly, the low frequency spectral maximum of the x- polarized component is increased twofold at $\chi = 0.002\pi$ and fourfold at $\chi = 0.02\pi$. Dropouts become more pronounced. The high frequency pulsations in the orthogonally polarized components become antiphased as do the low frequency dropouts. At larger values of χ (about 0.05π) the system typically reverts to a limit cycle oscillating at the feedback frequency.

For large values of the feedback strength σ the external anisotropy suppresses the intrinsic anisotropy and a scenario of dynamic chaos in certain intervals of σ corresponds to the case of a one-mode semiconductor laser with optical feedback, i.e. to the case $E_y = 0$. A small misalignment χ perturbs the chaotic structure significantly.

Along with the appearance of weak fast oscillations, strong low frequency spikes arise in the y- component. The low frequency component correspondingly is changed also in the spectrum of the x- polarized component. The peak of the low frequency spectral component is situated at zero frequency and the spectrum is similar to the $1/f$ -noise spectra for very small values of the misalignment angle (less than about 0.001π). At larger χ, as shown in figure 5 the peak is shifted.

Thus we have shown that three types of complex polarization dynamics can be distinguished when the feedback strength is increased. Their appearance is caused by the competition among the external cavity modes as well as among orthogonally polarized modes. The competition depends on the value of the intrinsic and external anisotropies and on spin-flip relaxation processes. In its turn, the external anisotropy is determined by the feedback strength, phase and polarization distortion.

4. ACKNOWLEDGEMENT

The work has been funded in part by the Byelorussian Republic Fund for Fundamental Research.

REFERENCES

1. Pecora L.M., Carol T.L., *Phys.Rev.* **64** p. 821, 1990; Cuomo K.M., Oppennheim A.V., *Phys.Rev. A* **71**, p. 65, 1993.
2. Mirasso C.R., Colet P. and Garcia-Fernandez P., *Phot Tech Lett* **8**, p. 299, 1996; Sivaprakamsam S. and Shore K.A., *Optics Lett.* **24**, p. 466, 1999.
3. Robert F., Besnard P., Chares M.L. and Stephan G.M., *Optical and Quantum Electron.* **27**, p. 805, 1995; *IEE Proc.-Optoelectron.* **143**, p. 1041, 1996.
4. Besnard P., Robert F., Chares M.L. and Stephan G.M., *Phys. Rev. A* **56**, p. 3191, 1997.
5. Loiko N.A., Naumenko A.V. and Abraham N.B., *Quantum and Semiclass. Opt.* **10**, p. 125, 1998.
6. Loiko N.A., Naumenko A.V. and Abraham N.B., *in Laser Optics'98: Fundamental Problems of Laser Optics, N.N. Rosanov, Editor, Proc. of SPIE* **3685**, p. 2, 1999; *Laser Physics* (accepted).
7. San Miguel M., Feng Q. and Moloney J.V., *Phys. Rev. A* **52**, p. 1728, 1995.
8. van Tartwijk G.H.M., Levin A.M. and Lenstra D., *IEEE Sel. Top. Quantum Electron.* **1**, p. 466, 1995.
9. Lang R. and Kobayashi K., *IEEE J. Quantum Electron.* **16**, p. 347, 1980.

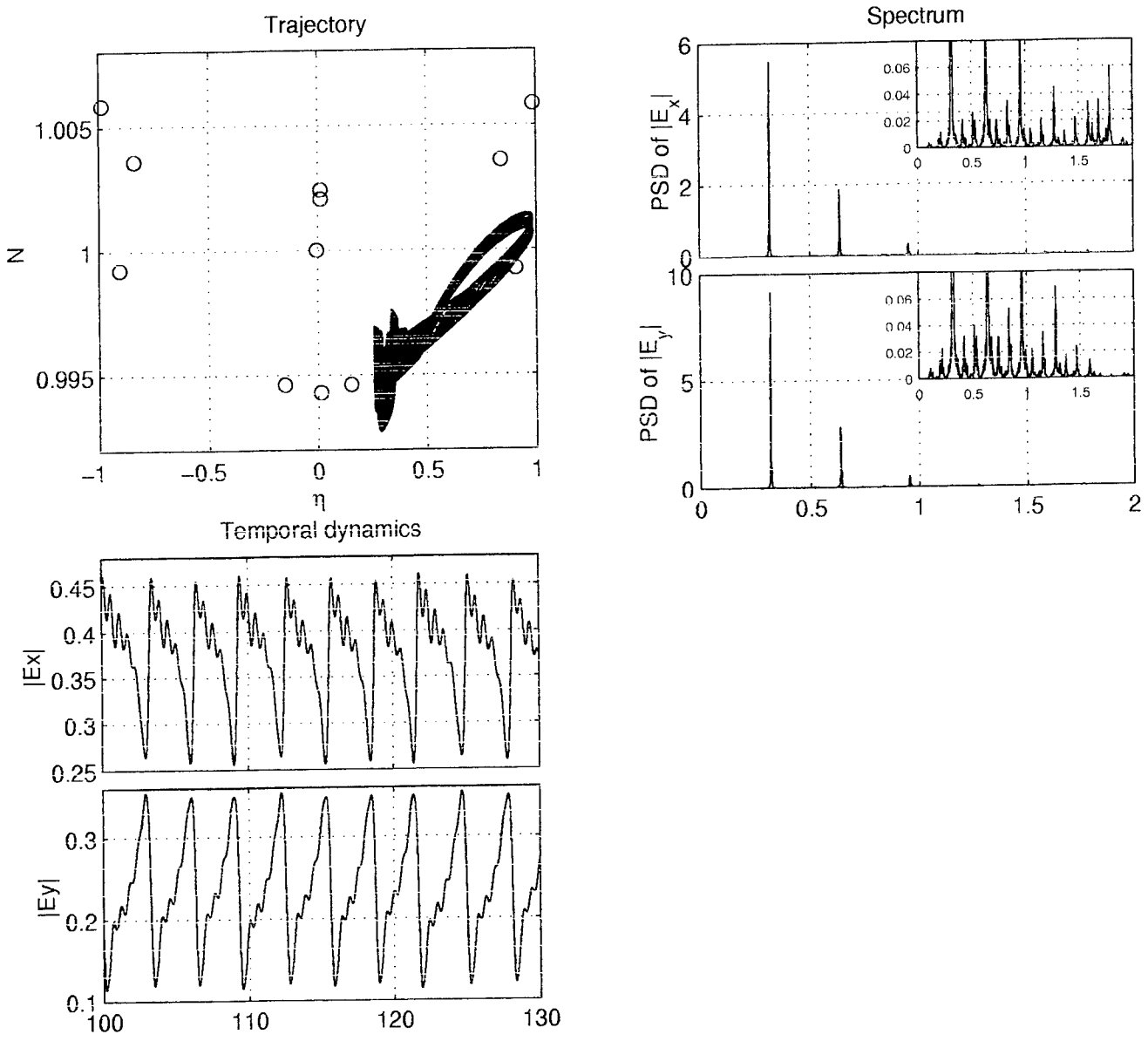

Figure 1. Evolution in time, trajectories in the plane (N, η) and corresponding power spectral densities of the amplitudes $|E_x|$ and $|E_y|$. The parameters are $\kappa = 300$, $\alpha = 3$, $\gamma_s = 50$, $\mu = 1.2$, $\gamma_a = 0$, $\gamma_p = 1$, $\omega\tau = 0.8\pi$, $\tau = 0.6$, $\chi = 0$, $\sigma = 2$.

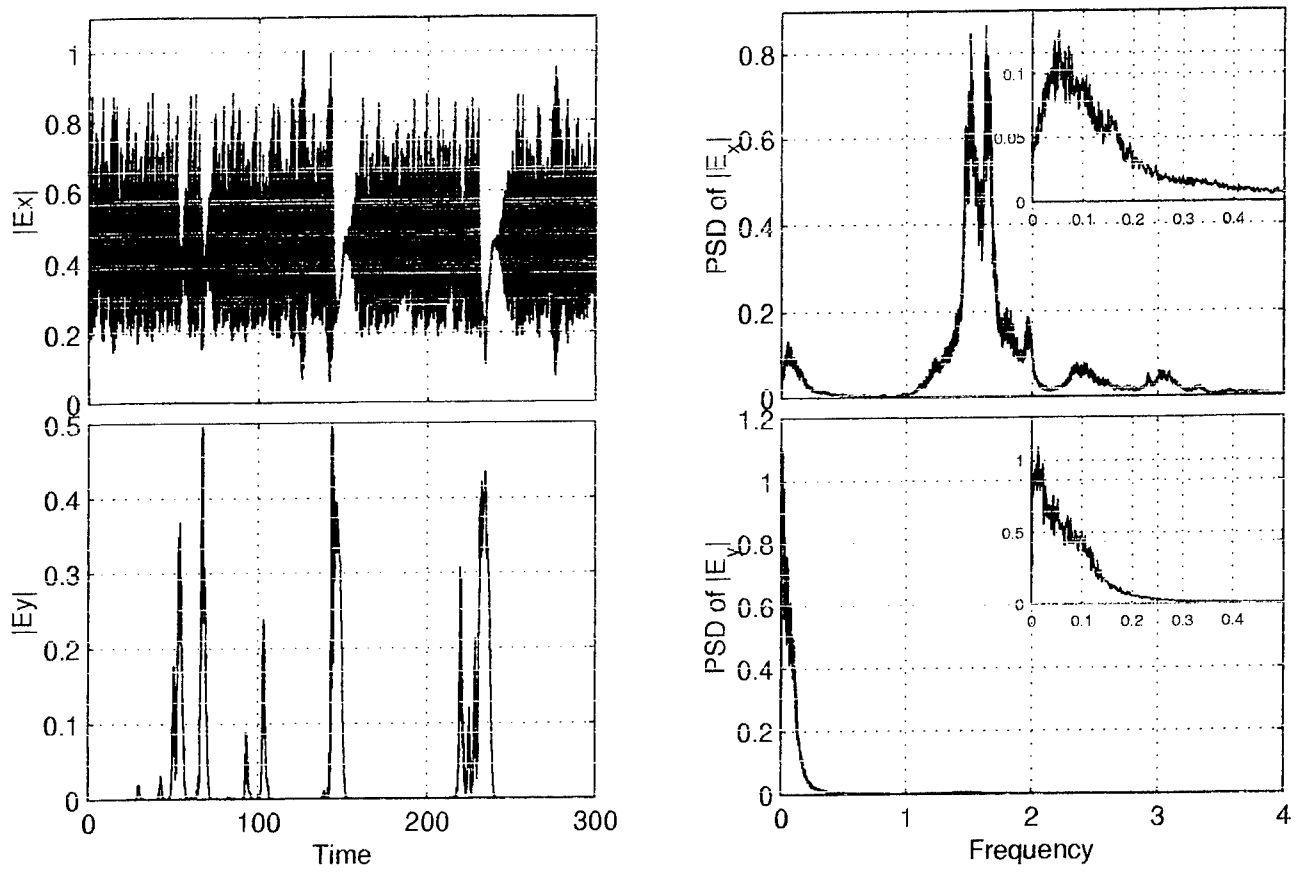

Figure 2. Evolution in time and corresponding power spectral densities of amplitudes $|E_x|$ and $|E_y|$. The parameters are $\omega\tau = 0$, $\sigma = 2.5$; other parameters are as in figure 1.

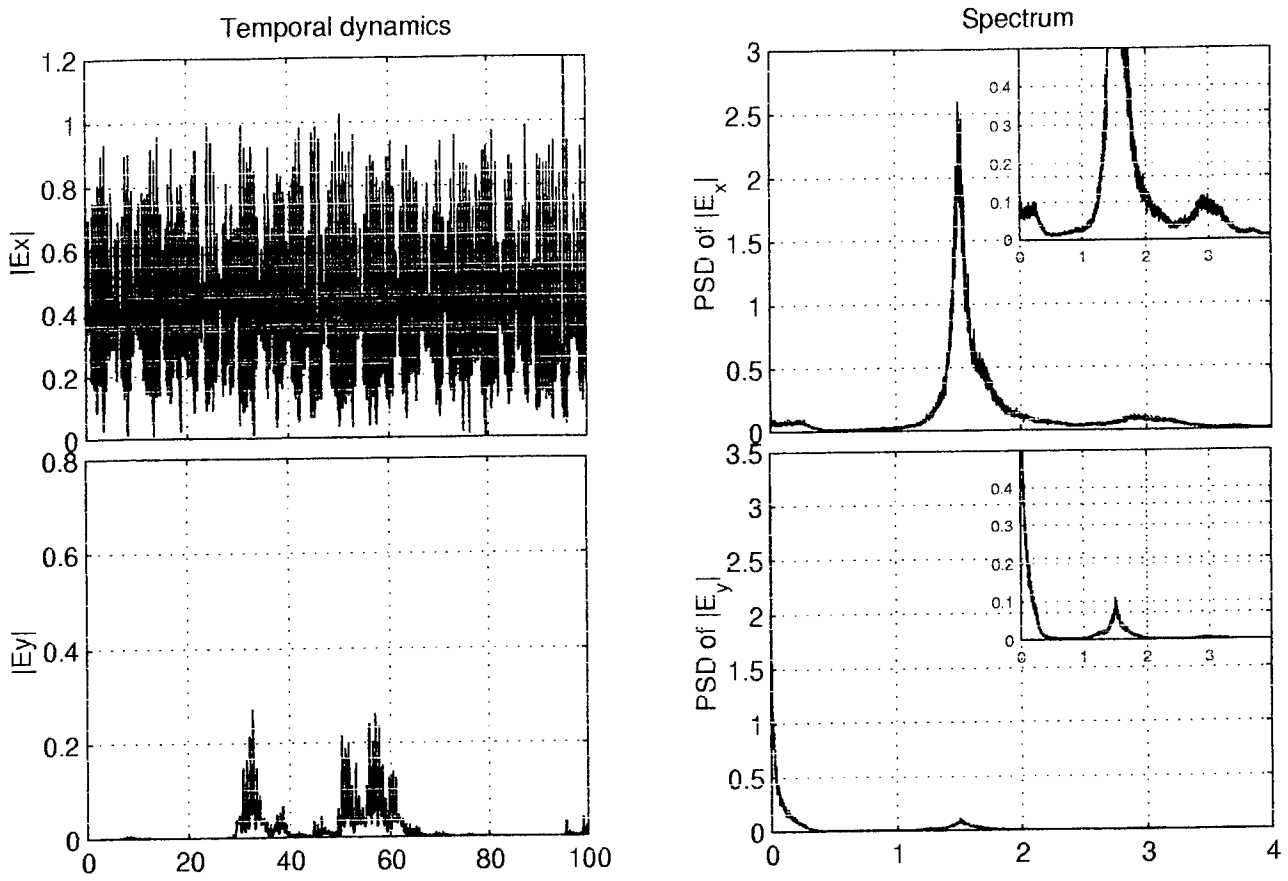

Figure 3. Evolution in time and corresponding power spectral densities of amplitudes $|E_x|$ and $|E_y|$. Parameters are $\gamma_s \to \infty$, $\omega\tau = 0$, $\sigma = 3.5$; other parameters are as in figure 1.

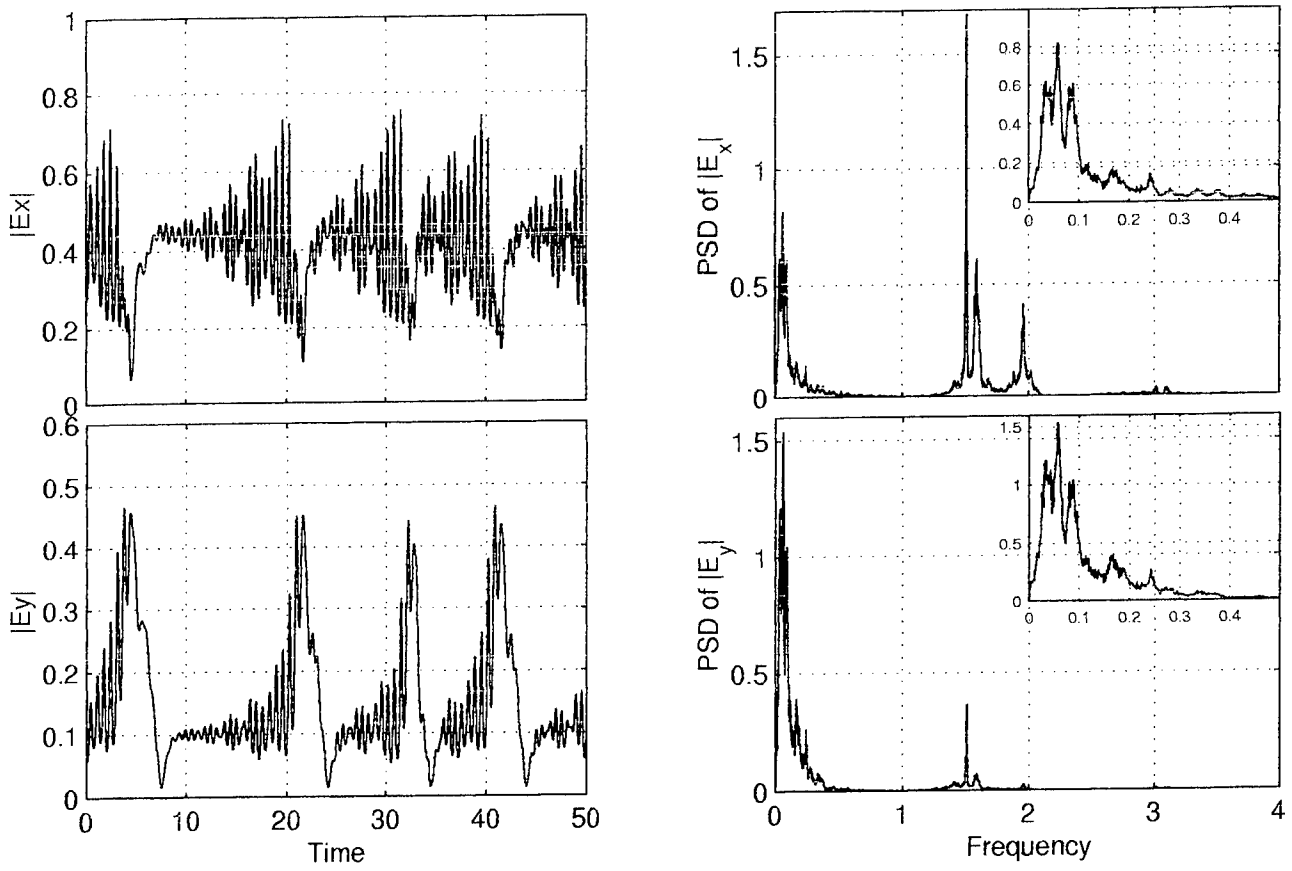

Figure 4. Evolution in time and corresponding power spectral densities of amplitudes $|E_x|$ and $|E_y|$. Parameters are $\chi = 0.02\pi$; other parameters are as in figure 2.

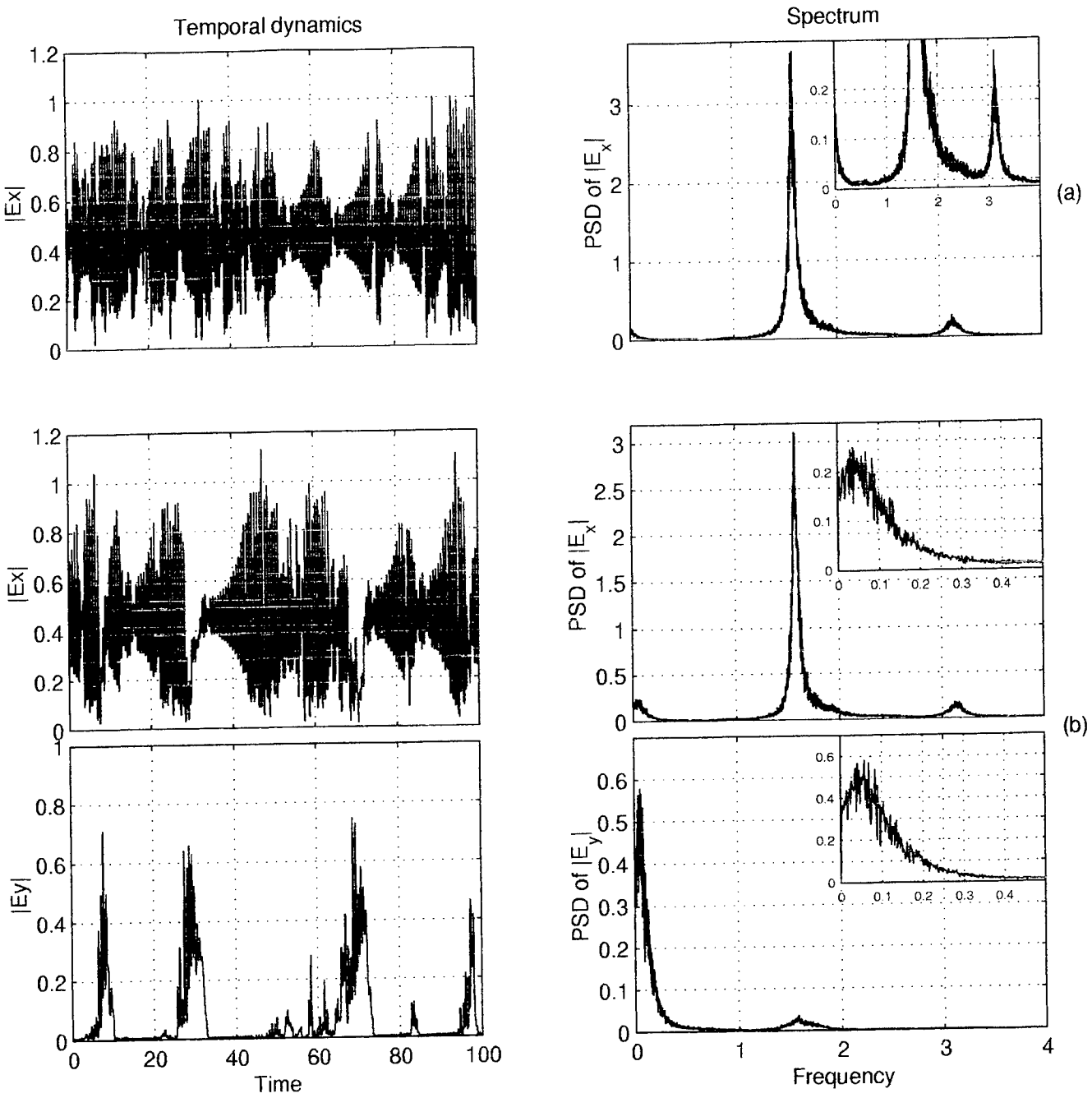

Figure 5. Evolution in time (left column) and corresponding power spectral densities (right column) of amplitudes $|E_x|$ and $|E_y|$. Parameters are $\chi = 0$ (a), 0.002π (b), $\sigma = 4$; other parameters are as in figure 1.

Cavity solitons in semiconductor microcavities: fundamental and applicative aspects

M. Brambilla, T. Maggipinto, I. M. Perrini and F. Rizzi

INFM, Dipartimento di Fisica Interateneo, Universitá e Politecnico di Bari,
Via Orabona 4, 70126 Bari, Italy

ABSTRACT

Cavity solitons appear as stationary, isolated peaks of light superimposed onto a homogeneous background field in the transverse profile of the coherent field transmitted or reflected by a non-linear resonator. These self-organised structures are theoretically predicted and simulated in a broad area multi-quantum-well vertical microresonator. We develop models suited to describe the macroscopic properties of the medium and the nonlinear interaction with the coherent field. Parametric domains and operational regimes for stable solitons are investigated along with some quantitative appreciation of their characteristics. Intrinsic stability properties of solitons are investigated by means of semi-analytical techniques and this allows to describe the destabilising mechanisms for solitons, mutual interaction properties, their response to perturbations and some of their dynamical features.

Keywords: Cavity solitons, pattern formation, semiconductor microcavities

1. INTRODUCTION

Cavity solitons are self-organized light structures appearing as nondiffracting light peaks in the transverse profile of the coherent field propagating in a nonlinear resonator. They are somehow similar to spatial solitons but arise in dissipative systems, which bestows them with special properties. They are generated by shining short and narrow laser pulses into resonant cavities filled with nonlinear samples of large section, and driven by a cw coherent holding beam. The cavity soliton, persists after the passage of the pulse, until it is switched off by another pulse. The motion of cavity solitons is governed by the transverse configuration of the holding beam; e.g. a modulated profile allows to realise arrays of spatial solitons which are easily reconfigurable, while constant gradients lead to a drift of the solitons with uniform velocity.[1] In Section 2, we present the recent progress in the theoretical/numerical studies of cavity solitons in semiconductor microresonators, following the development of more refined models to adequately describe the complex physics of broad-area semiconductor microresonators. Section 3 containes a brief analysis of instabilities affecting the homogeneous steady state in the parameter space supplies the correct parametrical choices necessary for realising cavity solitons which are observed for different values of the frequency and intensity of the driving field. The stability properties of cavity solitons and their competition with other stable patterns are described in Section 4. We adopt a general semi-analytical approach, valid for any specific form of the nonlinear susceptivity.[2] The analysis of the eigenvalues and the associated eigenvectors yields a perspicuous insight about the destabilising mechanisms of the solitons and their response to local perturbations. The latter issue can be profitably applied to predict the short-time dynamics of solitons and to assess certain characteristics of their attraction basin, thus providing guidelines to experiments for successful cavity soliton observation.

2. MODEL

The system we are considering consists of microcavity of the fabry-Perot type containing a nonlinear medium and driven by an external coherent field; the nonlinear medium can be either a Multiple Quantum Well (MQW) or a bulk sample of GaAs. In both cases the equations describing the evolution of the electric field inside the cavity and

Further author information: (Send correspondence to M.B.)
M.B.: E-mail: brambilla@fisica.uniba.it

Laser Optics 2000: Semiconductor Lasers and Optical Communication, Serguei A. Gurevich, Nikolay N. Rosanov, Editors, Proceedings of SPIE Vol. 4354 (2001) © 2001 SPIE · 0277-786X/01/$15.00

the carrier density of the active material are formally identical. In the slowly varying envelope approximation and in the mean field limit the dynamical equations reduce to the following set of partial differential equations[3,4]:

$$\frac{\partial E}{\partial t} = -(1+\eta+i\,\theta)E + E_I + i\,\Sigma\chi_{nl}E + i\,\nabla_\perp^2 E \tag{1}$$

$$\frac{\partial N}{\partial t} = -\gamma\left[N + \beta N^2 - Im\,(\chi_{nl})|E|^2 - d\,\nabla_\perp^2 N\right] \tag{2}$$

where E and E_I are the normalized slowly varying amplitudes of the intracavity field and external driving field, respectively; θ is the cavity detuning; η is the linear absorption coefficient due to the material in the regions between the semiconductor and the mirrors; Σ is the bistability parameter; N is the carrier density scaled to its transparency value; γ and β are the normalized decay rates of the carrier density that describe the nonradiative and radiative carrier recombination, respectively; d is the diffusion coefficient.
The transverse Laplacian, which describes diffraction in the paraxial approximation, is defined as

$$\nabla_\perp^2 = \frac{\partial^2}{\partial x^2} + \frac{\partial^2}{\partial y^2} = \frac{\partial^2}{\partial r^2} + \frac{1}{r}\frac{\partial}{\partial r} + \frac{1}{r^2}\frac{\partial^2}{\partial \phi^2} \tag{3}$$

where (x, y) are Cartesian and (r, ϕ) polar coordinates, in the transverse plane. Below we will consider for simplicity that the driving field E_I is independent of the transverse coordinates, i.e. a plane wave. The results we derive will be approximately valid for cavity solitons supported by an input beam much broader than the individual CS.
The complex susceptibility χ_{nl} describes the nature of the radiation-matter interaction and can be satisfactorily modeled[5,3,4] for both the MQW and the bulk cases.
In MQW structures we consider an optical nonlinearity governed by an excitonic resonance and described *via* a Lorentzian curve. A linear dependence of χ_{nl} on the carrier density N is assumed. The radiation-matter interaction is therefore described by

$$\chi_{nl}(N, \omega_0) = -\frac{1}{Im\,(\Theta)}\,\Theta\,(N-1) \tag{4}$$

with $\Theta = (\Delta + i)/(1+\Delta^2)$; here $\Delta = (\omega_e - \omega_0)/\gamma_e$ is the excitonic detuning, where ω_e and γ_e are the central frequency and the halfwidth of the excitonic line respectively, and ω_0 is the frequency of the input field. Under this assumption and introducing $C = \Sigma/(2\,Im\,(\Theta))$ equations (1) and (2) recover the original form considered in[5,3] .
The case of bulk medium[4,6] is interesting for several reasons. First of all, bulk samples are easier to grow and can be architectured with high accuracy; second, they offer the possibility of high levels of nonlinearity. Nevertheless the model is more complex and numerical simulations more demanding. Adopting the quasi-equilibrium approximation the complex susceptibility for the free carriers takes the form

$$\chi_{nl}(N, \omega_0) = -\frac{i}{\epsilon_0 \hbar V_A}\sum_{\vec{k}} |\mu_k|^2 \frac{f_{ek}(N) + f_{hk}(N) - 1}{i\,(\omega_k - \omega_0) + \gamma_p} \tag{5}$$

where $\vec{k}$ is the carrier momentum, μ_k is the dipole matrix element between the valence and the conduction band (calculated in[7,8]), γ_p is the polarization decay rate (about $10^{13} s^{-1}$), and $\hbar\omega_k = \epsilon_{gap} + \hbar^2 k^2/2m_R$ is the transition energy at the carrier momentum k, m_R being the electron–heavy hole reduced mass.[9] V_A is the active volume. The $f_{ek,hk}(N)$ are Fermi-Dirac distributions for electrons and holes, respectively. Two elements are then introduced phenomenologically to properly describe the behaviour of the bulk medium in the regimes of interest; one is band-gap renormalization and the other is the Urbach tail. Similarly to the MQW case, we define the band-gap detuning parameter $\Delta = (\omega_{gap} - \omega_0)/\gamma_p$ where ω_{gap} is the band-edge frequency and ω_0 the frequency of the input field.

As a further refinement we consider in this paper a first attempt to obtain a semi-empiric model which describes in a more complete way the nonlinear behaviour of a MQW. We describe the nonlinear susceptibility $\chi(N, \omega_0)$ by a sum of two contributions:

$$\chi_{nl}(N, \omega_0) = \chi_{free}^{2D}(N, \omega_0) + \chi_{exc}^{2D}(N, \omega_0) \tag{6}$$

where the first term is the free-carrier absorption, due to the transition between valence and conduction band, and the second term is the excitonic absorption, the most important contribution at room temperature. This approach,

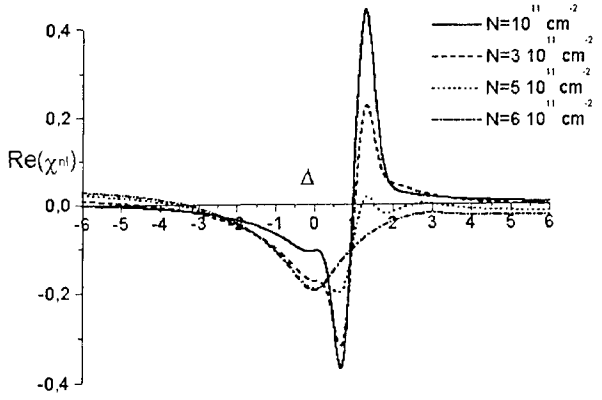

Figure 1. Real part of the nonlinear susceptibility as given by (6).

successfully considered in previous work,[10] allows to have a good agreement with experimental absorption spectra at room temperature. The free carrier nonlinearity is given by:

$$\chi^{2D}_{free}(N,\omega_0) = -\frac{in}{\epsilon_0 \hbar V_A} \sum_{\vec{K_\perp}} |\mu_{K_\perp}|^2 \frac{f_{eK_\perp}(N) + f_{hK_\perp}(N) - 1}{i\,(\omega_{K_\perp} - \omega_0) + \gamma_p} \tag{7}$$

where $K_\perp = (k_x, k_y)$ is the transverse carrier momentum, V_A is the volume of a single QW, n the number of the QW in the device. $\hbar\omega_{k_\perp} = \epsilon_{gap} + E_{e_\parallel} + E_{h_\parallel} + E_{e_\perp} + E_{h_\perp}$, where $E_{e,h_\parallel} = \hbar^2\pi^2/2m_{e,h_\parallel}w^2$, being w the QW width, and $E_{e,h_\perp} = \hbar^2 K_\perp^2/2m_{e,h_\perp}$; the $f_{e,h_{K_\perp}}$ are $2D$ Fermi-Dirac distribution for electrons and hole, respectively. As for the bulk case, appropriate bidimensional band-gap renormalization and Urbach tail are introduced.
The excitonic contribution is described by (4) being now $\Theta = A(i+\Delta)\exp(-\frac{1}{2}\Delta^2)$. This expression presents a gaussian shape and is justified by experimental observation. The excitonic absorption line, infact, presents a rapid decay from the resonance, different from the typical lorentzian decay and a gaussian line can reproduce in a better way than a lorentian the experimental results. Here $\Delta = \omega_e^{2D} - \omega_0/\gamma_e^{2D}$ is the bidimensional excitonic detuning, A is the amplitude of the exciton absorption line and N is the carrier density normalized to the excitonic saturation density.
Although ω_e^{2D}, γ_e^{2D} and A have a theoretical expression we prefer to set phenomenological values to have an expression nearer than possible to experiments. Fig. 1 and 2 show the calcuated real and imaginary part of the susceptibility for a typical device. This last model represents an attempt to consider a full description of the susceptibility where bulk and MQW behaviour are considered together and in the following will be called *hybrid model.* We note that a complete description of the nonlinear response of a MQW can be derived in a more fundamental way by means of a many-body theory. This approach, though, is more demanding from a computational point of view and so the hybrid model can be seen as a first good approximation. The results obtained with a many-body model have been investigated elsewhere[11]

3. ANALYSIS OF THE HYBRID MODEL

3.1. Homogeneous steady state and linear stability analysis

The homogeneous solution (E_S, N_S) of equations (1) and (2) is obtained by setting the time derivatives equals to zero and neglecting the Laplacian. We obtain:

$$|E_I|^2 = |E_S|^2 \left\{ [1 + \Sigma Im(\chi_{nl})]^2 + [\theta - \Sigma Re(\chi_{nl})]^2 \right\} \tag{8}$$

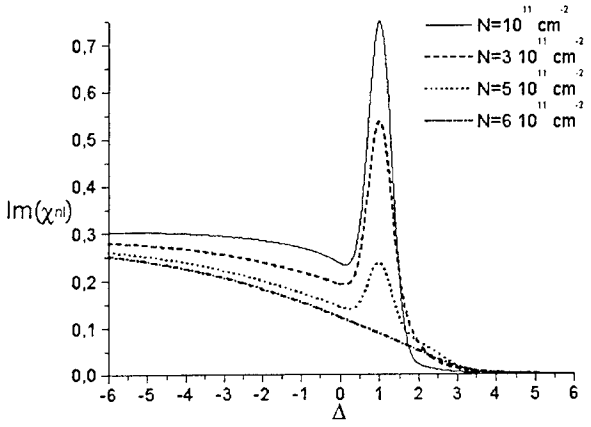

Figure 2. Imaginary part of the nonlinear susceptibility as given by (6).

$$|E_S|^2 = \frac{N_S + \beta N_S^2}{Im(\chi_{nl})} \tag{9}$$

For apprpopriate choices of the parameters, the curve of $|E_S|^2$ as a function of $|E_I|^2$ turns out to be S shaped showing a bistable behaviour.

We study now the instabilities of the homogeneous steady-state, which give rise either to another homogeneous state (plane-wave instability (PWI)) or to a spatially modulated pattern (MI). To this aim, we perform a linear stability analysis of the homogeneous solution and study the response of the system to small fluctuations around the steady state. To do this we consider

$$\begin{pmatrix} E(x,y,t) \\ E^*(x,y,t) \\ N(x,y,t) \end{pmatrix} = \begin{pmatrix} E_S \\ E_S^* \\ N_S \end{pmatrix} + \exp\left[\lambda t + i(K_x x + K_y y)\right] \begin{pmatrix} \delta E_0 \\ \delta E_0^* \\ \delta N_0 \end{pmatrix} \tag{10}$$

where we have assumed that the fluctuations grow (or decay) exponentially in time and that they are modulated with transvers wave vector (K_x, K_y). The set of equations obtained linearising (1) its complex conjiugate and (2) using (10) admits nontrivial solutions only if the eigenvalues λ satisfies the cubic equation[6]

$$\lambda^3 + a_2\lambda^2 + a_1\lambda + a_0 = 0 \tag{11}$$

where the coefficients a_i, $i = 0, 1, 2$ depend on the system parameters, on the input field and on the square modulus K^2 of the transvers wave vector. Equation (11) has usually one real and two complex conjugate roots. It is possible to show that the two complex roots have always a negative real part[4]; thus, if present, any instability is related to the real eigenvalue.

The instability associated with the real eigenvalue, called Turing instability, brings the system from the homogeneous state to a new non-homogeneous stationary state. The system passes from the stable to the unstable domain when the real eigenvalue changes its sign from negative to positive. Therefore, the stability boundary is assigned by the condition $\lambda = 0$, or equivalent, $a_0 = 0$. This last condition leads to a cubic equation for K^2.[4] If we fix all the parameters characterizing our model, the boundary of the Turing domain can be drawn in the plane $(|E_S|, K^2)$. The interval of unstable wave vectors corresponds to the internal region of the Turing curves. Then from the Turing domain we can determine the portion of the homogeneous solution $|E_S|^2$ that is unstable against a spatially modulated perturbation (MI instability). The intersection of the Turing domain with $K^2 = 0$ axis, if present, corresponds to an instability against a plane-wave perturbation (bistable behaviour).

On the basis of our previous studies[3,4] we are aware of some favorable or necessary conditions for the existence of CS, namely:

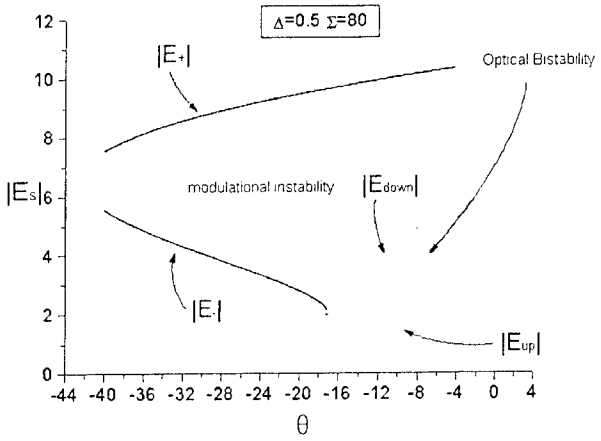

Figure 3. Hybrid model. MI and PWI boudaries as function of the caity detuning θ. Parameters are $\Delta = 0.5$, $\Sigma = 80$, $d = 0.2$ and $\beta = 0$.

1) A bistable steady-state curve for the homogeneous fields;

2) The stability of the lower homogeneous branch on which CS sit;

3) A fairly large interval of values of the injected field for which the upper homogeneous branch is modulationally unstable.

Following the path outlined in[4] we performed a detailed study of the instabilities in the parameter space. Our analysis has showed that these three conditions can be met for different choices of parameters. To illustrate the procedure let us draw the attention to the case $\Delta = 0.5$, corresponding to a self-focusing behaviour, and $\Sigma = 80$ which turns out to be close to the experimental value. From the inspection of Fig. 3 we see how it is possible to choose a value of the cavity detuning θ which could lead to the formation of CS according to the previoues stated conditions. The range of interest is for $-18 < \theta < -4$; for these values the homogeneous curve is, infact, bistable, the upper branch is modulationally unstable and the lower branch is fully stable. A good compromise between the extension of the bistability region and that of the unstable upper branch is given by $\theta = -10$.

3.2. Numerical results

The dynamical equations were integrated numerically using a split-step method with periodic boundary conditions. More details on the method and on the operating scheme can be found in.[3] Here we present the results obtained for the following choice of parameters: $\Delta = 0.5$, $\Sigma = 80$, $\theta = -10$.
As can be seen from Fig. 4 we have found roll solutions together with a CS branch. It is worth noting that on the right side of the branch CS loses stability exactly where the lower homogeneous branch terminates; this gives a confirmation of role of the lower homogeneous branch as a blackboard on which CS can written and erased.

A series of simulations have been devoted to determining the possibility of controlling CS for all-optical information processing. We analysed the on-off switching of CS in any desired location in the transverse plane. The numerical technique adopted[6] consists in superimposing upon the homogeneous background, a narrow Gaussian pulse, centered at the point (x_0, y_0) where we want to create or annihilate the CS. We investigated the minimum power required for switching a CS on as well as for erasing an existent CS; numerical results are reported in Tables 1 and 2. We have also analysed the interaction properties of CS; for the case under study two solitons are independent one from each other if their distance is greater than $d = 20.48\mu m$ (the width of a soliton is $14.9\mu m$) and they merge together in one soliton for smaller peak to peak distances.

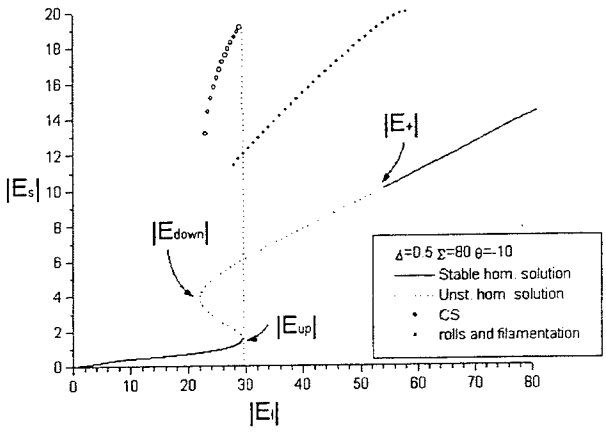

Figure 4. Hybrid model. Homogeneous steady-state and branches of the different structures. Parameters are $\Delta = 0.5$, $\Sigma = 80$, $d = 0.2$, $\beta = 0$ and $\theta = -10$.

Table 1. Self-focusing case $\Delta = 0.5$: minimum power P_{min} needed to excite a CS for different values of the width σ of the addressing pulse. The phase φ of the addressing pulse is set to zero and its duration $t = 1ns$.

$\sigma(\mu m)$	5.27	10.54	13.17	15.80	21.07
$P_{min}(\mu W)$	120	283.75	406.9	548	931.3

Table 2. Self-focusing case $\Delta = 0.5$: minimum power P_{min} required for erasing a CS for different values of the addressing pulse width σ. The addressing pulse is centered on the CS peak; its phase relative to the homogeneous background is $\varphi = \pi$ and its duration is $t = 117ps$.

$\sigma(\mu m)$	5.27	10.54	13.17	15.80	21.07
$P_{min}(\mu W)$	9.4	29.6	43.3	60.6	105.6

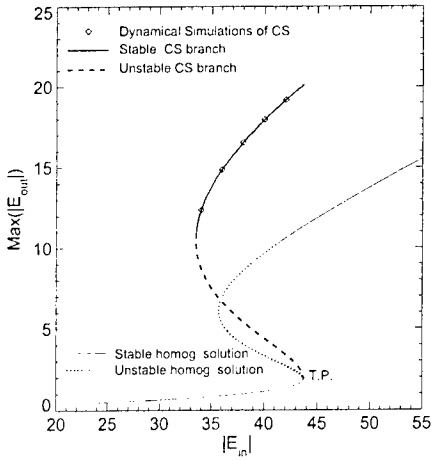

Figure 5. $1D$ MQW model. Steady-state curve of the homogeneous solution and results of numerical evaluations and of simulations for cavity soliton stationary solutions. Parameters are $\Delta = 0$, $C = 30$, $\theta = -3$, $d = 0.2$, $\eta = 0.25$, $\beta = 1.6$ and $\gamma = 0.002$. T.P. indicates the turning point of the homogeneous steady-state curve.

4. STATIONARY SOLUTIONS AND STABILITY

We look now for stationary solutions ($\partial/\partial t = 0$) of equations (1) and (2). We discretise the space variable(s) on N grid points; on the assumption of periodic boundary conditions, valid for the model under investigation, we use a fast Fourier Transform (FFT) algorithm to numerically evaluate the spatial derivatives.[2,12] This procedure gives a highly accurate, $O(N)$, set of coupled nonlinear algebraic equations which can be solved using a Newton method. Given a suitably close initial guess, this method rapidly converges to a stationary solution of the original equations. In particular CS are found from initial isolated peaks of suitable width and amplitude. Once a stationary solution is located it can then be tracked in parameter space. The benefit of such a procedure is that it yield all stationary solutions, not only those that are dynamically stable.

The use of a Newton method is advantageous because, as a by-product of this process, we evaluate the Jacobian matrix of the linearisation around the solution found. The resultant eigenvalues λ give the solutions' stability and the eigenvetors $\vec{u}$ the associated modes. Using the method described above $1D$ and cylindrically symmetric cavity soliton solutions have been found numerically for both MQW at resonance[3] and bulk model.[4]

For $1D$, typical results are shown in Fig. 5 for a MQW. The stable soliton branch is represented by a thicker solid line and the unstable branch by a thicker dashed line. Diamonds correspond to direct dynamical simulations (only for stable CS). The stability assignation, as previously told, derives directly from the method used.

In Fig. 6 we plot as a function of the input intensity some of the perturbation eigenvalues of the CS, to be precise the six least-negative eigenvalues. The CS negative slope branch is characterized throughout its existence range by the presence of a single eigenvalue with positive real part. Both CS branches always exhibit a zero eigenvalue, i.e. a *neutral mode*. This is characteristic of models with translational symmetry. The presence of this mode is of great importance for applications, as it will be discussed below. The inspection of eigenspectrum gives also a deeper insight on the mechanism by which CS loses stability when a second eigenvalue approaches zero.[2]

It is worth noting here that the central part of the CS stable branch is the most desirable in view of optical processing applications. Here the magnitude of the largest eigenvalues is comparable to that of γ and this means that any perturbation dies out in a few response time of the medium. As a consequence all internal degrees of freedom of CS are strongly damped; only translational symmetry is left out and this gives CS a particle-like character.

For $2D$ other interesting features are found; in the bulk case the soliton branch shows a spiralling behaviour which might suggest a region of bistability between solitons of different intensity (see Fig. 7).

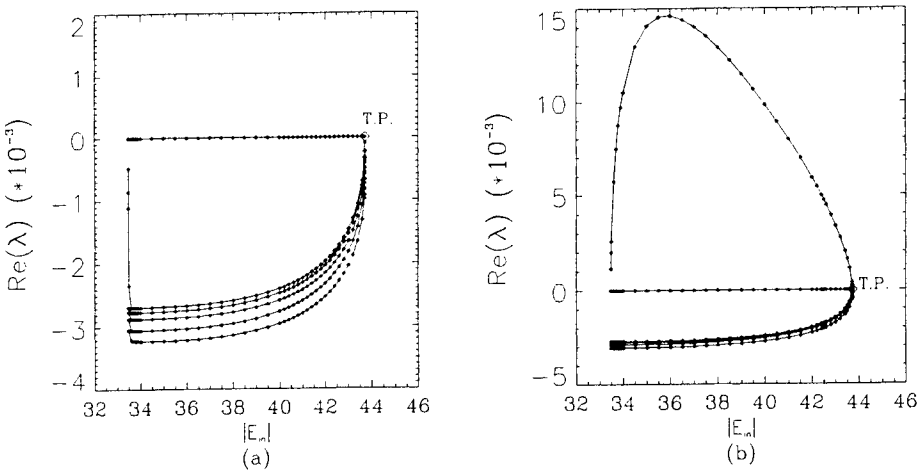

Figure 6. $1D$ MQW model. Parameters are as Fig. 5. The six eigenvalues with largest real parts as a function of the input field. (a) Positive-slope (stable) CS branch; (b) Negative-slope (unstable) CS branch. T.P. corresponds to the turning point of the homogeneous steady-state curve.

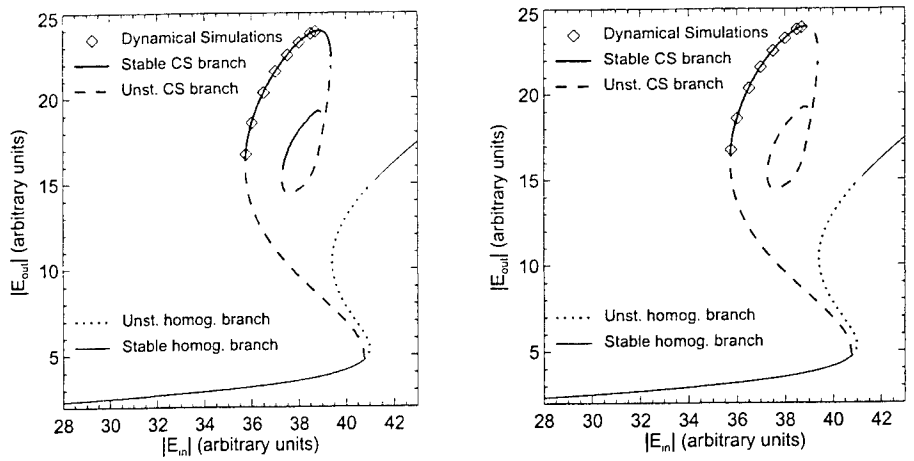

Figure 7. $2D$ bulk model. Parameters are $\Delta = 1$, $\Sigma = 80$, $\theta = -9$, $d = 0.2$, $\eta = 0$, $\beta = 0$ and $\gamma = 0.0014$. Stability assignations on the left refer to purely radial perturbations, those on the right include azimuthal perturbations also. The dynamical simulations agree only with the latter.

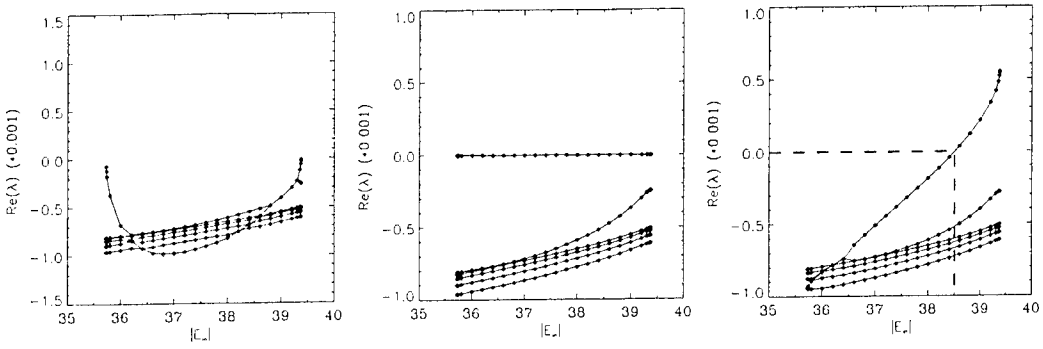

Figure 8. $2D$ bulk model. Perturbation eigenvalues as a function of the input field for a CS branch. Perturbations have azimuthal index: $m = 0$ (left); $|m| = 1$ (centre); $|m| = 2$ (right).

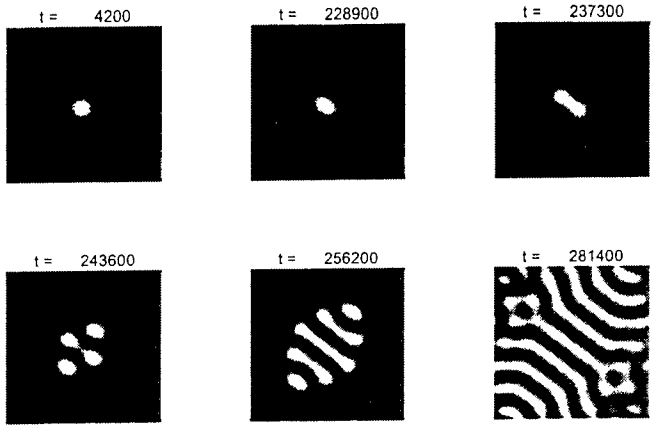

Figure 9. $2D$ bulk model. Dynamical evolution of a soliton solution for input field $|E_I| = 38.6$; the soliton destabilises via an $m = 2$ azimuthal instability.[2]

We should also, however, consider azimuthally varying perturbations of the form $\varepsilon = R(r)r^{|m|}e^{im\phi}$; $m = 0$ correspond to purely radial perturbations. The stability analysis is easily generalized for non-zero m, yelding a separate eigenspectrum for each azimuhal index. We can see in Fig. 8 that for $m = 0, 1$ we have no unstable modes, but with a neutral mode for $m = 1$. It is easy to show that this neutral mode is again associated with the translational symmetry of the governing equations. Finally for $m = \pm 2$ we see that the upper CS branch loses its stability at $E_{in} = 38.5$ in accordance with the dynamical simulations.

In Fig. 9 we display frames from a dynamical simulation which correspond to the destabilization of a cavity soliton for an input field slightly above $E_{in} = 38.5$ and we clearly see that it loses its stability *via* an asymmetric deformation of $m = 2$ type.

4.1. Response to perturbation

Now we analyse the effect of perturbations on stationary CS solutions; this issue merits investigation in view of possible applications to optical processing. We identify three types of perturbation: those due to imposed modifications to the external driving field, due to noise, and due to interactions between cavity solitons. The first can be used to

manipulate CS, the other two are undesirable in most cases.
For a stable stationary solution, all eigenvalues have negative real part except the neutral mode $\vec{u}_0$. This means that as $t \to \infty$, its amplitude a_0 dominates over all other a_i. Thus the dynamical effect of any perturbation $\mathcal{P}$ on a stationary stable state is primarily determined by its projection onto the neutral mode, which yields the equation[2]:

$$\frac{\mathrm{d}a_0}{\mathrm{d}t} = \frac{1}{\langle \vec{v}_0 | \vec{u}_0 \rangle} \langle \vec{v}_0 | \vec{\mathcal{P}} \rangle \tag{12}$$

Here $\vec{v}_0$ is the neutral mode of the corresponding adjoint problem. It can be shown that, being the neutral mode the gradient of the CS, the physical meaning of $\mathrm{d}a_0/\mathrm{d}t$ is the translational velocity of the CS under the influence of the perturbation.
Among the various types of perturbation, three of particular relevance are a phase or amplitude gradient of the driving field, and perturbation of one soliton by another. In the case of a weak phase gradient imposed on the homogeneous background E_0, the input field around a CS at $x = 0$ can be locally approximated by $E_{in} = E_0(1 + ikx)$. Inserting the perturbation part $E_0 ikx$ into (12) we can calculate the drift velocity of a cavity soliton due to the phase gradient (or, similarly, an amplitude gradient). The results obtained are in very good agreement with direct dynamical simulations.[2]
Consider now the perturbation of a soliton with respect to another soliton. The oscillations of the phase and amplitude of the CS field as it dies away into the background field can be regarded as somewhat equivalent, in their effects on a second nearby soliton, to imposition of varying gradients on the input field. The resulting induced relative motion of the two CS will be positive or negative depending on their separation. We can expect to find equilibrium positions where the relative velocity is zero, and that these define stable or unstable bound states of two CS. Such behaviour is indeed found in both semiconducotr models.[2] Adopting the same technique, interaction of cavity solitons in a degenerate optical parametric oscillator has recently been investigated,[13] showing one stable bound state for in-phase CS.
Finally, an important result concerning the role of the unstable branch acting as a separatrix can be obtained exploiting the consideration developed so far. The dynamics of the unstable CS, both in MQW and in bulk model, is governed by a single eigenvalue, with a corresponding eigenvector whose shape is similar to the unstable soliton. We can infer that the unstable CS is *metastable*, in that it is an attractor for all nearby states of broadly similar shape and strength. These will reshape towards the unstable CS configuration along its stable manifold, before escaping along its *one-dimensional* unstable manifold. Given this essentially single-mode behaviour we can anticipate that the locus of the unstable CS will act as a separatrix of the two stable coexisting solutions: the homogeneous solution and the CS. Dynamical simulation confirm this, for both MQW and bulk, in $1D$ snd in $2D$.[2]

5. CONCLUSIONS

We have presented briefly the main results concerning new modelistic approaches to description of pattern and cavity soliton in semiconductor microresonators, the analysis of stability domains for such structures and we have set forth critieria to predict soliton stability, dynamics and interaction schemes. The reader is referred to the bibliography for more detailed, full-length publications, some of which will appear soon or are being completed at the moment.

ACKNOWLEDGMENTS

This work was carried out within the framework of the ESPRIT LTR Project *Processing of Information by Arrays of Nonlinear Optical Solitons* (PIANOS, n.28235) and of the project MURST-PRIN *Spatial Structures in Nonlinear Optical Systems* (n. 9702268683-004).

REFERENCES

1. M. Brambilla, L. A. Lugiato, and M. Stefani, "Interaction and control of optical localized structures," *Europhys. Lett.* **34**, pp. 109–114, 1996.
2. T. Maggipinto, M. Brambilla, G. K. Harkness, and W. J. Firth, "Cavity solitons in semiconductor microresonators: existence, stability and dynamical properties," *Submitted for publication to Phys. Rev. E* .
3. L. Spinelli, G. Tissoni, M. Brambilla, F. Prati, and L. A. Lugiato, "Spatial solitons in semiconductor microcavities," *Phys. Rev. A* **58**, pp. 2542–2559, 1998.

4. G. Tissoni, L. Spinelli, M. Brambilla, T. Maggipinto, I. M. Perrini, and L. A. Lugiato, "Cavity solitons in passive bulk semiconductor microcavities. i. microscopic model and modulational instabilities," *J. Opt. Soc. Am. B* **16**, pp. 2083–2094, 1999.
5. M. Brambilla, L. A. Lugiato, F. prati, L. Spinelli, and W. J. Firth, "Spatial solitons pixels in semiconductor devices," *Phys. Rev. Lett.* **79**, pp. 2042–2045, 1997.
6. G. Tissoni, L. Spinelli, M. Bambilla, T. Maggipinto, I. M. Perrini, and L. A. Lugiato, "Cavity solitons in passive bulk semiconductor microcavities. ii. dynamical properties and control," *J. Opt. Soc. Am. B* **16**, pp. 2095–2105, 1999.
7. G. P. Bava, P. Debernardi, and A. Pisoni, "Qw optical response including valence band mixing and many body effects," *Internal Report* **DE/GE 91–002**, Politecnico di Torino 1993.
8. K. W. Boer, *Survey of semiconductor physics*, Van Nostrand Reinhold, New York, 1990.
9. W. W. Chow, S. W. Koch, and M. Sargent III, *Semiconductor Laser Physics*, Springer Verlag, Berlin Heidelberg, 1994.
10. D. S. Chemla, D. A. B. Miller, P. W. Smith, A. C. Gossard, and W. Wiegmann, "Room temperature excitonic nonlinear absorption and refraction in GaAs/AlGaAs multiple quantum well structures," *IEEE Journ. Quant. Elect.* **20**, pp. 265–275, 1984.
11. M. Brambilla, T. Maggipinto, F. Rizzi, L. Spinelli, and G. Tissoni *In Preparation* .
12. W. J. Firth and G. K. Harkness, "Cavity solitons," *Asian Journal of Physics* **7**, pp. 665–676, 1998.
13. D. V. Skryabin and W. J. Firth, "Interaction of cavity solitons in degenerate optical parametric oscillators," *Opt. Lett.* **24**, pp. 1056–1058, 1999.

Transformation of the light beams transverse structure upon coherent interaction in nonlinear interferometers

O.G.Romanov*

Department of Laser Physics and Spectroscopy, Belarusian State University
4, Fr.Skaryna av., 220050 Minsk, Belarus

ABSTRACT

The theoretical and numerical modelling of the light beams transverse structure formation upon coherent interaction in the interferometers with resonant nonlinearity has been proposed. The analysis has been performed on the base of the modal theory for the scheme of counterpropagating beams in the ring cavity and for the scheme of oblique symmetrical incidence of two beams on the Fabry-Perot interferometer. Complex spatio-temporal evolution of the light beams structure, such as formation of bound states, symmetry breaking instability, asymmetrical self-oscillations has been demonstrated.

Keywords: wave mixing, nonlinear interferometer, symmetry breaking instability.

1. INTRODUCTION

The theoretical modelling of self-organisation phenomena and co-operative processes in nonlinear optical systems is the fast developing area of investigation. Much attention has been paid to the effect of optical bistability in systems with external feedback under exciting of one or several light beams[1-9]. The coherent interaction of the light beams in the cavity volume provides an additional kind of feedback. This distributed feedback is due to dynamic gratings, nonlinearly formed in the medium volume. One of the effects that arises from longitudinal coupling of two light beams in the nonlinear interferometer is the symmetry breaking bifurcation[2]. In the process, intensity of two light beams is different on the output of the interferometer, while it is equal on the input. Most investigations of the symmetry breaking instability have been related to the plane-wave limit[2,4,5,7,8]. However, transverse coupling (due to the diffraction of radiation) leads to a complicated transformation in a cross-section of the light beams[9].

In this work the consideration is being given to the results of theoretical investigation into the interaction of two light beams counterpropagating in the ring cavity (RC) and in the scheme of oblique incidence on the Fabry-Perot interferometer (FPI) with a two-level resonant medium. Effects of intracavity distributed feedback and transverse coupling of the light beams have been included into consideration. The possibility for realisation of asymmetrical transverse profiles for two light beams has been demonstrated and the influence of geometry of the light beams interaction has been investigated. The paper is organised as follows. In Section II the results of theoretical modelling of two-beam interaction in RC are presented. The particular attention has been paid to the formation of asymmetrical intensity profiles under incidence of Gaussian light beams on the bistable interferometer. The problem of two-beam interaction under symmetrical oblique incidence on the FPI is studied in Section III.

2. SYMMETRY BREAKING IN THE SCHEME OF TWO BEAMS INTERACTION IN RC

The problem of symmetry breaking instability in RC has been studied for Kerr-like nonlinearity in the plane-wave limit[2]. In this Section we would like to recall some results of theoretical modelling of this task for the resonant type of nonlinearity and investigate the transverse structure of the output light beams. The process of two-beam interaction in the mean-field limit for high fineness RC[10] can be described by the following set of coupled-mode equations[9]:

$$\begin{aligned} t_R \frac{\partial e_1}{\partial t} &= e_{10} - e_1 + i\Delta_0 e_1 + iC\left(\frac{\hat{\Theta}_{12}}{B_{12}} e_1 + \frac{\hat{\alpha}}{\alpha}(\chi_0 e_1 + \chi_1 e_2)\right) + i\beta\frac{\partial^2 e_1}{\partial x^2} \\ t_R \frac{\partial e_2}{\partial t} &= e_{20} - e_2 + i\Delta_0 e_2 + iC\left(\frac{\hat{\Theta}_{12}}{B_{12}} e_2 + \frac{\hat{\alpha}}{\alpha}(\chi_0 e_2 + \chi_1^* e_1)\right) + i\beta\frac{\partial^2 e_2}{\partial x^2} \end{aligned} \quad (1)$$

where $e_{10,20}$ are the amplitudes of the pump fields, co-operative parameter $C = \kappa_0(\omega)L/2T$, cavity build-up time $t_R = L/vT$, $v = c/n_0$ is the light velocity in the medium, L - thickness of the cavity, T - transmission coefficient of

* e-mail:romanov@phys.bsu.unibel.by

Laser Optics 2000: Semiconductor Lasers and Optical Communication, Serguei A. Gurevich, Nikolay N. Rosanov, Editors, Proceedings of SPIE Vol. 4354 (2001) © 2001 SPIE · 0277-786X/01/$15.00

the cavity mirrors, dimensionless diffraction parameter $\beta = \lambda L / 4\pi T x_0^2$, transverse variable x is normalised to the input Gaussian intensity profile half-width x_0, Δ_0 is the cavity detuning parameter. $\hat{\alpha} = a + i\alpha = \left(\hat{\Theta}_{12} + \hat{\Theta}_{21}\right)/vp_{21}$ is a complex nonlinearity parameter for a two-level resonant medium, the real part of which determines a light-induced change in the refractive index, and the imaginary part characterises a change in the absorption coefficient[11]; $\hat{\Theta}_{ij} = \Theta_{ij} + iB_{ij}$, where the coefficients $\Theta_{ij}(\omega)$ are related by the Kramers-Kronig (dispersion) relations to the Einstein coefficients $B_{ij}(\omega)$, p_{21} is the total probability of spontaneous and nonradiative transitions, n_0 and κ_0 are the linear refraction and extinction coefficients. The coefficient $\alpha = \left(B_{12} + B_{21}\right)/vp_{21}$ determines the saturation intensity of the resonant transition ($I_{SAT} = \alpha^{-1}$). An expansion of nonlinear susceptibility in the Fourie series of dynamic gratings formed by counterpropagating waves has been used. In the inertialess limit the equations for the space harmonics of nonlinear susceptibility have the form[8]:

$$\chi_0 = -1 + \frac{1 + \alpha\left(I_1 + I_2\right)}{A_0}, \quad \chi_1 = -\frac{\alpha' e_1 e_2^*}{A_0} \tag{2}$$

where $\alpha' = \alpha c n_0 / 8\pi$, $A_0 = 1 + 2\alpha\left(I_1 + I_2\right) + \alpha^2\left(I_1^2 + I_2^2\right)$.

The steady-state equations for the intensity of the light beams $I_{1,2}$ can be easily obtained from (1, 2), and with the assumption of coincident absorption and emission bands ($\hat{\Theta}_{12} / B_{12} = \hat{\alpha} / \alpha$) and the incident intensity of beams $I_{10} = I_{20} = I_0$ they have the form:

$$I_0 = I_{1,2}\left[\left\{1 + \frac{C}{A_0}(1 + \alpha I_{1,2})\right\}^2 + \left\{\Delta_0 + \frac{a}{\alpha}\frac{C}{A_0}(1 + \alpha I_{1,2})\right\}^2\right] \tag{3}$$

Under the appropriate conditions[8] the asymmetrical bistable solution of (3) can be obtained. Such an interaction mode is depicted in Fig.1. It is characterised by the inequality of the output light beam intensities and arises from coherent intracavity interaction of the light beams.

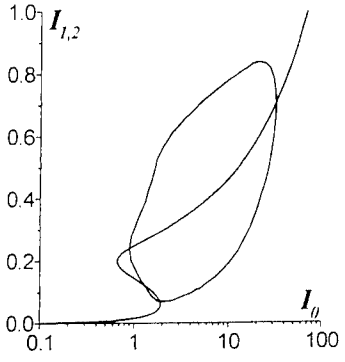

Fig.1 Steady-state plane-wave transmission function in conditions of symmetry breaking. $C(\omega_{12}) = 70$, frequency detuning away from absorption band centre $\xi = (\omega - \omega_{12})/\Gamma = \pm 2$ (Γ is the half-width of the Gaussian profiles of absorption band), $\Delta_0 = \pm 15$.

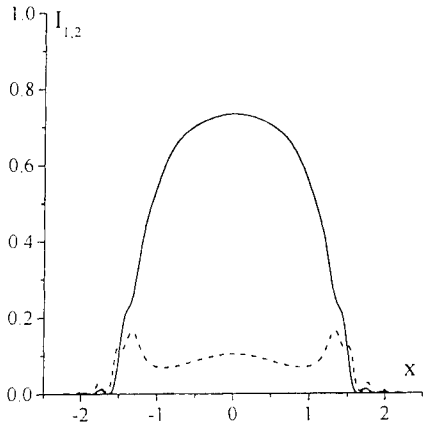

Fig.2 Steady-state of intensity redistribution in transverse profiles of the light beams counterpropagating in RC. $\beta = 10^{-2}$, $\alpha I_0 = 5$.

The formation of the light beam transverse profiles has been analysed by numerical modelling of the equations (1) with the use of the explicit two-layer finite-difference approximation. The modelling has been carried out for the defocusing

nonlinearity (long-wavelength region of the absorption band) and relatively wide light beams (small values of the diffraction parameter β). Typically, in the steady-state we observe two profiles with significantly different integral intensity (Fig.2[12]).

3. OBLIQUE INCIDENCE OF TWO LIGHT BEAMS ON FPI

Let us consider the scheme of two-beam interaction upon oblique incidence on the front mirror of FPI with the small angle symmetrically relative to the normal[4,7,9]. Under oblique incidence the coupled-mode equations in the mean-field limit for high fineness FPI have the form[9]:

$$t_R \frac{\partial e_1}{\partial t} = e_{10} - e_1 + i\Delta_0 e_1 + iC\left(\frac{\hat{\Theta}_{12}}{B_{12}} e_1 + \frac{\hat{\alpha}}{\alpha}(\chi_0 e_1 + \chi_1 e_2)\right) + i\beta\frac{\partial^2 e_1}{\partial x^2} + \alpha_0^{'}\frac{\partial e_1}{\partial x},$$
$$t_R \frac{\partial e_2}{\partial t} = e_{20} - e_2 + i\Delta_0 e_2 + iC\left(\frac{\hat{\Theta}_{12}}{B_{12}} e_2 + \frac{\hat{\alpha}}{\alpha}(\chi_0 e_2 + \chi_1^{*} e_1)\right) + i\beta\frac{\partial^2 e_2}{\partial x^2} - \alpha_0^{'}\frac{\partial e_2}{\partial x}, \quad (4)$$

where the co-operative parameter $C = \kappa_0(\omega)L/T$, cavity build-up time $t_R = 2L/vT$, dimensionless diffraction parameter $\beta = \lambda L/2\pi T x_0^2$, coefficient $\alpha_0^{'} = \alpha_0 L/2\pi T x_0$ is proportional to the small angle α_0 between the wave vector and the normal to the front mirror of the interferometer.

The numerical modelling of the system (4) has been carried out by the same method as for the case of RC. The parameters of resonator and radiation under which the symmetry breaking instability takes place have been used. Let us notice, that in the plane-wave limit these equations with re-scaling of the variables are equivalent to the system of coupled-mode equations, describing the process of two-beam interaction in RC. This similarity leads to the same steady-state transmission functions of different interferometers. In the case of symmetry breaking instability the output light beams intensity are significantly different. In this section we would like to point out, that transverse interaction due to diffraction and transverse drift of radiation due to oblique incidence of the light beams on the FPI significantly change the character of energy exchange between the light beams. The results of numerical calculations are presented in Fig.3-6.

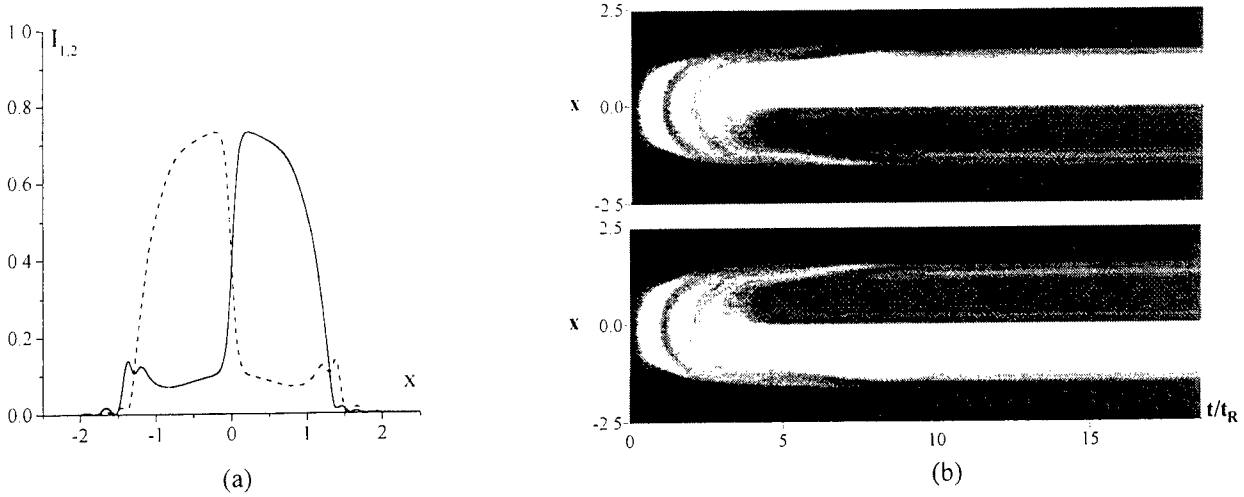

Fig.3 Dynamics (a) and steady-state (b) of intensity redistribution in transverse profiles of the light beams for the scheme of oblique incidence on FPI. $\alpha_0^{'} = 0.1$, $\beta = 10^{-2}$, $\alpha I_0 = 5$.

The symmetrical steady-state transverse profiles of two light beams are characterised by the mirror symmetry relative to the axis $x = 0$, edge front between the switch-on and switch-off parts of the profiles and equality of the integral intensity (Fig.3a). Moreover, each beam stays on the switch-on state in the half-plane from which the incidence takes place. To describe the formation of the mirror symmetrical intensity profiles let us consider the dynamics of the light beams formation in the FPI. The first stage is a quite typical process of switch-on of the light beams in the central zone (Fig.3b, $t \approx 3t_R$). Then, the effect of symmetry breaking develops in all parts of transverse section. The reason of such a process is the transverse drift of beam intensity in the direction of propagation. Under oblique incidence each beam undergoes intensity redistribution in transverse section. When the incidence angle is rather small the more intensively part remains in the half-

plane from which the incidence takes place, while the less intensity part drifts in the direction of beam propagation. Since the structure with a little different values of intensity of two beams is unstable, the process of energy transfer between beams develops very fast (Fig.3b, $t \approx 3-6t_R$). As a result the intensity of each beams increases significantly in the half-plane from which the incidence takes place. This steady-state, however, can be switched to the state with different integral intensity (similar to Fig.2) by applying the positive impulse on the input of one of the light beams.

From the problem of oblique incidence of a single beam on the front mirror of the nonlinear FPI[13] it follows that with the increasing of the incidence angle the maximum of the light beam intensity drifts in the direction of the wave vector and under some value of $\alpha_0^{'}$ intersects the axis $x = 0$. For the case of two-beam interaction it means that the modes opposite to the case of repulsion demonstrated previously should be realised. When the incidence angle and the velocity of transverse drift of radiation are rather great the effective time of interaction and the energy exchange are decreasing. Thus, the energy transfer from one beam to the another one is almost absent. Let us consider these tasks in detail.

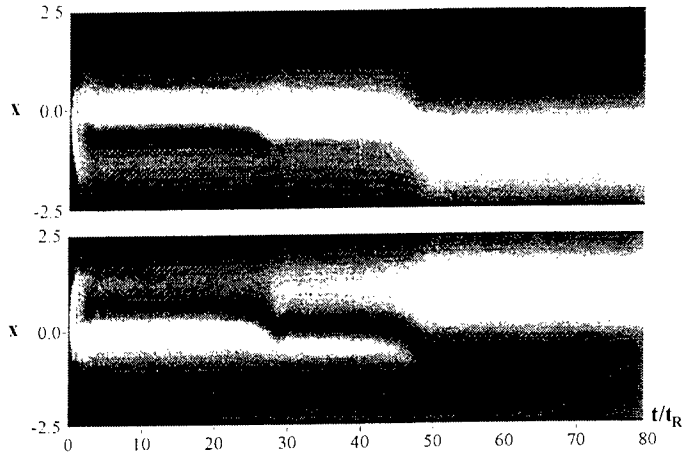

(a)

By the numerical modelling of two-beam interaction has been established, that with the increasing of coefficient $\alpha_0^{'}$ the steady-state intensity profiles undergo the following changes: at first, the switching front between beams in the area $x = 0$ vanishes, at second, the formation of two intensity spikes for each beam takes place. One of them is located in the centre of beam, while the another one stays on the periphery of the transverse profile in the direction of beam propagation. At that, the light beams, as before, have the mirror symmetry relative to the axis $x = 0$, and they central spikes form the bound state. It is natural to suppose, that under some value of the parameter $\alpha_0^{'}$ the transformation of such a structure into the another one should occurs. This process is connected with drift of intensity spike of each beam

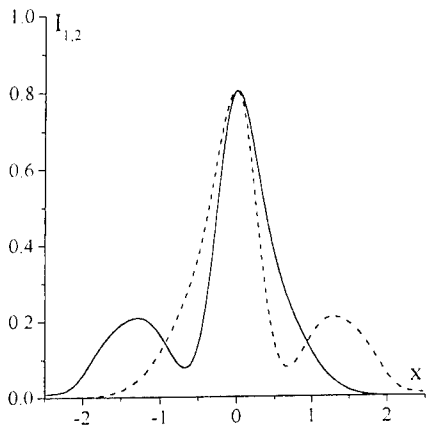

(b)

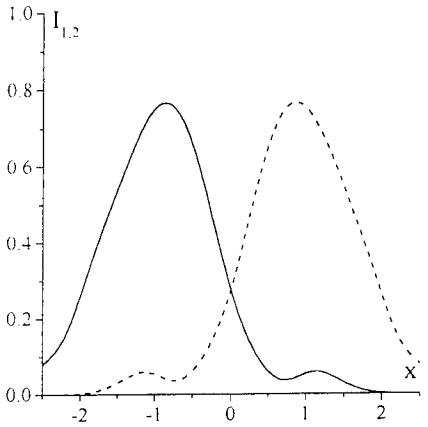

(c)

Fig.4 Dynamics (a) and the snapshots in the moments $t = 10t_R$ (b) and $t = 100t_R$ (c) of intensity distribution in transverse profiles of two light beams. $\alpha_0^{'} = 1.27$, $\beta = 10^{-2}$, $\alpha I_0 = 5$.

in the another half-plane relative to the axis $x = 0$. As seen from Fig.4, the transverse structure from the bound state (Fig.4b), when the maximum of both beam near the axis $x = 0$ is practically coincident, transforms into the state of two independent beams, when the spikes separate on two half-width of Gaussian profiles (Fig.4c). In the process, the energy transfer from the central maximums to the peripheral ones of each beam takes place (Fig.4a). The steady-state transverse structure is rather stable relative to the initial difference in the input intensity of the light beams. The energy exchange between well separated spikes is almost absent.

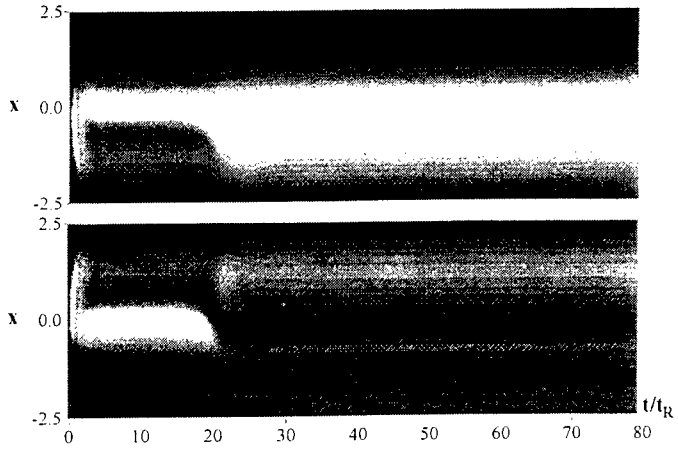

(a)

Another mode of bound state transformation is demonstrated in Fig.5 for the higher values of the incidence angle. In the process of quasi steady-state structure destruction (Fig.5a) the intensity spikes separate on sizeable smaller distance. In consequence of this energy exchange between beams should be rather effective and the steady-state transverse profiles have the considerable difference in integral intensity (Fig.5c). Under the intermediate values of the incidence angle the dynamics of the light beams interaction can be rather complicated. As seen from previous figures (Fig.4,5) there is two type of steady-state transverse structure, when the intensity spikes are separated on different distance. The intermediate state is characterised by pulsation between these two modes (Fig.6a). The time dependence of integral intensity

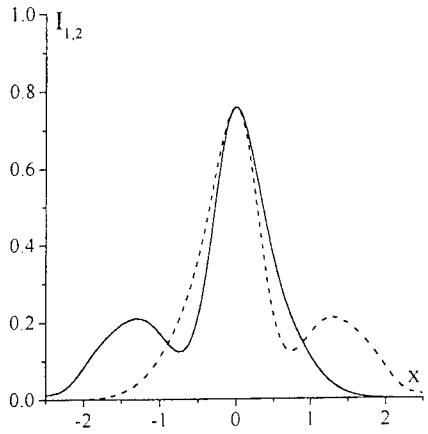

(b)

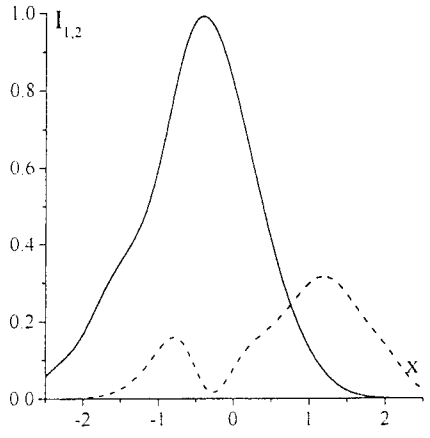

(c)

Fig.5 Dynamics (a) and the snapshots in the moments $t = 10t_R$ (b) and $t = 100t_R$ (c) of intensity distribution in transverse profiles of two light beams. $\alpha_0' = 1.4$, $\beta = 10^{-2}$, $\alpha I_0 = 5$.

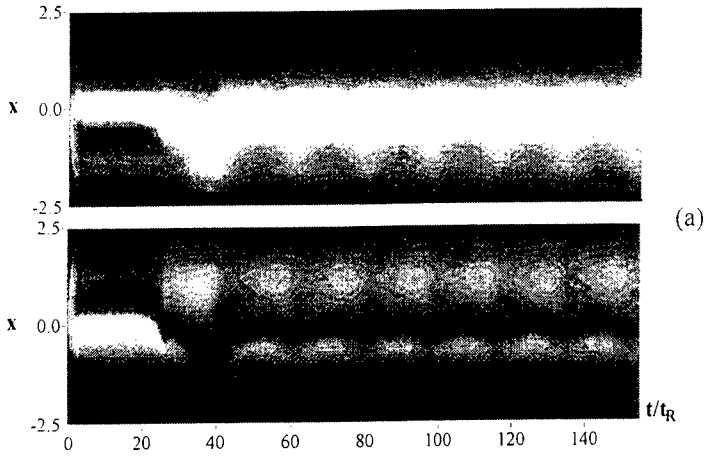

(a)

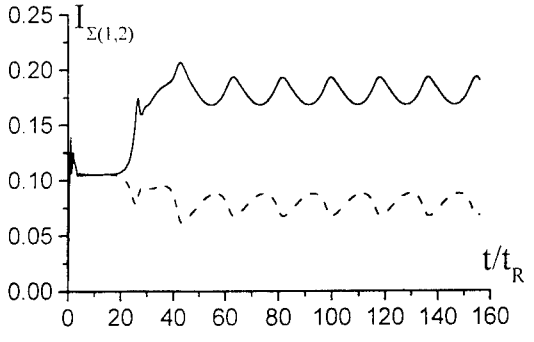

(b)

Fig.6 Dynamics of intensity distribution in transverse profiles of two light beams (a) and integral intensity (b). $\alpha_0' = 1.3$, $\beta = 10^{-2}$, $\alpha I_0 = 5$.

corresponds to asymmetrical antiphase oscillations (Fig.6b). With further increasing of the incidence angle the effective time of the light beams interaction decreases due to increasing of the transverse drift velocity of each beam. At that, the light beams pass through each other without any energy exchange due to symmetry breaking instability. The steady-state profiles are characterised by the great distance between two intensity spikes and equal integral intensity.

4. CONCLUSION

In conclusion, the transverse interaction of the light beams due to diffraction of radiation and transverse drift due to oblique incidence lead to asymmetrical transverse profiles in the scheme of two beams interaction in the FPI. Under the smaller values of the incidence angle the symmetry breaking instability results to formation of bound states of light beams with mirror symmetrical relatively to the axis $x = 0$ intensity profiles. With the increasing of the incidence angle the symmetry breaking of bound state takes place and the modes with equal or significantly different integral intensity as well as asymmetric self-oscillation have been demonstrated.

ACKNOWLEDGMENTS

This research was supported by Belarusian Foundation of Fundamental Research.

REFERENCES

1. N.N. Rosanov, *Optical bistability and hysteresis in distributed nonlinear systems*, Moscow, Nauka, 1997.
2. A.E. Kaplan, P. Meystre, "Directionally asymmetrical bistability in symmetrically pumped nonlinear ring interferometer," Optics Comm. **40**, pp.229-232, 1982.
3. N.C. Kothary, R. Frey, "Bistable behavior of pump, probe, and conjugate signals through collinear intracavity nearly degenerate four-wave mixing," Phys.Rev. A **34**, pp.2013-2024, 1986.
4. M. Haelterman, P. Mandel, J. Danckaert, H. Thienpont, I. Veretennicoff, "Two-beam nonlinear Fabry-Perot transmission characteristics," Optics Comm. **74**, pp.238-244, 1989.
5. K. Otsuka, "Pitchfork bifurcation and all-optical digital signal processing with a coupled-element bistable system," Optics Lett. **14**, pp.72-74, 1989.
6. I.V. Babushkin, Yu.A. Logvin, N.A. Loiko, "Symmetry breaking bifurcation in the light-dynamics of two bistable thin films," Kvant Electron. **25**, pp.110-115, 1998.
7. S.M. Karpuk, O.G. Romanov, A.L. Tolstik, "Different types of bistability upon multiwave mixing in a nonlinear interferometer," NPCS **2**, pp.50-55, 1999.
8. O.G. Romanov, A.L. Tolstik, "Symmetry breaking and dynamics of four-wave mixing in the nonlinear interferometer," Proc. SPIE **4016**, pp.459-464, 2000.
9. O.G. Romanov, A.S. Rubanov, A.L. Tolstik, "Transverse effects upon interaction of light beams in nonlinear interferometers," Lith. Phys. J. **39**, pp.250-256, 1999.
10. L.A. Lugiato, C. Oldano, "Stationary patterns in passive optical systems: two-level atoms," Phys. Rev. A **37**, pp.3896-3908, 1988.
11. V.V. Kabanov, A.S. Rubanov, "Spectral dependence of refractive index in the range of absorption and emission bands of organic dyes," Dokl. Akad. Nauk BSSR **24**, pp.34-37, 1980.
12. Only the central half of the computational window along the axis x is shown in Figs. 2-7.
13. M. Haelterman, G. Vitrant, R. Reinisch, "Transverse effects in nonlinear planar resonators 2. Modal analysis for normal and oblique incidence," JOSA (B) **7**, pp.1319-1327, 1990.

Dissipative soliton lasers: multistability and hysteresis phenomena

A.K.Komarov, K.P.Komarov[1)]

Institute of Automation and Electrometry, the Russian Academy of Sciences, the Siberian Branch, Acad. Koptyug Pr. 1, Novosibirsk, 630090, Russia

ABSTRACT

Multiple pulse operation of passive mode-locked lasers with nonlinear refractive index of intracavity elements has been investigated. The hysteresis dependence of number of pulses in established regime on the pump power has been found. It is shown that this number depends also on initial condition of generation. The application of discovered multistability and hysteresis to optical communications and information processing is discussed.

Keywords: passive mode-locking, phase-modulation instability, multistability, propagation of ultrashort pulses through nonlinear dispersion media

1. INTRODUCTION

The evolution of the radiation in the ring laser cavity is described by the following normalized equation[1]:

$$\frac{\partial}{\partial t}E = (1+i\theta)\frac{\partial^2}{\partial z^2}E + \frac{1}{2}\left(\frac{1+a}{1+b\int|E|^2\,dz} - 1 + \frac{p}{1+|E|^2}|E|^2 + iq|E|^2\right)E, \qquad (1)$$

where $E(z,t)$ is the amplitude of the field, t is the time variable expressed in units of the decay time of the field in an empty cavity, z is the coordinate expressed in units of the dispersion length (geometric-mean of the reciprocal of the decay time of the field in empty cavity and the frequency dispersion of the imaginary part of the permittivity), θ is the ratio of the real and imaginary parts of the frequency dispersion of the intracavity medium. The first term in the second parentheses describes the gain, where a is the relative pump excess above threshold; b is the ratio of saturation intensities of nonlinear losses and amplification divided by the dimensionless cavity length. The saturation is determined by the total intracavity radiation energy and accordingly the integration is carried out over the whole cavity volume. The second term is due to the linear losses. The third term accounts for the decrease in the nonlinear losses connected with saturable absorption (or in the nonlinear diffraction losses). The last term describes the nonlinear refractive index.

For sufficiently small pump excess above threshold, $|E|^2 \ll 1$, the change in the nonlinear losses is defined by the expression $\delta\sigma \approx p|E|^2$. In this case the passive mode-locking based on approximation of Eq. (1) with $\theta = 0$, $q = 0$ was analysed in papers[2,3]. The solution in the form of a sech pulse was found and the problem of its stability for small disturbances was solved. In the paper[4] it was shown with using Lyapunov functional that the transient evolution of passive mode-locking described by (1) with $\theta = 0$, $q = 0$ from any initial conditions passes into the steady-state single pulse mode.

[1)]e-mail: komarov@iae.nsk.su

Laser Optics 2000: Semiconductor Lasers and Optical Communication, Serguei A. Gurevich, Nikolay N. Rosanov, Editors, Proceedings of SPIE Vol. 4354 (2001) © 2001 SPIE · 0277-786X/01/$15.00

The passive mode-locking in the frame of Eq. (1) with nonlinear losses $\delta\sigma \approx p\,|E|^2$ and with regard to both frequency dispersion and nonlinearity of refractive index was analysed in papers[1,5]. It was found a solution in the form of a sech pulse with a frequency chirp.

The aim of our investigation is to determine regularities in the change of regimes of passive mode-locking due to phase-modulation instability in the frame of model described by Eq. (1). The investigation is based on the numerical simulation with using of various schemes.

2. THE RESULTS OF NUMERICAL SIMULATION

The necessary condition for stability of any stationary soliton solution of Eq. (1) is $g = (1+a)/(1+b\int |E|^2\,dz) - 1 < 0$. Otherwise the net gain g in the wings of the pulse is above zero, and small amplitude noise grows. The condition $g < 0$ is obeyed under the following restriction on parameters of nonlinearities $\xi = q/p$ and dispersions θ [6]

$$\frac{3\sqrt{1+\theta^2} - 2\theta + 2\theta^2\left(\sqrt{1+\theta^2} - \theta\right)}{1 - \theta\left(\sqrt{1+\theta^2} - \theta\right)} > \xi > \\ > -\frac{3\sqrt{1+\theta^2} + 2\theta + 2\theta^2\left(\sqrt{1+\theta^2} + \theta\right)}{1 + \theta\left(\sqrt{1+\theta^2} + \theta\right)}. \qquad (2)$$

Our numerical simulation shows the following. If the condition (2) breaks down then in the course of transient process the whole laser cavity is filled with radiation, that is, the passive mode-locking is absent. In Fig. 1 the corresponding area on the plane ξ, θ is indicated as the area 2. In Fig. 2 one can see the corresponding transient evolution with the single pulse initial condition.

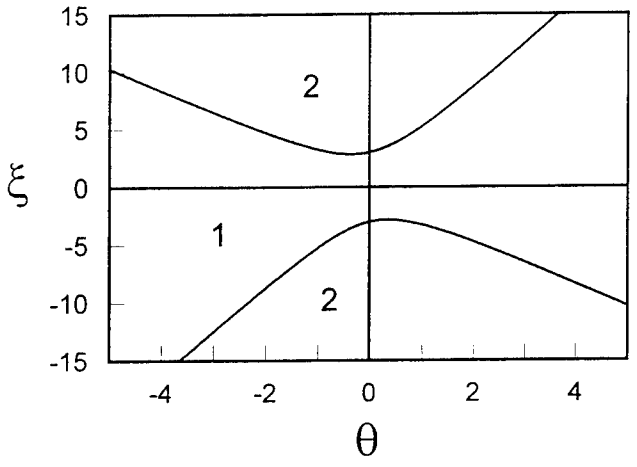

Figure 1: With parameters θ, ξ from the area 1 the passive mode-locking is realized. Otherwise (θ, ξ from the area 2) the passive mode-locking is suppressed.

If the condition (2) is fulfilled the single pulse stationary regime is realized at small pump power (see Fig. 3a). The multiple pulse initial condition with various amplitudes of pulses in Fig. 3

models the variance of amplitudes of initial noise pulses. If the pump power exceeds a certain threshold than this regime becomes unstable and the operation with two identical stationary pulses is established (see Fig. 3b). Further increase of the pump power leads to three-pulse regime (see Fig. 3c), then to four-pulse regime, and so on. The increase of number of pulses in established operation with increasing pump power is realized both with multiple pulse initial condition and with single initial pulse. The multiple pulse generation of this type are realized experimentally in Ti:sapphire lasers[7,8] (see also paper[6]).

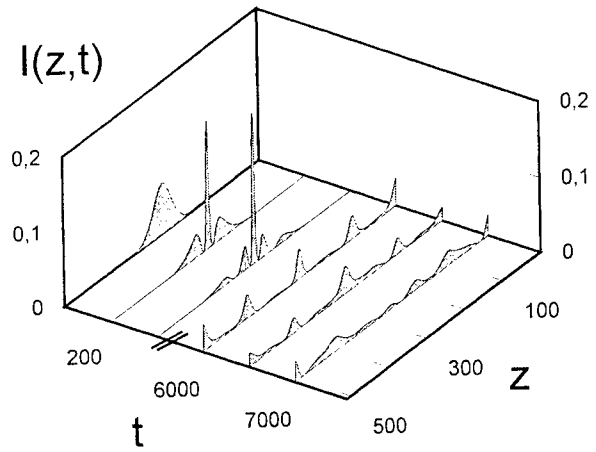

Figure 2: The characteristic transient evolution and established operation with parameters θ, ξ from the area 2 of Fig. 1.

In Fig. 4 one can see the dependence of the number of pulses N in steady-state on the pump power a. This dependence has been found by us from numerical simulation. The increase of number of pulses is possible only in accordance with lower stepwise curve marked by corresponding arrows. The decrease of number of pulses is realized in accordance with upper stepwise curve. The horizontal lines show constancy of number of pulses under changes of pumping a. These horizontal lines in combination with stepwise curves form closed hysteresis loops. As can be seen from Fig. 4, the dependence of pulse number N on pumping a is many-valued function, that is, the laser operation is multistable. The number of pulses in established regime depends also on initial conditions. The number of possible steady states increases with increasing pump power.

3. DISCUSSION

The nonlinear losses play the role of a positive feedback. As is generally known, this positive feedback selects the most intensive pulse and suppresses pulses with lesser amplitudes.

Owing to a nonlinear refractive index the frequency chirp occurs, and the spectrum of the pulse is broadened. As a result, the amplification efficiency in the active medium having the finite amplification frequency band drops. By this means the negative feedback mechanism occurs: the greater amplitude of the pulse entails its less amplification in active medium. In contrast, the negative feedback levels amplitudes of pulses. (Notice that the response time of this negative feedback is equal to the time of formation of the equilibrium frequency chirp for the given amplitude of the pulse. This equilibrium frequency chirp is determined by the balance between mechanisms inducing the pulse phase-modulation and causing its degradation. In a similar manner, the equilibrium duration of pulse is determined.)

Playing of parameters determining positive and negative feedbacks determines the competition and the coexistence of pulses, and accordingly the type of established regime.

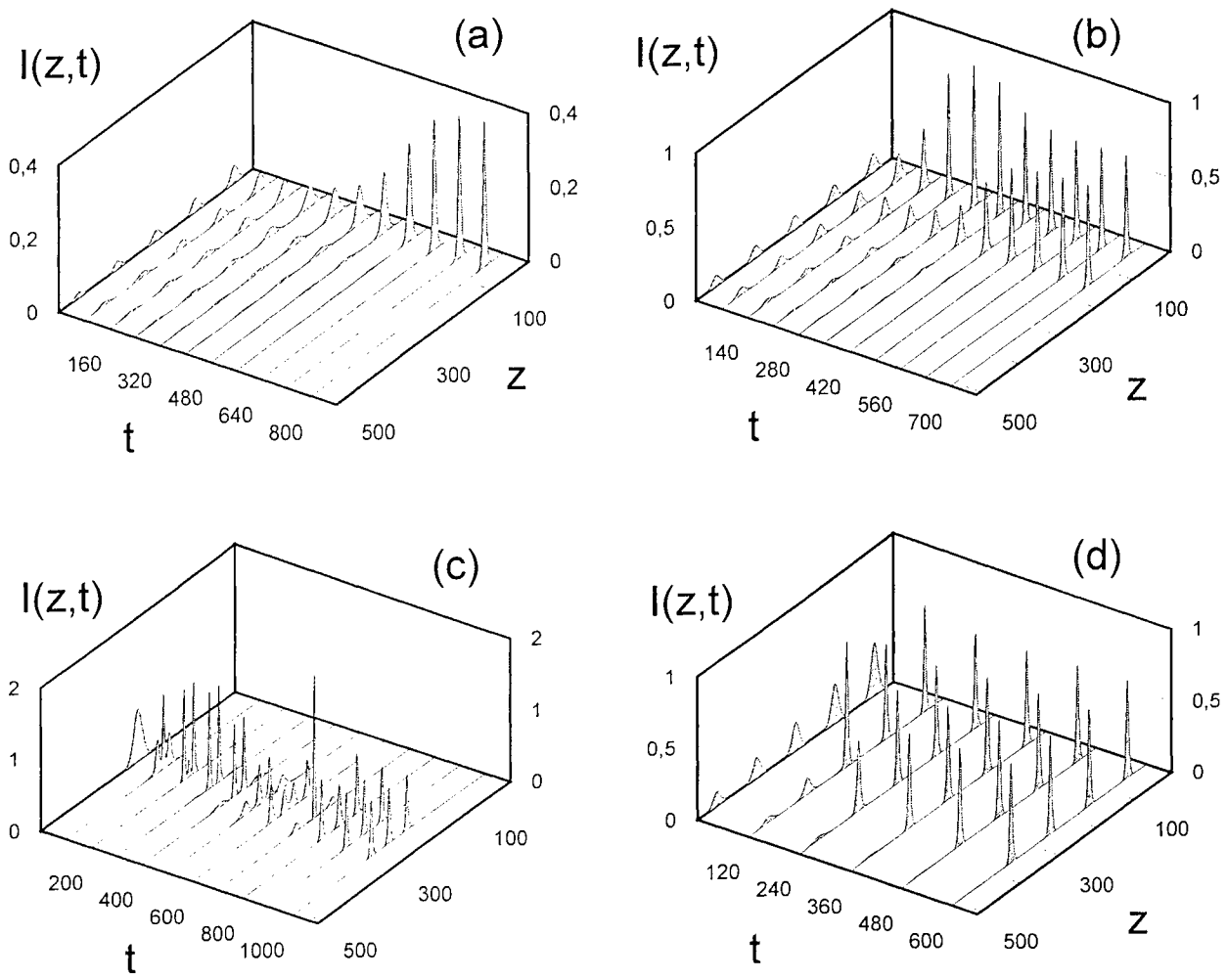

Figure 3: The increase of the number of pulses in steady-state with increasing pump power. (a) $a = 0.6$, (b) $a = 1.2$, (c) $a = 2.0$, (d) $a = 2.5$. ($\theta = 0.4$, $p = 0.2$, $q = 1.2$, $b = 0.1$).

Let us estimate quantitatively the net feedback. Here we use the following model approximation of the nonlinearity of losses $p_{ef} = p/(1 + |E|^2) \approx p/(1 + |E_{ok}|^2)$, where E_{ok} is the peak amplitude of k-th pulse. The solution of Eq. (1) is searched in the form several pulses with various amplitudes and with equilibrium duration and frequency chirp

$$E(z,t) = \sum_k E_{ok} \frac{e^{(\lambda_k + i\delta\omega_k)t}}{\cosh^{1+i\alpha_k}(\beta_k z)}, \tag{3}$$

where α_k, β_k, $\delta\omega_k$, and λ_k are the equilibrium frequency chirp, the equilibrium inverse duration, the frequency shift, and the parameter of temporal increment for k-th pulse. Substituting (3) in (1) allows to receive algebraic equations determining these parameters of pulses. The equilibrium frequency chirp and the equilibrium inverse duration are determined as functions of the peak amplitude of pulse $\alpha_k = \alpha_k(|E_{ok}|^2)$, $\beta_k = \beta_k(|E_{ok}|^2)$. For the temporal increment of k-th pulse we have the following expression

$$\lambda_k = \frac{p_{ef}}{2 - \alpha_k^2} |E_{ok}|^2 (1 - \alpha_k^2) + g, \tag{4}$$

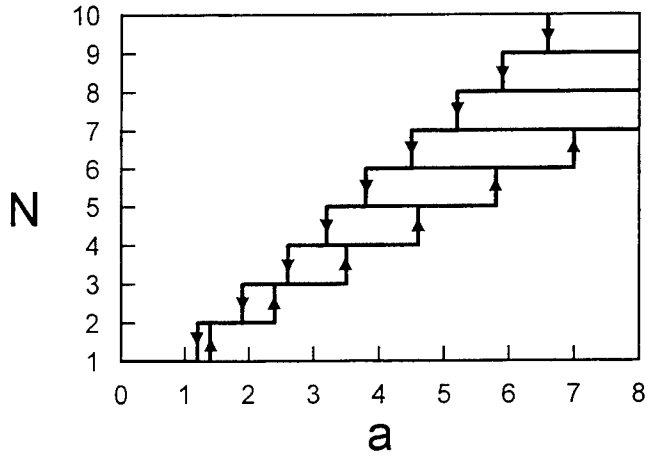

Figure 4: The multistable operation and the hysteresis dependence of the number of pulses N in steady-state on pump power a. ($\theta = 0$, $p = 0.2$, $q = 0.3$, $b = 0.1$).

where the equilibrium frequency chirp α_k is determining by the equation

$$\frac{\alpha_k}{2-\alpha_k^2} \approx \frac{q}{3p_{ef}} \approx \frac{q\left(1+|E_{0k}|^2\right)}{3p}. \tag{5}$$

Hereinafter for simplicity assume that $\theta = 0$. The solution (3) is correct with $\lambda_k t \ll 1$ when $\exp(2\lambda_k t) \approx 1$.

The temporal increment λ_k can be treated as the net coefficient for amplification of k-th pulse. With p, q satisfying the condition (2) the characteristic form of the dependence of $\delta\lambda_k = \lambda_k - g$ on the peak intensity is presented in Fig. 5 as the solid curve. At small peak intensity $I_{0k} = |E_{0k}|^2$ this dependence is linear. With increasing peak intensity the frequency chirp increases and at $|E_{ok}|^2 = 3p/q - 1$ it reaches the level $\alpha_k^2 = 1$. Therewith $\delta\lambda_k = 0$.

The form of the dependence of the amplification coefficient for pulse λ_k on its peak intensity I_{ok} allows understanding of absent of passive mode-locking (Fig. 2), of multiple pulse operation (Fig. 3), of hysteresis phenomena and multistability (Fig. 4).

In the case that the condition (2) is fulfilled (that corresponds to the area 1 in Fig. 1 and the solid curve 1 in Fig. 5) at small pump power a for all peak intensities $I_{ok} < I_{cr2}$, and the greater intensity of pulse entails its greater amplification. As a result, the single pulse established operation is realized. With increasing pump power a the peak intensity of this single pulse in steady-state increases. When it becomes greater than I_{cr1} the amplification for small amplitude pulses becomes positive and the second pulse arises in generation. For peak intensities $I_{ok} > I_{cr2}$ the greater intensity of pulse entails its less amplification and accordingly amplitudes of these pulses are equalized. As this takes place, the peak intensities of these two pulses becomes less than I_{cr1} because of energy balance. With further increasing pump power a the peak intensities of these two pulses increase and again reach the level I_{cr1} and then third pulse arises in generation, and so on. This process is determined the lower stepwise curve in Fig. 4.

In the case of multiple pulse operation with decreasing pump power a (the condition (2) is fulfilled) the peak intensities of all pulses are the same and decrease. As long as their peak intensities are remained greater than I_{cr2}, the number of these pulses doesn't change. This process

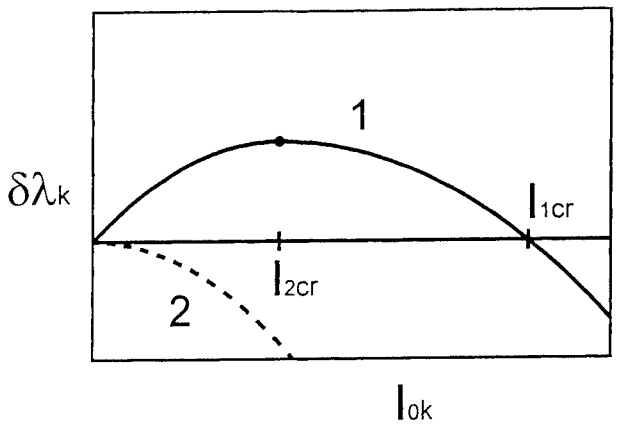

Figure 5: The amplification coefficient $\delta\lambda_k$ for k-th pulse as function its peak intensity I_{ok} (the solid curve corresponds to parameters θ, ξ from area 1 in Fig. 1, the dashed curve does to ones from area 2).

is described by horizontal lines in Fig. 4. When the peak intensities of pulses reach the value I_{cr2} then because of perturbations the peak intensity of one of them becomes less than I_{cr2}, and this pulse is suppressed. Thereafter the peak intensities of the remained pulses becomes greater than I_{cr2} because of energy balance. With further decreasing pump power the peak intensities of these pulses decrease and reach again the level I_{cr2} and then a successive pulse is suppressed, and so on. This process is determined the upper stepwise curve in Fig. 4.

In the case that the condition (2) breaks down (that corresponds to the area 2 in Fig. 1 and the dashed curve 2 in Fig. 5) the amplification coefficient for pulse λ_k decreases monotonously as the peak intensity I_{ok} increases. Accordingly, the smaller intensity of pulse entails its greater amplification. As result, new and new light pulses formed originally from spontaneous radiation (or from perturbations of stationary pulse) goes out to generation. This process lasts until the whole cavity is filled with the generated radiation (Fig. 2). In this case the passive mode-locking is not realized.

4. THE POTENTIAL FOR APPLICATIONS

The discovered multistability is of interest to storing of information in the form of sequence of ultrashort light pulses.

This multistability is likely may be used for preparation of the pulse sequence carrying information. Pulses can be added to or subtracted from this pulse sequence.

The described multistable system can be used for filtering of the pulse sequence. In such system the small-amplitude noise pulse are suppressed, and amplitudes of powerful pulses are equalized. In a similar manner, for this purpose the corresponding nonlinear elements can be inserted in communication line.

5. CONCLUSION

Thus, it has been found that in passive mode-locked lasers with a nonlinearity of losses decreasing as radiation intensity increases the phase-modulation instability can result in multiple

pulse operation, multistability, hysteresis phenomena, and also in suppression of passive mode-locking. The number of pulses in steady-state depends on the pump power and initial condition. The discovered peculiarities of passive mode-locking can be of interest for optical communications and information processing.

6. ACKNOWLEDGMENTS

This work has been supported by the Russian Fund for Fundamental Research (Grant 99–02–17117) and the State Science and Technology Program "Laser Physics" (Grant 3.20). The work of A.K. has been supported by ISSEP (grant № s'99–400).

7. REFERENCES

1. K.P.Komarov, "On the theory of steady-state ultrashort pulses in passively mode-locked lasers", *Opt. Spektrosc. (USSR)*, Vol.60, № 2, pp.231–235, 1986. (Optika i spektroskopiya, Vol.60, № 2, pp.379–383, 1986.)

2. H.A.Haus, "Theory of mode-locking with a fast saturable absorber", *J. Appl. Phys.*, Vol.46, № 7, pp.3049–3058, 1975.

3. C.P.Ausschnitt, "Transient evolution of passive mode locking", *IEEE J. Quant. Electron.*, Vol.13, № 5, pp.321–333, 1977.

4. K.P.Komarov, "On the theory of transient evolution of the passive mode-locking", *Optics Communications*, Vol.54, № 4, pp.233–235, 1985.

5. H.A.Haus, J.G. Fujimoto, E.P.Ippen, *J. Opt. Soc. Am. B*, Vol.8, p.2068, 1991.

6. A.K.Komarov, K.P.Komarov, "Pulse splitting in a passive mode-locked laser", *Optics Communication*, (to be published).

7. M.Lai, J.Nicholson, W.Rudolph, "Multiple pulse operation of a Ti:sapphire laser", *Optics Communication*, vol.142, pp.45–49, 1997.

8. C.Wang, W.Zhang, K.F.Lee, K.M.Yoo, "Pulse splitting in a self-mode-locked Ti:sapphire laser", *Optics Communication*, vol.137, pp.89–92, 1997.

Three-dimensional dissipative optical solitons – "laser bullets"

Nikolay N. Rosanov

199034, Research Institute for Laser Physics, Birzhevaya, 12, St.-Petersburg, Russia
Phone: (812) 328-10-93. Fax: (812) 328-58-91. E-mail: rosanov@ilph.spb.su

ABSTRACTS

Paper presents the results of theoretical study and numerical simulations of the laser bullets - three-dimensional dissipative optical solitons in continuous media with saturable resonance amplification and absorption, constant (non-resonant) absorption, and quadratic frequency dispersion. We have performed bifurcation analysis of stationary symmetric bullets, have determined conditions of their existence in dependence of frequency detunings, investigated possibility of existence of topological three-dimensional dissipative solitons, and studied different regimes of interaction of two laser bullets.

Keywords: optical solitons, dissipative solitons, optical and laser bullets, lasers with a saturable absorber.

1. INTRODUCTION

Three-dimensional optical solitons present not only purely scientific, but potential applied interest as natural units of information in optical information processing systems. Stability of conservative solitons in transparent media with saturating nonlinearity of refractive index was proved by Vakhitov and Kolokolov[1]. These solitons currently referred to as light bullets[2], have a continuous spectrum of parameters, including their maximum intensity. Therefore, under effect of noise the conservative soliton parameters change stochastically. Different type – the dissipative optical solitons – was predicted in optical nonlinear media and systems with considerable exchange of energy gain and losses[3-5], (see also reviews[6,7] and monograph[8]). Because of requirement of energetic balance, the dissipative solitons have a discrete spectrum of their main parameters, contrary to the case of conservative solitons. This feature results in suppression of noise and drift of parameters, which makes the dissipative solitons promising for application in the systems with special requirements to operation reliability. The three-dimensional dissipative optical solitons, or "laser bullets" were predicted in continuous media with saturable gain and losses and linear frequency dispersion[9,10] and demonstrated by means of numerical simulations in[11-13]. In the present paper, recent results of the laser bullets theoretical and numerical study are presented, including their bifurcation analysis and regimes of their interaction.

2. THE MODEL AND GOVERNING EQUATIONS

For formulation of the "laser bullets" theoretical model, the following factors are essential. First, it is ratio of the "bullet" sizes to the light wavelength in a linear medium that determines a measure of soliton nonparaxiality. As the main variant we consider fairly wide solitons and neglect nonparaxial phenomena; the latter ones are studied in [14]. The second factor is connected with the model of optical media, namely with the role of relaxation processes and finite width of spectral lines. These questions have been considered in up to present for 1D laser solitons only[15]. In the main variant we adopt the model of fast optical nonlinearity with a simplified account for relaxation and finite width of spectral lines (by introduction of effective diffusion coefficient d, which moreover can be neglected in many cases). Therefore, the main model corresponds to paraxial solitons in media with fast nonlinearity.

Under conditions indicated, approximation of paraxial equation for a slowly varying electric field E is appropriate. In dimensionless form it has the form

$$\frac{\partial E}{\partial z} - (i+d)\Delta_3 E = f(|E|^2)E. \qquad (1)$$

Here we introduced 3D Laplacian

Laser Optics 2000: Semiconductor Lasers and Optical Communication, Serguei A. Gurevich, Nikolay N. Rosanov, Editors, Proceedings of SPIE Vol. 4354 (2001) © 2001 SPIE · 0277-786X/01/$15.00

$$\Delta_3 = \frac{\partial^2}{\partial x^2} + \frac{\partial^2}{\partial y^2} + \frac{\partial^2}{\partial \tau^2} \tag{2}$$

and a complex function of nonlinearity f for a medium with a constant (no resonant) absorption and saturating (resonant) amplification and absorption, and quadratic frequency dispersion of refractive index

$$f(I) = -1 + \frac{g_0}{(1+i\Delta_g)(1+I)} - \frac{a_0}{(1+i\Delta_g)\left(1+bI\,\frac{1+\Delta_g^2}{1+\Delta_a^2}\right)}. \tag{3}$$

Radiation propagates mainly along the longitudinal axis z, x,y are the transverse coordinates, variable $\tau = t - z/v_g$ represents time in coordinate frame moving along the axis z with group velocity v_g, and it is scaled so that the coefficient of quadratic dispersion is equal to unity. Δ_g and Δ_a are frequency detunings, or differences between the radiation central frequency and central frequencies of spectral lines of amplification and absorption, correspondingly (in units of line width), g_0 and a_0 are linear coefficients of gain and absorption, b is a ratio of saturation intensities for amplification and absorption (intensity is expressed in units of amplification saturation intensity). Coefficient of non-resonant absorption is taken in Eq. (3) as unity because of scaling of the longitudinal coordinate z.

If we restrict our consideration by stationary spherically symmetric "bullets" only with the envelope of the form

$$E = A(r)\exp(-i\alpha z), \tag{4}$$

then Eq. (1) is reduced to an ordinary differential equation (ODE) for the radial function $A(r)$ and eigenvalue α – shift of soliton propagation constant

$$\frac{d^2A}{dr^2} + \frac{2}{r}\frac{dA}{dr} + \alpha A + \frac{1}{i+d} f(|A|^2)A = 0. \tag{5}$$

As mentioned above, unlike the conservative "light bullets" with a continuous spectrum of α, for the "laser bullets" this spectrum is a discrete one. Besides, the amplitude $A(r)$ is complex now. It is possible to depress ODE (5) by introduction of real amplitude and phase and using symmetry feature of the initial equation with respect to phase shift. To determine the stability of stationary solitons found in such a way, it is necessary to study corresponding linearized equations. It is possible for 1D and 2D solitons[8,12], but involves difficulties for 3D solitons. In the latter case the stability can be checked by direct solution of Eq. (1).

In the case of "laser bullets" the problem is multi-parameter and multi-dimensional ((3+1) problem). Dimensionality can be decreased in particular cases, when cylindrical or spherical field symmetry is realized. It is easier to find a structure with such symmetry and then to check its stability by solution of full Eq. (1).

The most effective way of numerical solution of Eq. (1) with (3+1) dimensionality is based on splitting method with use of the fast Fourier transform algorithm. This approach gives a possibility to determine dynamics of "bullets" formation, their stability, interaction, and so on. For the problems with depressed dimensionality mentioned above, other methods are appropriate. In particular, in the problem with cylindrical symmetry it is convenient to use field decomposition in terms of function system, including Bessel functions. For solution of ODEs (the case of spherical symmetry, Eq. (5)) it is sufficient to use the standard finite difference methods.

3. BIFURCATION ANALYSIS

To analyze spherically symmetric (in the space x,y,τ) stationary "laser bullets", we will use Eq. (5) for the case of zero frequency detunings (function $f(I)$ is real). Because we study the case of hard (threshold-like) excitation, total absorption has to be greater than gain for a weak signal. Therefore

$$f_0 = f(0) < 0. \tag{6}$$

Boundary conditions to Eq. (5) consist of requirement of finiteness of the amplitude A at $r = 0$ and sufficiently fast decay of A ($A(r) \to 0$) at $r \to \infty$. More precisely, for the field distributions of interest their asymptotic at infinity follows

from the equation itself with the replacement $f \to f_0 = \text{const}$

$$A = \frac{C}{r\sqrt{-\alpha + if_0}} \exp(-r\sqrt{-\alpha + if_0}), \quad r \to \infty . \tag{7}$$

Because the total phase is arbitrary, it is possible to take the constant C as real.

Phase arbitrariness permits to depress ODE (5). To do so, let us introduce real amplitude and phase

$$A(r) = a(r)\exp(i\theta(r)) \tag{8}$$

and real variables

$$p = \frac{1}{a}\frac{da}{dr}, \quad q = \frac{d\theta}{dr} \tag{9}$$

(we suppose that $a \neq 0$). Then we have the system of 3 real ODEs

$$\frac{da}{dr} = ap, \quad \frac{dp}{dr} = -p^2 + q^2 - 2\frac{p}{r} - \alpha, \quad \frac{dq}{dr} = -2pq - 2\frac{q}{r} + f(a^2). \tag{10}$$

For the spherically symmetric soliton the following requirements have to be held

$$p(0) = 0, \quad q(0) = 0 . \tag{11}$$

These conditions, jointly with the conditions at infinity (7), permit to find from Eqs. (10) both eigenvalues α and radial profiles of the "bullets" characteristics. This problem was solved numerically. To do so, some values of parameters α and C were fixed, and for sufficiently large distance $r = r_\infty$ the values a, p and q were defined by relations (8), (9). Then by the Runge-Kutta method of the 4th order system (10) was solved and the values $p(0)$ and $q(0)$ were determined (more exactly, because of singularity of Eqs. (10) at $r = 0$, numerical integration was performed from the two sides of the radial interval and matched at some intermediate value of r). Subsequent applying of two conditions (11) permits to determine parameters α and C.

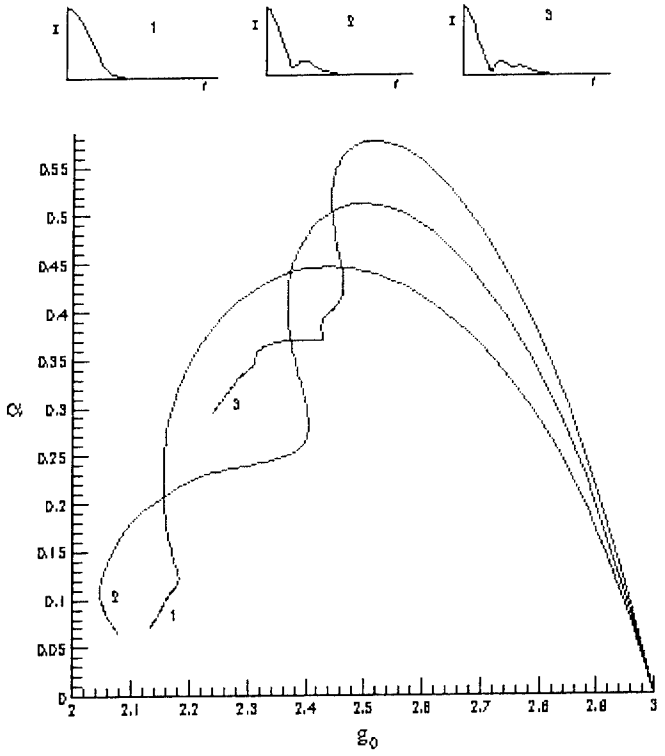

Fig. 1. Dependence of spectral parameter of symmetrical "laser bullet" α on linear gain coefficient g_0 for three types of localized structures (corresponding amplitude radial profiles are given in upper inserts)[15].

Results of calculations performed for parameters $a_0 = 2$ and $b = 10$, are given in Fig. 1. It turns out that there are a great number of branches (only three of them are shown in the figure) of symmetric localized structures with different type of amplitude radial profile (see the upper inserts at the figure). All the branches start from the same point on the plane α, g_0 ($\alpha = 0, g_0 = 1 + a_0 = 3$, that corresponds to the stability boundary of non-lasing mode, $A = 0$). As follows from the calculations, all the branches have a tendency to last in the same point corresponding to the limiting point of similar spiral for 1D and 2D laser localized structures). In this limiting point the width of localized structures tends to infinity, therefore the structure geometrical dimensionality is not essential.

Next step of the analysis is check of the stability of localized structures found. It was done by numerical solution of Eq. (1), with substitution for $z = 0$ of corresponding solution of system (10) with additional small asymmetric perturbation. It was found that only for one of the branches (with a monotonic radial decrease of amplitude) there is interval corresponding to stable regimes[15].

4. EFFECT OF FREQUENCY DETUNINGS

In the previous study we supposed that frequency detunings $\Delta_a = \Delta_g = 0$. In Fig. 2 we present the boundaries of the "laser bullets" existence and the stability on the plane of two parameters – detunings Δ_g and Δ_a between radiation frequency and central frequencies of spectral lines of amplification and absorption. Single bullets are stable inside the domain marked by label S including case of absence of detunings $\Delta_a = \Delta_g = 0$. When the parameters change crossing stability boundary, two different scenario of stability lost were found. Near the boundary part marked by C, the bullet collapse and disappears, while there are also cases of the bullet unrestricted widening marked by B.

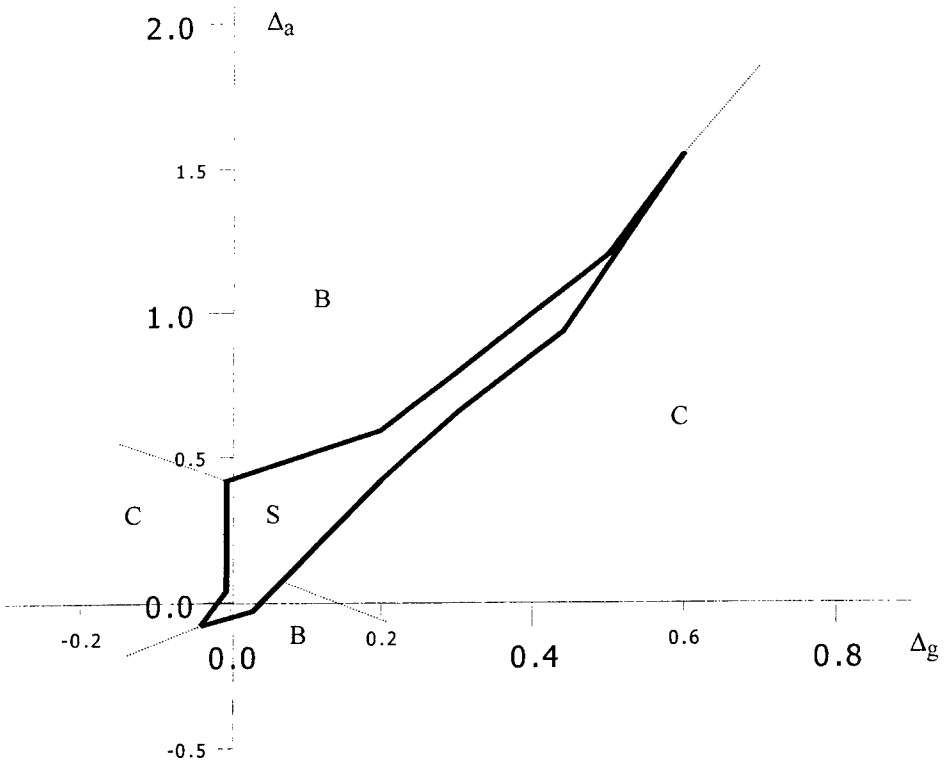

Fig. 2. Domain of stability S of the "spherical laser bullets" on the plane of frequency detunings Δ_g, Δ_a for $g_0 = 2.156$, $a_0 = 2$, $b = 10$, $d = 0$. C is the domain of soliton collapse, B is the domain of their unrestricted widening[15].

5. TOPOLOGICAL LASER BULLETS

In the numerical simulations in this section we fix the parameters $\Delta_a = \Delta_g = 0$, $d = 0$, $a_0 = 2$ and $\beta = 10$. The field envelope of a single stationary laser bullet has the form

$$E^{(3.0)}(x, y, \tau, z) = E^{(3.0)}(x, y, \tau)\exp(-i\alpha_{3.0} z). \tag{12}$$

The localized solution of Eq. (1) in the form of the topological soliton was found near the "Maxwellian value" of the gain, where velocity of switching waves $v = 0$ [6,8]. It can be described as

$$E_t(r, \varphi, \tau, z) = E_t(r, \tau)\exp(i\varphi)\exp(-i\alpha_t z), \quad x = r\cos\varphi, \quad y = r\sin\varphi\ . \tag{13}$$

According to (13), if one follows round the point $x = y = 0$ in the plane x,y along a reserved contour the field phase changes on 2π (topological charge $m = 1$), in the central point of the topological soliton the field turns into zero. It turned out that topological (toroidal) soliton exists only for such values of the parameter g_0 when the symmetric 2-dimensional soliton exists, satisfying to equation

$$\frac{\partial E}{\partial z} = i\Delta_2 E + f(|E|^2)E, \quad \Delta_2 = \frac{\partial^2}{\partial x^2} + \frac{\partial^2}{\partial y^2}. \tag{14}$$

Eq. (14) is the same equation as Eq. (1), but without the variable τ. Solution (13) was obtained by fixing field azimuthal dependence, i.e. by exclusion azimuth perturbations. The intensity distribution of radiation in various sections of the topological soliton is shown in Fig. 3. One may say, that the topological (toroidal) soliton is the 2-dimensional soliton, prolonged into 3-dimensional space and bended into the ring (toroid), with matched phase shifts and local field profiles.

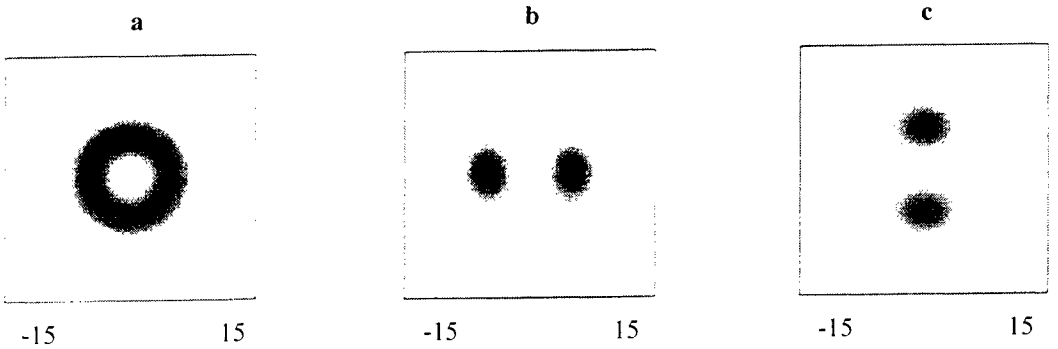

Fig. 3. Intensity profiles of stationary topological (toroidal) soliton. a: xy - section ($\tau = 0$), b: $x\tau$ - section ($y = 0$), c: $y\tau$ - section ($x = 0$), $g_0 = 2.11$ [16].

Let's remind that the topological soliton was obtained by fixing azimuthal dependence of the field. The numerical simulation shows that even weak perturbations with another azimuthal dependence destroy such soliton, so the topological solitons are unstable. After switching-on of perturbations, the topological soliton is preserved during quite a large interval of z. Then it decays to "non-topological" structures, which disappear soon, as it is shown in Fig. 4, since the fundamental solitons do not exist as localized solutions of Eq. (1) for $g_0 = 2.11$.

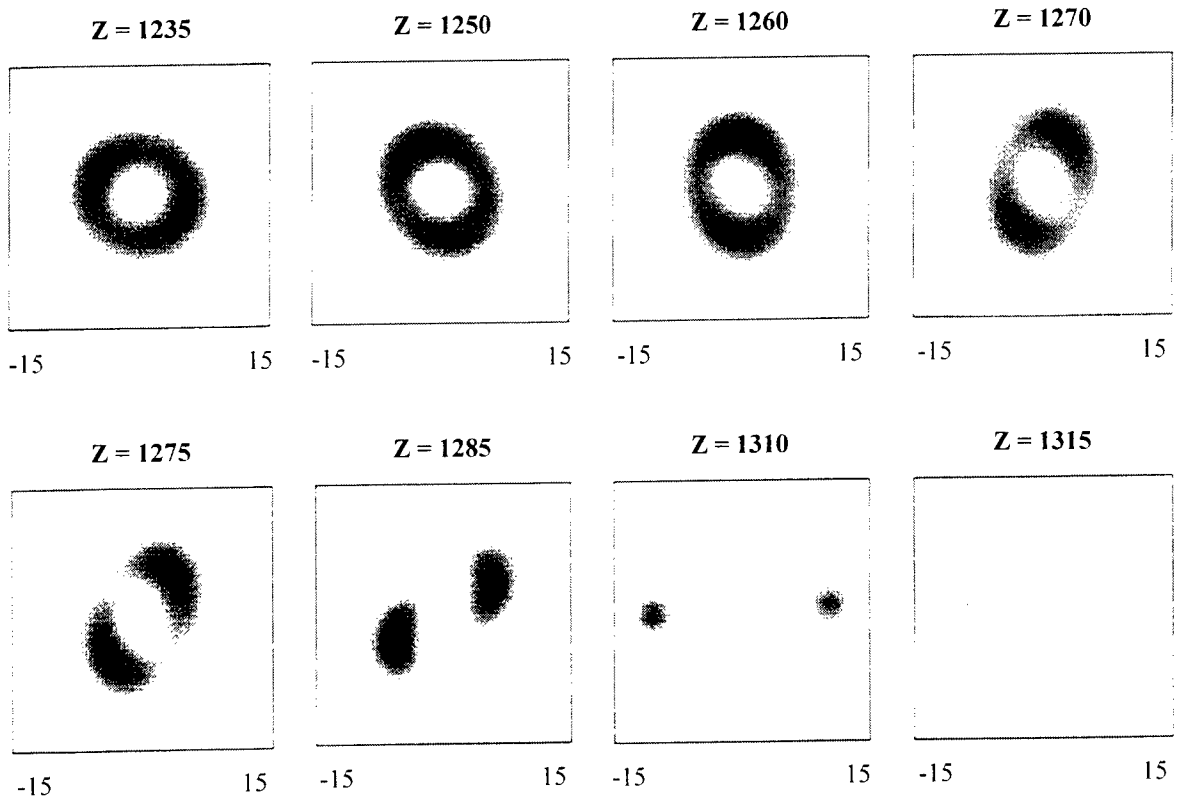

Fig. 4. Intensity profiles for various values of the longitudinal coordinate z for decay of 3-dimensional topological soliton (xy – section, $\tau = 0$, $g_0 = 2.11$)[16].

6. INTERACTION OF TWO LASER BULLETS

If the distance between centers of bullets exceeds significantly theirs characteristic width then interaction of bullets is negligibly small. So the field envelope of two laser bullets moving one towards another with relative velocity $2v$ (in lateral direction) has the following form:

$$E^{(2)}(x,y,\tau,z) = E^{(-x_0,v)}(x,y,\tau,z) + E^{(x_0,-v)}(x,y,\tau,z)\exp(i\theta), \tag{15}$$

where

$$E^{(x_0,v)}(x,y,\tau,z) = E^{(3.0)}(x - x_0 + vz, y, \tau, z)\exp(-ivz/2)\exp\left[-i\left(\alpha_{3.0} + \frac{v^2}{4}\right)z\right], \tag{16}$$

and the field envelope of a single stationary laser bullet has the form

$$E^{(3,0)}(x,y,\tau,z) = E^{(3.0)}(x,y,\tau)\exp(-i\alpha_{3.0}z). \tag{17}$$

For the main (fundamental) laser bullet the function $E^{(3,0)}(x,y,\tau)$ is spherically symmetric with appropriate scaling of the coordinates.

The result of collision depends on velocity v most of all, and also it depends on gain g_0 and phase difference θ. The following typical scenarios of collision are obtained (other parameters are fixed as in the previous section):

1. passing of "bullets" one through another $(g_0 = 2.156, v = 2.0, \theta = 0)$;
2. repulsion $(g_0 = 2.156, v = 1.0, \theta = \pi)$;

3. generation of a new (third) "bullet" $(g_0 = 2.156, v = 1.0, \theta = 0)$;
4. generation of switching waves in result of the collision, with progressive filling out all the space by radiation $(g_0 = 2.16, v = 1.0, \theta = 0)$.

Scenarios 1-3 are not unexpected; the similar regimes were obtained earlier for 1-dimensional and 2-dimensional solitons[6,8]. The most non-trivial results of collisions – scenarios 3 and 4 – are represented on Fig. 5. Scenario 4 (formation and propagation of switching wave after collision) was obtained for the first time for 3-dimensional solitons. The existence of such solution may be explained as follows. The parameter value $g_0 = 2.16$, for which the switching wave is generated, exceeds significantly the "Maxwellian value" $g_0 \approx 2.111$, for which the velocity of switching wave is equal to zero[6,8]. For $g_0 = 2.16$, 1-dimensional and 2-dimensional localized solutions do not exist really.

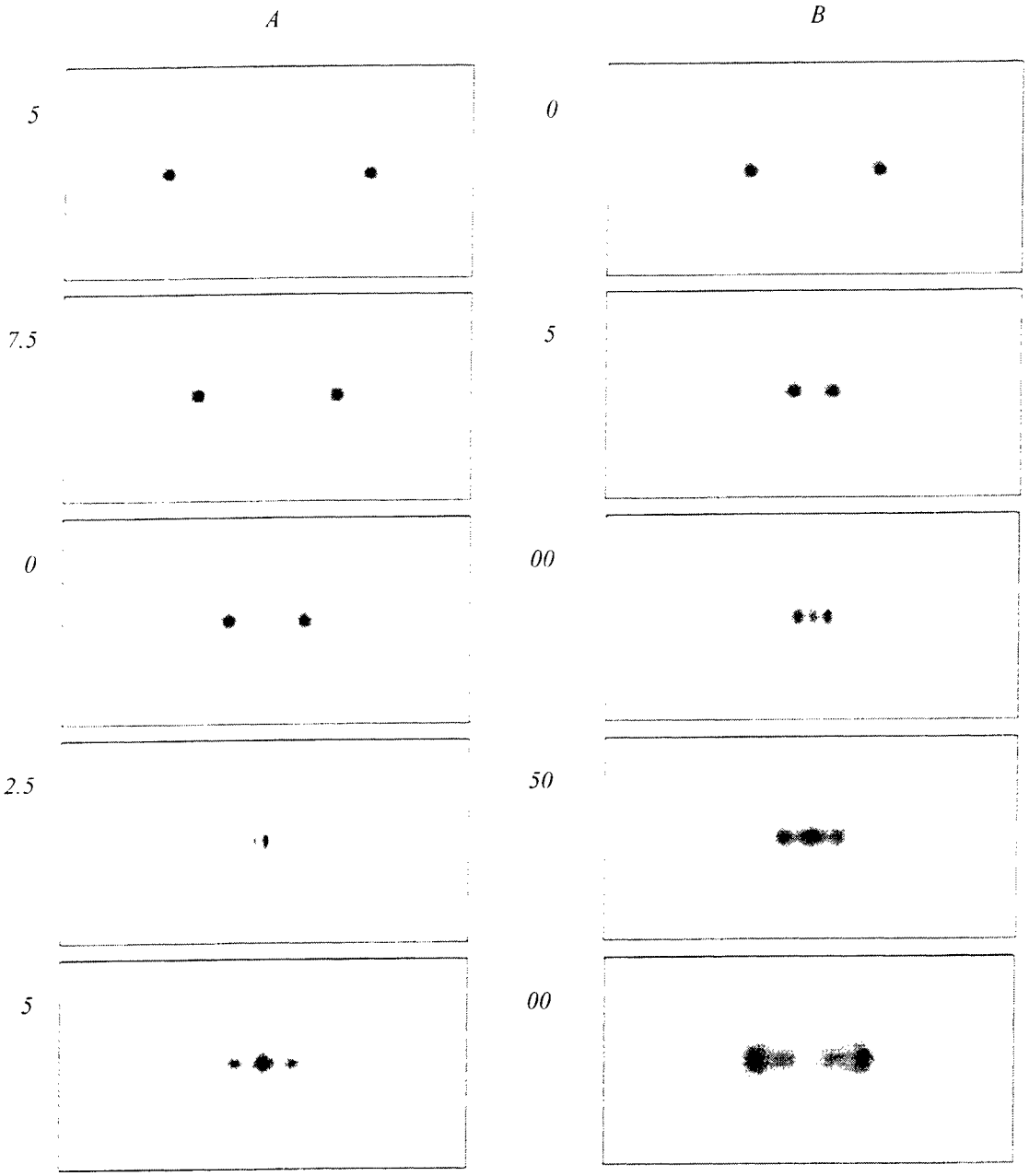

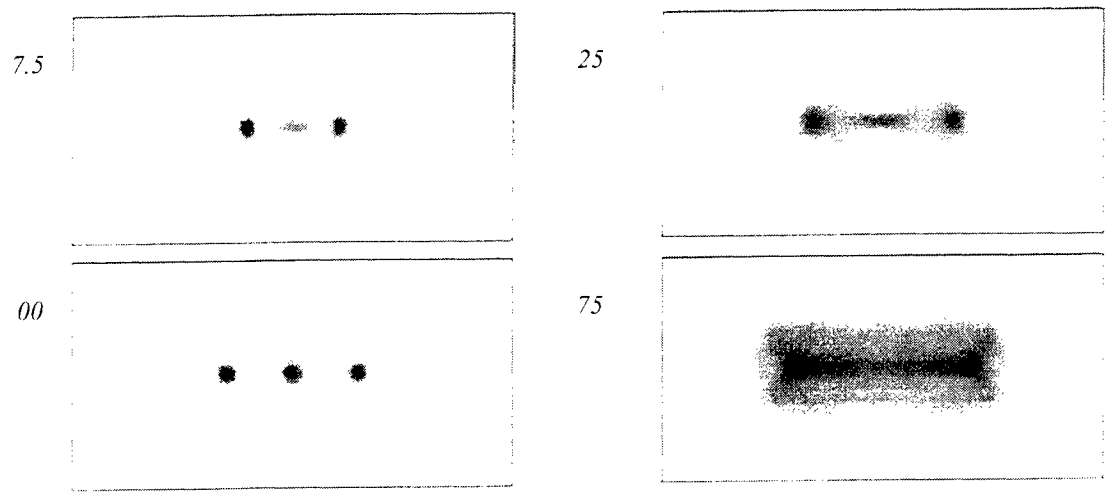

Fig. 5. Intensity distributions in the section $x\tau$ $(y = 0)$ for various values of longitudinal coordinate z for two scenarios of interaction of two laser bullets: A – generation of 3rd soliton, B - generation of a switching wave[16].

7. CONCLUSION

We have performed further theoretical analysis and numerical simulations of three-dimensional dissipative optical solitons – the "laser bullets". The results confirm possibility to form such the solitons in a continuous medium with constant (non-resonant) absorption, saturable (resonant) absorption and gain, and quadratic frequency dispersion. Bifurcation analysis reveals existence of a number of branches of localized solutions of the governing equation with different radial shape of the envelope, but only one of the branches includes stable solitons. Requirements on the frequency detunings are determined necessary for existence of stable laser bullets. Regimes of interaction of two laser bullets were investigated that include a new scenario with formation of switching wave.

Among other topics, we could mention non-paraxial effects[14], which are important for extremely narrow laser bullets, and effect of finite relaxation rates[17-19], when new types of dissipative solitons arise. These effects can be important for the laser bullets also, and they will be the subjects of further investigations. Further study is necessary also for choice of the concrete medium with features described above that are optimal for experimental demonstration and investigations of the laser bullets.

ACKNOWLEDGEMENTS

In the paper, results are presented obtained jointly with S. V. Fedorov, N. A. Kaliteevskij, A. N. Shatsev, N. A. Veretenov, and A. G. Vladimirov. The work was supported by the ISTC (project # 666) and INTAS (grant 97-0581).

REFERENCES

1. N.G.Vakhitov, A.A.Kolokolov. Izv. Vyssh. Uchebn. Zaved., Radiofiz. **16** (1973) 1020.
2. Y.Silberberg. Opt. Letters **15** (1990) 1282.
3. N.N.Rosanov, G.V.Khodova. Opt.&Spectr. **65** (1988) 1375.
4. N.N.Rosanov, A.V.Fedorov, G.V.Khodova. Phys. Stat. Sol. B **150** (1988) 545.
5. N.N.Rosanov, S.V.Fedorov. Opt.&Spectr. **72** (1992) 1394.
6. N.N.Rosanov. Progress in Optics **35** (1996) 1.
7. N.N.Rosanov. Uspekhi Phys. Nauk, **170** (2000) 462.
8. N.N.Rosanov. Optical bistability and hysteresis in distributed nonlinear systems. Moscow, Nauka, PhysMathLit, 1997.

9. N.N.Rosanov, G.V.Khodova. Opt.&Spectr. **76** (1994) 621.
10. N.N.Rosanov. Opt.&Spectr. **81** (1996) 276.
11. N.A.Kaliteevskii, N.N.Rosanov, S.V.Fedorov. Opt.&Spectr. **85** (1998) 485.
12. A.G.Vladimirov, S.V.Fedorov, N.A.Kaliteevskii, G.V.Khodova, N.N.Rosanov. J. Opt. B: Quantum and Semiclass. Opt. **1** (1999) 101.
13. D.Pieroux, S.V.Fedorov, N.N.Rosanov, P.Mandel. Europhys. Letters **49** (2000) 322.
14. N.N.Rosanov. Opt.&Spectr. **89** (2000) No 6.
15. N.A.Veretenov, A.G.Vladimirov, N.A.Kaliteevskii, N.N.Rosanov, S.V.Fedorov, A.N.Shatsev. Opt.&Spectr. **89** (2000) No 3.
16. N.A.Kaliteevskii, N.N.Rosanov. Opt.&Spectr. **89** (2000) 623.

Pulse pair propagation under conditions of induced transparency: adiabatic approximation

V. G. Arkhipkin[a] and I. V. Timofeev[b]

[a]L.V.Kirensky Institute of Physics, Krasnoyarsks 660036 Russia

[b]Krasnoyarsk State University 660041 Russia

ABSTRACT

The features of spatial and temporal evolution of two short laser pulses propagating in three-level medium under conditions of coherent population trapping and adiabatic population transfer is investigated in adiabatic approximation. It is shown that in both cases pulses can penetrate into a medium at a distance considerably exceeding the length of linear absorption of a single weak probe pulse in absence of a coupling pulse at adjacent transition. The difference of spatial and temporal evolution of level populations in processes of coherent population trapping and adiabatic population transfer is demonstrated. Also we show that the concept of dressed-field pulses is consequence of Manley-Raw relation.

Keywords: adiabatic population transfer, coherent population trapping, electromagnetically induced transparency, counterintuitive pulse sequence

1. INTRODUCTION

The possibility to render optically thick media transparent for coherent laser radiation via electromagnetically induced transparency (EIT) gained considerable interest over last years. The EIT is achieved using quantum interference effects such as nonlinear interference effect,[1] coherent population trapping (CPT),[2,3] adiabatic population transfer (APT).[4] These effects cardinally change optical characteristics of a matter and allow to manipulate them. Many interesting proposed applications were in part experimentally realized.[2–5]

Quantum interference phenomena lead to interesting and curious effects at propagation of laser pulses in resonant three-level medium. The pulses propagating in conditions of EIT were investigated.[6–11] As a rule, the situations are considered, when both pulses have an identical form, and their duration is more than the relaxation time of an intermediate resonant state (matched pulses[6]; dressed field pulses[7,8]) or the duration of a coupling radiation considerably exceeds the duration of probe (adiabatons[10,11]).

The process of APT is closely connected to the formation of trapped states (and therefore with CPT) and produces complete population transfer between two quantum states of atom or molecule. Such states lead to dark resonances when the sum of frequencies of two radiation fields is tuned to the two-photon resonance in a three-level system. The temporal evolution of APT is well investigated theoretically and experimentally.[4,12–16]

Here we study the propagation of two short laser pulses in resonant three-level medium under conditions of CPT and APT, using the adiabatic approximation. It is assumed that envelopes of pulses satisfy the criterion of adiabaticity[3]:

$$|G_{1,2}|T_{1,2} \gg 1, \tag{1}$$

The Rabi frequencies $G_{1,2}$ are of comparable strength; $T_{1,2}$ are the durations of interacting pulses.

This adiabaticity condition can be achieved for strong enough pulses even if the pulse duration is short ($\Gamma_{ij}T_{1,2} << 1$).[3,15] Physically, this means that the pulse envelopes should vary slowly in a time interval equal to the reciprocal of the effective Rabi frequency $G = \sqrt{|G_1|^2 + |G_2|^2}$. The condition (1) can be fulfilled for cases of pulse switching depicted on Fig.1b,c. An interaction of pulses with such temporal configuration can lead to CPT. The effect of APT

Correspondence: Email: lco@cc.krascience.rssi.ru; Telephone: (3912)494613; Fax: (3912)438923

Laser Optics 2000: Semiconductor Lasers and Optical Communication, Serguei A. Gurevich, Nikolay N. Rosanov, Editors, Proceedings of SPIE Vol. 4354 (2001) © 2001 SPIE · 0277-786X/01/$15.00

takes place for pulses of counterintuitive sequence (Fig.1b), when coupling pulse with envelope $G_2(t)$ is switched on and off earlier than the probe pulse $G_1(t)$.

For both cases the theoretical model consists of a system of coupled Schrödinger equations and reduced wave equations, describing simultaneously temporal and space evolution of atomic system and radiation. In adiabatic approximation (1) the analytic solution is constructed. It is shown, that the probe pulse can propagate over a distance considerably exceeding the length of linear absorption, but finally it is completely transferred into the coupling pulse. The difference of spatial and temporal evolution of level population in processes of CPT and APT is also demonstrated.

2. BASIC EQUATIONS

We consider the three-level Λ system shown schematically in Fig.1a. Transition $|2\rangle$-$|1\rangle$ is driven by a strong field with Rabi frequency $G_2(t)$ (coupling field). The second strong field (probe) with Rabi frequency $G_1(t)$ is applied on the transition $|0\rangle$-$|1\rangle$. The waves are assumed to be plane with time envelopes, satisfying the adiabatic criterion (1). They propagate in the medium in the same direction. All atoms are initially in the ground state $|0\rangle$. The intermediate state $|1\rangle$ is one-photon resonant to both fields. Each field interacts only with the correspondent transition.

The equations that describe the spatial and temporal evolution of two pulses in a medium of three-level atoms of Λ-configuration are:

$$\frac{\partial b_0}{\partial \tau} = iG_1^* b_1 \exp(-ik_1 z), \quad \frac{\partial b_2}{\partial \tau} = iG_2^* b_1 \exp(-ik_2 z), \frac{\partial b_1}{\partial \tau} = iG_1 b_0 \exp(ik_1 z) + iG_2 b_2 \exp(ik_2 z), \tag{2}$$

$$\frac{\partial G_1}{\partial z} = iK_1 b_1 b_0^* \exp(ik_1 z), \quad \frac{\partial G_2}{\partial z} = iK_2 b_1 b_2^* \exp(ik_2 z). \tag{3}$$

Here $b_{0,1,2}$ - the probability amplitudes of states $|0>, |1>$ and $|2>$, respectively; $K_{1,2} = \pi\omega_1 |d_{10,12}|^2 N/c\hbar$ - the propagation coefficients; N - the atom concentration, d_{ij} - the dipole transition matrix elements; $k_{1,2}$ - the absolute values of wave vectors of interacting waves in vacuum; $\tau = t - z/c$ - the local time. All the dynamical variables are functions of both z and τ.

In terms $a_0 = b_0 \exp(ik_1 z)$, $a_2 = b_2 \exp(ik_2 z)$, $a_1 = ib_1$, the equations (2) and (3) can be written as:

$$\frac{\partial a_0}{\partial \tau} = G_1^* a_1, \quad \frac{\partial a_2}{\partial \tau} = G_2^* a_1, \quad \frac{\partial a_1}{\partial \tau} = -G_1 a_0 - G_2 a_2, \tag{4}$$

$$\frac{\partial G_1}{\partial z} = K_1 a_1 a_0^*, \quad \frac{\partial G_2}{\partial z} = K_2 a_1 a_2^*. \tag{5}$$

In adiabatic approximation the solution of the system (4) has the form:

$$a_0 \simeq \frac{G_2}{G}, \quad a_2 \simeq -\frac{G_1}{G}, \quad a_1 \simeq \frac{1}{G_1}\frac{\partial (G_2/G)}{\partial \tau} \simeq -\frac{1}{G_2}\frac{\partial (G_1/G)}{\partial \tau}, \tag{6}$$

where $G = \sqrt{G_1^2 + G_2^2}$. In the given approximation this solution does not depend on specific form of pulses.

Substituting the solution (6) in the field equations (5), we obtain a system of the connected nonlinear equations:

$$\frac{\partial G_1}{\partial z} = -(K_1/G)\frac{\partial (G_1/G)}{\partial \tau}, \qquad \frac{\partial G_2}{\partial z} = -(K_2/G)\frac{\partial (G_2/G)}{\partial \tau}. \tag{7}$$

If $K_1 = K_2 = K$, the equations (7) can be solved analytically, for example, by characteristic method. The exact solutions are:

$$G_1 = G(0,\tau)\frac{G_1(0,p)}{G(0,p)}, \qquad G_2 = G(0,\tau)\frac{G_2(0,p)}{G(0,p)}. \tag{8}$$

Here $p = Z^{-1}(Z(\tau) - z)$, $Z(\tau) = K^{-1}\int_{-\infty}^{\tau} d\tau' G^2(0,\tau')$, $Z^{-1}(z)$ - inverse function of $Z(\tau)$.

It is seen from (8), that the sum $G_1^2(\tau,z) + G_2^2(\tau,z)$ does not depend on coordinate z and is equal to $G^2(\tau,0) = G_1^2(\tau,z=0) + G_2^2(\tau,z=0)$. It is not difficult to show that $\sqrt{G_1^2(\tau,z) + G_2^2(\tau,z)}$ coincides with definition of dressed field pulses[7,8]: $G_- = a_0 G_2 - a_2 G_1$. Thus, in this case the pulses may be identified as dressed field states. Let's notice that the other combination $G_+ = a_0 G_1 + a_2 G_2 \equiv 0$ (see also[7]). When $K_1 \neq K_2$ it is not true. However in both cases the Manley-Raw relation take place, because its formulation is more general.

One can show from (7), that the value $K_2 G_1^2(\tau,z) + K_1 G_2^2(\tau,z)$ does not depend on coordinate z and is equal to $\tilde{G}^2(\tau) = K_2 G_1^2(\tau,z=0) + K_1 G_2^2(\tau,z=0)$. It is not difficult to show that $K_2 G_1^2(\tau,z) + K_1 G_2^2(\tau,z) = n_1(\tau,z) + n_2(\tau,z) = F(\tau)$ - does not depend on z, where $n_{1,2}(\tau,z)$ is the photons density. It is the Manley-Raw relation. Let's mark, that an integral $\int_{-\infty}^{\infty} d\tau [K_2 G_1^2(\tau,z) + K_1 G_2^2(\tau,z)] = constant$.

3. DISCUSSION OF RESULTS

3.1. The case of coherent population trapping

For demonstration of the main features of propagation of pulses under conditions of CPT we used gaussian envelope at the entrance of the medium: $G_{1,2}(\tau) = G_{1,2}^0 \exp(-\tau^2/2T_{1,2}^2)$, $T_1 > T_2$ (fig. 1,b). Here the coupling pulse with envelope $G_2(t)$ switches on earlier and switches off later than the probe pulse $G_1(t)$.

The expression for a_1 can be reduced in a form:

$$a_1 = (G_2\dot{G}_1 - G_1\dot{G}_2)/G^3. \tag{9}$$

It is easy to show, that in approximation (1) $|a_1| << 1$, i.e. the population of an intermediate state $|1\rangle$ is negligible during all time of interaction with pulses. The last physically means, that the resonant absorption of pulses is low. It is the electromagnetically induced transparency. Thus pulses will propagate over the distance essentially exceeding the length of linear absorption of a single weak probe radiation.

The population is distributed between initial $|0>$ and final $|2>$ states. So, there is an approximate equality:

$$|a_0|^2 + |a_2|^2 \simeq 1. \tag{10}$$

And solution for probability amplitudes $a_{0,2}$ is convenient to be presented as:

$$a_0 = \cos\theta, \qquad a_2 = -\sin\theta, \tag{11}$$

where $\cos\theta = \frac{G_2}{G}$, $\sin\theta = \frac{G_1}{G}$.

It is interesting to remark, that the equality (10) also reflects the fact, that atoms are trapped in a state of coherent population trapping with probability amplitude $a_- = (G_2/G)a_0 - (G_1/G)a_2 = \cos(\theta)a_0 - \sin(\theta)a_2 = 1$. Thus the reduction of resonance absorption of interacting pulses is due to coherent population trapping.

The atomic coherence of nonallowed transition $|0\rangle$-$|2\rangle$ $\rho_{20} = a_2 a_0^*$ is

$$\rho_{20} = -\frac{G_1 G_2}{G^2} = -\frac{1}{2}\sin 2\theta \tag{12}$$

If pulses have the same amplitude, then in the time moment $\tau = 0$ it reaches value $\rho_{20}(\tau = 0) = -\frac{1}{2}$ corresponding to the maximum coherence.

In Fig.2 and Fig.3 the level populations $\rho_{0,2} = |a_{0,2}|^2$ and the atomic coherence $|\rho_{20}| = |a_2 a_0^*|$ versus time and length of medium are shown. It is seen that populations are varied nonmonotonously with the length. This spatial dependence is similar to the temporal dependence. Thus, we can speak about spatio-temporal analogy at propagation of such pulses. Fig.3 demonstrates that maximal atomic coherence is conserved over the length of a medium, considerably exceeding the length of linear absorption of a single probe pulse.

Fig.4 shows the normalizes Rabi frequencies $g_{1,2} = G_{1,2}T_1$ versus time and length of a medium calculated from (8). The dependencies illustrate that in resonant medium the pulses can propagate over a distance, which is several orders greater than the length of the linear absorption of weak probe pulse.

3.2. The case of adiabatic population transfer

Here we also used gaussian pulses, but with the counterintuitive sequence: $G_1(\tau) = G_1^0 \exp(-\tau^2/2T^2)$, $G_2(\tau) = G_2^0 \exp[-(\tau - \tau_0)^2/2T^2]$, τ_0 - the delay time between pulses. It follows from (6) that in the tail of the coupling pulse $|a_0|^2 \simeq 0$, and $|a_2|^2 \simeq 1$. In other words, the population of the ground state $|0\rangle$ is transferred into state $|2\rangle$.

In Fig.5 the normalized Rabi frequencies $g_{1,2} = G_{1,2}T$ versus time and depth of penetration of radiation in a medium calculated from formula (8) are shown. They demonstrate, that in a resonant medium the probe pulse can propagate over a distance, which is several orders greater than the length of linear absorption of weak probe pulse. However the energy of the leading edge of the probe pulse is partially absorbed, and the energy of the coupling pulse is amplified. The absorbed energy is used for the adiabatic transfer of the atomic system to an excited state and for amplification of the coupling pulse. Eventually the probe pulse is completely transferred into the coupling pulse.

In Fig.6 the populations $\rho_{0,2} = |a_{0,2}|^2$ versus time and length of medium are shown. APT thus makes it possible to achieve practically 100% inversion on dipole-forbidden transition in extensive media.

In both cases obtained analytic results coincide with the results of the numeric analysis of system of equations (4) and (5) (see also[17]).

4. CONCLUSION

We have presented the results of analytical calculation of spatial propagation of short laser pulses pairs in absorbing three-level media under conditions of coherent population trapping and adiabatic population transfer. The results show that in both cases a transparency can be maintained over several thousands one-photon absorption lengths. But complete transfer of energy from probe pulse to coupling pulse takes place at some pre-defined optical length. When the propagation coefficients are equal, i.e. $K_1 = K_2$, the process can be understood in terms of dressed fields pulses. For the case $K_1 \neq K_2$ it is not true, but the pulses comply with Manley-Raw relation which have more general character than conception of dressed fields pulses.

It is shown also how the population in initial and target states can evolve spatially, i.e. in the course of pulses propagation. APT leads to practically complete inversion at dipole-forbidden transition at a characteristic propagation distance of the probe pulse which can be over several thousands Beers lengths. In the case of CPT the maximal atomic coherence is also maintained on the large length. In this sense our results provide additional information on EIT propagation in case of short pulses with duration much less than atomic relaxation times.

REFERENCES

1. S.G.Rautian, A.M.Shalagin, *Kinetic Problem of Nonlinear Spectroscopy* (North-Holland: Amsterdam, 1991); A.K.Popov, *Vvedenie v nelineinuyu spectroscopiyu* (Novosibirsk: Nauka, 1983).
2. B.D.Agap'ev, M.B.Gornyi, B.G.Matisov, Yu.V.Rozhdestvensky, Usp. Fiz. Nauk **163**, 1 (1993).
3. E.Arimondo, in *Progress in Optics* ed by Wolf (Elsevier, Amsterdam, 1996), **35**, p.257.
4. K.Bergman, H.Theuer, B.W.Shore, Rev.Mod.Phys., **70**, 1003 (1998).
5. S.E.Harris, Physics Today **50**, No.7, 36 (1997).
6. S.E.Harris, Phys. Rev. Lett., **72**, 525 (1994).
7. J.H.Eberly, M.L.Pons, H.R.Hag, *Phys. Rev. Lett.* **72**, 56, (1994).
8. J.H.Eberly, Quantum Semiclass. Opt. **7**, 373 (1995).
9. N.Wang, H.Rabit,. Phys. Rev. A **51**, 5029, (1995).
10. J.H.Eberly, A.Rahman, Phys. Rev. Lett. **76**, 3687, (1996).
11. M.Fleischhauer, A.S.Manka, Phys. Rev. A **54**, 794 (1996).
12. L.V. Kuz'min, V.N.Sazonov, ZhETF, **79**, 1759, 1980.
13. J.Oreg, F.T.Hioe, J.H.Eberly, Phys. Rev. A. **29**, 690 (1984).
14. F.T.Hioe, Phys. Letters. **99A**, 150 (1983).
15. J.R.Kuklinski, U.Gaubats, F.T.Hioe, K.Bergman, Phys. Rev. A. **40**, 6741 (1989).
16. U.Gaubats, P.Rudecki, S.Schiemann and K.Bergman, J.Chem Phys. **92**, 5363 (1990).
17. V.G.Arkhipkin, D.V.Manushkin, V.P.Timofeev. Quantum Electronics, **28**, 1055 (1998).
18. L.Allen, J. Eberly. *Optical resonance and two-level atoms* (New York, 1975).

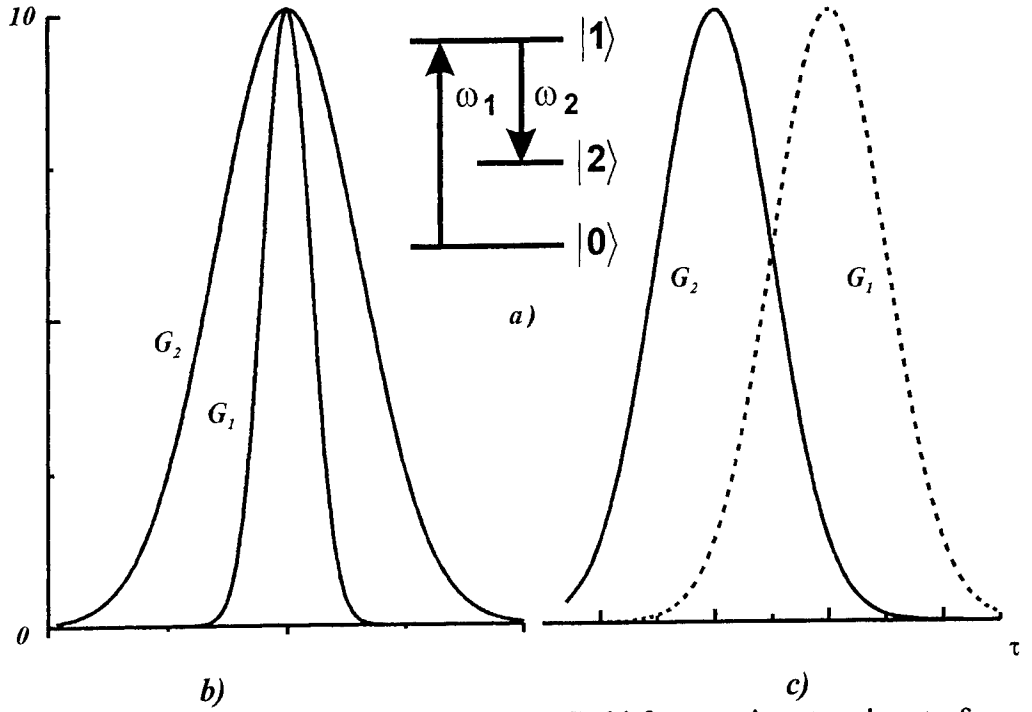

Fig.1. Configurations of energy levels in atom (a), Rabi frequencies at an input of a medium (b,c). $\omega_{1,2}$ — carrier frequencies of probe G_1 and coupling G_2 pulses, consequently: (b) — case of coherent population trapping (the duration of coupling pulse is more, than the duration of probe ($T_2 > T_1$)), (c) - case of adiabatic population transfer.

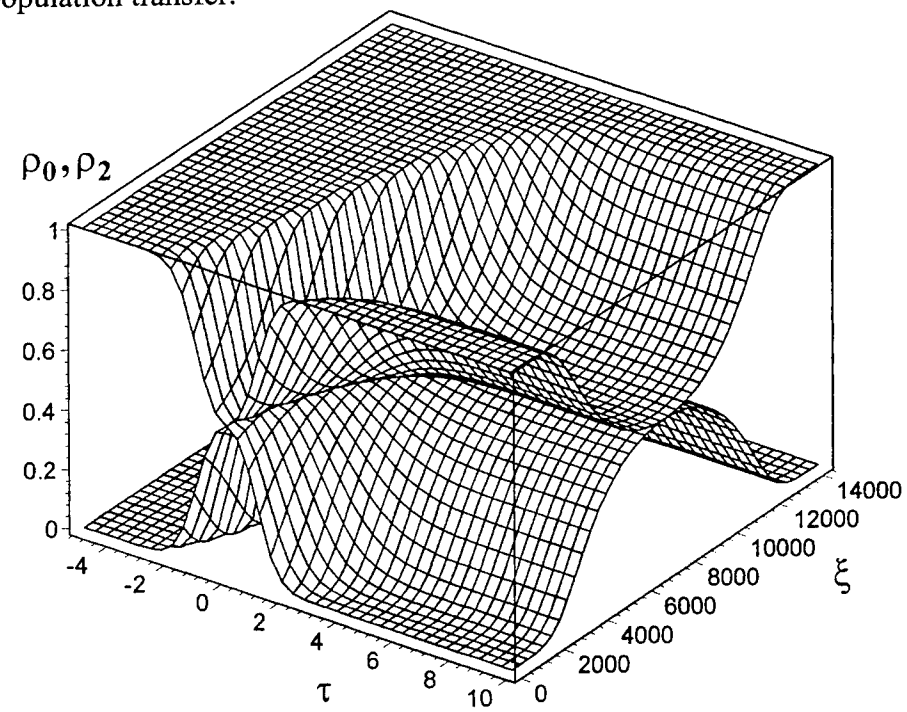

Fig.2. The dependencies of level populations $\rho_{0,2} = |a_{0,2}|^2$ from the time and the depth of penetration of radiation into a medium. The parameters are as follows: $T_2/T_1 = 3$, $G^0_{1,2}T_1 = 10$, $\Gamma_{10}T_1 = 0.1$, $\Gamma_{12}T_1 = 0.1$, $K_1 = K_2$.

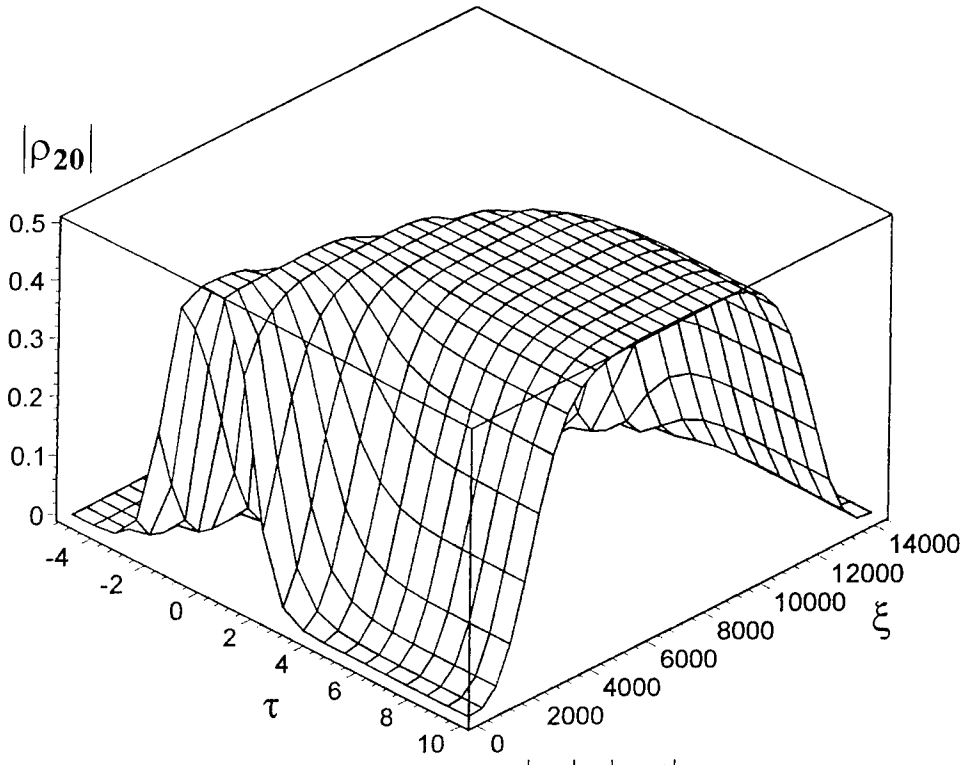

Fig.3. The dependencies of an atomic coherence $|\rho_{20}| = |a_2 a_0^*|$ from the time and the length of a medium. The parameters are the same as in fig.2

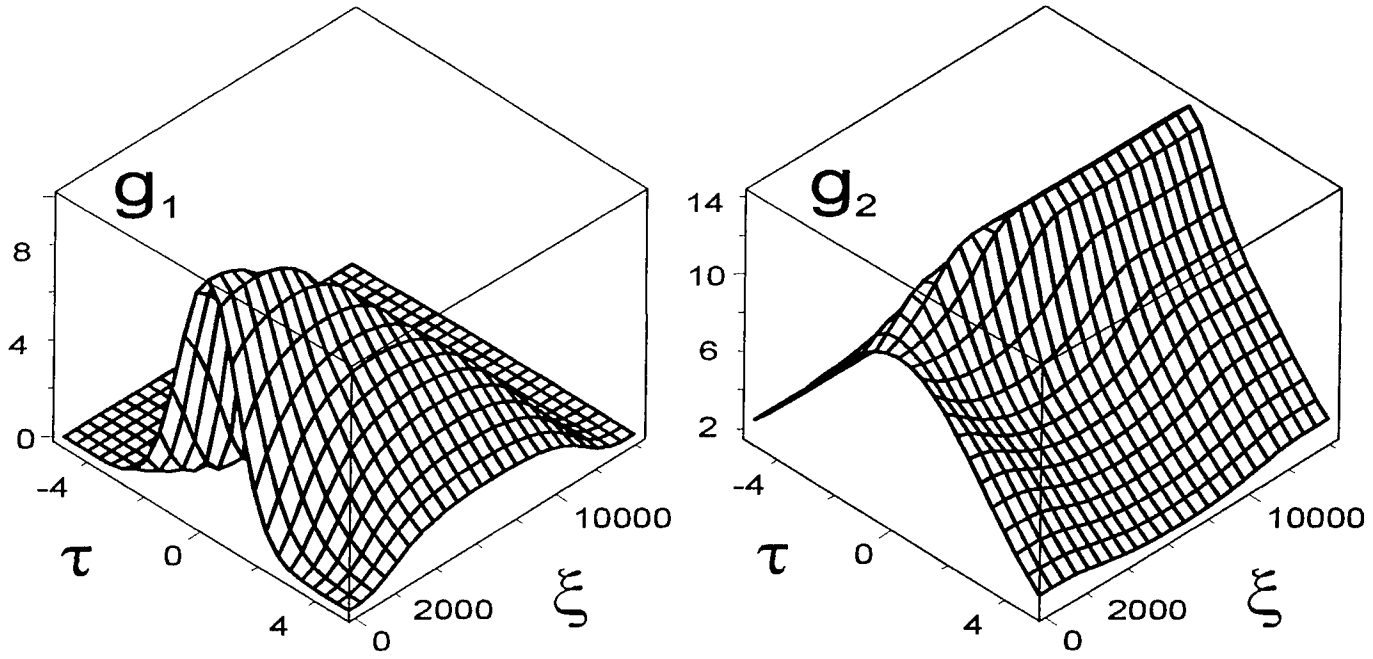

Fig.4. The dependencies of envelopes of Rabi frequencies $g_{1,2} = G_{1,2}T_1$ from the time and the depth of penetration of radiation into a medium. The parameters are the same as in fig.2

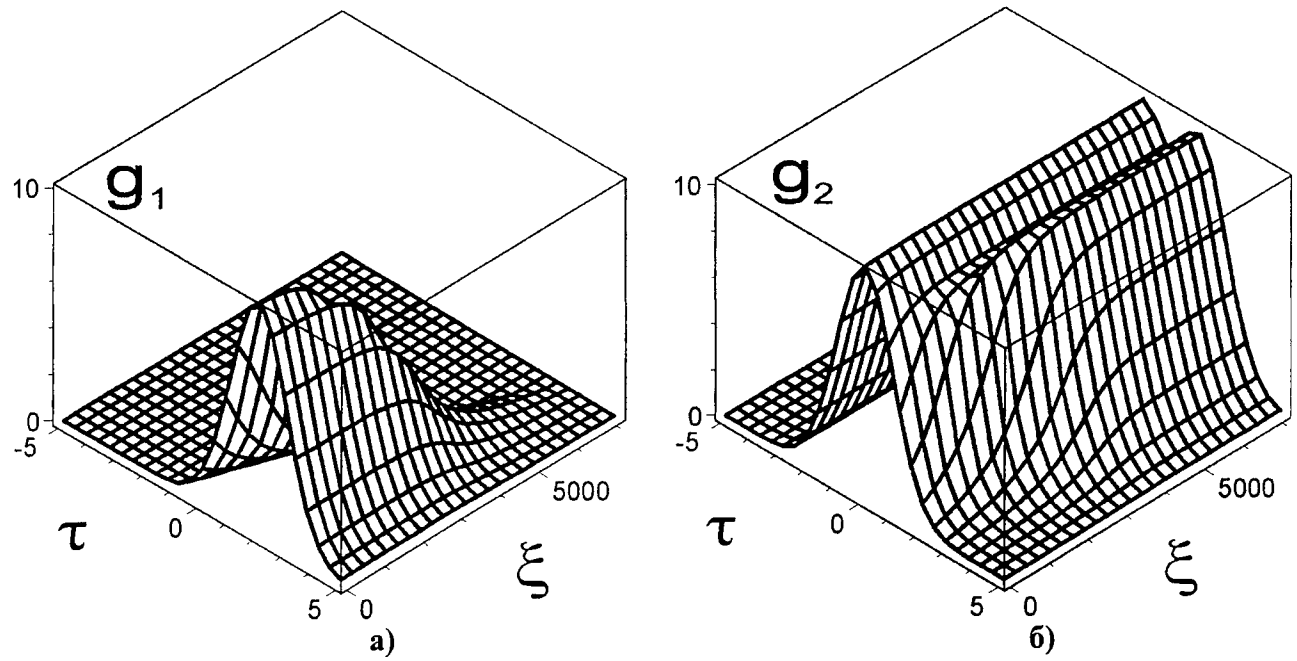

Fig.5. The normalized Rabi frequencies $g_1 = G_1 T$ (a) and $g_2 = G_2 T$ (b) versus time and length of a medium. The parameters are as follows: $t_0/T = 2$, $G_1^0 T = 10$, $G_2^0 T = 10$ ($G_{1,2}^0$— value of Rabi frequency $G_{1,2}$ in a maximum); $\Gamma_{10} T = 0.1$, $\Gamma_{12} T = 0.1$, $K_1 = K_2$.The time τ is measured in terms of pulse duration T, and length of a medium ξ — in terms of the length of linear absorption of a probe radiation with frequency ω_1

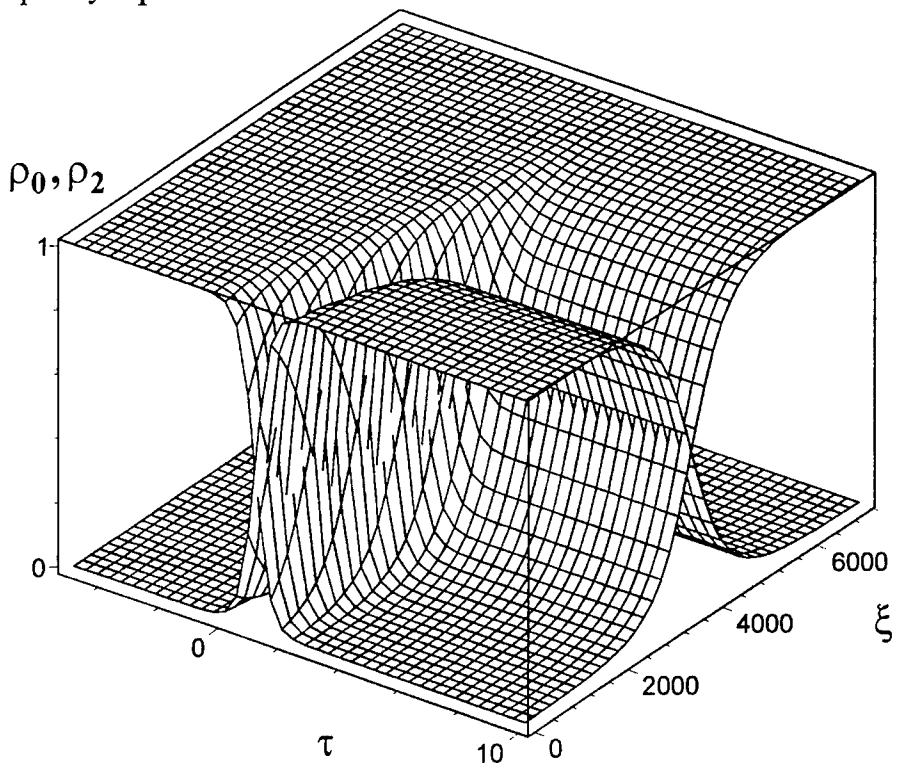

Fig.6. The level populations $\rho_{0,2} = |a_{0,2}|^2$ versus time and length of a medium. The parameters are the same as in Fig.5.

Ultra-short pulse propagation in quadratic medium with regard to the dispersion of non-linear susceptibility.

A.I. Maimistov[1], E.V. Kazantseva[2]

Department of Solid State Physics, Moscow Engineering Physics Institute,
Kashirskoe sh. 31, Moscow, 115409 Russia

ABSTRACT

System of evolution equations describing ultra-short optical pulse propagation in quadratic non-linear medium is derived with taking into account the dispersion of the non-linear susceptibility and second-order group-velocity dispersion. Both type I and type II of phase matching were considered. The case of a finite phase mismatch was analysed by an analytical method. The steady state pulses of the fundamental and second harmonic waves were found. There are new kinds of ultra-short pulses propagating in quadratic medium in the anomalous and normal dispersion regime.

Keywords: second harmonic, anharmonic oscillator, phase matching, quasi-harmonic electromagnetic waves

1. INTRODUCTIOM

Second harmonic generation (SHG) was one of the effects that give rise to the development of nonlinear optics. In the last years this phenomenon newly attracts great attention[1]. The point is that solitary wave propagation and soliton phenomena in quadratic nonlinear medium can be investigated with less energy consumption that in the case of cubic nonlinear medium. If the width of an electromagnetic pulse is much larger than the period of the optical cycle, the pulse can be naturally described by means of its slowly varying envelope. This approximation is adequate for pulses of 10^{-9} – 10^{-12} second region. However, this approximation should be upgrade if we remove to consideration of the pulse duration of 10^{-11} – 10^{-14} seconds interval. The modification of slowly varying envelope approximation can be done in framework of some relevant model of nonlinear medium. The nonlinear dynamics of the medium driven by the electromagnetic filed is frequently modelled in terms of anharmonic oscillators[2]. In particular, the propagation of a linearly polarised ultra-short pulse (USP) was considered in the framework of the material model based on the Duffing oscillators[3,4], with the non-linear response of the medium being cubic. The propagation of a linearly polarised USP in a dispersive medium was modeled by means of quadratically non-linear oscillators[5,6]. The propagation of femtosecond pulses in a medium with the nonlinearity determined by both electronic and ionic (Raman-scattering) degrees of freedom was considered in Ref. 7.

An objective of the present work is to derive the modified system of equations describing the evolution of the USPs of fundamental and second harmonic radiation. Some approximate solutions of these equations will be obtained.

2. CONSTITUENT MODEL

Let us consider the model in where the non-resonant medium is represented by ensemble of anharmonic oscillator that described by Hamiltonian:

$$H = (m/2)\{(\partial x_o/\partial t)^2 + (\partial x_e/\partial t)^2\} + \gamma_o x_o^2 + \gamma_e x_e^2 +$$
$$+ (1/3)\{Ax_o^3 + 3Bx_o^2 x_e + 3Cx_o x_e^2 + Dx_e^3\} - m\beta_o x_o E_o - m\beta_e x_e E_e$$

[1] Email: maimistov@pico.mephi.ru
[2] Email: e-lena@pico.mephi.ru

Laser Optics 2000: Semiconductor Lasers and Optical Communication, Serguei A. Gurevich, Nikolay N. Rosanov, Editors, Proceedings of SPIE Vol. 4354 (2001) © 2001 SPIE · 0277-786X/01/$15.00

Normal coordinates x_o and x_e are corresponded to ordinary and extraordinary axes. Polarization components are determined by expressions $P_o = Nex_o$, $P_e = Nex_e$. Eigenfrequencies of oscillator are determined by parameters $2\gamma_o = m\omega_o^2$, $2\gamma_e = m\omega_e^2$, Let us introduce the notations for anharmonic parameters λ_{ijk} as $A = m\lambda_{111}$, $B = m\lambda_{112}$, $C = m\lambda_{122}$, $D = m\lambda_{222}$. The Hamiltonian under consideration leads to the following equations

$$\frac{\partial^2 x_o}{\partial t^2} + \omega_o^2 x_o + \lambda_{111} x_o^2 + 2\lambda_{112} x_o x_e + \lambda_{122} x_e^2 = \beta_o E_o, \tag{1a}$$

$$\frac{\partial^2 x_e}{\partial t^2} + \omega_e^2 x_e + \lambda_{112} x_o^2 + 2\lambda_{122} x_o x_e + \lambda_{222} x_e^2 = \beta_e E_e \tag{1b}$$

As usually, we consider the quasi-harmonic electromagnetic waves:

$$E_j = \mathcal{E}_{1j}(z,t)\exp(-i\omega_L t + ik_{1j}z) + \mathcal{E}_{2j}(z,t)\exp(-2i\omega_L t + ik_{2j}z) + c.c.,$$
$$P_j = \mathcal{P}_{1j}(z,t)\exp(-i\omega_L t + ik_{1j}z) + \mathcal{P}_{2j}(z,t)\exp(-2i\omega_L t + ik_{2j}z) + c.c.,$$

where $\mathcal{E}_{aj}(z,t)$ and $\mathcal{P}_{aj}(z,t)$ are slowly varying envelopes of electric field of the pulse and polarization of medium ($a = 1, 2$ is frequency index, $j = o, e$ polarization index, *ordinary* or *extraordinary* waves). The normal coordinates of oscillator are represented in like manner

$$x_o = Q_{1o}(z,t)\exp(-i\omega_L t + ik_{1o}z) + Q_{2o}(z,t)\exp(-2i\omega_L t + ik_{2o}z) + c.c.,$$
$$x_e = Q_{1e}(z,t)\exp(-i\omega_L t + ik_{1e}z) + Q_{2e}(z,t)\exp(-2i\omega_L t + ik_{2e}z) + c.c.$$

Thus, $\mathcal{P}_{aj}(k,\omega) = NQ_{aj}(k,\omega)$. The solutions of the equations (1) can find as series in terms of power of λ_{ijk}

$$x_o = x_o^{(0)} + x_o^{(1)} + x_o^{(2)} + \ldots, \quad x_e = x_e^{(0)} + x_e^{(1)} + x_e^{(2)} + \ldots$$

For the functions $x_o^{(n)}$ and $x_e^{(n)}$ it leads to infinite coupled equations

$$\frac{\partial^2 x_o^{(0)}}{\partial t^2} + \omega_o^2 x_o^{(0)} = \beta_o E_o, \qquad \frac{\partial^2 x_e^{(0)}}{\partial t^2} + \omega_e^2 x_e^{(0)} = \beta_e E_e, \tag{2a}$$

$$\frac{\partial^2 x_o^{(1)}}{\partial t^2} + \omega_o^2 x_o^{(1)} = -\lambda_{111} x_o^{(0)} x_o^{(0)} - 2\lambda_{112} x_o^{(0)} x_e^{(0)} - \lambda_{122} x_e^{(0)} x_e^{(0)}, \tag{2b}$$

$$\frac{\partial^2 x_e^{(1)}}{\partial t^2} + \omega_e^2 x_e^{(1)} = -\lambda_{222} x_e^{(0)} x_e^{(0)} - 2\lambda_{122} x_o^{(0)} x_e^{(0)} - \lambda_{112} x_o^{(0)} x_o^{(0)},$$

.....

The expansion of the normal coordinates in terms of the anharmonicity parameters allows us to represent the Fourier components of slowly varying envelope of polarisation $\mathcal{P}_{aj}(k,\omega) = NeQ_{aj}(k,\omega)$ as a power series

$$\mathcal{P}_{aj}(k,\omega) = \sum_{n=0} \mathcal{P}_{aj}^{(n)}(k,\omega), \quad \mathcal{P}_{aj}^{(n)}(k,\omega) = NeQ_{aj}^{(n)}(k,\omega).$$

From (2a) it follows that $\mathcal{P}_{aj}^{(0)}(k,\omega) = N\alpha_j(\omega_a+\omega)\mathcal{E}_{aj}(k,\omega)$, where $\alpha_j(\omega)$ is linear susceptibility. Thus we can introduce a linear penetration $\varepsilon_j(\omega) = 1 + 4\pi N\alpha_j(\omega)$ and represent the dispersion relation for electromagnetic waves in form:

$$-(k_{aj}+k)^2\mathcal{E}_{aj}(k,\omega) + (\omega_a+\omega)^2\varepsilon_j(\omega_a+\omega)c^{-2}\mathcal{E}_{aj}(k,\omega) = \\ = -(4\pi/c^2)(\omega_a+\omega)^2\mathcal{P}_{aj}^{(1)}(k,\omega), \tag{3}$$

If we take into account inequalities $k << k_{aj}$ and $\omega << \omega_a$ then relation (3) leads to dynamical equations for the ultra-short pulse envelopes of the fundamental and second-harmonic waves[8]. In the second order of (ω/ω_a) we can obtain following system:

$$i\left(\frac{\partial}{\partial z} + \frac{1}{v_{g,aj}}\frac{\partial}{\partial t}\right)\mathcal{E}_{aj}(z,t) - \frac{D_{aj}}{2}\frac{\partial^2}{\partial t^2}\mathcal{E}_{aj}(z,t) = \\ = -\frac{2\pi eN\omega_a}{c\sqrt{\varepsilon_j(\omega_a)}}\left[Q_{aj}^{(1)}(t) + \frac{2i}{\omega_a}\frac{\partial Q_{aj}^{(1)}}{\partial t} - \frac{1}{\omega_a^2}\frac{\partial^2 Q_{aj}^{(1)}}{\partial t^2}\right]. \tag{4}$$

Where the group-velocity and dispersion parameter of fundamental and harmonic solitary waves were introduced as $v_{g,aj} = v_{gj}(\omega_a) = (d\omega/dk_j)(\omega_a)$ and $D_{aj} = (2k_{aj})^{-1}(d^2k_j/d\omega^2)(\omega_a)$ respectively.

Equations for oscillator variables $Q_{aj}^{(1)}(t)$ can be simplified if it take into account phase-matching conditions. There are two kinds of relations between wave vectors of the interacting waves. Second harmonic generation in scheme $o+o\rightarrow e$ is high effective under conditions $2k_{1o} \approx k_{2e}$. It was referred to *type I phase matching*. Interaction of three waves corresponding scheme $o+e\rightarrow e$ is high effective under condition $k_{1o}+k_{1o} \approx k_{2e}$ that corresponds to *type II phase matching*.

If we consider type I phase matching, then the reduced equations describing slowly varying oscillator variables in this case can be written as follows

$$\frac{\partial^2 Q_{1o}^{(1)}}{\partial t^2} - 2i\omega_1\frac{\partial Q_{1o}^{(1)}}{\partial t} + (\omega_o^2-\omega_1^2)Q_{1o}^{(1)} = -2\lambda_{112}Q_{2e}^{(0)}Q_{1o}^{(0)*}\exp[iz(k_{2e}-2k_{1o})], \\ \frac{\partial^2 Q_{2e}^{(1)}}{\partial t^2} - 2i\omega_2\frac{\partial Q_{2e}^{(1)}}{\partial t} + (\omega_e^2-\omega_2^2)Q_{2e}^{(1)} = -\lambda_{112}Q_{1o}^{(0)}Q_{1o}^{(0)}\exp[iz(2k_{1o}-k_{2e})].$$

In the case of the type II phase matching the oscillator variables are satisfied the system of equations:

$$\frac{\partial^2 Q_{1o}^{(1)}}{\partial t^2} - 2i\omega_1\frac{\partial Q_{1o}^{(1)}}{\partial t} + (\omega_o^2-\omega_1^2)Q_{1o}^{(1)} = -2\lambda_{122}Q_{2e}^{(0)}Q_{1e}^{(0)*}\exp[iz(k_{2e}-k_{1e}-k_{1o})], \\ \frac{\partial^2 Q_{1e}^{(1)}}{\partial t^2} - 2i\omega_1\frac{\partial Q_{1e}^{(1)}}{\partial t} + (\omega_e^2-\omega_1^2)Q_{1e}^{(1)} = -2\lambda_{122}Q_{2e}^{(0)}Q_{1o}^{(0)*}\exp[iz(k_{2e}-k_{1e}-k_{1o})], \\ \frac{\partial^2 Q_{2e}^{(1)}}{\partial t^2} - 2i\omega_2\frac{\partial Q_{2e}^{(1)}}{\partial t} + (\omega_e^2-\omega_2^2)Q_{2e}^{(1)} = -2\lambda_{122}Q_{1o}^{(0)}Q_{1e}^{(0)}\exp[iz(k_{1o}+k_{1e}-k_{2e})].$$

Solution of these systems of equations with taking into account $\eta = (\omega_L t_p)^{-1} << 1$ leads to generalized equations of Second-Harmonic Generation in ultra-short pulses under consideration. For the case of the type I phase matching we have

$$i\left(\frac{\partial}{\partial z}+\frac{1}{v_{g,1}}\frac{\partial}{\partial t}\right)\mathcal{E}_1(z,t)-\frac{D_1}{2}\frac{\partial^2}{\partial t^2}\mathcal{E}_1(z,t)= \\ =-\frac{\omega_1^2 2K_1}{k_1}\left\{\mathcal{E}_1^*\mathcal{E}_2+\frac{i}{\omega_1}\left(2\mathcal{E}_2\frac{\partial\mathcal{E}_1^*}{\partial t}-\mathcal{E}_1^*\frac{\partial\mathcal{E}_2}{\partial t}\right)\right\}\exp\{i\Delta kz\}, \tag{5.1}$$

$$i\left(\frac{\partial}{\partial z}+\frac{1}{v_{g,2}}\frac{\partial}{\partial t}\right)\mathcal{E}_2(z,t)-\frac{D_2}{2}\frac{\partial^2}{\partial t^2}\mathcal{E}_2(z,t)= \\ =-\frac{\omega_2^2 K_1}{k_2}\left\{\mathcal{E}_1^2-\frac{4i}{\omega_1}\mathcal{E}_1\frac{\partial\mathcal{E}_1}{\partial t}\right\}\exp\{-i\Delta kz\}. \tag{5.2}$$

where $\Delta k = k_{2e} - 2k_{1o}$ and

$$K_1=\frac{\pi e^3 N\lambda_{112}}{2m^2c^2\omega_1^6}=\frac{2\pi}{c^2}\chi^{(2)}(2\omega=\omega+\omega)=\frac{\pi}{c^2}\chi^{(2)}(\omega=-\omega+2\omega),$$

Here we introduce nonlinear susceptibilities of second order to obtain results, which are independent from model. For the case of the type II phase matching SHG equations has the following form

$$i\left(\frac{\partial}{\partial z}+\frac{1}{v_{g,1o}}\frac{\partial}{\partial t}\right)\mathcal{E}_{1o}(z,t)-\frac{D_{1o}}{2}\frac{\partial^2}{\partial t^2}\mathcal{E}_{1o}(z,t)= \\ =-\frac{\omega_1^2 K_2}{k_1}\left\{\mathcal{E}_{1e}^*\mathcal{E}_{2e}+\frac{i}{\omega_1}\left(2\mathcal{E}_{2e}\frac{\partial\mathcal{E}_{1e}^*}{\partial t}-\mathcal{E}_{1e}^*\frac{\partial\mathcal{E}_{2e}}{\partial t}\right)\right\}\exp\{i\Delta kz\}, \tag{6.1}$$

$$i\left(\frac{\partial}{\partial z}+\frac{1}{v_{g,1e}}\frac{\partial}{\partial t}\right)\mathcal{E}_{1e}(z,t)-\frac{D_{1e}}{2}\frac{\partial^2}{\partial t^2}\mathcal{E}_{1e}(z,t)= \\ =-\frac{\omega_1^2 K_2}{k_1}\left\{\mathcal{E}_{1o}^*\mathcal{E}_{2e}+\frac{i}{\omega_1}\left(2\mathcal{E}_{2e}\frac{\partial\mathcal{E}_{1o}^*}{\partial t}-\mathcal{E}_{1o}^*\frac{\partial\mathcal{E}_{2e}}{\partial t}\right)\right\}\exp\{i\Delta kz\}, \tag{6.2}$$

$$i\left(\frac{\partial}{\partial z}+\frac{1}{v_{g,2e}}\frac{\partial}{\partial t}\right)\mathcal{E}_{2e}(z,t)-\frac{D_{2e}}{2}\frac{\partial^2}{\partial t^2}\mathcal{E}_{2e}(z,t)= \\ =-\frac{\omega_2^2 K_2}{k_2}\left\{\mathcal{E}_{1o}\mathcal{E}_{1e}-\frac{2i}{\omega_1}\left(\mathcal{E}_{1e}\frac{\partial\mathcal{E}_{1o}}{\partial t}+\mathcal{E}_{1o}\frac{\partial\mathcal{E}_{1e}}{\partial t}\right)\right\}\exp\{-i\Delta kz\}. \tag{6.3}$$

where $\Delta k = k_{2e} - k_{1o} - k_{1e}$ and

$$K_2 = \frac{\pi e^3 N \lambda_{122}}{m^2 c^2 \omega_1^6} = \frac{2\pi}{c^2}\chi_{eff}^{(2)}(2\omega = \omega + \omega) = \frac{\pi}{c^2}\chi_{eff}^{(2)}(\omega = -\omega + 2\omega)$$

Thus, we obtain the system of equation to describe the propagation of the two connected fundamental and second harmonic waves. It takes into account corrections of the first order $(\omega_L t_p)^{-1}$ only.

3. SOME EXAMPL

Let consider the pulse propagation of fundamental and harmonic radiation under condition of phase mismatch $\Delta = \Delta k L >> 1$. If one introduce the new variables as

$$\mathcal{E}_1 = A_0 q_1 , \quad \mathcal{E}_2 = A_0 q_2 \exp\{-i\Delta k z\}$$

with

$$A_0^{-1} = 2K_1\omega_1^2 / k_1 ,$$

then the equations of the pulse propagation in quadratic non-linear medium at type I phase matching can be rewritten in the following form

$$i\left(\frac{\partial}{\partial\zeta} - \delta\frac{\partial}{\partial\tau}\right)q_1 - \sigma_1\frac{\partial^2 q_1}{\partial\tau^2} = -q_1^* q_2 - i\eta\left(2q_2\frac{\partial q_1^*}{\partial\tau} - q_1^*\frac{\partial q_2}{\partial\tau}\right), \tag{7.1}$$

$$i\left(\frac{\partial}{\partial\zeta} + \delta\frac{\partial}{\partial\tau}\right)q_2 - \sigma_2\frac{\partial^2 q_2}{\partial\tau^2} + \Delta q_2 = -\gamma\left(q_1^2 - 4i\eta q_1\frac{\partial q_1}{\partial\tau}\right), \tag{7.2}$$

where $\sigma_1 = \mathrm{sgn}\, D_1$, $\sigma_2 = D_2 / |D_1|$, $\gamma = 2k_1 / k_2$ and $\eta = (\omega_1 t_p)^{-1}$.

From second equation, at order $1/\Delta$, we can get approximately

$$q_2 \approx -\frac{\gamma}{\Delta}\left(q_1^2 - 4i\eta q_1\frac{\partial q_1}{\partial\tau}\right). \tag{8}$$

Substitution of this expression into first equation gives

$$i\frac{\partial}{\partial\xi}q - \sigma\frac{\partial^2 q}{\partial\tau^2} = \frac{\gamma}{\Delta}|q|^2 q - 2if\left(5|q|^2\frac{\partial q}{\partial\tau} - \frac{\partial(|q|^2 q)}{\partial\tau}\right), \tag{9}$$

where $\tau = (t - z/v_{g,1})t_p^{-1}$, $\xi = z/L$, $f = \eta\gamma/\Delta$ and $q(\xi,\tau) = q_1(z,t)$ is normalized envelope of the fundamental radiation pulse. It is generation of Nonlinear Schrödinger equation with derivative nonlinearity and shock-like nonlinearity. By proposing that

$$q(\xi,\tau) = a(y)\cdot\exp(i\phi) \quad y = \tau - \alpha\xi$$

we can find the exact solutions of the resulting equations. There are two solutions exponentially decaying at $\tau \to \pm\infty$

$$a_{\pm}^2(y) = \frac{2b_1}{\sqrt{4b_1b_3 + b_2^2}\cosh\left[2\sqrt{b_1}(y - y_0)\right] \pm |b_2|}, \tag{10}$$

and the new "algebraic" (algebraic decaying) solution

$$a^2(y) = \frac{b_2}{b_3 + b_2^2(y - y_0)^2}. \tag{11}$$

The phase of complex envelope can be written as

$$\phi(\xi, \tau) = \sigma(K\xi - \Omega\tau) + \frac{\sigma f\sqrt{b_1}}{\sqrt{b_2^2 + 4b_1b_3}} \int_{-\infty}^{2\sqrt{b_1}y} \frac{du}{\cosh u + \cos\vartheta}, \tag{12}$$

where $\cos\vartheta = b_2(b_2^2 + 4b_1b_3)^{-1/2}$. In these expressions we used parameters

$$b_1 = (\alpha^2/4 - K), \quad b_2 = (2\alpha f - \sigma\gamma/2\Delta) = (\gamma/2\Delta)(4\alpha\eta - \sigma), \quad b_3 = 7f^2/3,$$

and free constant K. Sings plus or minus indicate the region of dispersion: "plus" correspond to anormal dispersion ($\sigma = -1$) and $\Delta = \Delta kL < 0$ or to normal dispersion ($\sigma = +1$) and $\Delta = \Delta kL > 0$. The sign "minus" correspond anormal dispersion ($\sigma = -1$) and $\Delta = \Delta kL > 0$. The complex envelope of second harmonic can be expressed in term of the real envelope and phase of fundamental wave as

$$q_2 \approx -\frac{\gamma}{\Delta}\left\{a_{\pm}^2(y)\left[1 - 2\sigma\alpha\eta + 4\sigma\eta f a_{\pm}^2(y)\right] - 2i\eta\frac{\partial a_{\pm}^2(y)}{\partial y}\right\}\exp(i2\phi). \tag{13}$$

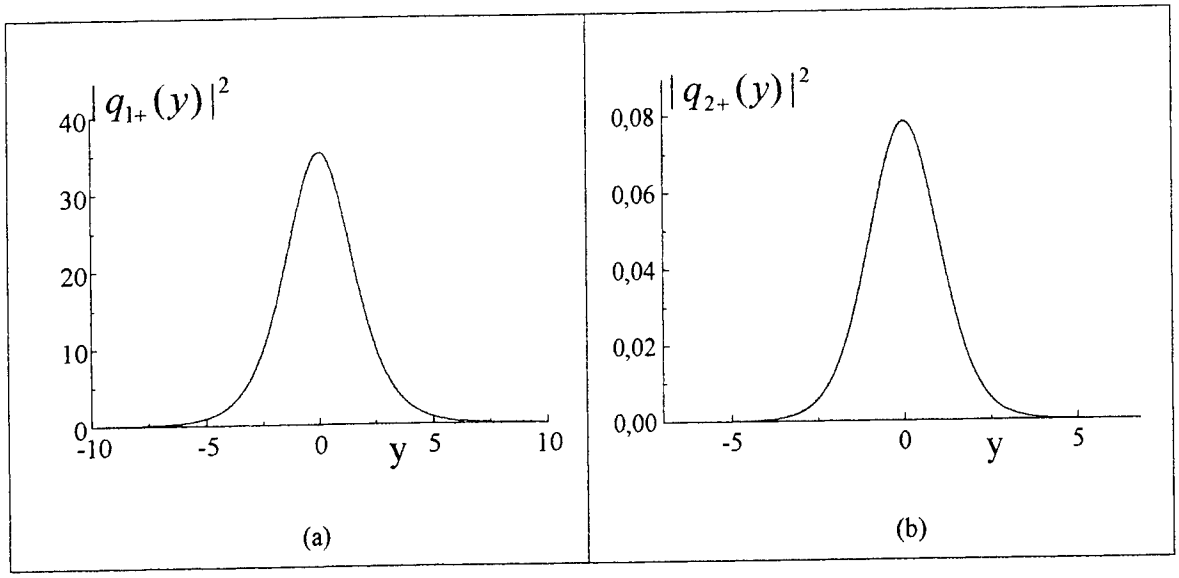

Fig.1. Envelope of steady state pulses of pump (a) and harmonic (b) in the anomalous dispersion region ($\sigma = -1$)

Fig. 1 shows the square of real envelopes, which are corresponded to fundamental and harmonic USP propagating in media under condition of anomalous group-velocity dispersion. These USPs exist in usually case of SHG and in the Kerr-like medium. If pulses propagate in medium with normal group-velocity dispersion, soliton-like USP can be obtained from (8), (10), and.(13) too. Some example of these USPs are represented in Fig.2.

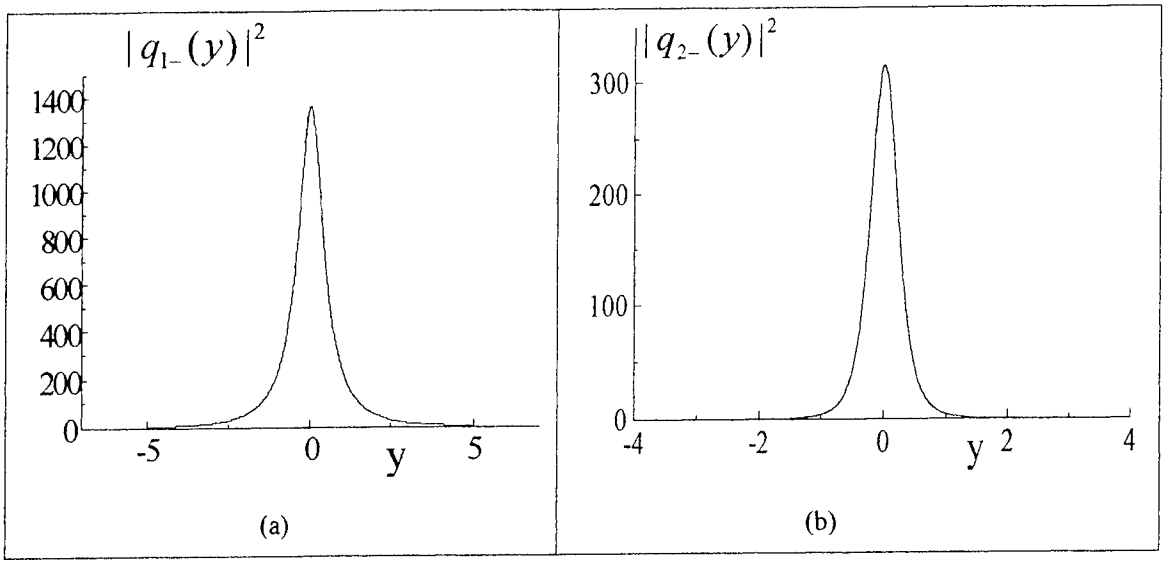

Fig.2. Envelope of steady state pulses of pump (a) and harmonic (b) in the normal dispersion region ($\sigma = +1$)

It is noteworthy that if the correction terms in equations (7) were omitted, the solution for the case of normal dispersion region would convert into singular one.

4. CONCLUSION

We have introduced and analyzed a model for the propagation of ultra-short pulses of the electromagnetic field in a material medium represented by quadratic anharmonic oscillators. In frame of this model new systems of equations of SHG were derived. It was found that the dispersion of second order nonlinear susceptibility of the medium results in new regime of ultra-short pulse propagation. Furthermore, there is new "algebraic" steady state pulse.

5. ACKNOWLEGEMENTS

We are grateful to Pr. S.A. Kozlov and Pr. S. Sazonov for enlightening discussions. This work has been supported by INTAS under grant №: 96-0339.

4. REFERENCES

1. Malomed B.A., "Solitons in optical media with quadratic nonlinearity" in *Nonlinear science at the dawn of the 21th century*, Eds. P.L.Christiansen, M.P.Sorensen, A.C.Scott, Springer-Verlag, Berlin 1999.
2. A. Yariv., *Quantum Electronics* Ch. 21, John Wiley and Sons, Inc., New York and London, 1967.
3. A. E. Kaplan, S.F. Straub and P. L. Shkolnikov, " Electromagnetic bubbles: subcycle near-femtosecond and subfemtosecond field solitons" *J.Opt.Soc.Amer.* **B 14**, pp. 3013-3024, 1997.
4. A.I. Maimistov and S.O. Elyutin, " Ultrashort optical pulse propagation in nonlinear nonresonance medium", *J. Mod. Opt.* **39**, pp. 2201-2208, 1992
5. O. B. Dubrovskaya and A. P. Sukhorukov, "On interaction of optical pulses with small number of cycles in quadratic nonlinear medium", *Izv. RAN, ser. Phys.* **56**, pp.184-188, 1992.
6. E.V. Kazantseva and A.I. Maimistov, "Propagation and interaction of extremely short electro-magnetic pulses in quadratic-nonlinear medium" *Phys. Lett.* **A 263**, pp. 434-438, 1999.
7. S.A. Kozlov and S.V. Sazonov, "Nonlinear propagation of the pulses with some number of optical cycles in dielectrics", *JETP* **84**, pp.221-234 (1997).
8. A.I. Maimistov, and A.M. Basharov, *Nonlinear Optical Waves.* Ch.1., Kluwer Academic Publishers, Dortrecht, Boston, London, 1999.

Dynamics of passive Q-switching in SBS/Er fiber laser at low pump power

Andrei A. Fotiadi [a,b], Olivier Deparis [b], Roman Kiyan [b], Stas Chernikov [c], Aris Ikiades [d]

[a] Ioffe Physico-Technical Institute of Russian Academy of Sciences
194021 Politekhnicheskaya 26, St.Petersburg, Russia

[b] Advanced Research in Optics, Electromagn. & Telecom. Dept.,
Faculté Polytechnique de Mons, 31 Boulevard Dolez, B-7000, Mons, Belgium

[c] Imperial College, Prince Consort Road, London SW7 2BW, UK

[d] Institute of Electronic Structure and Laser (FORTH),
P.O.Box 1527, Heraklion, Greece

ABSTRACT

We observed and investigated self-starting quasi-periodic pulsation in Er-doped fiber laser at 30-100 mW pump power. Pulses with duration of 10 - 50 ns (FWHM) and peak power of 50-200 W are generated at a quite stable repetition rate in the range of 300-500 μs. In contrast with previous experiments the pump level in our experiment is significantly lower. At this low pump power we found no nonlinear effect except SBS influencing on the laser dynamics. The experimental results were explained by a theoretical model based on cooperative dynamics of Rayleigh backscattering (RS) and Stimulated Brillouin Scattering (SBS). Using digital oscilloscope, we traced in details different stages of Q-switching pulse formation process: growth of the spontaneous radiation, lasing due to Rayleigh backscattering, appearance and growth of the first order SBS Stokes radiation and the second order Stokes radiation, lasing suppression due to saturation of the population inversion in Er-doped fiber by the SBS Stokes radiation. Good agreement between theory and experiment have been demonstrated.

Keywords: Q-switched fiber lasers, Er-doped fiber lasers, Rayleigh scattering, stimulated Brillouin scattering, nonlinearities in fibers, distributed feedback.

1. INTRODUCTION

Recently a novel mechanism for passive Q-switching in fiber lasers based on cooperative dynamics of linear Rayleigh backscattering (RS) and Stimulated Brillouin Scattering (SBS) has been reported[1,2]. The matter of the mechanism[3-5] is the following. Rayleigh backscattering of the light propagating in the laser cavity creates additional distributed feedback in the fiber cavity leading to a very effective linewidth narrowing. This in turn creates the conditions for SBS in the fiber. The growth of SBS then causes a series of avalanche processes leading to Q-switching.

In the experiments[1,2] passive Q-switching caused by the above-mentioned mechanism has been investigated experimentally but only with pump powers higher than 2 W. In a self-Q-switched Yb-doped fiber laser, generation of short, 2 - 15 ns pulses was observed at a repetition rate in the range of 1-20 kHz, which was different from relaxation oscillation pulsation.[1] A prelasing pulse with duration about ~ 50 ns and peak power ~ 40 W followed by gigantic 2-ns pulses with record high peak powers exceeding 10 kW were produced from a single-mode fiber laser with the use of 2-3 W diode pumping. Such extremely high peak powers in single-mode fiber, followed ~20 ns later by the secondary echo pulse, produced extreme spectral broadening from 0.8 to 2.3 μm with the involvement of literally all possible nonlinear processes

Other author information: A.A.F.: Tel: +07 (812) 515-66-60; Fax: + 07 (812) 5156747; E-mail: A.Fotiadi@shuvpop.ioffe.rssi.ru
or Tel.: +32 65 37 41 98; Fax: +32 65 37 41 99; E-mail: Fotiadi@telecom.fpms.ac.be

Laser Optics 2000: Semiconductor Lasers and Optical Communication, Serguei A. Gurevich,
Nikolay N. Rosanov, Editors, Proceedings of SPIE Vol. 4354 (2001) © 2001 SPIE · 0277-786X/01/$15.00

in silica optical fibers, including four-wave mixing, Raman scattering, etc. Such a rich laser dynamics at high pump power which is caused by a multiplicity of competing nonlinear phenomena's impeded both the recognition of initial process leading to Q-switching and direct comparison of experimental and theoretical results.

In this paper, we report our experiments with Er-doped fiber lasers pumped by low-power 980 nm laser diode. Pulsation operational mode caused by RS-SBS mechanism was successfully observed at pump power levels of 30 - 80 mW. Self-starting pulses generation occurred at a quite stable repetition rate in the range of 300-500 μs and peak power of 50-200 W with ~50 % fluctuation. In contrast with previous experiments, the laser dynamics was more simple and slower. Using digital oscilloscope we could recognize different stages of the Q-switching pulse formation process and investigated each of them experimentally in details. Commonly we observed a small pulse with duration of 50 - 200 ns and peak power of 0.5 - 5 W followed by gigantic Q-switched pulse with duration of 10 - 50 ns. No extra echo pulses following the main pulse were observed. It was concluded that no nonlinear effect except SBS[6,7] influenced on the laser dynamics. Therefore, we could compare in details the experimentally observed laser dynamics with the theoretical behavior as predicted by the RS-SBS model[3-5]. Fine structures of small and gigantic pulses were investigated for number of laser configurations. On this way certain relations between fine structure of the pulses and laser parameters were found. In a complete agreement with theoretical predictions, by varying the laser cavity length we observed two qualitatively different laser behaviors in pulsed mode. In the experiment with ~8 m cavity configuration, gigantic pulse had duration of 40 – 80 ns and peak power of less than 50 W. Leading edges of the small and gigantic pulses were separated in time by the cavity round-trip time. When the length of cavity was increased up to ~44 m, leading edges of the small and gigantic pulses were separated by a period, which was smaller than the cavity round-trip time, and gigantic pulses became more powerful with peak power of 200 W and duration of 10 – 15 ns.

Numerical simulations of the laser behavior were based on the set of dynamical equations for cooperative RS-SBS process[8] in fiber laser. Comparison of experimental and theoretical results allowed us to recognize different stages of pulse formation process, namely, growth of the spontaneous radiation, lasing due to Rayleigh backscattering, appearance and growth of the first order SBS Stokes radiation and the second order Stokes radiation, lasing suppression due to saturation of the population inversion in Er-doped fiber by the SBS Stokes radiation. By this way, we explained the difference in laser behavior for different laser configurations and proved that pulsation was caused by the RS-SBS Q-switching mechanism. [3-5]

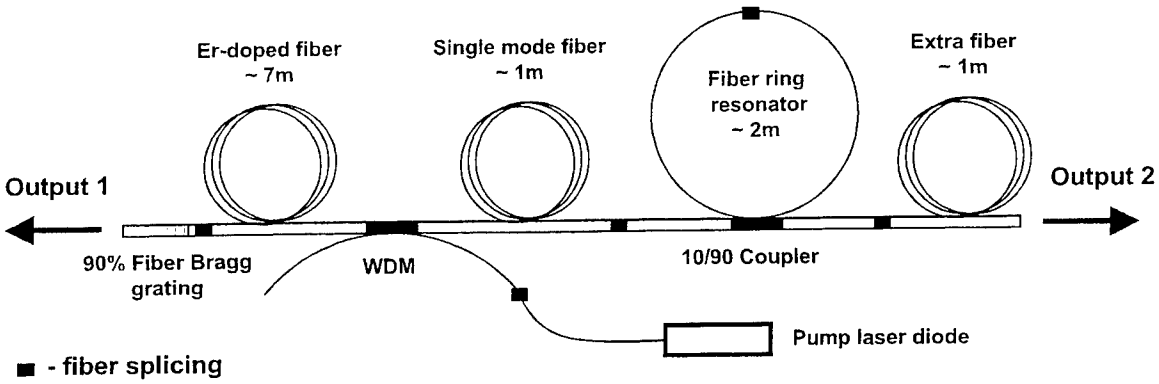

Figure 1. Experimental setup (lengths of fibers are indicated for the basic configuration).

2. EXPERIMENT

1. Experimental setup

In our experiment, the laser configuration employed in refs. [1,3-5] was realized with the use of an Er-doped fiber pumped by 980 nm laser diode with maximal output power of 100 mW. The basic experimental setup is shown in Fig.1. The laser consists of a linear fiber cavity, comprising 90% reflecting fiber Bragg grating (FBG), Er-doped fiber, piece of single-mode fiber (SMF), and a single-mode fiber ring resonator (RR) attached to the cavity through a 10/90 single-mode fiber coupler. The laser is pumped by a laser diode through a WDM coupler, which is inserted between Er-doped fiber and SMF. Typically, a piece of extra single-mode fiber (EF) is spliced with the free end of the 10/90 coupler. If the output end of the

extra fiber is protected from backreflection, feedback in the linear fiber cavity occurs due to reflection from FBG and backreflection caused by RS or SBS in the fiber ring resonator. The laser output radiation from both cavity ends (output 1 and output 2) is detected simultaneously by two photodiodes. The signals from photodiodes are digitized and recorded by oscilloscope for further comparison and analysis. The temporal resolution of the detection system is less than ~ 1 ns. Optical spectra of the output 2 radiation was monitored by optical spectrum analyzer.

2. Laser in the basic configuration

In a first experiment, we investigated the laser behavior in the basic configuration shown in Fig.1. The lengths of all fibers are indicated in Fig. 1. At pump power level in the range of 10 - 100 mW, lasing caused by backreflection from the free fiber end (2-4%) of the extra fiber takes place. The central wavelength of the laser radiation was 1532 nm. No regular pulsation, except relaxation oscillations, was observed in oscilloscope traces above the noise level.

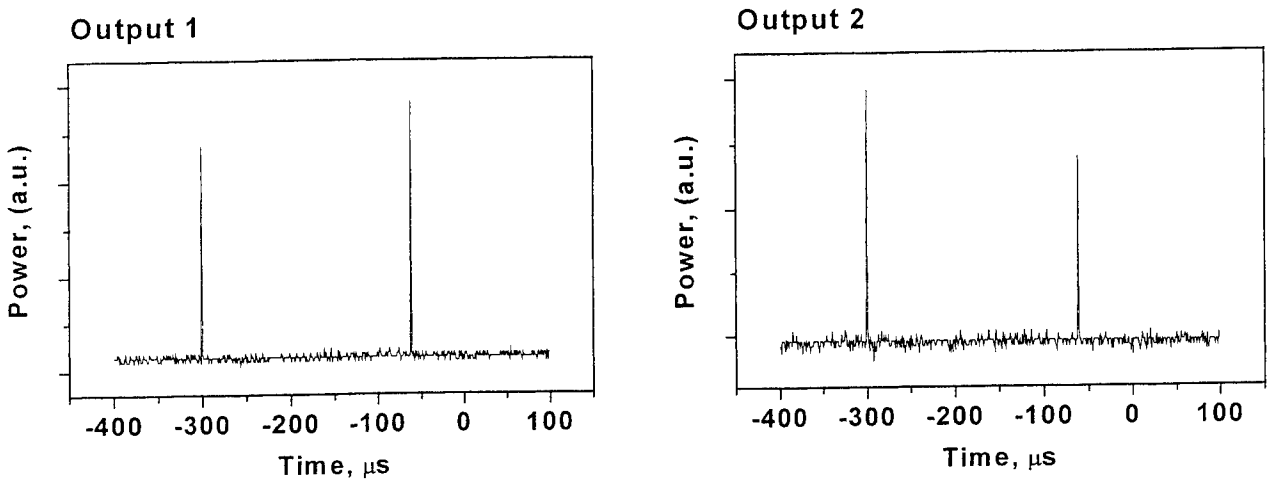

Figure 2. Typical oscilloscope traces recorded at 90 mW pump power (basic cavity configuration).

When the free end of the extra fiber (EF) was cut at angle to eliminate backreflection from this fiber end, the laser could operate in pulsed mode. At pump power of 90 mW, self-starting generation of pulses occurred (Fig. 2) at a quite stable repetition rate in the range of 300-500 μs and peak power estimated to 10 W with ~50% fluctuation. There was a correlation between the amplitude of pulse and its temporal delay. Pulses with higher delay were generally more powerful. Besides, the double-pass amplified pulses from output 2 demonstrated higher stability of their amplitude than single-pass amplified pulses recorded from output 1. The typical duration of the pulse was ~ 40-50 ns. It was much more stable in comparison with other pulse characteristics. Similar self-starting behavior of the laser could be observed at pump powers lower than 90 mW.

We found that the coefficient of backreflection from the angled fiber end influenced the pump power threshold at which repeating pulsation became self-starting. Careful angled cutting of the fiber end allowed us to reduce backreflection from the fiber end and to decrease the threshold down to 70 mW. It was found that the environmental noise, unavoidably present in the room, could decrease the threshold when pulsations appear. When the laser was entirely protected from environmental perturbations by a foam plastic box the threshold of process could not be attained for pump power less than 100 mW. However, the pulse generation was achieved with threshold pump power as low as 30 mW when the laser was affected by a weak acoustic signal. It is important to note that the way of starting did not influence the pulsation behavior and its parameters (peak power, repetition rate, pulse duration), which were mainly determined by the laser configuration and pump power level.

3. Specific features of laser dynamic behavior in basic configuration

Typical oscilloscope traces of laser pulses recorded from both laser outputs are shown in Fig. 3. They were recorded at pump power level of 80 mW. Fig. 3 (a) shows the behavior of the gigantic pulse. At the output 1, a gigantic pulse of ~50 ns FWHM duration is seen on a CW background. At the output 2, an additional small hump precedes a gigantic pulse of ~40 ns

FWHM duration. From the CW background estimated to about 10 mW, the peak power of the gigantic pulse at the output 2 is estimated to ~10 – 20 W from average output power measurements.

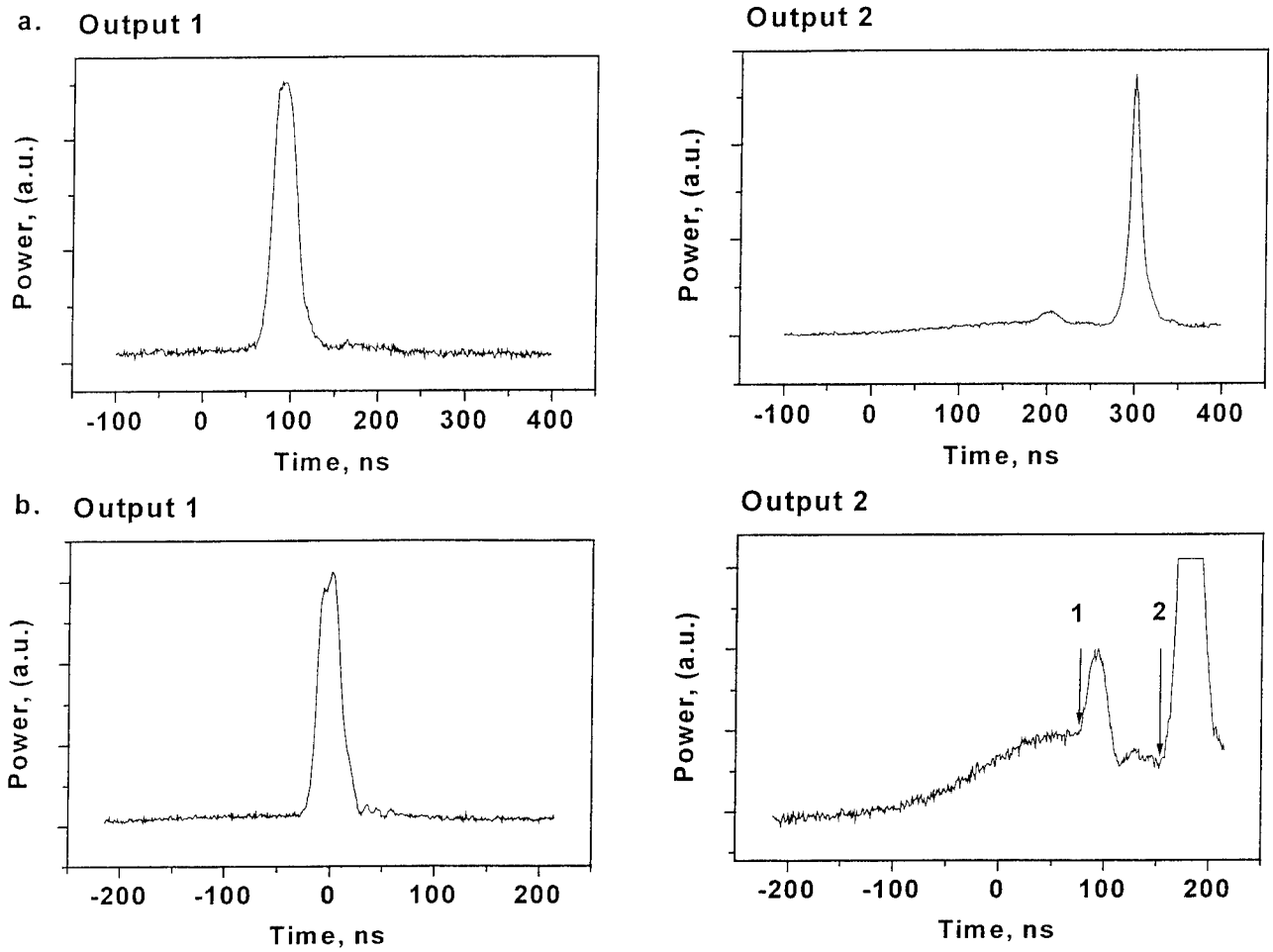

Figure 3. Typical oscilloscope traces recorded at 80 mW pump power (basic cavity configuration). (a - large scale, b – small scale on y-axis).

Oscilloscope traces with expanded y-axis scale are shown in Fig. 3(b). Several stages of the pulse formation can be clearly recognized in the oscilloscope traces of the output 2. Initially, the power grows exponentially with a characteristic time of ~ 70 ns. Then inflection in the curve happens and the growth becomes slower. At the time indicated by arrow 1 in fig.3(b) (point 1), a small pulse is generated before the gigantic pulse that appears at point 2. It is important to note that all the above-mentioned stages were always present in all traces that were recorded at pump power of 80 mW. The growth time of the exponential part at the output 2 was the same for all the recorded traces. Point 1 where small pulse starts and point 2 where gigantic pulse starts were always separated in time with a delay exactly equal to ~ 80 ns, that is the round trip time through the SMF and the Er-doped fiber.

4. Laser configuration with long linear part of the cavity

In a second experiment, the length of the linear part of the cavity was increased to 44 m. We used 12.5 m of Er-doped fiber and 32 m of single-mode fiber (SMF), instead of 7 m and 1 m in the basic configuration respectively. Self-starting pulsation in this long cavity configuration was observed at pump power level in the range of 50 - 80 mW. We found that the output pulse from the laser became much more intense and shorter than in the previous experiment. The typical duration of the gigantic pulse was ~ 10 – 20 ns. The peak power was estimated to ~ 100 – 200 W. Typical oscilloscope traces recorded at pump power of 80 mW are shown in Fig. 4. In general, they reproduce the temporal behavior we observed in the basic

configuration. Fig. 4 (a) shows the behavior of the gigantic pulse. In contrast with previous experiment (see Fig. 3 (a)), the pulse shape at the output 2 is considerably different from that at the output 1. The first pulse has a FWHM duration of ~ 50 ns while the second has a FWHM duration of ~ 15 ns. It is surprising because the signal from output 2 should be the same as the signal from output 1, the former being the same as the later but only reflected from mirror and amplified in Er-doped fiber. The reason of this disparity could be the saturation of the population inversion in amplifier, which could lead to the sharp trailing edge of the pulse from output 2. However, this pulse demonstrates also some specific features on its leading edge, which can not be connected with saturation effect. Fig. 4 (b) shows that several stages are present in the temporal behavior of output 2 (slowly growing part, small pulse and gigantic pulse), which are likely the same as those shown in Fig. 3(b). Starting points of small and gigantic pulses (points 1 and 2 respectively) are separated in time by ~ 200 ns, which is significantly smaller than the time that light takes to travel a round trip through SMF and Er-doped fiber (~ 440 ns).

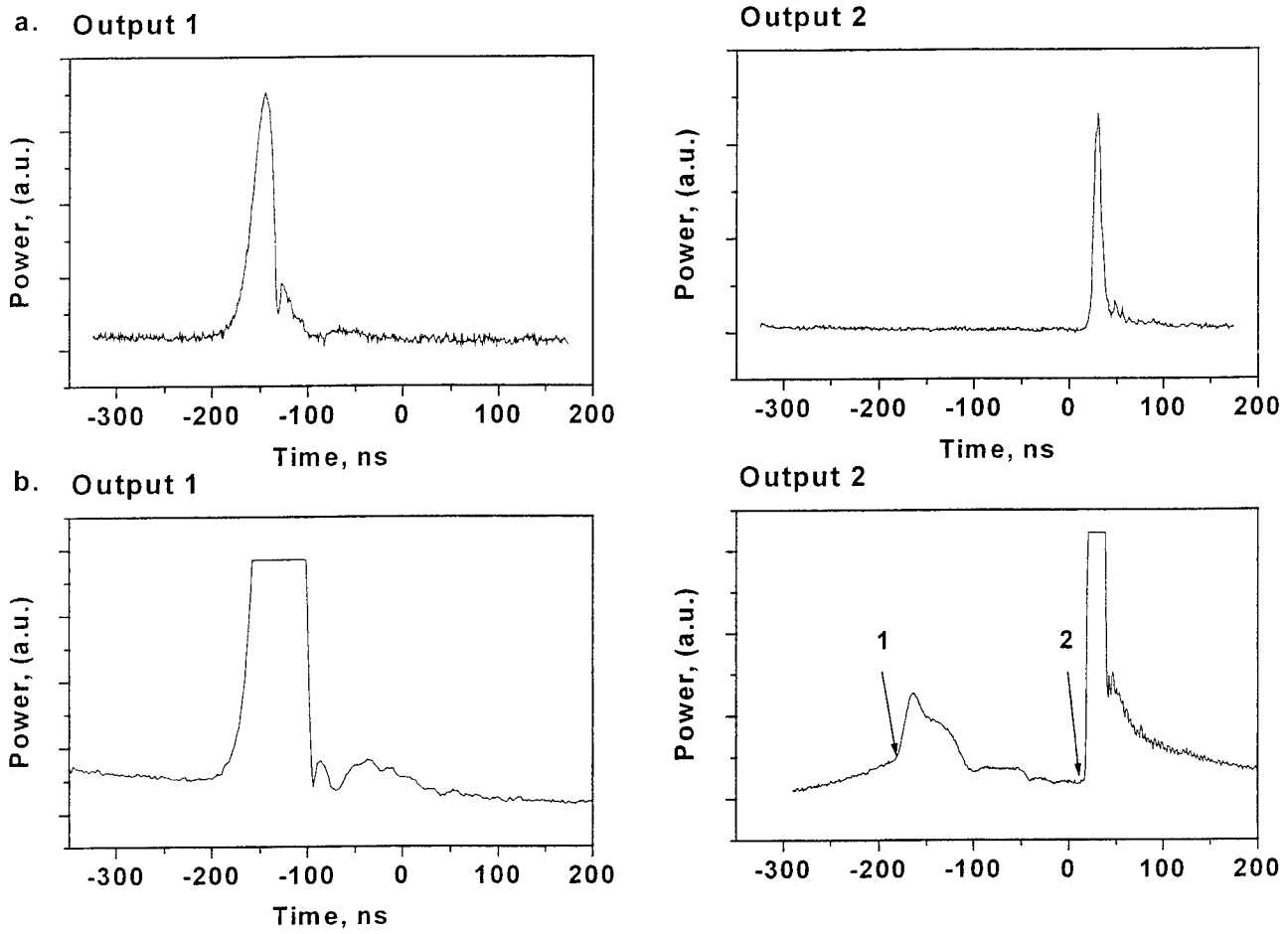

Figure 4. Typical oscilloscope traces recorded at pump power of 80 mW (configuration with long linear part of the cavity). (a - large scale, b – small scale on y-axis).

3. DISCUSSION OF THE RESULTS

1. Brief description of laser model.

In our experiments, we observed the Q-switching behavior of the Er-doped fiber laser shown in Fig. 1. This Q-switching behavior of the laser and the observed fine temporal structure of the pulses can be explained by the model[3-5] that we early

exploited for high power lasers. According with this model Q-switching occurs due to cascaded Rayleigh and stimulated Brillouin scattering dynamical process rising in the laser cavity. For the experiment in the basic configuration this mechanism is following.

Because feedback caused by reflection from the fiber end at the laser output 2 is suppressed by angled cutting of the fiber end, the lasing is caused by feedback due to Rayleigh scattering in the ring resonator. Although the Rayleigh backscattering coefficient Λ for single-mode optical fiber is rather low (commonly, it is about 1/600 part from Rayleigh losses), backreflection coefficient R (on intensity) from the ring is enhanced at resonance frequencies of the ring resonator $\nu_R = m(c/nL_R)$ (where c- light velocity, n-refractive index, L_R - ring interferometer length, m- arbitrary integer). Resulting reflection coefficient at the resonant frequencies ν_R is $R \sim Q^2 \Lambda L_R$, where Q is Q-factor of the ring resonator. In our experiment Q is about ~38. Thanks to this backreflection enhancement the double-pass gain of the Er-doped fiber is sufficiently high to provide lasing. The lasing frequency ν_A have to coincide simultaneously with both one of the resonant frequency of the ring resonator ν_R and one of the resonant frequency of the linear cavity ν_L. The linear cavity is formed by FBG mirror and Rayleigh backreflection from ring resonator. Thanks to the high spectral selectivity of Rayleigh scattering only one of all possible frequencies ν_R is selected. So, the laser radiation is single frequency at ν_A with very narrow linewidth. At the beginning of the cycle, the population inversion in the Er-doped fiber is growing and lasing in the cavity builds up exponentially with characteristic time in the microsecond's range. Growing laser radiation circulates in the ring in both directions. However, the clockwise circulating radiation is due to Rayleigh backscattering of the counterclockwise one and the intensity of the former much lower than intensity of the latter.

When SBS amplification along the length L_R of the ring becomes greater then losses in the ring thanks to growing of the counterclockwise radiation intensity, the threshold of SBS is reached and a first order Stokes pulse of hundreds nanosecond duration is generated in the ring resonator. The frequency of the pulse ν_B is downshifted by about $\Delta\nu_{SBS} \sim 11GHz$ ($\nu_B \approx \nu_A - \Delta\nu_{SBS}$) The frequency ν_B is coincident with one of the resonance frequencies of the ring resonator. This SBS process causes the depletion of the counterclockwise radiation in the ring resonator which leads to the reduction of Rayleigh reflection from the ring resonator and, eventually, to suppression of the lasing at ν_A. The Stokes pulse propagates in the clockwise direction in the ring resonator. It is partly extracted from the ring through the coupler and experiences strong amplification through double pass the linear part of the cavity. Then, the amplified Stokes pulse is again injected into the ring resonator and circulates in the counterclockwise direction. Part of the amplified Stokes pulse is extracted from the cavity through the coupler.

A new SBS process is initiated by this Stokes pulse propagating in the ring in counterclockwise direction. A second order Stokes (at frequency $\nu_{C'} \approx \nu_A - 2\Delta_{SBS}$) is generated in the ring while the initiating first order Stokes pulse is depleted. The depletion of the first order Stokes in the ring leads as dynamical response to the appearance of low-power pulse directed toward output 2 and is detected at output 2 as small hump (point 1 in oscilloscope traces). The second order Stokes pulse propagates in the clockwise direction in the ring resonator and is extracted from the ring through the coupler. Then it passes through SMF, experiences strong double-pass amplification in the Er-doped fiber, depleting the population inversion and extracting most of the energy stored in the cavity, once more passes SMF and results in a gigantic pulse at the output 2 of the laser (point 2 in oscilloscope traces). This last stage of the process turns the system back to the initial state. It is clear that, in this case, starting points of small hump and gigantic pulse in output 2 (points 1 and 2 respectively) are separated in time by exactly the time that light takes to travel a round trip through SMF and Er-doped fiber.

In the experiment with a long linear part of the cavity, the third stage of the Q-switching process (i.e. generation of the second Stokes pulse) is modified. In this case, due to the long length of the linear part of the cavity, generation of the second order Stokes occurs in the linear part of the cavity before the first order Stokes reaches the coupler after a round-trip in linear cavity and is injected into the ring. Therefore, in this case, the second Stokes pulses reaches output 2 of a time (point 2) that is shorter then a round trip of the linear cavity. On the other hand, as the depletion of the first order Stokes occurs in the SMF, the small hump appears after depleted part of the first order Stokes reaches the coupler. For these reasons, the delay between the small hump and the gigantic pulse (points 1 and 2, Fig. 5) is smaller than the time that light takes to make a round-trip through the linear part of the cavity.

2. Numerical simulations.

Computer simulation of the RS/SBS process for different laser configurations were performed. Simulations were based on the set of dynamical SBS/RS equations[8] for complex amplitudes of all waves are involved to the process:

$$\frac{n}{c}\frac{\partial E_A}{\partial t}+\frac{\partial E_A}{\partial z}=-K_1\rho_{A\dot{B}}E_{\dot{B}}+\eta_1(z)E_{\dot{A}}-\mu E_A \qquad \frac{n}{c}\frac{\partial E_{\dot{A}}}{\partial t}-\frac{\partial E_{\dot{A}}}{\partial z}=-K_1\rho_{\dot{A}B}E_B+\eta_3(z)E_A-\mu E_{\dot{A}}$$

$$\frac{n}{c}\frac{\partial E_{\dot{B}}}{\partial t}-\frac{\partial E_{\dot{B}}}{\partial z}=K_1\rho^*_{A\dot{B}}E_A-K_1\rho_{\dot{B}C}E_{C}+\eta_2(z)E_B-\mu E_{\dot{B}} \qquad \frac{n}{c}\frac{\partial E_B}{\partial t}+\frac{\partial E_B}{\partial z}=K_1\rho^*_{\dot{A}B}E_{\dot{A}}-K_1\rho_{B\dot{C}}E_{\dot{C}}+\eta_4(z)E_{\dot{B}}-\mu E_B$$

$$\frac{n}{c}\frac{\partial E_{C}}{\partial t}+\frac{\partial E_{C}}{\partial z}=K_1\rho_{\dot{B}C}E_{\dot{B}} \qquad \frac{n}{c}\frac{\partial E_{\dot{C}}}{\partial t}-\frac{\partial E_{\dot{C}}}{\partial z}=K_1\rho_{B\dot{C}}E_B$$

$$T_2\frac{\partial\rho_{A\dot{B}}}{\partial t}+\rho_{A\dot{B}}=K_2E_AE^*_{\dot{B}}+f_1(z,t) \qquad T_2\frac{\partial\rho_{\dot{A}B}}{\partial t}+\rho_{\dot{A}B}=K_2E_{\dot{A}}E^*_B+f_3(z,t)$$

$$T_2\frac{\partial\rho_{\dot{B}C}}{\partial t}+\rho_{\dot{B}C}=K_2E_BE^*_{C}+f_2(z,t) \qquad T_2\frac{\partial\rho_{B\dot{C}}}{\partial t}+\rho_{B\dot{C}}=K_2E_BE^*_{\dot{C}}+f_4(z,t)$$

where, $E_A(z,t)$, $E_{\dot{A}}(z,t)$, $E_B(z,t)$, $E_{\dot{B}}(z,t)$, $E_C(z,t)$, $E_{\dot{C}}(z,t)$ - complex amplitudes of counterclockwise and clockwise propagating light waves at frequencies ν_A, ν_B and ν_C, respectively; $\rho_{A\dot{B}}$, $\rho_{\dot{B}C}$, $\rho_{\dot{A}B}$, $\rho_{B\dot{C}}$ - complex amplitudes of hypersound waves, generating by the pairs of light waves; K_1 and K_2 are Brillouin coupling constants; T_2 - hypersound lifetime, μ is the linear loss coefficient; $\eta_i(z)$ are the Rayleigh backscattering coefficients. These scattering coefficients are considered as δ-correlated Gaussian random complex functions with zero mean and dispersion $\langle\eta_i\,\eta_i^*\rangle=k\,\mu$, where k is backward Rayleigh capture fraction, which is determined by fiber geometry and estimated to be about 1/600. The Langevin noise sources $f_i(z,t)$ is δ-correlated in space-time and Gaussian random process with zero mean. It describes the thermal fluctuations of the medium density that lead to spontaneous Brillouin scattering. Numerical calculation were performed with use of 4-order Runge-Kutta algorithm. Fiber amplifier was assumed to be linear with linear temporal growing of the field, gain $G(t)=20\,t/50\mu s$.

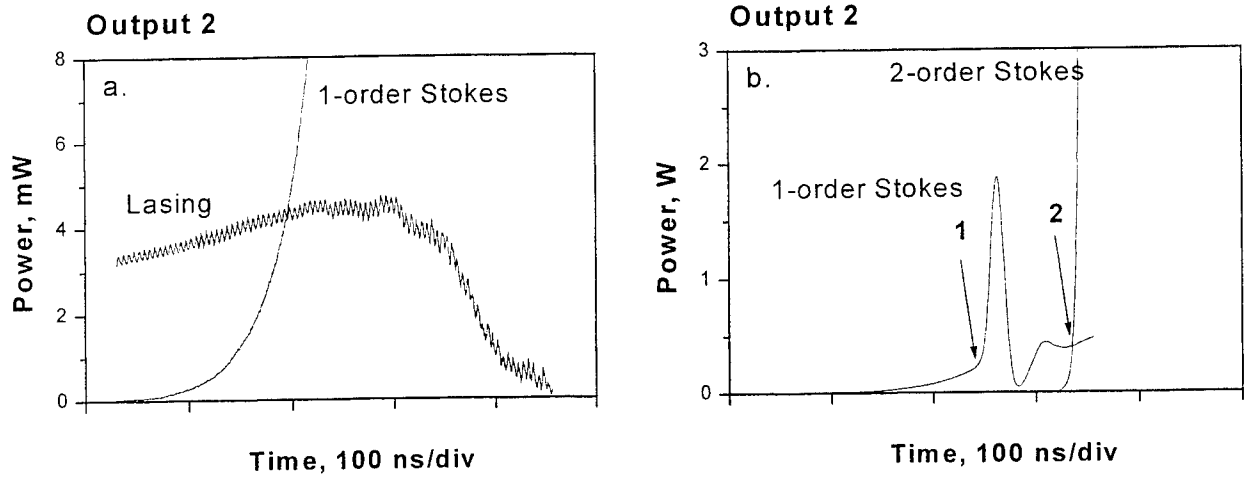

Figure 5. Computer simulated traces of the lasing radiation at ν_A, the first-order Stokes radiation at ν_B (a), the first-order Stokes at $\nu_{\dot{B}}$ and the second-order Stokes radiation at ν_C (b) calculated at output 2 for basic configuration.

The calculations were performed for both laser configurations exploited in the experiment. The calculated radiations at the output 2 for basic configuration are shown in Figs. 5, 6. The components that form the total output radiation are shown separately in Fig. 5. Fig. 5(a) demonstrates the mutual dynamics of the lasing radiation and the first order Stokes radiation at the first and second stages of the process. One can see that the threshold of SBS in the ring resonator is reached at a very small lasing intensity of ~ 4 mW. Therefore, we did not observe lasing due to Rayleigh feedback in the experiment, simply

because it was below the noise level (~ 10 mW). What we observed in the experiment was the mutual dynamics of the first and the second order Stokes pulses mutual dynamics, which is shown in Fig. 5(b). Initially, the first order Stokes builds up slowly in the laser cavity with a characteristic time of about 70 ns. When output Stokes radiation reaches ~0.25 W the generation of second Stokes pulse at ν_C occurs in the ring and simultaneously the first order Stokes is depleted in the ring, leading to generation of dynamical response pulse at ν_B. The starting points of small hump and gigantic pulse (points 1 and 2 respectively) at the output 2 are separated by ~80 ns, which is exactly the time that light takes to travel a round trip through SMF and Er-doped fiber. Fig.6 demonstrates the dynamics of the total laser radiation calculated for output 2. The peak power of gigantic pulse is about 17 W. There is a very good qualitative agreement Fig.6 with experimental oscilloscope traces shown in Fig.3.

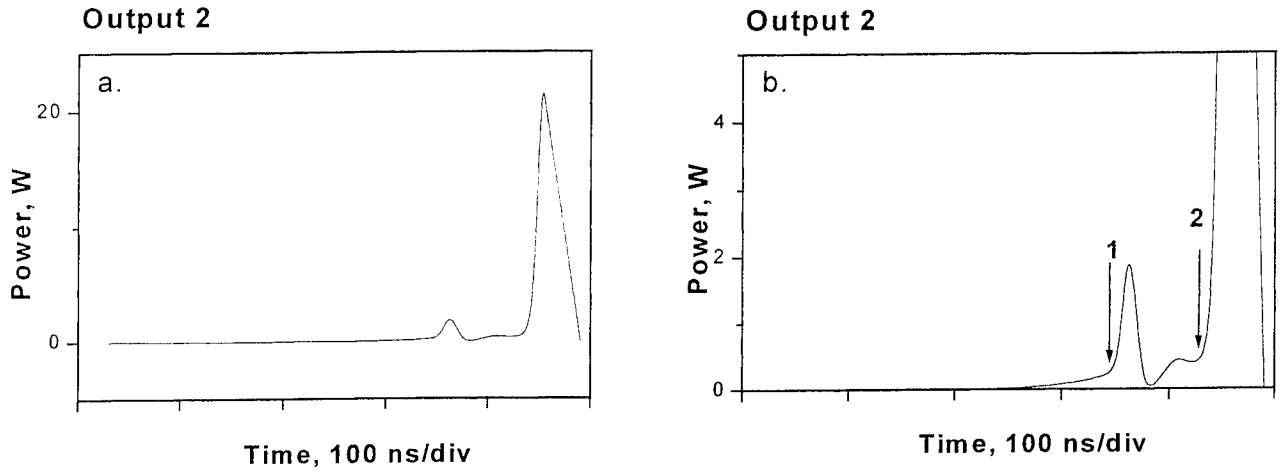

Figure 6. Computer simulated traces of the total radiation from output 2 for basic configuration (a - large scale, b – zoom on y-axis).

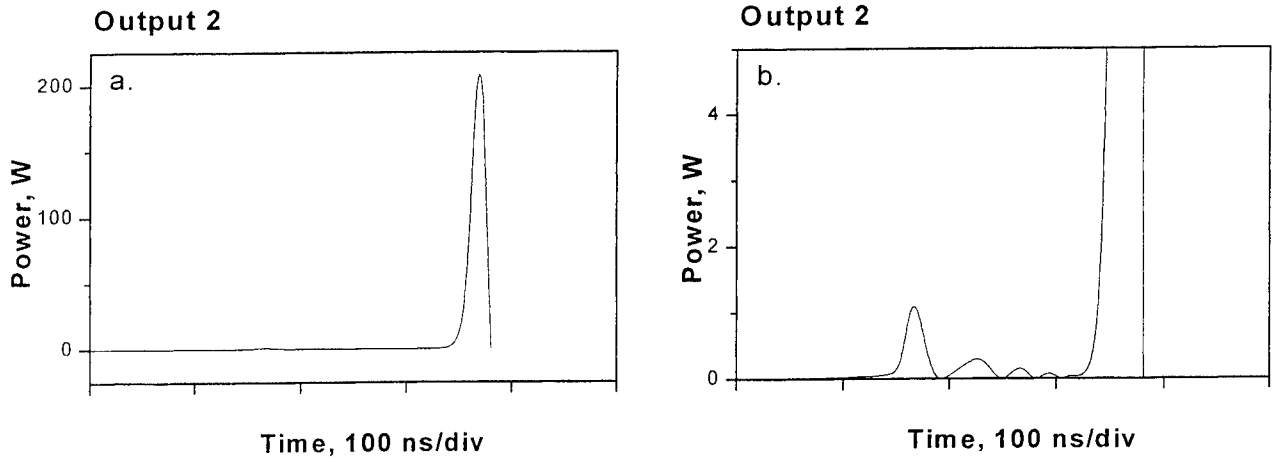

Figure 7. Computer simulated traces of the total output radiation from output 2 for configuration with long linear cavity (a - large scale, b – zoom on y-axis).

The calculated total radiation at the output 2 for laser configuration with long linear cavity is shown in Fig.7. Similar to previous case at beginning, the first order Stokes builds up slowly in the laser cavity with characteristic time of about 70 ns. When output Stokes radiation reaches ~0.1 W generation of second Stokes pulse at ν_C occurs in the SMF and simultaneously the first order Stokes in the ring is depleted. Depleted part of the first Stokes propagates toward output 2 and causes generation of the dynamical response pulse at ν_B when reaches the coupler. The starting points of small hump and

gigantic pulse (points 1 and 2 respectively) in output 2 are separated in time by ~200 ns, which is much smaller than the time that light takes to travel a round trip through SMF and Er-doped fiber (~440 ns). The peak power of gigantic pulse is about ~200 W. There is a very good qualitative agreement between calculations in Fig.7 and experimental oscilloscope traces shown in Fig.4.

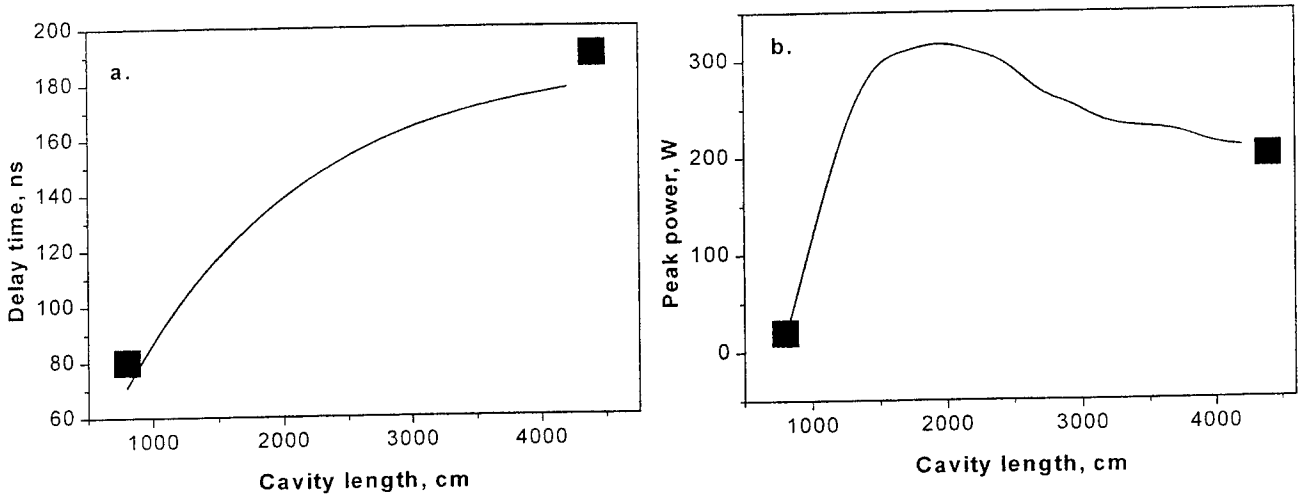

Figure 8. Computer simulated dependencies of the delay between small and gigantic pulses (a) and peak power of the gigantic pulse (b) on the length of the linear cavity. Experimental results are indicated by squares.

Theoretical dependencies of the delay between small and gigantic pulses and peak power of the gigantic pulse on the length of the linear part of the cavity are shown on Fig. 8 (a) and Fig. 8 (b), respectively. These dependencies are obtained by computer simulation. Due to stochastic nature of the SBS process a number of simulations was carried out for each length of the linear part of the cavity. Dependencies on Fig. 8 are averaged on the number of realizations. Two experimental points are shown on the same figures. Increasing the length of linear part of the cavity moves the second Stokes generation from the ring resonator to linear part of the cavity (SMF). As result, temporal delay between small hump and gigantic pulse is equal to the round-trip time in the linear part of the cavity for short lengths and becomes less than this round-trip time for longer lengths. As it is demonstrated in Fig. 8 (b), much higher peak power of the gigantic pulse can be obtained with longer length of the linear part of the cavity. The optimal length is about 20 m.

4. CONCLUSION

In conclusion we have successfully demonstrated passive Q-switching in a Er-doped fiber laser configuration at very low pump power. We have investigated the laser dynamics and described a number of specific features of the temporal behavior that accompanied the generation of gigantic pulse. Comparison of the experimental and theoretical oscilloscope traces allowed us to recognize different stages of pulse formation process and to obtain important information about its key parameters. We proved that pulsation was caused by the RS-SBS Q-switching mechanism that was exploited early but only with high-power fiber lasers. More than 100 W peak power pulses with duration of ~ 10 ns have been observed in Er-doped fiber laser at pump power of only 80 mW. Such a light source, which could be very flexible, may be useful for many applications. Of course, these are preliminary experiments and some important issues such as laser instabilities, influence of polarization, noise fluctuations and back reflection from cleaved fiber end should be investigated in future.

5. ACKNOWLEDGMENT

This research was supported by Interuniversity Attraction Pole program (IAP IV 07) of the Belgian Government (SSTC) and Russian Fund of Basic Research (grant N 00-02-16903). The work of Andrei A. Fotiadi was supported also by the Research Fellowship of OSTC.

6. REFERENCES

1. S.V. Chernikov, Y. Zhu, J.R. Taylor, V.P. Gapontsev, "Supercontinuum self-Q-switch Ytterbium laser ", Opt. Lett., 22, pp.298-301, 1997.
2. Z.J. Chen, A.B. Grudinin, J. Porta, J.D. Minely, "Enhanced Q-switch in double-clad fiber laser ", Opt. Lett., 23, pp.454-456, 1998.
3. S.V. Chernikov, A.A. Fotiadi, "Q-switching of fiber lasers with use of a dynamic SBS silica fiber mirror ", in: Conference on Laser and Electro-Optics 1997, Technical Digest Series, (Optical Society of America, Washington, D.C., 1997), Baltimore, USA, pp.477- 478, 1997.
4. A.A. Fotiadi, R.V. Kiyan, " Backward light scattering in optical fibers and fiber interferometers: new methods for lasing control in fiber configurations ", Ioffe Institute Prize Winners 1997, (Ioffe Institute, St.Petersburg, 1998 -see also http://www.ioffe.rssi.ru/winners), pp. 41-48, 1998.
5. A.A. Fotiadi, R.V. Kiyan, S.V. Chernikov, "Backward light scattering in fiber lasers ", SPIE Proc.,vol.3685, IX Conference on Laser Optics, St.Petersburg, Russia, pp.52-57, 1998.
6. G.P. Agrawal. "Nonlinear fiber optics", second edition, San Diego-Boston-New York: Academic Press Inc., 1995.
7. E.A. Kuzin, M.P. Petrov, A.A. Fotiadi., "Phase conjugation by SMBS in optical fibers", in: "Optical phase conjugation", ed. by M.Gower, D.Proch., Springer-Verlag, pp.74-96, 1994.
8. A.A. Fotiadi, R.V. Kiyan, "Cooperative stimulated Brillouin and Rayleigh backscattering process in optical fiber", Opt. Lett., 23, pp. 1805-1807, 1998.

Noise Enhancement of Optical Binary Signals Transmission

S. Barbay[a], G. Giacomelli[a] and F. Marin[b]

[a] Istituto Nazionale di Ottica Applicata, Largo E. Fermi 6, I-50125 Firenze, Italy.
[b] Dipartimento di Fisica, Università di Firenze,
and LENS, Largo E. Fermi 2, I-50125 Firenze, Italy
and INFM, Unità di Firenze.

ABSTRACT

We report the evidence a novel phenomenon which is observed in VCSELs working in a bistable region, that we have called Noise Assisted Binary Information Transmission: the addition of noise to the pump current up to an optimal value leads to a strong improvement of the transmission quality, measured by the Bit Error Rate. We analyze different indicators to define the output string and the comparison of the input with the output signal is eventually reduced to a comparison of binary strings and can treated by means of standard methods of information theory. These results represent the first experimental evidence of Aperiodic Stochastic Resonance. We analyse the possible application to optical communications and compare it to a standard amplitude modulation scheme.

Keywords: vcsel, binary transmission, polarization, stochastic process, optical communication

1. INTRODUCTION

Vertical Cavity Surface Emitting Lasers (VCSELs) are commonly used in optical communications, and their impact in telecom industry should be even more important in the future. This is due to their on-chip test ability, low threshold current, good spatial structure of the output beam and single longitudinal frequency operation. By contrast, due to their quasi circular transverse symetry, they can emit in two perpendicular linear polarizations. It is then possible to observe a bistable behaviour between the two polarization modes. The bistable operation of VCSELs in some critical current regions is a well established phenomenon.[1,2] It has also been studied theoretically by several authors.[3] In the bistable current region, noise induced jumps can occur. The dynamics of noise-driven jumps has been studied for single mode lasers,[4] for multi-transverse mode VCSELs[5–7] and even for laser sources characterized by a complicated transverse pattern caused by gain and cavity spatial inhomogeneities.[8,9]

More importantly from a signal processing point of view, Stochastic Resonance (SR) has been reported for the first time in VCSELs in.[8] SR can be defined as the specific response of a bistable system to a small modulation in the presence of noise.[12,13] The small modulation is amplified up to a maximum for a non-zero input noise, giving a resonant-like behaviour versus noise of the Signal to Noise Ratio.

In this paper, we study the response of VCSELs to a small amplitude pseudo-random binary signal in the presence of noise.[10] This system could prove very interesting with respect to data communications[11] , and is of fundamental importance in the study of Aperiodic Stochastic Resonance[14,15] (ASR) – a term coined to describe SR-type behaviours with non periodic or stochastic inputs.

2. EXPERIMENTAL SETUP

We employ a commercial, quantum-well VCSEL, lasing at 840 nm with distributed-Bragg reflectors. The emission window has a diameter of about 15μ m; the current confinement and isolation is provided by proton implantation. The laser is thermally stabilized (better than 1 mK) and the pump current is carefully controlled with a noise of about 70 pA/$\sqrt{\text{Hz}}$ in the range 1kHz to 3 MHz. The overall stability allows long time measurements, even in presence of critical behaviors. An optical isolator prevents from optical feedback effects, while an half-wave plate before the input polarizer permits to select a linear polarization. The experimental setup is shown in Fig.1.

In our laser, the critical current region is characterized by a complex transverse spatial structure (see Fig.2). The laser emits in several laser spots, having different optical frequencies. For some value of the pump current,

emails: barbay@ino.it, gianni@ino.it, marin@lens.unifi.it

Laser Optics 2000: Semiconductor Lasers and Optical Communication, Serguei A. Gurevich, Nikolay N. Rosanov, Editors, Proceedings of SPIE Vol. 4354 (2001) © 2001 SPIE · 0277-786X/01/$15.00

a polarization switch is observed, accompanied by a change in spatial structure and optical spectrum. The total intensity remains almost constant, due to a strong anticorrelation between the two polarizations. Selecting a spatial region in the transverse section, or choosing a polarization, it is possible to observe the switches as light intensity hops.

Scanning the pump current we can identify several bistable regions. In such regions, the laser performs polarization jumps induced by internal noise according to the Kramers law[16]: the probability distribution $P(T)$ of the residence time T in one state has an exponential behavior, with a mean residence time T_K (Kramers time) decreasing with the noise strength. In our experiment, the Kramers time can range from a few seconds to a few tens of nanoseconds.

Since we wish to control the statistics of the jumps, we choose a bistable region characterized by very rare hops. In this way we can control the residence times by adding a suitable amount of noise to the laser current. In particular, the results presented in this paper have been obtained by operating the laser at a pump current I=11.2 mA. The bistable region has a width of 0.5 mA; the average residence time, due to the internal noise alone, is of a few seconds. The corresponding hysteresis cycle, obtained by sweeping the pump current, is shown on Fig. 3.

The signals from a variable intensity, white noise generator (10 MHz bandwidth) and a pseudo-random binary sequence generator are summed and coupled into the laser input current. The binary sequence is a 16,000 bit word with a bit duration of 4 μs (bit rate: 250 kbit/s). Its amplitude is 0.4 mA, smaller that the width of the bistable region. As a consequence, the current steps alone are not large enough to induce a jump of the laser state.

The laser intensity is monitored by a fast avalanche detector whose signal is acquired by a digital scope. The output signal is then low-pass filtered with a bandwidth of 350 kHz, acquired by the digital scope at a sampling rate of 5 MSamples/s and processed. The analog bandwidth of the filter is chosen in order to optimally detect the transmitted signal. Indeed, the behavior of the laser can be described in terms of a linear response when close to a stable state and a nonlinear response (hopping between the stable states). The linear response gives rise to intensity fluctuations and tends to deteriorate the signal-to-noise ratio.

3. EXPERIMENTAL RESULTS AND DISCUSSION

The signal detected by the photodiode, for different values of the input noise strength, is shown in Fig. 4. For low noise (Fig. 4a) the laser mainly remains in its initial state, even if a small amplitude modulation is visible. For an input noise around 0.30 mA_rms, the output follows very well the input signal (Fig. 4b). For larger noise strengths, the laser dynamics is determined by the noise more than by the input string, with a strong decorrelation between input and output (Fig. 4c).

To quantify how-well the input string is reproduced in the output string, a commonly used indicator is the Bit Error Rate (BER), defined as the percentage of wrong transmitted bits. The output bit is obtained by averaging the output signal over the bit duration and then comparing the result with a threshold to assign the 0 or 1 value for the output bit. The threshold is set halfway between the two output intensity levels.

The result is shown on Fig.5. At low noise intensity, the BER is close to 0.5, a value for which the input and output string are completely uncorrelated. As the noise increases, the BER decreases dramatically up to a minimum value of 3×10^{-3}, and then increases again as the noise further increases.

The noise-induced modulation-free dynamics can be described by the overdamped motion of a particle in a symmetric bistable potential, as happens in standard SR. In our case, the potential can be retrieved experimentally.[9] The stable points of the bistable potential represent a polarized intensity level of the laser. The time-varying modulation can be included in the potential providing that the laser can follow it adiabatically. The situation is schematized on Fig. 6. To a given input bit (0 or 1) corresponds two output stable states ('+' and '−'). However, since the potential is asymmetric, the two output states have different energies. In the case of a symmetric binary modulation, we have then two very different time scales T_{Kl} and T_{Ks}, which correspond respectively to a long and a short Kramers time, associated with a high (resp. low) activation energy. The two times can be directly related to the potential barrier height by

$$T_{Kl} \propto \exp\left(\frac{\Delta V + A}{D}\right)$$

and

$$T_{Ks} \propto \exp\left(\frac{\Delta V - A}{D}\right),$$

where ΔV is the modulation-free barrier height, A is the amplitude of the modulation and D is the noise intensity. These times are to be compared with the bit duration T_b. If the noise is low, then T_{Kl} and T_{Ks} are bigger than T_b, hence the laser remains for a long period in its initial state. In such case, the BER is very high since the system doesn't follow the input modulation. On the other hand, for a rather high noise the two times tend to equalize and eventually become both smaller that T_b. In that case the system randomly switches between the two output states whatever input is present. The BER is also very high in that case. We have shown that it exists an intermediate situation for which the noise is such that the inequalities

$$T_{Kl} >> T_b \text{ and } T_{Ks} << T_b \tag{1}$$

hold. As a consequence, if the system starts in the right (lower energy) state, it has a high probability to remain there for a time longer than the bit duration. If it starts in the wrong (higher energy) state, it has also a high probability to jump in the right one during a bit, and then to remain in that state. In this noise regime, the BER decreases up to its minimal value.

In standard SR, the resonance coincide with a noise such that the time matching condition holds approximatevely $2T_K \simeq T_\Omega$, where T_Ω is the period of the harmonic modulation. Although a more precise condition can be derived depending on the indicator used to characterize SR, this condition always gives a good approximation. By contrast in Binary ASR, the time matching condition is replaced by the inequalities (1).

4. APPLICATIONS TO OPTICAL DATA COMMUNICATION

In this section we briefly discuss the features that can lead to prefer our method in some applications, instead of using the standard, linear, amplitude modulation scheme. A key point in optical communication is the possibility to generate a strong optical signal, with a large contrast, starting from a weak current modulation. As an example, for the system investigated here, the contrast between the two states is

$$C = (v_{max} - v_{min})/(v_{max} + v_{min}) = 0.90$$

, where v is the detector signal. A standard amplitude modulation in the linear regime, with the same modulation depth, yields a value of $C = 0.03$.

By contrast to a the standard amplitude modulation, the minimum obtainable BER is limited by random jumps, rather than by the Gaussian noise. As a consequence, it can be kept constant even if the laser light is attenuated down to very low levels, as can be checked by attenuating the laser beam before the detection. In Fig. 5 we report the curves of the BER versus input noise for two different values of attenuation, down to a minimum detected power of -65 dBm. The curves are roughly the same, even if for low intensity levels (i.e. for higher relative noise) the setting of the binarization threshold is more critical.

On Fig. 7 we show the degradation of the BER versus input noise and detected intensity in the linear case, using the same averaging procedure as before. For a -5.5 dBm detected intensity, the BER is very low (and indeed we don't have enough statistics in our input string to actually have a reasonable estimate of its value). However, it monotonically increases with noise. The same happens for a much lower detected intensity (-45 dBm), although the minimum BER is in that case quite high, yet 1.5×10^{-2}. This has to be compared with the BER obtained with the same detection, in the presence of noise at an intensity of -65 dBm, using the polarization selection of $3 \times 10^{-}3$.

The attenuation values correspond approximatively to the minimum attenuation achievable before we detect only the detector noise. For illustration purposes, we show on Fig.8 the actual shape of the signals in both schemes at the two minimum detectedd intensity levels, before the averaging procedure. The input signal is clearly recognizable in the polarized intensity, while in the other case the signal is masked by the noise. Nevertheless, the averaging procedure combined to a carefull choice of the binarization threshold let us retrieve part of the input string information.

An estimation of the optimal BER we can get in both cases can be made on the basis of the classical formula

$$BER = \frac{1}{4}\left(erfc(\frac{v_1 - v_d}{\sqrt{2}\sigma_1}) + erfc(\frac{v_d - v_0}{\sqrt{2}\sigma_0})\right)$$

where v_d and $v_{0,1}$ are respectively the output levels associated to the binarization threshold and to the '0' or '1' bits. Eq. (ref{eq:BER}) predicts that the threshold leading to the minimum BER is

$$v_d = \frac{\sigma_0 v_1 + \sigma_1 v_0}{\sigma_0 + \sigma_1}$$

We find (see[10]) a BER of 8×10^{-3}, to be compared with the measured value of 3×10^{-3}. The agreement is satisfactory, considering the fast dependence of the BER on the variances and that the averaging procedure over the bit duration leads to a reduction of the effective noise bandwidth.

The same calculation can be carried out in the standard amplitude modulation scheme, a -45 dBm input laser power and a contrast $C = 0.03$. The shot-noise limited BER calculation yields 0.8×10^{-2}, close to the value of 1.5×10^{-2} that we have measured. Our detection scheme is in this case close to optimal.

5. CONCLUSION

The phenomenon presented here can be of great interest in the case of strongly attenuated transmissions or for nonlinear optical amplification. Although the minimum BER attained is still too high for many practical applications (because we restricted ourselves to very small input modulation amplitude), we wish to point to the fact that this scheme is rather insensitive to the amplitude of the input message and to the detected laser power, and therefore proves to be much superior to a standard amplitude modulation in terms of BER or contrast for very low input current modulation. A crucial point for applications is the maximum bit rate reachable. It is closely related to the physics of the polarization switch itself, and is currently under investigation.

ACKNOWLEDGMENTS

We thank I. Rabbiosi and V. Voignier for the help provided during this work. S. B. acknowledges EU support through the TMR grant "Marie-Curie" nu. ERBFMBICT983351. The authors wish also to thank Lo Spera for his very useful hints.

REFERENCES

1. K. Choquette, D. Ritchie, and R. Leibenguth *Appl. Phys. Lett.* **64**, p. 2062, 1994.
2. J. Epler, S. Gehrsitz, K. H. Gulden, M. Moser, and H. C. Sigg *Appl. Phys. Lett.* **69**, p. 722, 1996.
3. M. SanMiguel, Q. Feng, and J. V. Moloney *Phys. Rev. A* **52**, p. 1728, 1995.
4. M. Willemsen, M. Khalid, M. van Exter, and J. Woerdman, *Phys. Rev. Lett.* **82**, p. 4815, 1999.
5. G. Giacomelli, F. Marin, M. Gabrisch, K. H. Gulden, and M. Moser *Opt. Commun.* **146**, p. 136, 1998.
6. G. Giacomelli and F. Marin, *Quantum Semiclass. Opt.* **10**, p. 469, 1998.
7. F. Marin and G. Giacomelli *J. Opt. B* **1**, p. 128, 1999.
8. G. Giacomelli, F. Marin, and I. Rabbiosi *Phys. Rev. Lett.* **82**, p. 675, 1999.
9. S. Barbay, G. Giacomelli, and F. Marin, *Phys. Rev. E* **61**, p. 157, 2000.
10. S. Barbay, G. Giacomelli, and F. Marin, *Opt. Lett.*, to appear.
11. S. Barbay, G. Giacomelli, and F. Marin, "Un procedimento ed un dispositivo di trasmissione ottica di informazioni codificate", patented in Italy, 15 February 2000.
12. R. Benzi, A. Sutera, and A. Vulpiani *J. Phys. A* **14**, p. 453, 1981.
13. R. Benzi, G. Parisi, A. Sutera, and A. Vulpiani *Tellus* **34**, p. 10, 1982.
14. J. Collins, C. Chow, and T. Imhoff *Phys. Rev. E* **52**, p. R3321, 1995.
15. J. Collins, C. Chow, and T. Imhoff *Nature (London)* **376**, p. 236, 1995.
16. H. Kramers *Physica (Utrecht)* **7**, p. 284, 1940.

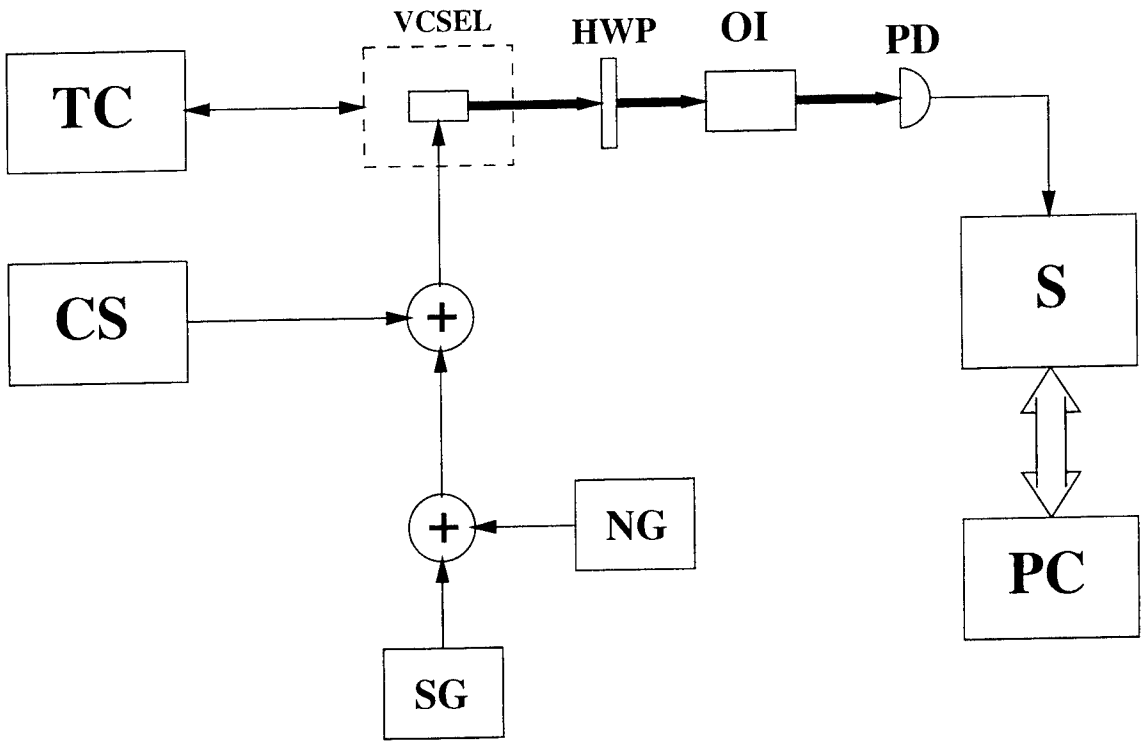

Figure 1. Experimental setup. CS: current source; TC: temperature controller; SG: signal generator; NG: noise generator; HWP: half wave plate; OI: optical isolator; PD: photodiode; S: digital scope.

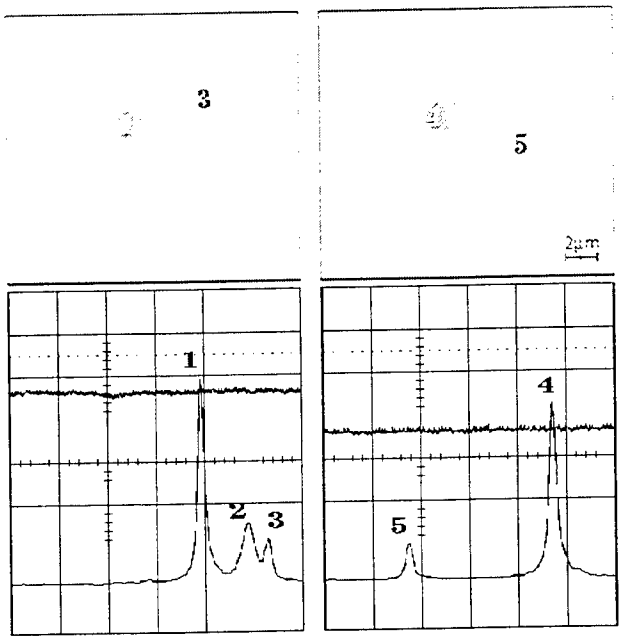

Figure 2. Polarized optical spectrum and transverse structure in a bistable region. The two stable states correspond to the left and right columns. The optical spectrum is obtained with a Fabry-Perot interferometer after polarization selection (the free spectral range is 6 divisions on the scope and equals 1.5 GHz). On the two bottom figures are also shown the polarized intensities corresponding to the two levels (straight line).

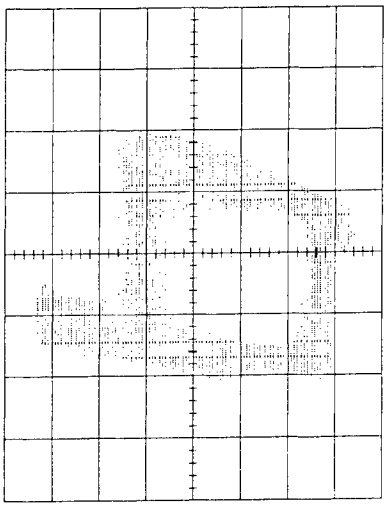

Figure 3. Hysteresis cycle of the polarized intensity $I(t)$. In the abscissa we report the input modulation signal, while the output laser intensity is plotted in the ordinate axis. The laser current increases from right to left.

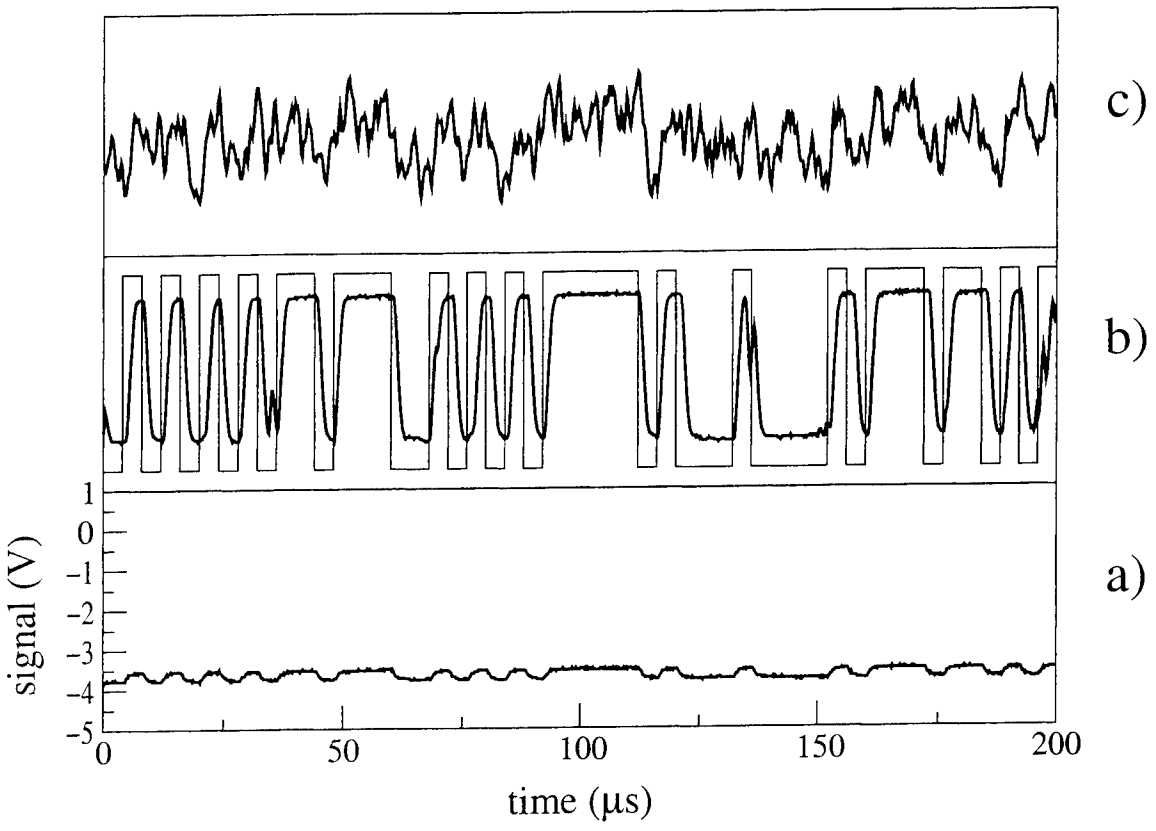

Figure 4. Output signal from the photodetector in the bistable case. The input noise intensity is: a) 0.07 mA_{rms}, b) 0.30 mA_{rms} and c) 0.78 mA_{rms}. The input power on the photodetector is -10 dBm. In b) is also shown (thin line)the input sequence.

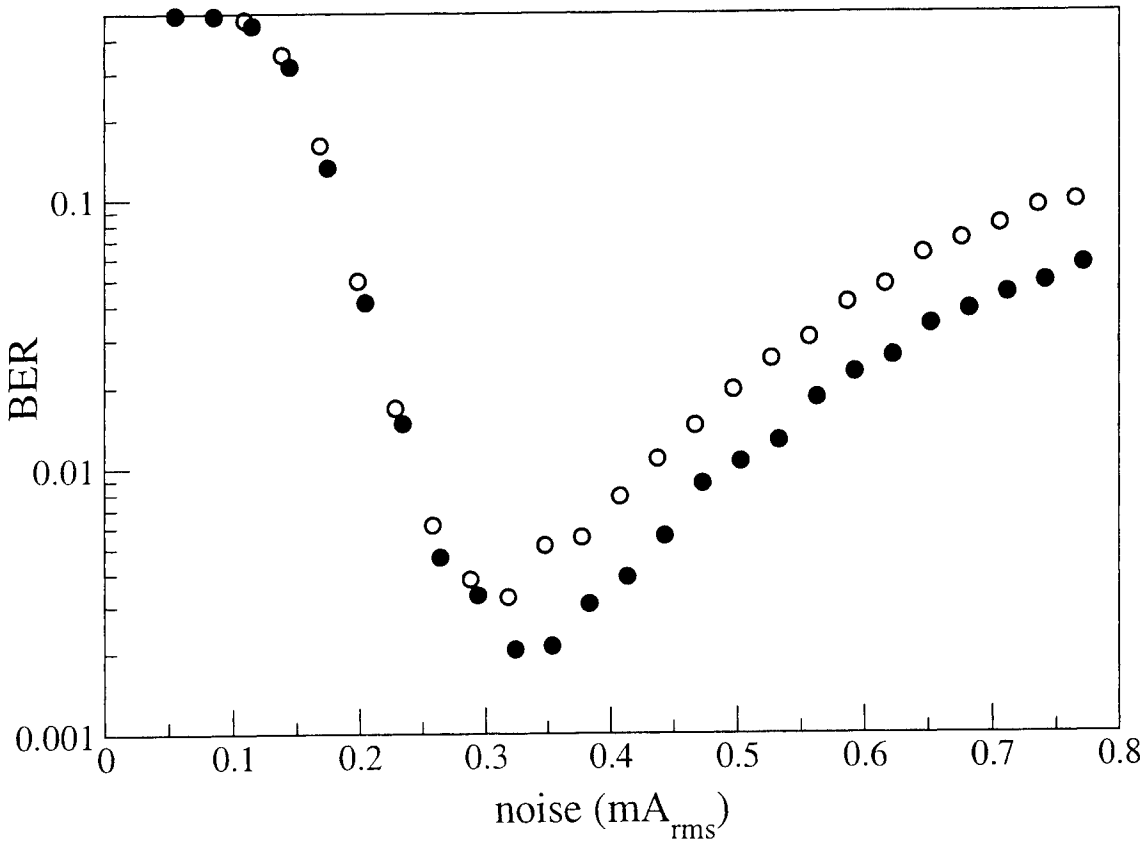

Figure 5. Bit Error Rate as a function of the input noise in the bistable case. The input power on the photodetector is -10 dBm (full circles) and -65 dBm(empty circles).

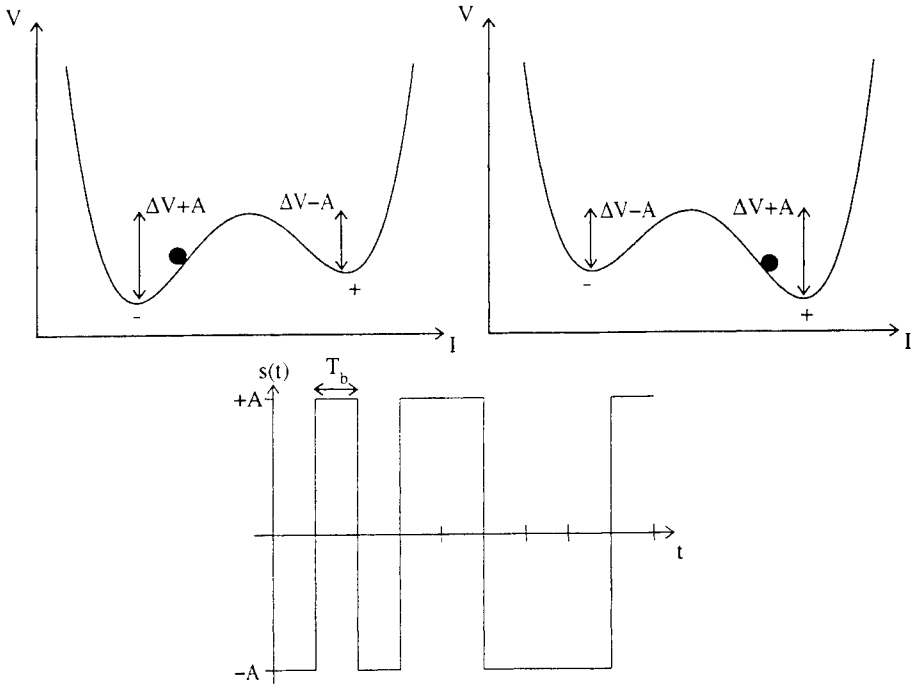

Figure 6. Potential V versus polarized intensity I for an input bit 0 (left) and 1 (right). The bottom figure is a schematic representation of the binary modulation sent to the laser.

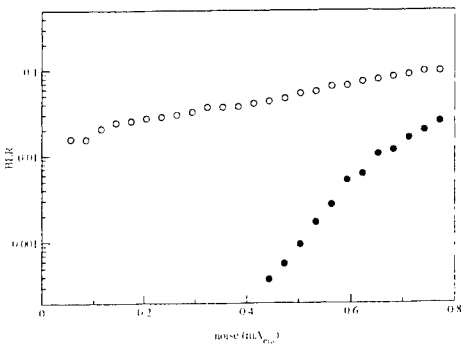

Figure 7. BER in the linear case versus input noise intensity. The detected intensity is: -10 dBm (empty circles), and -45dBm (filled circles).

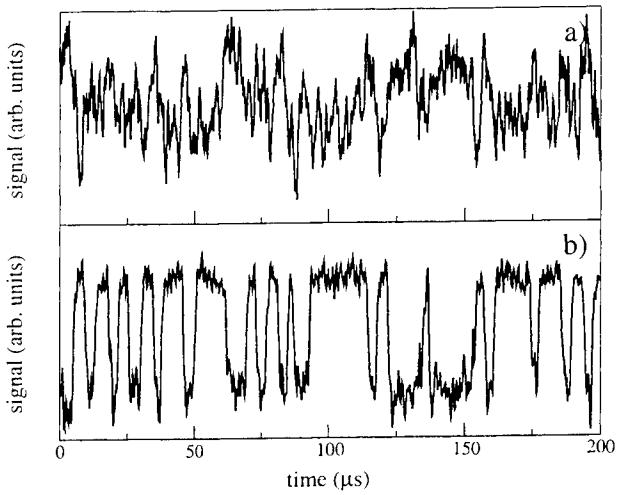

Figure 8. Polarized laser intensity signal: a) linear case (detected power -45 dBm), b) bistable case (detected power -65 dBm). The input noise is 0.06 mA_{rms} in a) and 0.30 mA_{rms} in b).

The compensation method for cancellation of excess noise in quantum nondemolition measurements of optical solitons

V. V. Kozlov[a,b], A. B. Matsko[c], and V. B. Smirnov[b]

[a] Department of Physics and Astronomy, University of Rochester, Rochester, New York 14627;
[b] Russian Center of Laser Physics, St. Petersburg State University, 1 Ulianovskaya, Petrodvoretz, St. Petersburg, 198904, Russia;
[c] Department of Physics, Texas A & M University, College Station, Texas 77843

ABSTRACT

Cancellation of excess noise of quantum optical solitons is based on successive passage of a soliton through an optical fiber with positive nonlinearity and negative dispersion and then through a near-resonant two-level system with negative nonlinearity and positive dispersion. An evolution of a quantum fluctuation in one medium will be reversed in the other. In such a way, the unwanted excess noise due to self-phase modulation in optical fibers can be fully suppressed leading to a radical improvement of accuracy of quantum nondemolition measurements of optical solitons. A detailed discussion of the compensation method with thorough numerical estimations for existing resonant media is provided.

Keywords: quantum soliton, optical fiber, Gordon-Haus effect, quantum measurement, self-induced transparency

1. INTRODUCTION

During the last dozen years quantum optical solitons attract considerable attention. Three basic reasons underlie the interest: 1) the development of laser sources generating solitons with noise properties at the quantum limit; 2) the manufacturing of silica fibers with small losses; and 3) the availability of photodetectors with high efficiency. Quantum properties of optical solitons propagating through nonlinear fibers were already probed in experiments on soliton squeezing and quantum-nondemolition (QND) measurements.

The excess noise owing to self-phase modulation is accumulated during propagation of solitons in fibers. The extra fluctuations build up a correlation between photon number and phase giving rise to a squeezing of the soliton's quantum state. The positive role of the excess noise in squeezing experiments is inverse in the QND measurements, where a desirable information gained through cross-phase modulation of two solitons appears to be hidden under the self-phase modulation noise.

Whether positive or negative, the quantum properties of optical solitons emerge from the same origin. Description of quantum solitons is based on a quantum version of nonlinear Schrödinger equation. The evolution of the soliton's initial state, i.e. an accumulation of the excess noise, is governed by group-velocity dispersion and Kerr-type nonlinearity. A control over those effects simultaneously provides the tool for managing quantum fluctuations.

The article proposes a general method for such kind of control, and particularly treats the cases when there is a need to suppress the unwanted excess quantum noise. This is accomplished by use of a near-resonant two-level system (NRTLS). A pulse detuned above the resonance, will experience a negative $\chi^{(3)}$-nonlinearity and positive group-velocity dispersion, i.e. the medium in regard of its properties behaves as a *mirror reflection* of an optical fiber. Thus, an evolution of fields including accumulation of excess quantum fluctuations in one medium will be reversed in the other. A proper combination of the NRTLS and the fiber may form an "effective vacuum" for propagating pulse, such that the overall evolution through the system will eventually recover the same quantum state as it was at the entrance.

The concept of the cancellation of the excess quantum noise was first proposed in[1] and[2] and called as "compensation method". Here, we further develop the concept concentrating on its realizability and applicability.

Laser Optics 2000: Semiconductor Lasers and Optical Communication, Serguei A. Gurevich, Nikolay N. Rosanov, Editors, Proceedings of SPIE Vol. 4354 (2001) © 2001 SPIE · 0277-786X/01/$15.00

2. QUANTUM DESCRIPTION OF OPTICAL SOLITONS

Propagation of classical solitons in nonlinear fibers is well described by nonlinear Schrödinger equation (NLSE), which accounts for $\chi^{(3)}$-nonlinearity and group-velocity dispersion of the fiber. Then, it is quite natural to expect that the behavior of a quantum soliton is governed by a corresponding quantized form of the NLSE where field amplitude $\phi(x,t)$ is replaced by a field operator $\hat{\phi}(x,t)$:

$$i\frac{\partial\hat{\phi}}{\partial t} = \mathrm{sgn}(D_f)\,\frac{\partial^2\hat{\phi}}{\partial x^2} + 2c_f\hat{\phi}^\dagger\hat{\phi}^2\,, \tag{1}$$

with $x = \bar{t} - (n_f/c)z$ as time coordinate in the frame moving with the group-velocity, $t = |D_f|z$ as normalized propagation distance, and $c_f = N_f/2|D_f|$ as the halved ratio of nonlinearity $N_f = \hbar\omega^2 n_2/\mathcal{A}_f c$ and the absolute value of the group-velocity dispersion $D_f = (1/2)k''$. Here, $\bar{t}$ is real time, n_f is the host refractive index, n_2 is the Kerr coefficient, and $\mathcal{A}_f$ is the effective fiber core area. As it is required by quantum-mechanical laws, the optical field operator $\hat{\phi}(x,t)$ must obey equal-time commutation relations

$$\begin{aligned}\left[\hat{\phi}(x,t'),\,\hat{\phi}^\dagger(x,t)\right] &= \delta(t-t')\,,\\ \left[\hat{\phi}(x,t'),\,\hat{\phi}(x,t)\right] &= 0\,.\end{aligned} \tag{2}$$

Indeed, the intuitive correctness of (1) with (2) is formally proved by Drummond and Carter in.[3] The authors use the lossless approximation, which is expected to work reasonably well for description of an experiment with optical fibers up to $1-2$-km in length.

It is quite useful to pose phenomenological *equal-space* commutation relations

$$\begin{aligned}\left[\hat{\phi}(x',t),\,\hat{\phi}^\dagger(x,t)\right] &= \delta(x-x')\,,\\ \left[\hat{\phi}(x,t'),\,\hat{\phi}(x,t)\right] &= 0\end{aligned} \tag{3}$$

instead of canonical *equal-time* commutators (2). This way out has been proposed in[4-6] for the case of optical solitons. Then, classical methods for treating optical solitons become easily extendable to the quantum domain. Recent investigation in[7] proves the validity of use of phenomenological commutation relations (3) in the field of fiber quantum optics. Basing on the conclusion, from here on we shall solve the quantum NLSE (1) with equal-space commutators (3).

We now reproduce essential elements of the perturbation theory for quantum solitons, which has been proposed in[4] and gained further development in[5] and.[6] Our main interest is in quantum fluctuations of the soliton with a large average photon number n_0 and a well-defined mean field. Typically, a picosecond soliton carries 10^8 photons. Then the field operator can be decomposed into its mean value $\phi_0(x,t)$ and a remainder $\hat{v}(x,t)$ responsible for the quantum fluctuations:

$$\hat{\phi}(x,t) = \phi_0(x,t) + \hat{v}(x,t)\,. \tag{4}$$

The perturbation operator $\hat{v}$ carries the full quantum character of the soliton, and obeys the same commutation relations as the original field operator $\hat{\phi}$:

$$\begin{aligned}\left[\hat{v}(x',t),\,\hat{v}^\dagger(x,t)\right] &= \delta(x-x')\,,\\ \left[\hat{v}(x,t'),\,\hat{v}(x,t)\right] &= 0\,.\end{aligned} \tag{5}$$

The quantum field is a solution of the perturbed linearized operator equation

$$i\frac{\partial\hat{v}}{\partial t} = \mathrm{sgn}(D_f)\,\frac{\partial^2\hat{v}}{\partial x^2} + 4c_f|\phi_0|^2\hat{v}^2 + 2c_f\phi_0^2\hat{v}^\dagger\,. \tag{6}$$

The linearization approximation remains up to phase shifts of the order of $n_0^{1/4}$.[8,9] This limit corresponds to nonlinear phase shifts $\sim 30\pi$ for a 1-ps soliton in a conventional fiber. Accumulation of such large shifts requires a fairly long distance of the order of 10 km. Thus the linearization approximation perfectly fits our starting assumption, where we have restricted ourselves to $1-2$-km fiber lengths.

In the following, our basic interest concerns quantum evolution of a single soliton propagating through nonlinear fibers. The corresponding classical description is given by fundamental soliton solution:

$$\begin{aligned}\phi_0(x,t) &= \frac{n_0\sqrt{|c_f|}}{2}\,\mathrm{sech}\left[\frac{n_0|c_f|}{2}(x-x_0-2p_0t)\right]\times \\ &\quad \exp\left[ip_0(x-x_0)-ip_0^2t+i\theta_0+i\theta_{\mathrm{spm}}\right]. \end{aligned} \tag{7}$$

Since the nonlinearity of optical fibers is always positive, the soliton can be realized only in the region of negative dispersion, i.e. $\mathrm{sgn}(D_f)=-1$ and $c_f>0$ in (1) and (6). Nonlinear phase shift

$$\theta_{\mathrm{spm}} \equiv \frac{n_0^2|c_f|^2}{4}t \tag{8}$$

appears due to self-phase modulation (SPM) in nonlinear fibers.

The derivatives of classical fundamental soliton (7) with respect to n_0, θ_0, p_0, and x_0 are all solutions of the linearized equation (6). Then, $\hat{v}(x,t)$ can be expanded as

$$\hat{v} = \frac{\partial\phi_0}{\partial n_0}\Delta\hat{n}_0 + \frac{\partial\phi_0}{\partial\theta_0}\Delta\hat{\theta}_0 + \frac{\partial\phi_0}{\partial p_0}\Delta\hat{p}_0 + \frac{\partial\phi_0}{\partial x_0}\Delta\hat{x}_0 + \hat{v}_{\mathrm{c}}\,, \tag{9}$$

where the first four terms account for quantum perturbations localized within the soliton, while the last term $\hat{v}_{\mathrm{c}}$ describes the continuum part of the noise operator $\hat{v}$. The four quantum operators $\Delta\hat{n}_0$, $\Delta\hat{\theta}_0$, $\Delta\hat{p}_0$, and $\Delta\hat{x}_0$ have the simple physical meaning in that they describe small initial quantum perturbations of the collective coordinates associated with classical intensity n_0, classical phase θ_0, classical momentum p_0, and classical position x_0 of the soliton.

The anzatz (9) is a general form of evolution of a quantum perturbation $\hat{v}(x,t)$ starting from initial quantum uncertainties $\Delta\hat{n}_0 \equiv \Delta\hat{n}(0)$, $\Delta\hat{\theta}_0 \equiv \Delta\hat{\theta}(0)$, $\Delta\hat{p}_0 \equiv \Delta\hat{p}(0)$, and $\hat{v}_{\mathrm{c}}(x,0)$. Skipping details of the derivation, which can be found in,[6] we jump to the final result — the formulation of a set of equations for quantum evolution of the four collective soliton operators:

$$\Delta\hat{n}(t) = \Delta\hat{n}_0\,, \tag{10}$$

$$\Delta\hat{\theta}(t) = \Delta\hat{\theta}_0 + \frac{n_0|c_f|^2}{2}t\Delta\hat{n}_0\,, \tag{11}$$

$$\Delta\hat{p}(t) = \Delta\hat{p}_0\,, \tag{12}$$

$$\Delta\hat{x}(t) = \Delta\hat{x}_0 + 2t\Delta\hat{p}_0\,, \tag{13}$$

with the following commutation relations:

$$\left[\Delta\hat{n},\,\Delta\hat{\theta}\right] = i\,, \quad [\Delta\hat{x},\,n_0\Delta\hat{p}] = i\,. \tag{14}$$

These are among the usual forms of commutation relations for photon number and phase, and momentum and position. All other pairs of operators commute with each other.

Eqs. (10)-(13) show that the photon number and momentum do not change (integrals of motion). However, their initial fluctuations cause a spread of the phase and position. On one side, it is these spreads that are used for generating number-phase and momentum-position quadrature squeezing. On the other side, in the QND measurements they appear as the sources of extra noise which veil desirable information encoded into the soliton. Control over the extra uncertainties, their decrease and cancellation, is the goal of the rest of the paper.

3. PROPAGATION OF A SOLITON THROUGH A NEAR-RESONANT TWO-LEVEL MEDIUM

A observation of the structure of Eqs. (10)-(13) immediately reveals the way how to reverse the extra noise back. For that, one has to reverse the sign of distance t. It is formally equivalent to simultaneous change of signs of dispersion and nonlinearity in Eq. (1). A NLS soliton, propagating through such medium would accumulate phase and position

fluctuations according to (11) and (13), but now with negative signs prior to the evolution terms. A combination of the optical fiber and such hypothetical medium would allow us a decrease or full cancellation of the extra noise. In the latter case, the soliton experiences neither classical nor quantum changes, as if it propagated through *vacuum*. It is the essence of the compensation method.

The mathematical formulation of the compensation concept is quite clear. However, a practical implementation of the idea needs a suggestion of a real medium. Optical fibers are not good candidates for that. Though regions of positive dispersion are available in silica fibers, the negative sign of the Kerr nonlinearity is not possible. A solution comes with use of a NRTLS.

A resonant interaction is described by a coupled wave equation for the field and Bloch equations for the medium. When a pulse shorter than polarization and population decay times enters the medium the self-induced transparency (SIT)[10,11] effect arises. If area of the pulse exceeds a value of π, the pulse will form a SIT soliton (2π-pulse) or break into a sequence of SIT solitons. The soliton emerges due to a self-consistent coherent dynamics between resonantly absorbing medium and specially shaped optical field: the leading edge of the pulse is absorbed exciting the two-level system, while the trailing edge induces stimulated emission from the upper level, thus returning all the absorbed energy back to the soliton. The complete absorption-reemission cycle occurs for the unique pulse with area of 2π and with sech-shape envelope.

SIT and NLS solitons are different in regard of their interaction with nonlinear media. Thus, NLS solitons are shaped by a balance between group-velocity dispersion in fibers and *conservative* nonlinearity of $\chi^{(3)}$-type. The interaction is a virtual one occurring through a far-distanced resonant transition without populating an excited state of the medium. Contrary, SIT solitons are shaped through a real energy transfer from the optical field to atoms and back. Such mechanism of nonlinearity is classified as a *dissipative* one.

The interesting feature of SIT solitons is that they can be formed at any value of detuning of the carrier frequency from exact resonance. With moving away from the resonance the field-matter interaction weakens, the upper level is populated at the lesser extent, and the resonant dissipative response of the medium is gradually transformed into a conservative type of interaction. The intuitive picture can be formally justified by an expansion of Bloch equations into asymptotic series on powers of small parameter $(\delta\tau_p)^{-1}$ with τ_p as soliton's duration and δ as frequency detuning. Indeed, as shown in,[12] the Maxwell-Bloch equations describing the propagation of a short pulse in a two-level system are reduced to a NLSE in the limit of large detunings. Group-velocity dispersion D_{nrtls} and $\chi^{(3)}$-type of nonlinearity N_{nrtls} of the NRTLS give the largest contribution when compared to the other, higher order, near-resonant nonlinearities and dispersion. The higher order corrections appear only in the next order of the perturbation theory. The main advantage of NRTLS is that it exhibits a *negative nonlinearity and positive group-velocity dispersion* for pulses detuned above (below, for the case of amplifier) the resonance and that is not available with conventional fibers. Formally, the NLS equations for the fiber and NRTLS are almost equivalent, differing only in signs of propagation distance. It is this difference that constitutes the key point of our analysis.

The transformation of Maxwell-Bloch equations into NLSE in the NRTLS immediately provides the corresponding transformation of solitons from SIT-type to NLS-type. In that sense, NLS solitons appear as the limiting case of SIT solitons for large values of detuning. The more carrier frequency is shifted off the resonance, the better the SIT-to-NLS transformation is. Thus, the perfect NLS soliton appears relatively far from the resonance line. Practically, the value of detuning solely depends on a particular application.

Without going into details of the asymptotic expansion of Maxwell-Bloch equations, we borrow from[12] the final result in the form of classical NLSE. A generalization of it to the description of quantized fields can be justified by a phenomenological reference to the corresponding principle of quantum mechanics, and to the rigorous derivation of Hillery and Mlodinow in.[13] There, the authors performed quantization of the two-level system, and derived a quantized NLSE in the limit of large detunings. So, we are in position to write

$$i\frac{\partial\hat{\varphi}}{\partial t'} = \operatorname{sgn}(D_{\text{nrtls}})\frac{\partial^2\hat{\varphi}}{\partial x'^2} + 2c_{\text{nrtls}}\hat{\varphi}^{\dagger}\hat{\varphi}^2 . \tag{15}$$

Here $t' = |D_{\text{nrtls}}|z$ is normalized distance and $x' = \bar{t} - (n_{\text{nrtls}}/c)z$ is retarded time. Near-resonant dispersion and nonlinearity are determined through the medium parameters as

$$D_{\text{nrtls}} = \frac{S}{c\delta} \quad \text{and} \quad N_{\text{nrtls}} = -\left(\frac{d}{\hbar}\right)^2 \frac{\hbar\omega}{\mathcal{A}_{\text{nrtls}}}\frac{S}{c\delta} . \tag{16}$$

$n_{\rm nrtls}$ is the nonresonant refractive index, d is the dipole moment, $\mathcal{A}_{\rm nrtls}$ is the cross-sectional area of the beam in the resonant medium, and S is the coupling strength,

$$S = \frac{2\pi\omega_{ab}Nd^2}{\hbar\epsilon_0 n_{\rm nrtls}\delta^2}\,, \tag{17}$$

where ω_{ab} is the frequency of the optical transition and N is the concentration of two-level systems. Similarly to the case of optical fibers, $c_{\rm nrtls}$ is given by the half of ratio of the nonlinearity and absolute value of dispersion, $c_{\rm nrtls} = N_{\rm nrtls}/2|D_{\rm nrtls}|$.

Definitions (16) clearly demonstrates that nonlinearity and dispersion of a NRTLS *always* have opposite signs, and, hence, the medium supports soliton propagation for any sign of detuning. Here, we are interested in the case of negative nonlinearity and positive dispersion, which are possible with the carrier frequency of the pulse detuned above (below, for the amplifier) the frequency of the resonant transition. Such choice gives $\mathrm{sgn}(D_{\rm nrtls}) > 0$ and $c_{\rm nrtls} < 0$, that is opposite to the case of optical fibers. Then, two NLSE (1) and (15) look identically differing only in signs prior to distances t and t'.

Formal identity of the master equation for quantized fields in NRTLS and quantum NLSE allows us to apply the soliton perturbation theory developed for the case of optical fibers in the previous section. Eq. (15) has a solution in the form of fundamental soliton:

$$\begin{aligned}\varphi_0(x',t') &= \frac{\tilde{n}_0\sqrt{|c_{\rm nrtls}|}}{2}\,\mathrm{sech}\left[\frac{\tilde{n}_0|c_{\rm nrtls}|}{2}(x'-\tilde{x}_0+2\tilde{p}_0t')\right]\times \\ &\quad \exp\left[i\tilde{p}_0(x'-\tilde{x}_0)+i\tilde{p}_0^2t'+i\tilde{\theta}_0+i\theta_{\rm nrtls}\right]\,.\end{aligned} \tag{18}$$

with parameters $\tilde{n}_0$, $\tilde{p}_0$, $\tilde{\theta}_0$, and $\tilde{x}_0$ introduced in the same way as for the solution (7). Nonlinear phase shift evolves with distance as

$$\theta_{\rm nrtls} = -\frac{\tilde{n}_0^2|c_{\rm nrtls}|^2}{4}t'\,. \tag{19}$$

Performing linearization of quantum field $\hat{\varphi}$ near the classical solution φ_0 and formulating four collective operators associated with initial quantum perturbations of photon number, phase, position, and momentum, we end up with definitions of four soliton operators at a given point t' as

$$\Delta\hat{\tilde{n}}(t') = \Delta\hat{\tilde{n}}_0\,, \tag{20}$$

$$\Delta\hat{\tilde{\theta}}(t') = \Delta\hat{\tilde{\theta}}_0 - \frac{\tilde{n}_0|c_{\rm nrtls}|^2}{2}t'\Delta\hat{\tilde{n}}_0\,, \tag{21}$$

$$\Delta\hat{\tilde{p}}(t') = \Delta\hat{\tilde{p}}_0\,, \tag{22}$$

$$\Delta\hat{\tilde{x}}(t') = \Delta\hat{\tilde{x}}_0 - 2t'\Delta\hat{\tilde{p}}_0\,. \tag{23}$$

Similarly to (14), the operators obey commutation relations:

$$\left[\Delta\hat{\tilde{n}},\,\Delta\hat{\tilde{\theta}}\right] = i\,,\quad \left[\Delta\hat{\tilde{x}},\,\tilde{n}_0\Delta\hat{\tilde{p}}\right] = i\,. \tag{24}$$

4. ON COMPATABILITY OF FIBERS AND RESONANT SYSTEMS

The above analysis considers propagation of quantized fields through optical fibers and near-resonant two-level systems. For the fields detuned above the resonant transition, the two media appear as mirror reflections of each other. That is, any evolution of an optical pulse in one medium will be reversed when afterwards the pulse enters the other medium. The combination of these two systems offers a unique possibility of control over classical, and what is more important, over quantum properties of optical pulses.[1,2] In order to achieve the goal, we have to formulate proper matching conditions for linking fibers with resonant media particularly concentrating on transmission of solitons rather than pulses of arbitrary shape.

First of all, assuming a lossless interconnection between the two media, we must satisfy the obvious requirement that the soliton at the output of the fiber simultaneously appears as a soliton at the input of the resonant medium. Therefore the number of photons, durations, and frequencies of both pulses should be equal:

$$n_0 = \tilde{n}_0\,,\quad n_0|c_f| = \tilde{n}_0|c_{\rm nrtls}|\,,\quad p_0 = \tilde{p}_0\,. \tag{25}$$

Thus, we derive $|c_f| = |c_{\rm nrtls}|$, which can be rewritten as the requirement for the dipole moment:

$$d = \hbar \sqrt{\mathcal{A}_{\rm nrtls} \frac{N_f}{|D_f|}} = \hbar \sqrt{\frac{\mathcal{A}_{\rm nrtls}}{\mathcal{A}_f} \frac{2\pi}{\lambda} \frac{n_2}{|k''|}}, \tag{26}$$

A similar requirement for the dipole moment appears in,[14,15] where the NLS-SIT-soliton propagation in ion-doped fibers has been discussed. The mixed propagation medium implies an equality between cross-sectional areas, and then (26) turns into the rigid condition which leaves no realistic possibility of finding an atom with a prescribed value of dipole moment. Contrary, our scheme suggests the use of the two media as spatially separated blocks. Therefore we gain an additional "degree of freedom" associated with the possibility of controlling the ratio of the cross-sectional areas $\mathcal{A}_f$ and $\mathcal{A}_{\rm nrtls}$. Obviously, this is hardly possible when the resonant impurities are embedded directly into the optical fiber.

Now, we turn to next requirement. The description of NRTLS in the form of NLSE (15) is valid only if pulse duration τ_p satisfies the inequality

$$\gamma < \tau_p^{-1} < \delta, \tag{27}$$

where γ is the half width at half maximum (HWHM) of the absorption linewidth. The left inequality in (27) provides the coherent type of the field-matter interaction, which is necessary for a SIT experiment. Typical soliton's duration lies in range of $1 \div 10$ ps, therefore (27) becomes possible for resonant media with relatively narrow linewidths, < 1 THz. The right inequality in (27) is the key element of the asymptotic technique for making a reduction of original Maxwell-Bloch equations to NLSE.

The restriction on the value of detuning is not too rigid. Indeed, a NLS soliton simultaneously appears as a SIT soliton in a NRTLS, such that the solution (18) also satisfies the full system of Maxwell-Bloch equations. The only difference appears in the dispersion relation, namely in frequency and photon number dependence of phase $\theta_{\rm nrtls}$ and group velocity $v_{\rm g}$. So, operating close to a resonance, which involves higher order nonlinearities and dispersion, does not perturb the soliton shape, as shown in.[12] However, an additional phase noise arises due to the frequency uncertainty, and an additional position noise is induced by uncertainty in the photon number.[16]

There is a practical advantage for detuning relatively far from the resonance, where NLSE by its own, without higher order corrections, gives an adequate description. The problem with operating close to the resonance is that a short pulse typically interacts with more than two states of an atom. Fine and hyperfine splittings of each of two atomic electronic levels make the picture more complicated than a simple two-level model. The pulse appears to be simultaneously involved into resonant interactions with several transitions between the sublevels of the two manifolds. Since in general, the transitions have different oscillator strengths, it becomes unrealistic to satisfy transparency conditions (pulse area is an integer of 2π) for all of them. However, the condition of transparency weakens for the far detuned pulses, when the dissipative nonlinearity with real excitation-deexcitation cycles changes to the conservative $\chi^{(3)}$-nonlinearity with virtual population of upper states. Then, (15) will keep the same form with nonlinearity and dispersion redefined as

$$D_{\rm nrtls} = \sum_m^M \frac{S_m}{\delta_m c} \quad \text{and} \quad N_{\rm nrtls} = -\frac{\hbar\omega}{\mathcal{A}_{\rm nrtls}} \sum_m^M \left(\frac{d_m}{\hbar}\right)^2 \frac{S_m}{\delta_m c}, \tag{28}$$

where, index m numerates the transition with dipole moment d_m detuned by δ_m from the carrier frequency of the pulse, and M stands for the total number of the transitions. Thus, NRTLS appears to be insensitive to a particular structure of energy levels provided a pulse is far detuned from any of the resonant transitions.

We now address the problem of losses inevitably appearing in any dispersive medium. This issue gains a particular importance in experiments with quantum solitons, where unitary evolution of the quantum field must be preserved. The intensity loss coefficient for a NRTLS is derived in,[12]

$$2\Gamma_{\rm nrtls} = 2\gamma S/c, \tag{29}$$

and for the total loss on length $l_{\rm nrtls}$ we get

$$\text{Loss}\,[\text{dB}] = 4.343(\gamma\delta)|D_{\rm nrtls}|l_{\rm nrtls}\,. \tag{30}$$

We have summarized the desirable properties of the resonant medium in terms of the requirements on the three parameters: cross-sectional area $\mathcal{A}_{\text{nrtls}}$, detuning δ, and polarization decay rate γ; and now present some practical numerical estimations of those values for different types of resonant media. Orienting to fiber optical communications, we shall consider only those media which absorb (emit) the radiation in the transparency window around $1.5\,\mu$m wavelength region. So we come up with two examples: atomic medium — barium ($6s5d\,^1D_2 - 6s6p\,^1P_2^0$ transition with $\lambda = 1.5\,\mu$m), and $1.5\,\mu$m excitonic transitions in InGaAs. With typical values of dispersion $k'' = -12$ ps^2/km at $1.5\,\mu$m and nonlinearity as $n_2 = 1.2 \times 10^{-22}$ m^2/V^2, we rewrite (26) as the equation for the cross-section of the beam in NRTLS:

$$\mathcal{A}_{\text{nrtls}} = \left[5.2 \times 10^{28} d(C\,m)\right]^2 \mathcal{A}_f\,. \tag{31}$$

Excitonic transitions in InGaAs at liquid helium temperatures decay radiatively with time constant $T_1 = 500$ ps,,[17] corresponding to the dipole moment, $d = 76$ D$= 2.3 \times 10^{-28}$ C m. For cross-sectional area in the fiber $\mathcal{A}_f = 50\,\mu$m^2 with $4\,\mu$m in radius we get a radius in InGaAs sample of $48\,\mu$m, which is 12 times larger than that in the fiber. The same calculations for the radius in a barium cell with $T_1 = 200$ ns and $d = 3.6$ D$= 1.1 \times 10^{-29}$C m,[18] yields $2.4\,\mu$m.

Another critical issue arises as a requirement on small losses inside a NRTLS. Contrary to the common belief that for large dispersion/nonlinearity one has to pay a high price in the form of substantial losses, our numerical examples show comparable or even smaller attenuation in the NRTLS than that in a fiber with minimum losses of ~ 0.2 dB/km. A soliton propagating $l_f = 1$ km in the fiber experiences a total loss of 0.2 dB. On the other hand, for the full compensation of dispersion one needs a sample of $In_{0.53}Ga_{0.47}As$ of length $l_{\text{nrtls}} = 250$ nm or a cell with barium vapors of length $l_{\text{nrtls}} = 630\,\mu$m with total losses of ~ 0.3 dB and < 0.01 dB, correspondingly (detuning is taken as $\delta = 1$ THz). For the calculation we use (30) where the compensation condition (40) is substituted. The necessary numerical values for $In_{0.53}Ga_{0.47}As$: $\gamma = 140$ GHz (HFHM) and electron concentration of $N = 10^{15}$ cm^{-3}, are borrowed from.[17] The values for barium vapors: $\gamma < 20$ GHz and atomic concentration of the lower excited state $N = 5 \times 10^{14}$ cm^{-3} are taken from.[18]

Along with resonant absorption, the propagation of an optical pulse through a semiconductor waveguide is inevitably accompanied by nonresonant loss of various origin, the majority of which are free-carrier absorption, surface and interface scattering, and radiation leakage. Experimental measurements of propagation losses (Γ_s in our notations) in GaAs/AlGaAs,[19] give a value of 0.19 dB/cm. So, the total propagation losses in a semiconductor NRTLS of 250 nm in length are as small as 5×10^{-6} dB, that is definitely negligibly small.

The parameters of the semiconductor sample considered in the above example are far from ideal. The state of the art of growing semiconductor structures allows us to further decrease resonant losses. The value of $\gamma = 140$ GHz (HFHM) for InGaAs lattice used in our calculations is already of the order of the homogeneous linewidth[20] and hence is close to the limit of narrowness. However, the recent photoluminescence measurements of the linewidth of the bound-exciton transition in a high-purity n-type InP epilayer have overcome the limit, giving a much smaller value of $\gamma = 14$ GHz (HFHM).[21] Further dramatic narrowing in linewidth becomes possible with semiconductor quantum dots. The elastic scattering of carriers, which is responsible for the rapid dephasing process in two-dimensional and bulk systems, becomes inefficient in a zero-dimension structure. It is due to the discrete density-of-states and the absence of energy versus momentum dispersion, such that no elastic process to flip the electron spin can occur because there is no state available between the levels. A study on the spin relaxation in the zero-dimensional nanostructure (in InGaAs quantum disk) gives a value of $T_2 = 900$ ps,[17] which is two orders of magnitude less than that in bulk and two-dimensional structures. Promising results with densely packed and self-organized semiconductor dots in GaAs have been reported,[22] where the bound-exciton absorption line is estimated to be as narrow as 8 GHz (HFHM), and the measured homogeneous lifetime is $T_2 = 300$ ps.

The list of examples of atomic systems is also not complete. Along with barium, noble gases possessing large dipole moments, ~ 1 D, and narrow absorption lines, ~ 1 GHz, can be considered good candidates for a NRTLS in soliton transmission lines. At least 20 transitions between excited states of argon, krypton and neon in the 1.3- and 1.5-μm regions[23] are suitable for this purpose. We note here, that typical companions of fibers — rare-earth ions, are impractical. Their dipole moments are 1000 times smaller, and then, condition (31) requires an unrealizable focusing a light beam emerging from a single-mode fiber into the million times smaller spot.

The requirements are not so severe for purposes other than fiber communications, for example for quantum optical experiments with solitons. The range of wavelengths becomes wider and media other than silica fibers, i.e. photonic band-gap structures, can be used.

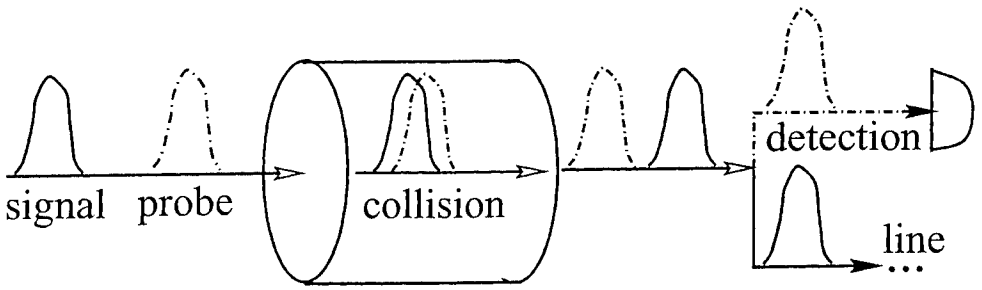

Figure 1. A schematic picture of quantum nondemolition measurements of solitons via collision of solitons in a fiber. An information about photon number of the signal soliton (solid line) is recorded into the phase of the probe soliton (dash-dot line). After emerging from the fiber, the solitons are separated. The phase of the probe soliton is measured my the detector. The signal soliton remains undisturbed and can be directed to a line for a further use.

5. QUANTUM NONDEMOLITION MEASUREMENTS OF OPTICAL SOLITONS

Usually an act of quantum measurement disturbs the system being observed. However, every quantum measurement does not necessarily disturb the variable being measured, and, if it occurs, the measurement satisfies the requirements for a QND measurement.[24,25] Such a measurement affects only a conjugate variable, leaving the QND observable unperturbed.

Measuring the photon number using collisions of coherent solitons in optical fibers[5,26-28] is a new technique for performing a QND measurement, see Fig. 1. If two solitons in an optical fiber have different center frequencies and/or photon numbers, they move with different velocities and can eventually collide. After a collision the two solitons experience only timing and phase shifts, retaining their shapes, velocities and energies. If the phase shift of one soliton (probe soliton) is measured, it is possible to determine the photon number of the other soliton (signal soliton). Since the photon number of a soliton changes neither with propagation nor by interaction with other solitons, the photon number of the signal soliton is a QND observable — noise is introduced only into the soliton's phase. This implies, in principle, that a signal soliton can be observed by an infinite number of QND receivers.

As a general rule, a sensitivity of a QND scheme is limited by so-called back-action noise.[29] In a QND measurement with optical solitons the phase of the probe soliton is correlated with photon number of the signal soliton, due to cross phase modulation, and simultaneously carries unwanted information about its own photon number, due to self-phase modulation. The latter effect severely limits the correlations, since an uncertainty of the probe soliton is recorded onto the probe phase along with the useful information. This back-action noise due to self-phase modulation is caused by a nonlinear evolution of initial quantum fluctuations in soliton parameters. Though the initial noise is stochastic by nature, for example caused by spontaneous emission while generating the soliton, its evolution in the fiber is governed by the deterministic equation — quantum NLSE. Therefore, in principle, the extra fluctuations accumulated during the propagation in nonlinear fibers can, in principle, be overcome. To our knowledge, two ways were proposed to cancel the unwanted probe excess noise.

One strategy, described by Drummond, Breslin and Shelby in,[30] exploits the fact, that the excess phase noise of the probe is correlated to the photon number of the probe. The authors show, that it is possible to measure an appropriate output quadrature variable which is a combination of phase and amplitude and thus reveal the correlation. While being a promising candidate for a QND measurement, this technique, nevertheless, does not compensate the back-action noise in full. The detection scheme in use is essentially linear and, thus, cannot remove a part of the back-action noise arised beyond the linearization approximation. Also, the technique proposes the method for measuring an alternative quadrature, while the original QND of number of photons does not gain an improvement.

The other strategy, proposed in,[31] utilizes a scheme where two SIT-solitons collide in a resonant medium. An important advantage of this technique is that it implies that the probe soliton being tuned to the exact resonance, where self-phase modulation is zero, exhibits a phase shift, which is dependent on the signal soliton's photon number and does not depend on number of photons in the probe soliton. However, as can be easily deduced from the formalism developed by Lai and Haus in,[16] the phase of a resonant SIT-soliton always carries unwanted information

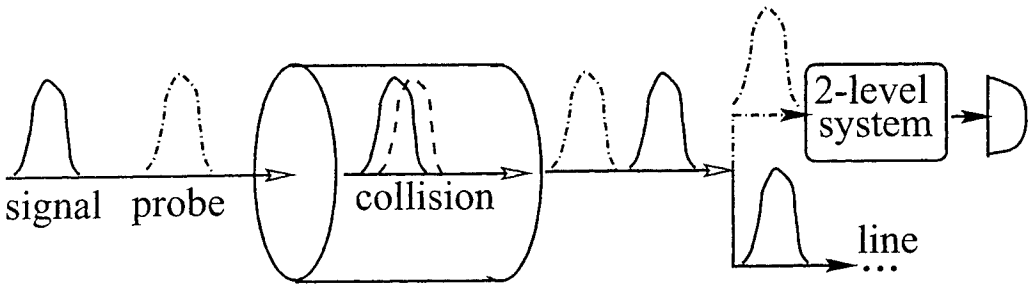

Figure 2. The compensation method applied for quantum nondemolition measurements of solitons. The setup in Fig. 1 is supplemented by a near-resonant two-level medium placed prior to detection of the probe soliton. In such a way, a self-phase modulation noise of the probe soliton accumulated while propagation in the fiber is canceled.

about the uncertainty of the soliton carrier frequency. This introduces a new source of back-action noise into the QND measurement with resonant solitons. The noise does not allow a real improvement in accuracy of the QND measurement, since its intensity is of approximately the same value as that of the noise due to self-phase modulation.

We here present a new method to cancel the back-action noise due to self-phase modulation in an optical fiber. This is accomplished by inserting a NRTLS prior to the detector of the probe soliton in the conventional collisional QND scheme,[5,26] as shown in Fig. 2. A mathematical description of dynamics of the solitons can be developed on the basis of the soliton perturbation theory after an appropriate generalization of it to the case of two-soliton collision. Instead of the detailed and rigorous formalism we better choose brief and more illustrative way. Though being less formal, it will give us correct results.

Let us consider in detail the modified collisional QND scheme. Signal and probe solitons collide in a single-mode optical fiber. After the collision the probe soliton experiences a phase shift, which includes two different contributions,[32] $\theta_{\rm xpm}$ and $\theta_{\rm spm}$,

$$\theta(l_f) = \theta_0 + \theta_{\rm xpm} + \theta_{\rm spm}\,, \tag{32}$$

where l_f is the length of the optical fiber. The first term is the initial phase, which we put to zero without a loss of generality. The second term in (32) carries useful information about the parameters of the signal soliton, which is transcribed onto $\theta_{\rm xpm}$ due to cross-phase modulation. The third term, $\theta_{\rm spm}$, appears as a result of self-phase modulation and contains unwanted information about the probe soliton itself.

Any soliton inevitably possesses initial uncertainties in photon number Δn_0 introduced on the stage of the soliton's preparation. As a result of the fiber nonlinearity the phase of the soliton depends on the photon number, and linearly increases with propagation distance, as in (11). For an initially coherent probe soliton the uncertainty in phase due to self-phase modulation becomes comparable with the initial phase uncertainty θ_0 at a distance as small as $z_{\rm sp}/8\pi$, where $z_{\rm sp}$ is the soliton period. Since a collisional scheme requires well separated solitons at the input and output, the fiber length must necessarily exceed one soliton period. At such lengths, the noise due to self-phase modulation becomes more than 25 times larger than the shot-noise limit. The enormous extra noise makes senseless all advantages of the QND scheme, which potentially might perform a nondestructive measurement of the photon number with the accuracy beyond the shot-noise limit. This points up the seriousness of the self-induced phase noise in soliton propagation, as noted in.[5]

Now the modified QND scheme implies that after the collision the probe soliton enters a NRTLS with negative $\chi^{(3)}$-nonlinearity acquiring a new phase shift $\theta_{\rm nrtls}$. Phase rotation goes in the reverse direction and the self-induced phase shift in the fiber $\theta_{\rm spm}$ can be completely canceled by a proper choice of the length of the NRTLS $l_{\rm nrtls}$, such that a final phase shift measured by a detector

$$\theta(l_f + l_{\rm nrtls}) = \theta_0 + \theta_{\rm xpm} + \theta_{\rm spm}(l_f) + \theta_{\rm nrtls}(l_{\rm nrtls})\,, \tag{33}$$

becomes

$$\theta(l_f + l_{\rm nrtls}) = \theta_0 + \theta_{\rm xpm}\,, \tag{34}$$

when compensation condition $\theta_{\rm spm}(l_f) = -\theta_{\rm nrtls}(l_{\rm nrtls})$ is held. So, the backaction noise due to self-phase modulation is avoided, while keeping the information about the signal ($\theta_{\rm xpm}$) unchanged. The proposed method of noise filtration is essentially nonlinear in the sense that it does not rely on a linearization procedure, and therefore it allows us to cancel the backaction noise in full. Additionally, we use the system far from the resonance, and an uncertainty in frequency does not contribute to the phase, like it happens for the case of resonant SIT solitons.

After a collision the probe soliton retains its shape and photon number,

$$\phi(x,t) = \frac{n_0|c_f|^{1/2}}{2}\mathrm{sech}\left[\frac{n_0|c_f|}{2}(x - x_0 - x_{\rm xpm} - 2p_0 t)\right] \exp\left[ip_0(x - x_0 - x_{\rm xpm}) - ip_0^2 t + i(\theta_0 + \theta_{\rm xpm} + \theta_{\rm spm})\right] \tag{35}$$

[parameters of the probe(signal) soliton are supplied with index "0"("s")], where the phase shift $\theta_{\rm xpm}$ and position shift $x_{\rm xpm}$ of the probe soliton due to the scattering is given by[32]

$$\tan\left(\frac{\theta_{\rm xpm}}{2}\right) = \frac{4\,n_s\,|c_f|\,(p_0 - p_s)}{(n_0 - n_s)^2|c_f|^2 + 4\,(p_0 - p_s)^2}\,, \tag{36}$$

$$t_{xpm} = \frac{2}{n_0\,|c_f|}\ln\left[\frac{(n_0 - n_s)^2|c_f|^2 + 4\,(p_0 - p_s)^2}{(n_0 + n_s)^2|c_f|^2 + 4\,(p_0 - p_s)^2}\right]\,, \tag{37}$$

where n_s and p_s are the photon number and the momentum per photon (frequency) of the signal soliton. The phase shift due to self-modulation in the optical fiber $\theta_{\rm spm}$ is determined by (8).

The soliton of the form of (35) then enters a NRTLS, where the master equation (15) supports its own fundamental soliton solution (18) with nonlinear phase shift given by (19). The soliton at the output of the fiber simultaneously appears as a soliton at the input of the NRTLS, if matching conditions (25) are satisfied. Also, the initial values of position and phase, $\tilde{t}_0$ and $\tilde{\theta}_0$, obviously coincide with the corresponding values of those at the fiber output:

$$\tilde{t}_0 = t_0 - t_{\rm xpm} - 2p_0|D_f|l_f\,, \tag{38}$$

$$\tilde{\theta}_0 = \theta_0 - \theta_{\rm xpm} - \theta_{\rm spm}(l_f)\,. \tag{39}$$

Finally, at the output of the NRTLS, i.e. for the whole transmission line of length $l = l_f + l_{\rm nrtls}$, the accumulated phase shift (34) contains only initial phase θ_0 and useful information about the signal photon number encoded in $\theta_{\rm xpm}$. The total compensation of nonlinear noise takes place for properly adjusted length of the NRTLS as

$$l_{\rm nrtls} = \frac{|D_f|}{|D_{\rm nrtls}|}\,l_f\,, \tag{40}$$

Eq. (40) implies only knowledge of values of dispersion of both media, so that the proposed QND setup can be constructed without *a priori* knowledge of the parameters of the solitons in use.

The above discussion is very simple and presented in purely classical terms. However, it remains valid even in quantum domain. Indeed, if the initial perturbation of photon number $\Delta\hat{n}_0$ is an operator, the corresponding quantum phase $\hat{\theta}$ at any distance t can be expanded (in linear approximation) as

$$\hat{\theta}(t) = \theta + \Delta\hat{\theta} = \left(\theta_0 + \frac{n_0^2|c_f|^2}{4}t\right) + \left(\Delta\hat{\theta}_0 + \frac{n_0|c_f|^2}{2}\Delta\hat{n}_0 t\right)\,, \tag{41}$$

just as in (11). Matching conditions (25) have a straightforward generalization to the operator equalities

$$\Delta\hat{n}_0 = \Delta\hat{\tilde{n}}_0\,, \quad \Delta\hat{n}_0|c_f| = \Delta\hat{\tilde{n}}_0|c_{\rm nrtls}|\,, \quad \Delta\hat{p}_0 = \Delta\hat{\tilde{p}}_0\,, \tag{42}$$

and all the above reasoning on the cancellation of accumulated nonlinear phase is readily reproducible, now in terms of quantum fluctuations. Obviously, all the conclusions remain valid beyond the linearization.

There is one important issue, which should not be forgotten in the above extension of the results into quantum domain. It is that number and phase operators do not commute, see (14), and therefore obey a corresponding

Heisenberg uncertainty relation. Thus, contrary to a classical consideration the number and phase uncertainties cannot simultaneously vanish.

A close look at the structure of cross-phase modulation term (36) reveals its dependence not only on signal photon number n_s, but also on momenta p_0 and p_s of the two solitons. Therefore, while measuring θ_{xpm} fluctuations of the frequencies deteriorate the accuracy of inference of n_s. Typically, this noise is rather small and can be decreased farther by a proper choice of parameters of the probe soliton.[30] The cross-phase θ_{xpm} also contains n_0. The dependence is of self-phase modulation origin, and n_0 together with its fluctuations can be eliminated from θ_{xpm} by use of the compensation technique, in the similar manner as it is done for elimination of θ_{spm}. So instead of zero path-average dispersion which provides the exact cancellation of θ_{spm}, one needs now to detune slightly from the zero point.

It is worth to mention a possibility of a QND measurement of momentum (frequency) of a soliton in close analogy with the above-described measurement of the photon number. The compensation technique will again provide an improved accuracy by eliminating the extra-noise caused by the group-velocity dispersion.

6. CONCLUSION

We present the method of cancellation of the extra noise, which is accumulated by a soliton of NLSE while propagating in nonlinear fibers. The extra noise appears in the soliton's phase due to its dependence on photon number through the effect of self-phase modulation. The method is based on the fact, that a NRTLS is formally described by a NLSE, and can exhibit negative nonlinearity and positive group-velocity dispersion, that is impossible in silica fibers. So, a fluctuation with positive sign accumulated in one medium will evolve in reverse direction in the other. A combination of the two media allows us a control over the sign and value of nonlinearity and dispersion (and hence, over fluctuations), for example in such a way that the path-average nonlinearity and dispersion of the combination may turn into zero. It is this combination that effectively acts as a vacuum for a soliton and is at the heart of the compensation method.

QND measurement of a soliton is based on cross-phase modulation appearing when two solitons collide in a nonlinear fiber. Through the cross-talk, the information about the number of photons in one soliton is recorded into the phase of the other (probe) soliton. Together with this useful information, an extra noise is accumulated in phase of the probe soliton due to self-phase modulation. The extra noise can be compensated, if the probe soliton after the fiber passes through the NRTLS, thus canceling the overall path-average nonlinearity. Then, the fluctuations due to self-phase modulation disappear completely, while the cross-phase modulation term remains unchanged. The accuracy of the QND in such setup reaches its maximum. Numerical estimations with existing gaseous media and semiconductor structures are provided. The media are proved to be good candidates as NRTLS for the compensation method demonstrating compatibility with optical fibers.

7. ACKNOWLEDGMENTS

VVK is grateful for numerous illuminating discussions with A. Basharov, J.H. Eberly, A.I. Maimistov, N.N. Rosanov, and I.V. Sokolov. Work was supported by the Rochester Theory Center, Russian Foundation for Basic Research # 97-02-16013-a and 00-02-17014, and Russian Federal Program "Fundamental Metrology".

REFERENCES

1. V.V. Kozlov and A.B. Matsko, J. Opt. Soc. Am. B **16**, 519 (1999).
2. A.B. Matsko, V.V. Kozlov, and M.O. Scully, Phys. Rev. Lett. **82**, 3246 (1999).
3. P. D. Drummond and S. J. Carter, J. Opt. Soc. Am. B **4**, 1565 (1987).
4. D. J. Kaup, J. Math. Phys. **16**, 2036 (1975).
5. H.A. Haus, K. Watanabe, and Y. Yamamoto, J. Opt. Soc. Am. B **6**, 1138 (1989).
6. H.A. Haus and Y. Lai, J. Opt. Soc. Am. B **7**, 386 (1990).
7. A. B. Matsko and V. V. Kozlov, Phys. Rev. A **62**(2), # 0238XX (2000).
8. Y. Lai and H. A. Haus, Phys. Rev. A **40**, 844 (1989); **40**, 854 (1989).
9. F. X. Kärtner and L. Boivin, Phys. Rev. A **53**, 454 (1996).
10. S. L. McCall and Hahn, Phys. Rev. Lett. **18**, 908 (1967).

11. S. L. McCall and Hahn, Phys. Rev. **183**, 457 (1969).
12. V.V. Kozlov, J. Opt. Soc. Am. B **14**, 1765 (1997).
13. L. Hillery and M. Mlodinow, Phys. Rev. A **55**, 678 (1997).
14. A.I. Maimistov and E.A. Manykin, Sov. Phys. JETP **58**, 685 (1983).
15. M. Nakazawa, E. Yamada, and H. Kubota, Phys. Rev. A **44**, 5973 (1991).
16. Y. Lai and H.A. Haus, Phys. Rev. **A 42**, 2925 (1990).
17. H. Gotoh, H. Ando, H. Kamada, A. Chacez-Pirson, and J. Temmyo, Appl. Phys. Lett. **72**, 1341 (1998).
18. R. W. Falcone and G. A. Zdasiuk, Opt. Lett. **5**, 155 (1980).
19. Y.T. Byun, K.H. Park, S. H. Kim, S.S. Choi, and T.K. Lim, Appl. Opt. **35**, 928 (1996).
20. M. Sugawara, T. Fujii, S. Yamazaki, and K. Nakajima, Appl. Phys. Lett. **54**, 1353 (1989).
21. R. Benzaquen, R. Leonelli, and A.P. Roth, Phys. Rev. B **52**, 1485 (1995).
22. H. Oohashi, H. Ando, and H. Kanbe, Phys. Rev. B **54**, 4702 (1996).
23. A.J. Lucero, Y.C. Chung, S. Reilly, and R.W. Tkach, Opt. Lett. **16**, 849 (1991).
24. V.B. Braginsky, Y.I. Vorontsov, and K.S. Thorne, Science **209**, 547 (1980).
25. V.B. Braginsky and F.Ya. Khalili, *Quantum measurement*, Cambrige University Press, 1992.
26. S.R. Friberg, S. Machida, and Y.Yamamoto, Phys. Rev. Lett. **69**, 3165 (1992).
27. Y. Sakai, R.J. Hawkins, S.R. Friberg, Opt. Lett **15**, 239 (1990).
28. S.R. Friberg, T. Mukai, and S. Machida, Phys. Rev. Lett. **84**, 59 (2000).
29. V.B. Braginsky and F.Ya. Khalili, Rev. Mod. Phys., **68**, 1 (1996).
30. P.D. Drummond, J. Breslin, R.M. Shelby, Phys. Rev. Lett. **73**, 2837 (1994).
31. K. Watanabe, H. Nakano, A. Honold, and Y. Yamamoto, Phys. Rev. Lett. **62**, 2257 (1989).
32. V.E. Zakharov and A.B. Shabat, Sov. Phys. JETP **34**, 62 (1972).

Polarization dynamics in non-linear birefringent active fibers

S.O. Elyutin and A.I. Maimistov

Moscow State Engineering Physics Institute, 115409, Moscow, Russia

ABSTRACT

Numerical solutions are obtained of the full self-consistent system of equations for the counter rotating polarization components of the field of short optical pulse propagating in birefringent non-linear fiber and the ensemble of the energy level degenerated dopant resonance atoms implanted in fiber material. In every cross-section of fiber the ellipticity of the polarized wave experiences a complex evolution in time accompanied by rapid changes of the azimuth angle due to interplay of dispersion and Kerr non-linear self- and cross-modulation. The reciprocal effect of the impurities on the traveling pulse causes the oscillations of the pulse envelope able to distort completely the shape of the input signal, while the resonance absorption can drive the birefringence from the non-linear back to linear regime.

Keywords: numerical simulation, polarization, non-linear fiber, resonance impurities, birefringence, short pulse

1. THE MODEL

The quasi-monochromatic field, which propagates along the doped fiber is the sum of two counter-rotating right and left handed circularly polarized modes $e_1(\zeta,\tau)$ and $e_2(\zeta,\tau)$ correspondingly. The complex normalised amplitudes obey the non-linear coupled equations

$$i\frac{\partial e_1}{\partial\zeta}+i\frac{1}{\ell_g}\frac{\partial e_2}{\partial\tau}-\frac{s}{\ell_d}\frac{\partial^2 e_1}{\partial\tau^2}+\frac{1}{\ell_c}e_2+\frac{1}{3\ell_k}\left(|e_1|^2+2|e_2|^2\right)e_1+\left(\frac{Lq}{A_0}\right)P_1=0, \tag{1a}$$

$$i\frac{\partial e_2}{\partial\zeta}+i\frac{1}{\ell_g}\frac{\partial e_1}{\partial\tau}-\frac{s}{\ell_d}\frac{\partial^2 e_2}{\partial\tau^2}+\frac{1}{\ell_c}e_1+\frac{1}{3\ell_k}\left(|e_2|^2+2|e_1|^2\right)e_2+\left(\frac{Lq}{A_0}\right)P_2=0,. \tag{1b}$$

In equations (1) P_1 and P_2 is resonance polarization, $\tau=(t-z/v)t_0^{-1}$, $z=\zeta L$, $v^{-1}=\left(v_1^{-1}+v_2^{-1}\right)/2$, L is a characteristic spatial scale, A_0 is an amplitude scale.

Group-velocity mismatch effect $\ell_g^{-1}=LL_g^{-1}=2^{-1}t_0^{-1}L\left(v_1^{-1}-v_2^{-1}\right)$, linear coupling $\ell_c^{-1}=LL_c^{-1}=\Delta\beta L$, Kerr-effect $\ell_k^{-1}=LL_k^{-1}=L\chi_{eff}A_0^2(\omega_0^2/2c^2\beta)$, dispersion $\ell_d^{-1}=LL_d^{-1}=Lt_0^{-2}\,|\sigma|$, where

$$L_g=\frac{2v_1v_2t_0}{v_2-v_1},\ L_c=\frac{1}{\Delta\beta},\ L_k=\frac{2\beta c^2}{\omega_0^2\chi_{eff}A_0^2},\ L_d=\frac{t_0^2}{|\sigma|}. \tag{2}$$

$s=\operatorname{sgn}\sigma$, $q=2\pi\omega_0 n_a d_{eff}/cn(\omega_0)$, n_a is the concentration of the impurity atoms, ω_0 is the carrier frequency, σ is the linear dispersion parameter, $\beta_x=\beta+\Delta\beta$ and $\beta_y=\beta-\Delta\beta$, where $\beta_x(\beta_y)$ is the linear propagation constant of the slow (fast) principal axis of the birefringent fiber.

Further information –
S.O.E.(correspondence): E-mail: sergeiPE@mtu-net.ru; Telephone: (095) 323-90-63
A.I.M.: E-mail: maimistov@pico.mephi.ru; Telephone: (095) 323-93-44

Laser Optics 2000: Semiconductor Lasers and Optical Communication, Serguei A. Gurevich, Nikolay N. Rosanov, Editors, Proceedings of SPIE Vol. 4354 (2001) © 2001 SPIE · 0277-786X/01/$15.00

The resonance polarization is defined by the elements of the density matrix of an ensemble of two-level atoms, whose levels are degenerated over the projections of angular momenta j_a and j_b. For the sake of definiteness we will consider the case $j_a = 1 \rightarrow j_b = 0$. The resonance transition is characterised by the element of dipole momentum operator $d_{13} = d_{23} = d_{31}^* = d_{32}^* = d_{eff}$. Following[1], we write the Bloch equations in the form:

$$\frac{\partial p_\alpha}{\partial \tau} = i\nu p_\alpha - if\left(\sum_{q'} e_{\alpha'} m_{\alpha'\alpha} - e_\alpha n\right), \tag{3a}$$

$$\frac{\partial m_{\alpha\alpha'}}{\partial \tau} = -if\left(e_\alpha^* p_{\alpha'} - e_{\alpha'} p_\alpha^*\right), \tag{3b}$$

$$\frac{\partial n}{\partial \tau} = -if\sum_\alpha \left(e_\alpha p_\alpha^* - e_\alpha^* p_\alpha\right), \quad \alpha, \alpha' = 1,2\,. \tag{3c}$$

where $|a,m> = |j_a = 1, m = \pm 1>$ and $|b> = |j_b = 0, m = 0>$. $m_{21} = < a,-1 | \hat{\rho} | a,+1 >$, $m_{11} = < a,-1 | \hat{\rho} | a,-1 >$, $m_{22} = < a,+1 | \hat{\rho} | a,+1 >$, $n = < b | \hat{\rho} | b >$, $p_1 = - < a,-1 | \hat{\rho} | b >$, $p_2 = - < a,+1 | \hat{\rho} | b >$.

Initial conditions are $n(0) = 1, m_{22}(0) = m_{11}(0) = 0, m_{21}(0) = p_1(0) = p_2(0) = 0$. The dimensionless quantities p_α in (3) correspond to the polarization terms in (1) by the relationship

$$\left(\frac{Lq}{A_0}\right) P_\alpha = P_\alpha\left(2L\pi\omega_0 n_a d_{eff} / cn(\omega_0) A_0\right) = < p_\alpha > \frac{L}{L_r} = \frac{1}{\ell_r} < p_\alpha >, \tag{4}$$

where $L_r = cnA_0\left(2\pi\omega n_a d_{eff}\right)^{-1}$. The latter quantity corresponds to the characteristic length of resonance interaction $L_r^{(2\pi)} = \left(cn\hbar\right)\left(\pi d_{eff}^2 \omega_0 n_a t_0\right)^{-1}$ by a relationship $L_r = A_0 A_{2\pi}^{-1} L_r^{(2\pi)}$, where $A_{2\pi} = 2\hbar d_{eff}^{-1} t_0^{-1}$ is the amplitude of the 2π-pulse of SIT effect. In the system of equations (3) $f = d_{eff} A_0 t_0 \hbar^{-1}/2$ is an effective normalized frequency of oscillation of the material variables of resonance subsystem, affected by the field of amplitude A_0, note that $L_r = f L_r^{(2\pi)}$.

The coupled system of the Maxwell-Bloch equations (1) and (3) provides the mathematical basis for the numerical simulation of the propagation of short pulses of circular polarized light in a nonlinear waveguide doped by resonance impurities. The solution of the field equations (1) were obtained by means of one of the popular finite difference implicit-explicit Crank-Nicolson numerical scheme[2] where the desired accuracy 0.001 was reached by iterations. The Bloch equations (3) coupled to the field equations (1) by the resonance polarization terms were solved by the predictor-corrector procedure. The predictor-corrector ran at every iteration in Crank-Nicolson algorithm until the accuracy about 0.001 for polarization components p_q in (3) was achieved. Though the code was able to produce the integration over the inhomogeneously broadened line of resonance absorption, on this stage of numerical simulation we restrict to only homogeneous case and exact resonance, i.e. $\nu = 0$ in (3a). The results of calculations were the absolute value of the complex amplitudes $e_{1,2}(\zeta, \tau)$ of the counter-rotating right and left-handed oppositely polarized fields. Following Winful[3], we examined the polarization state of the field in the optical pulse in terms of azimuth angle $\theta(\zeta, \tau) = \arg(\xi)/2$ and ellipticity $\varepsilon(\zeta, \tau) = \left(|\xi| - 1\right)\left(|\xi| + 1\right)^{-1}$, where complex quantity $\xi = e_1 e_2^{-1}$. The characteristic values of ε are: ε=0 for the linear polarized light, ε=+1 for the purely right hand circularly polarized light, and ε=-1 for the purely left hand circularly polarized light. Parameter θ is an angle between the axis of the polarization ellipse and the slow principal axis of the bire-

fringent fiber. It may vary within the interval (-45^0 - +45^0). The launched pulses are assumed having the *sech* form: $e_{1,2}(0,\tau) = e_{m1,2}\ \mathrm{sech}\left((\tau-\tau_0)\delta^{-1}\right)$, where $\delta = t_{p0}t_0^{-1}$, τ_0 is the temporal co-ordinate of the centre of the input pulse.

2. THE NUMERICAL ESTIMATES

We let the silica-based monomode fiber host material group velocity dispersion[4] $D = 4\pi c\sigma\lambda_0^{-1}$ at λ_0=1,55μm be typically D=15 ps·nm^{-1}·km^{-1}, the non-linear index $n_2 \approx 10^{-13}$ esu, then $\sigma = \left|d^2\beta\ d\omega^2\right|/2 \approx 10^{-28}$s^2·cm^{-1}. The effective nonlinear interaction parameter $\chi_{eff} \approx n_2 n/2\pi \approx 2.3\cdot10^{-14}$esu. We adopt the value of $d_{eff} \approx 5\cdot10^{-21}$ esu (transition $^4I_{5/2}\rightarrow{}^4I_{5/2}$ in Er^{3+} ions) and the impurity concentration $n_a \approx 10^{18}$cm^{-3} that complies the realistic samples[5].

With the input pulse duration $t_{p0} = t_0$ =0.1ps the dispersion length is $L_d = t_0^2\sigma^{-1} \approx 10^2$cm. The polarization modes coupling effect reveals at the distance $L_c = (\Delta\beta)^{-1} \approx \lambda_0(2\pi\Delta n)^{-1} \approx 25$cm. Here we let[6] $\Delta n \sim 10^{-6}$. The effect of group velocities mismatch becomes noticeable at the characteristic distance $L_g = 2v_1v_2(v_2-v_1)^{-1}t_0 \approx 2ct_0\Delta n^{-1} \approx 6\cdot10^4$cm. The spatial scale of the Kerr self- and cross-modulation process L_k depends on the field amplitude A_0: $L_k \approx n\lambda_0(\pi\chi_{eff}A_0^2)^{-1}$. The balance between the fiber group-velocity dispersion and non-linear pulse compression achieves when $L_k = L_d$. That gives the value of the one-soliton solution amplitude of a single non-linear Schrödinger (NLS) equation $A_{NLS} = (\sigma n\lambda_0)^{1/2}(\pi t_0^2\chi_{eff})^{-1/2} \approx 0.5\cdot10^4$esu for a 0.1ps pulse duration. The corresponded length scale is $L_k^{(NLS)} \approx 70$cm. The non-linear Schrödinger one-soliton peak intensity can be estimated as $I_{NLS} = c(A_{NLS})^2/8\pi \approx 4\cdot10^9$W/cm^2.

Another balance equality $L_k = L_c$ yields an electric field strength $A_c = (2n\Delta n\chi^{-1})^{1/2}$ known as a characteristic light wave field for a switch of nonlinear directional cw-waves coupler[7], $A_c \approx 10^4$esu, the intensity $I_c \approx 1.5\cdot10^{10}$ W/cm^2. This is broadly means that with the exceeding of A_c in the input field the nonlinear birefringence, initiated by Kerr processes, begins to have a noticeable effect.

The quantity $L_r^{(2\pi)} = (n\hbar\lambda_0)(2\pi^2 n_a d_{eff}^2 t_0)^{-1} \approx 5\cdot10^2$cm is the distance in resonance sample, where the reciprocal reaction of the medium in the form of polarization and population differences develops to produce a number of coherent transients such as self-induced transparency (SIT)[8], photon-echo[9,10], optical nutations, breather waves[11]. For the signals with small pulse area[11] θ parameter $L_r^{(2\pi)}$ serves as a length of absorption. The pulse area of the NLS soliton is extremely small $\theta_{NLS} = \pi d_{eff}\hbar^{-1}t_0A_{NLS}$ =3·10$^{-3}\pi$ in comparing with $\theta_{SIT} = 2\pi$.

The amplitude of a 0.1ps 2π-pulse is $A_{2\pi} = 2\hbar d_{eff}^{-1}t_0^{-1} \approx 4\cdot10^6$ esu. The peak intensity of the pulse reaches the magnitude of $I_{2\pi} \approx 2\cdot10^{15}$W/cm^2. This well-known result implies that the SIT soliton requires a power approximately 6 orders of magnitude larger than that for the NLS soliton, or that one 2π SIT-pulse corresponds to the hundreds of NLS solitons by power.

3. POLARISATION STATES EVOLUTION IN FIBRE. NUMERICAL ANALYSIS

We can proceed now to examine typical numerical results. We aim on the diagnostic of the temporal profile of the field amplitude and polarization parameters ε and θ at every cross-section of the nonlinear birefringent fiber. We assume the light wave to be in exact resonance with the homogeneously broadened atomic transition, i.e. ν =0. In order not to over complicate the problem we also ignore the walk-off effect in this paper, though we observed some of it obvious results in our preliminary computations. In the numerical simulations demonstrated below in figs.(1-5) the amplitudes of the input pulses were chosen as $e_{m1} = \sqrt{3}/2$, $e_{m2} = 1/2$, while initial phases were 0 and π correspondingly. We also set f =0.0015, thus assuming the resonance interaction being not a strong perturbation process to the fiber effects.

The propagation of the light pulse in undoped birefringent fiber is accompanied by the back and forth coupling between the orthogonal counter-rotating polarization modes with the spatial beat period $2\pi\Delta\beta^{-1}$. No dispersion is involved in the numerical simulation at this stage. For the linear fiber (i.e., when the contribution of the Kerr self- and cross-modulation effect can be yet neglected) the solution of (1) is quite simple (fig.1(a,b)). The period of the partial energy transfer between the modes is $\ell_b = \pi\ell_c$. It is seen from the 3D plot of azimuth θ and the ellipticity ε (fig.1(c,d)) that both functions are uniform across pulse duration and oscillate in the course of propagation inside the fiber[3]. It is worth to note that if the launched pulse amplitudes were $e_{m1} = 1$, $e_{m2} = 0$, the azimuth angle θ would change from -π/4 to π/4 and the polarization state - from a linear polarization (ε=0) to a circular polarization of the opposite direction (ε=±1).

When both polarization modes are excited in the asymmetrical manner, the ellipticity oscillates between elliptical clockwise and elliptical anti-clockwise polarization. It is well seen from the gray scale modular surface of $\theta(\zeta,\tau)$ and $\varepsilon(\zeta,\tau)$.(fig.1 (e) and fig1 (f)). The dark gray up to black corresponds to the maxima of the plotted function while the light gray down to white – to the minima. The phase trajectories on the ε vs θ plane (ε and θ are calculated at the moments of peak intensity of the pulse), parameterized by ζ are the closed circles (fig.1(g)). Each trajectory in this picture associates with the different $\eta = \left(e_{m1}e_{m2}^{-1}\right)^2$ ratio. The outer curve relates to η=999. The subsequent cycles corresponds to η=99, 9, 3, 1.5, and 1.22. The biggest circle is the ultimate trajectory related to a nearly net circularly right hand polarized light while small circles corresponds to a nearly linear polarized light. The circle in open dotes corresponds to the case which was numerically investigated $e_{m1} = \sqrt{3}/2$, $e_{m2} = 1/2$. This numerical picture is in a good accord with one presented in[3] for the cw-waves.

The mutual action of linear birefringence (ℓ_c=0.25) and dispersion (ℓ_d=1.0) (all other terms responsible for fiber effects are omitted in (1)) provides a well interpretable effect of the intensity humps spreading (fig.2(a,b)) in the depth of fiber as it well seen in the gray scale map (fig.2(c,d)). The polarization properties of the travelling field (fig.2(e,f)) in this case are quite similar to those in fig.1. The fields of spikes by both sides of the central area in fig.2(e,f) is the result of the numerical fluctuations provoking the random switchovers of ellipticity ε and azimuth θ on the wings of a propagating pulse, where the field in both polarizations is extremely weak. In fig.2(g) we display the phase plane (ε vs θ) for the coupling plus dispersion case for parameters η= 999, 9, 3, 1.22. The value η=3 corresponds to the case under numerical simulations. The plotted curves are quite similar to those depicted in fig.1(g).

The interference of the linear coupling and the non-linear phase modulation yields the picture not anticipated from the first sight (fig3.). We injected in fiber the pulses of the counter rotating polarization, whose amplitudes in physical units satisfied the conditions $A_{m1} \approx 2A_c$, $A_{m2} \approx A_c$. That corresponds to the choice ℓ_c=0.25 and ℓ_k=0.05 for the characteristic lengths. What one could expect in this case is the Kerr compressing every time when energy couples back to the mode from the conjugate polarization state. Instead, we observe the interference between the coupling processes with different beat periods. The coupling reveals in the form of the inserted cycles when every new growth of the amplitude begins at the time when the previous one have not yet finished. The physical explanation may be found if to note that both input amplitudes are chosen to be of the order of the critical switching (for cw-waves) strength of the electrical field A_c. For such intensities Kerr cross-modulation becomes sufficiently strong to make the birefringence a non-linear process when the beat period may even grow unlimited[12,13]. Attention should be drawn to that the periodicity of the onsets of the back and forth coupling cycles approaches the value prescribed by the choice ℓ_c=0.25 (compare with fig.1). The linear behaviour reveals only on the slopes of the pulse envelope, where the field intensity has not reached the critical value yet. The further growth of the pulse field strength in a pulse envelope forces the beat period to increase as well. The result is seen in fig3(a, b and c, d), where the 3D picture and the gray scale map of the polarization modes dynamics are depicted. The envelopes of the field in both polarization modes experience temporal counter phase modulation in the central part of the propagating waveform (fig.3(h)). The modulation of the amplitudes of the counter rotating polarization modes leads to the oscillation of the ε and θ over τ in the propagating light wave that is clearly seen from the gray scale maps fig.3 (e and f) and on the comparative plots of the fields, ellipticity, and azimuth at the exit from fiber placed in fig.3 (h). Picture (g) on the top of fig.3 shows the (ε,θ) phase plane for the same values of parameter η as it was done above. Unlike the

previous cases, the ultimate circle is distorted that agrees with[3] analysis. This cycle is smeared owing to the complex character of a spatial modulation of the peak intensity of the polarization components.

Our calculations, presented in fig.4, illustrate the combined action of linear birefringence, Kerr nonlinearity, and dispersion. The dispersion length ℓ_d=1 serves as a scale length, while the coupling length ℓ_c and the Kerr length ℓ_k are shorter: ℓ_k=0,1 and ℓ_c=0,25. The choice of parameters dictates the values of the amplitudes of polarization modes at the entrance to fiber $A_{m1} \approx \sqrt{2}A_c \approx 2.7A_{NLS}$, $A_{m2} \approx 0.8A_c \approx 1.6A_{NLS}$. The weak ripples at the edges of computational grid are due to the time boundary conditions.

The current case is not a completely integrable problem because of the inter-mode coupling. The propagating pulse can not find a stable form at least over the distance considered here. In one of our preliminary computations under the conditions similar to fig.4, but with $\ell_k \approx 0.05$ (i.e., for greater amplitude) we observed the breaking up of the input pulses of both polarizations into two separate subpulses subsequently scattering aside.

The periodical squeezing of the pulse shape, being a trace of a high order NLS solutions, produces new oscillations on the wings of the pulse (fig.4(a, b)) as Kerr processes and dispersion are spatially mismatched. The dispersion spreading is noticeable on several (~4) length when the dispersion chirp fills almost whole time window (fig.4(c, d)). Like in fig.3(h) the oscillations of the field in polarization modes remain out of phase (fig.4(e)). It is natural then that polarization properties of the light wave (i.e. the alternation of the dark and light shades of the gray) map the broadening area of the spatial-temporal oscillation of the polarization components (fig.4 (f, g)), caused by dispersion, thus making the whole picture rather complicated. We note that there are less coupling periods in fig.4(a, b) than in fig.1 or fig.2. Clearly, the nonlinear narrowing and peak amplification drives the propagation of the pulse into a non-linear birefringence regime. The further growth of the pulse input amplitudes will strengthen the inequality $\ell_k < \ell_d$, so making the process be somewhat analogous to that in fig.3 plus dispersion originated oscillations spreading away from the sharp central peak.

Let now the resonance interaction of a short pulse with the ensemble of resonance atoms is added to the conventional fiber effects as it has been suggested in (1), (3), and (4). The evolutionary behaviour of the counter circularly polarized components with the input amplitudes $A_{m1} \approx 2A_c \approx 4A_{NLS}$, $A_{m2} \approx A_c \approx 2A_{NLS}$ is plotted in fig.5 (a, b and c, d). We assume the resonance interaction to be weak by setting f=0.0015. Under this condition the population differences deviate insignificantly from their initial values. The spatial scale of the process is ℓ_d=1.0, whereas ℓ_k=0.05, ℓ_c=0.25, and ℓ_r=0.01. The value of resonance interaction length $L_r^{(2\pi)}$ can be estimated as (see (5)) $L_r^{(2\pi)} \approx 7L_d$. That means the total length of the fiber in fig.5 is about $0.6\,L_r^{(2\pi)}$ or $4\,L_d$. The resonance interaction process more effectively than the dispersion transfers energy off the pulse to the radiation born by the reciprocal reaction of the medium in the pulse after action region. It is clear then that in comparison with fig.4 the amplitudes of the humps rapidly decrease in the propagation direction (fig.5(a, b)).

Attention should be called to two humps in the center of fig.5(e). These are the above-mentioned relics of the NLS N-soliton break up. The visible asymmetry of the pattern relative to the initial pulse position results from the delayed response of the resonance subset. Generally, we may forecast that at the longer distance inside the doped fiber the well-evolved effects of dispersion and coherent 'ring' can hardly be distinguished.

The polarization properties of the light pulse are displayed in the gray scale maps fig.5(f,g). It is interesting to note that these pictures still keep the periodic alternation of the regions with the opposite ellipticity and azimuth angle owing to the linear coupling (see fig.2(e,f)). In our further computations (not shown), when we set ℓ_r=0.001 for the ten times larger concentration of impurities, we saw resonance oscillations fill the whole (ζ,τ) computational area already at the early stage of pulse propagation. It was interesting to observe how the increase of the dopant concentration developed the generic picture of periodic azimuth and ellipticity variations seen yet in fig.1 and 2 with the same beat period. Qualitatively speaking, that may be regarded as a result of resonance absorption when the progressive dumping of the field humps decreases the field amplitude below the critical value of the electrical field strength A_c, so driving the process back into the linear regime, when ℓ_c begins to be shorter than ℓ_k. Anyway, dispersion and resonance interaction being the time dependent processes introduce the temporal modulation to the basic polarization picture constituted by a linear birefringence.

4. CONCLUSION

We have considered the propagation of the pulse of elliptically polarized light in a non-linear doped birefringent fiber. The resonance impurities in the form of two-level atoms were included in the model in addition to the whole set of non-linear fiber effects. Our main concern was time-dependent polarization effects in the field of resonant optical pulse propagating in fiber. This problem was approached earlier separately in pure fiber[14] and in degenerated self-induced transparency[15]. In this paper the dynamics of the pulse was considered in full as a self-consistent problem. We have concentrated on the case of weak input field when the amplitude of the pulse was about the amplitude of a single NLS pulse, so the coupling to the resonance system was not strong. Even within this approximation the general picture proved to be rather complex. The polarization properties of the pulsed light are nonstationary across the pulse width and they can drastically change also in space. Our numerical simulations showed that the polarization dynamics is basically featured by the interplay between the Kerr non-linear self- and cross-modulation and dispersion, while linear birefringence brings regular spatial modulation of azimuth angle and ellipticity. There is a range of the input amplitudes where the birefringence becomes a non-linear power dependent process due to Kerr cross-phase modulation, so the power beat period may grow. At the same time, when the spatial scale of the resonance interaction is less or comparable with the characteristic lengths of fiber effects, the propagating pulse experiences a strong distortion and resonance absorption. The intensity dumping leads to the restoration of the linear beat period, thus converting the propagation process from nonlinear to linear regime.

5. ACKNOWLEDGMENTS

We are grateful to S.Kozlov, S.Sazonov, and V.Kozlov for useful discussions. This work has been supported by INTAS under grant No: 96-0339.

6. REFERENCES

1. A.I. Maimistov, A.M.Basharov, "Self-induced transparency in fiber with resonance impurities", *Izv. Rus. Acad. Nauk, ser. fiz.* **62,** pp. 354-361, 1998
2. T.R. Taha, M.J. Ablowitz, "Analytical and numerical aspects of certain nonlinear evolution equations. II. Numerical, nonlinear Schrödinger equation", *J. Comput. Phys.*, **55**, pp. 203-230, 1984
3. H.G. Winful, "Polarization instabilities in birefringent nonlinear media:application to fiber-optical devices", *Opt. Lett.*, **11(1)**, pp. 33-36, 1986
4. C.R. Menyuk, "Pulse propagation in an elliptically birefringent Kerr madium", *IEEE J.Quant.Electron.*, **QE-25**, pp. 2674-2682, 1989
5. M. Nakazawa, Y.Kimura, K.Kurokawa, and K.Suzuki, "Self-induced-transparency solitons in an erbium-doped fiber waveguide", *Phys. Rev.A* **45(1)**, pp. R23-R26, 1992
6. C.R. Menyuk, "Nonlinear pulse propagation in birefringent optical fibers", *IEEE J.Quant.Electron.* **QE-23(2)**, pp. 174-176, 1987
7. A.I. Maimistov, S.O. Elyutin, "Propagation of short light pulses in nonlinear birefringent fibre. Variational approach", *J. Mod. Opt.*, **39(11)**, pp. 2193-2200, 1992
8. A.I. Maimistov, A.M. Basharov, S.O. Elyutin, and Yu.M. Sklyarov, "Present state of self-induced transparency theory", *Physics Reports*, **191(1)**, pp. 1-108, 1990
9. V.L. daSilva, Y. Silberberg, "Photon echoes in an optical amplifier", *Phys.Rev.Lett.* **70(8)**, pp. 1097-1100, 1993
10. J. Hegarty, M.M. Broer, B. Golding, J.R. Simpson, J.B. MacChesney, "Photon echoes below 1K in Nd^{3+}-doped glass fiber", *Phys.Rev.Lett.* **51(22)**, pp. 2033-2035
11. L. Allen, J.H. Eberly, *Optical Resonance and Two-Level Atoms*, Wiley, New York, 1975
12. S. Trillo, S. Wabnitz, S., E.M. Wright, G.I. Stegeman, "Polarized soliton instability and branching in birefringent fibers", *Opt.Commun.* **70(2)**, pp. 166-171, 1989
13. S.O. Elyutin, A.I. Maimistov, "Waves of polarized light in nonlinear birefringent fiber", *Chaos, Solitons and Fractals* **11**, pp.1253-1259, 2000
14. M. Horowetz, Y. Silberberg, "Nonlinear filtering by use of intensity-dependent polarization rotation in birefringent fibers", *Opt. Lett.* **22(23)**, pp. 1760-1762, 1997
15. H. Steudel, "N-soliton solution to degenerate self-induced transparency", *J. Mod. Phys.*, **35(4),** pp. 693-702, 1988

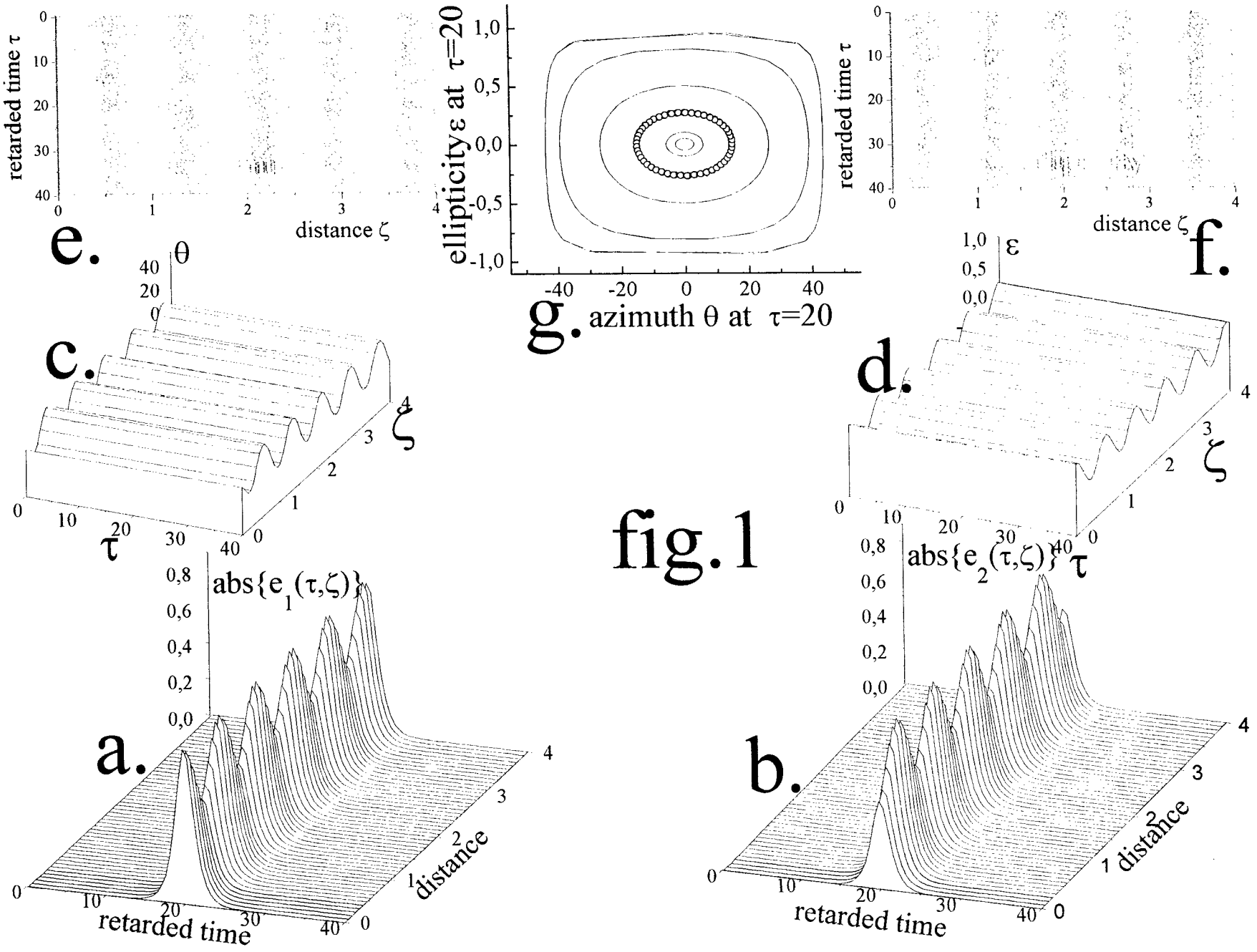
e.
retarded time τ
distance ζ
ellipticity ε at τ=20
g.
azimuth θ at τ=20
f.
retarded time τ
distance ζ
c.
θ
τ
ζ
d.
ε
ζ
τ
a.
abs{e1(τ,ζ)}
retarded time
distance
b.
abs{e2(τ,ζ)}
retarded time
distance

fig.1

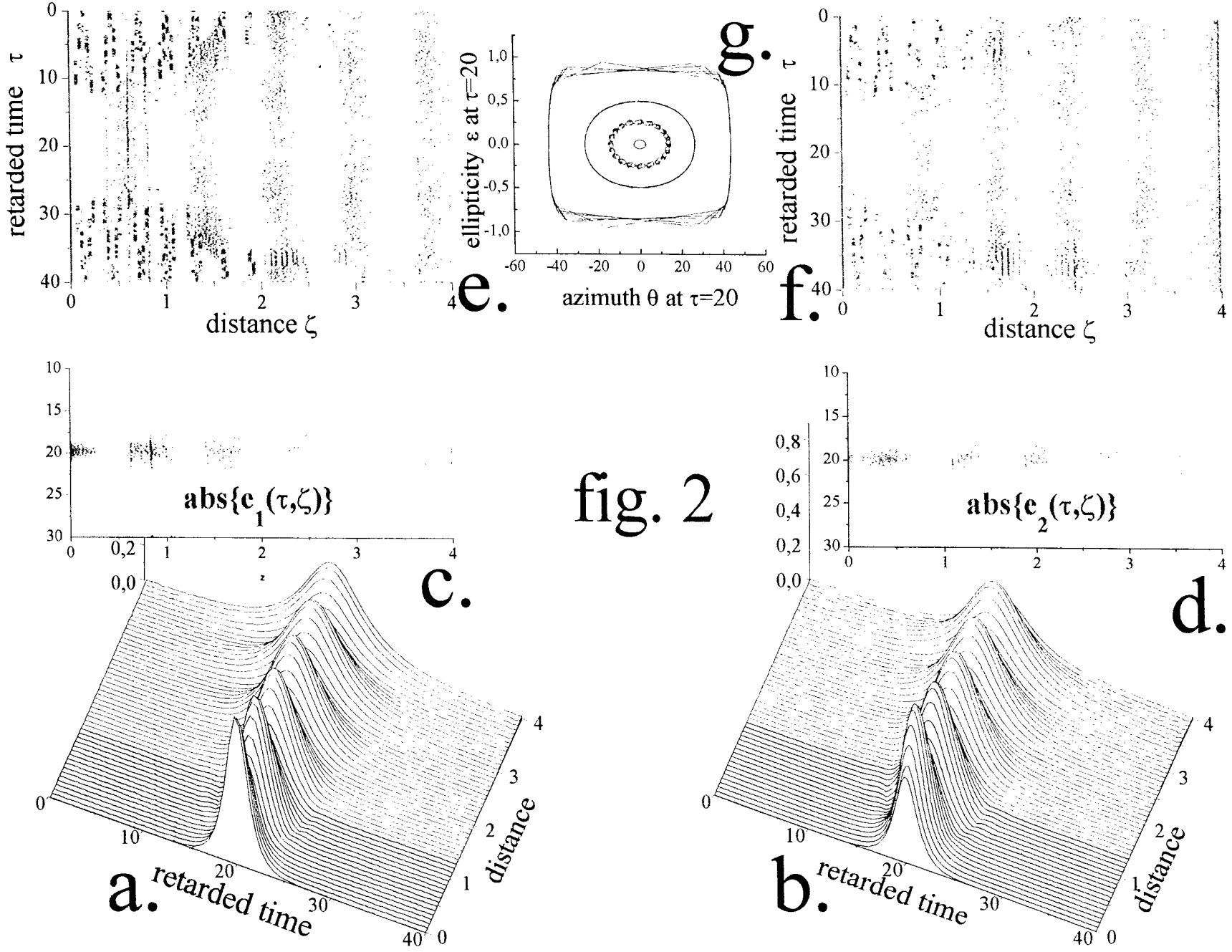
retarded time τ
distance ζ
e.
ellipticity ε at τ=20
azimuth θ at τ=20
g.
retarded time τ
distance ζ
f.
abs{e1(τ,ζ)}
c.
a.
retarded time
distance
abs{e2(τ,ζ)}
d.
b.
retarded time
distance

fig. 2

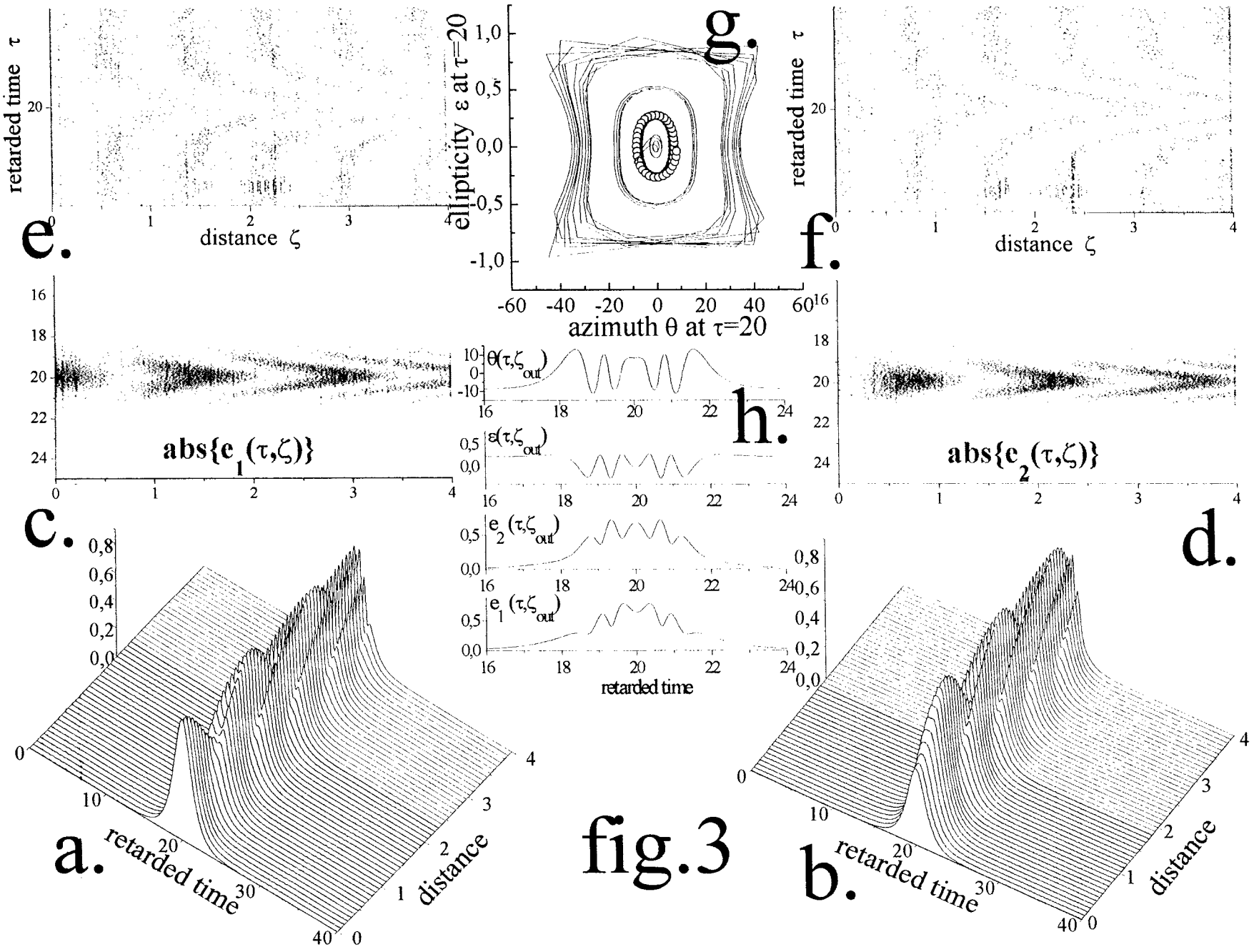
a.
b.
c.
d.
e.
f.
g.
h.
retarded time
distance
abs{e1(τ,ζ)}
abs{e2(τ,ζ)}
retarded time τ
distance ζ
ellipticity ε at τ=20
azimuth θ at τ=20
θ(τ,ζout)
ε(τ,ζout)
e2(τ,ζout)
e1(τ,ζout)

fig.3

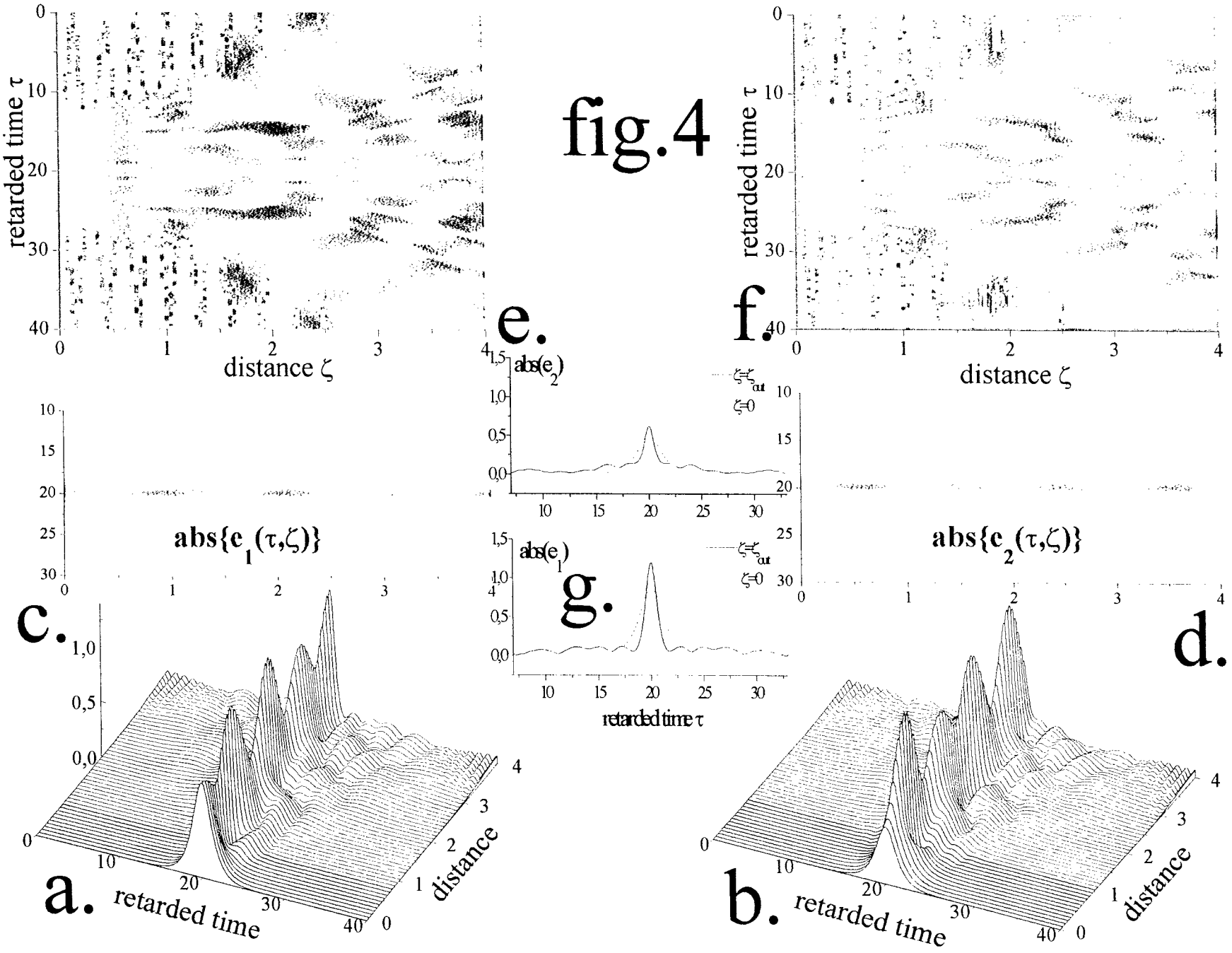
fig.4
retarded time τ
distance ζ
e.
f.
abs(e2)
ζ=ζout
ζ=0
abs{e1(τ,ζ)}
abs(e1)
g.
retarded time τ
abs{e2(τ,ζ)}
c.
d.
a.
retarded time
distance
b.
retarded time
distance

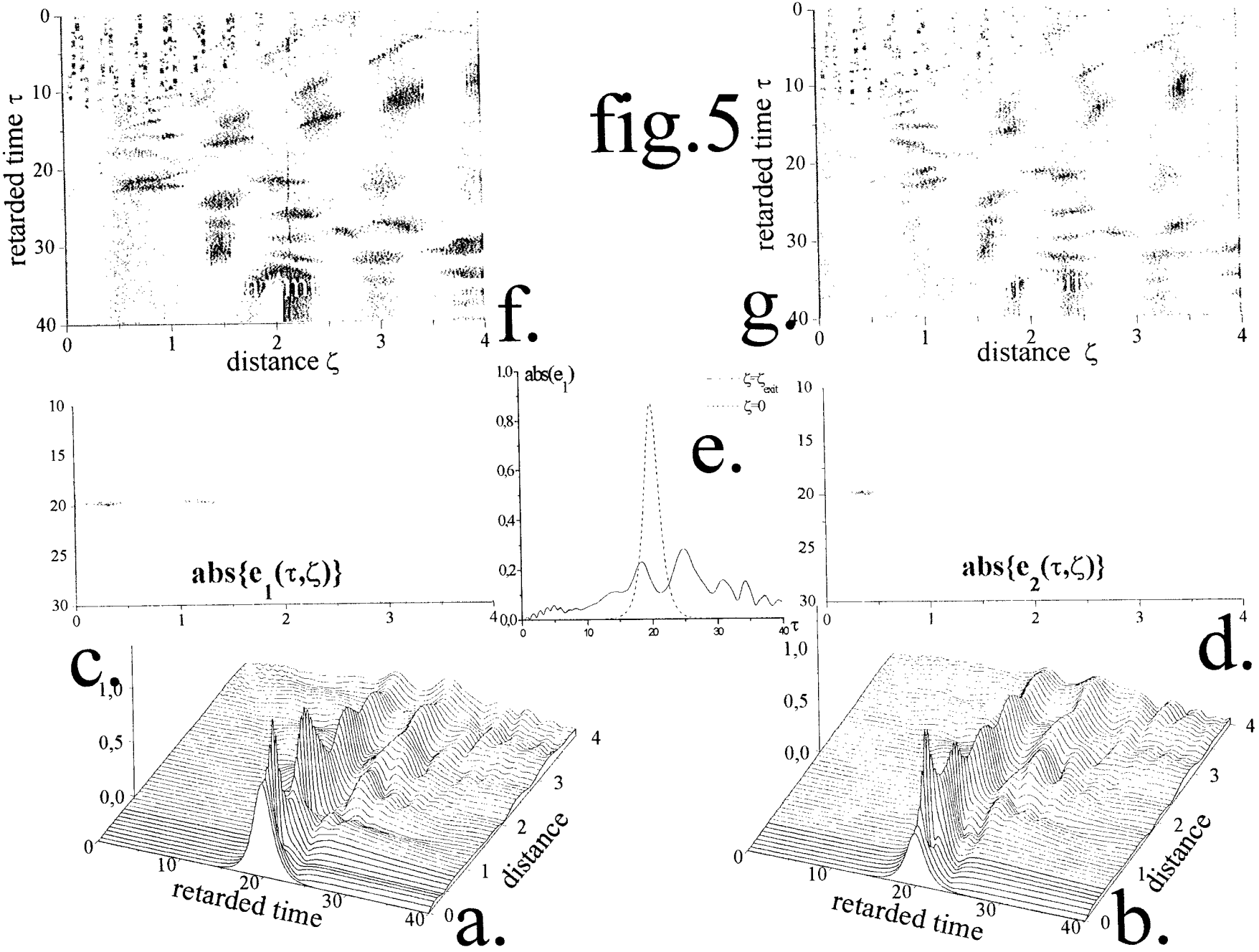
fig.5
retarded time τ
distance ζ
f.
g.
abs{e1(τ,ζ)}
abs{e2(τ,ζ)}
abs(e1)
ζ=ζexit
ζ=0
e.
c.
d.
a.
b.
retarded time
distance

Theoretical model for nonlinear homogeneous upconversion and clustering in Er^{3+}-doped waveguide amplifiers

S.V.Sergeyev*, B.Jaskorzynska

Royal Institute of Technology, Department of Electronics,
Laboratory of Photonics and Microwave Eng.,
Electrum 229, SE-164 40 Kista, Sweden

* On leave from the Belorusian State University, Dept. of Physics

ABSTRACT

We model upconversion and migration in an ensemble of inhomogeneously distributed erbium ions. Treating Er-clusters as fractal objects we find the dependence of the upconversion rate on the population inversion for different fractal dimensions.

Keywords: Upconversion, migration, erbium, amplifier, clustering, fractals

1. INTRODUCTION

The recent interest in ***Er***-doped planar amplifiers is motivated by their potential use for integrated active devices in optical communication systems at the 1.5 μm transmission window. In order to obtain sufficiently large gain in a short planar device two orders of magnitude higher ***Er***-concentrations $(10^{20} - 10^{21}\ cm^{-3})$ are required in comparison with a typical fiber amplifier. However, at high concentrations parasitic interactions between Er-ions are strongly enhanced. The resulting upconversion processes [1,2] reduce achievable gain and have to be properly taken into account while modelling the amplifier performance. It has been observed that the dependence of the upconversion rate *(W)* on the population inversion *(n)* is approximately linear for small population inversions $(n \to 0)$ whereas it becomes nonlinear when the population inversion increases [1,2].

Previously the nonlinear behavior has been explained by contribution from clustered Er ions [1,2]. However, strong nonlinearity was also observed in Er-doped fibers co-doped with Al_2O_3 where percentage of clustered Er ions is low [3].

First theories explaining the nonlinear dependence of the homogeneous upconversion (HUC) rate for statistically uniformly distributed centers (no excess of clusters) have been proposed by: Slobodyanyuk [4,5] for dye molecules in solution, and by Philipsen [6] for Er ions in silica matrix. However, in Refs. 4,5 the migration is not correctly described which leads to understimation of the resulted upconversion rate. The model of Ref. 6, in turn, uses approximations that are not proved to be justified, and it requires Monte Carlo simulations. Nevertheless, the main features predicted by this model have qualitatively been confirmed by our experiments [7, 8, 9].

Recently, we proposed[10] a statistical model for the HUC in Er-doped silica waveguides. The model is based on well established theories[11] with known maximum error due to the involved approximations. The model provides analytical solutions in the case of continuos wave (CW) excitation. In the dynamic case an integral equation has to be solved, however, we obtained analytical expressions for the asymptotes at: $t \to 0$, $t \to \infty$ $(n \to 0)$. By fitting the asymptotes to the experimental results[8] we find the critical distance for the upconversion be $R_{up} = 10.5$ Å, and its ratio r with the migration critical distance be $r = (R_m/R_{up})^6 = 60$. The result are in a good agreement with the corresponding measured values: $R_{up} = 9 - 10$ Å [12], $(R_m/R_{up})^6 = 60$ [13].

In the present work we extend our model developed for HUC to include Er clusters. The extension, presented for the CW case, is based on the fractal dimension concept[14]. It is well known that Er in a glass matrix tends to cluster[15] and that gain from the cluster ions is totally quenched. We believe that the proposed model will be a useful tool for both characterization and design of realistic Er-doped waveguide amplifiers.

Laser Optics 2000: Semiconductor Lasers and Optical Communication, Serguei A. Gurevich, Nikolay N. Rosanov, Editors, Proceedings of SPIE Vol. 4354 (2001) © 2001 SPIE · 0277-786X/01/$15.00

2. UPCONVERSION AND MIGRATION IN THE ENSEMBLE OF CLUSTERED ERBIUM IONS.

We treat the upconversion process by analogy to the self-quenching processes[11], where the excitation can migrate and can be quenched by another excited center of the same type. The theory of self-quenching shows that donors and acceptors can be treated as uncorrelated ensembles when the ratio of migration-to-self-quenching critical distances is large: $r=(R_m/R_{up})^6>>1$. Since this condition is satisfied for Er-doped glasses we consider excited ions and all the ions as two subsystems. The density distribution of Er-ions incorporated in a glass matrix by deposition processes can be described by the expression used for the process of diffusion-limited aggregation (DLA)[14, 16, 17, 18]:

$$\rho(R) = c_D R^{D-d} \tag{1}$$

Here R is the distance between ions, c_D is the concentration of the erbium ions on the fractal cluster, d is the Euclidean dimension, D is the fractal dimension[14].

The balance equation has the same form as in our model for HUC[10]:

$$\frac{dn(S_1,S_2)}{dt} = (1-n(S_1,S_2))\alpha - n(S_1,S_2)(1+S_1+S_2) + \langle n(S_1,S_2)\rangle_{S_1,S_2} S_2 \tag{2}$$

Where time t is normalized with respect to the fluorescence lifetime τ_2 of the metastable level, $n(S_1,S_2)$ is a local probability of ion excitation, $\langle n(S_1,S_2)\rangle_{S_1,S_2} = \int_0^\infty\int_0^\infty n(S_1,S_2)dS_1dS_2$ is the population inversion of the metastable level, α is the normalized pumping rate of the metastable level, $S_1 = \sum_{l\neq k} P_{kl}$, $S_2 = \sum_{j\neq k} W_{kj}$ are the stochastic variables which for the dipole-dipole mechanism of energy transfer and in the presence of the fractal clusters have the following distributions[17]:

$$f(S_i) = R(S_i,k_i)^{-1/2}\exp\left(-\frac{k_i^{1/(1-D/6)}}{(6/D)^{1/(1-D/6)}\,S_i^{D/(6-D)}}\right), \qquad i=1,2 \tag{3}$$

with:

$$R(S_i,k_i) = 2\pi(-S_i)^{(12-D)/(6-D)}\left(\frac{D}{6}-1\right)\left(\frac{6}{D}\right)^{\frac{6}{6-D}} k_i^{6/(D-6)}, \qquad k_1 = k\langle n(S_1,S_2)\rangle_{S_1,S_2}, \quad k_2 = k\left(\frac{r}{2}\right)^{\frac{D}{6}} \tag{4}$$

where $k=\Gamma(1-D/6)(c_D/c_{up})$, $c_{up} = \left(\frac{\pi^{D/2}}{\Gamma(1+D/2)}R_{up}^D\right)^{-1}$ is the critical concentration for the upconversion in the cluster with the fractal dimension D, $r=\left(\frac{R_m}{R_{up}}\right)^6$, $\left(\frac{1}{2}\right)^{\frac{D}{6}}$ is the Huber correction[11] taking into account the migration reversibility, $\Gamma(x)$ is the complete gamma function.

We consider CW excitation: $\frac{dn(S_1,S_2)}{dt}=0$. For averaging Eq. 2 with the distributions (3) we use the following identities:

$$\int_0^\infty\int_0^\infty \frac{f(S_1)f(S_2)}{1+S_1/(1+\alpha)+S_2/(1+\alpha)}dS_1dS_2 = \int_0^\infty\int_0^\infty\int_0^\infty \exp\left(-t-\frac{(S_1+S_2)t}{1+\alpha}\right)f(S_1)f(S_2)dS_1dS_2dt = F(k,\alpha,D,r) \tag{5}$$

where [18]:

$$F(k,\alpha,D,r)=\int_0^{\infty}\exp\left(-t-\gamma\left(\frac{t}{1+\alpha}\right)^{\frac{D}{6}}\Gamma(1-D/6)\left(n+\left(\frac{r}{2}\right)^{\frac{D}{6}}\right)\right)dt \tag{6}$$

Finally, we arrive at the following transcendental equation for the population inversion:

$$n=\langle n(S_1,S_2)\rangle_{S_1,S_2}=\frac{\alpha\,(n+(r/2)^{D/6})}{1+\alpha}\,\frac{F(k,\alpha,D,r)}{n+(r/2)^{D/6}F(k,\alpha,D,r)}, \tag{7}$$

The rate of upconversion for the CW case takes the following form[10]:

$$W_{up}^{CW}=\frac{\langle n(S_1,S_2)S_1\rangle_{S_1,S_2}}{\langle n(S_1,S_2)\rangle_{S_1,S_2}}=\frac{\alpha(1-n)}{n}-1 \tag{8}$$

Using (7) and (8) we calculated the CW upconversion rate in the presence of clustered ions. The resulting dependence on the population inversion is shown in Fig. 1:

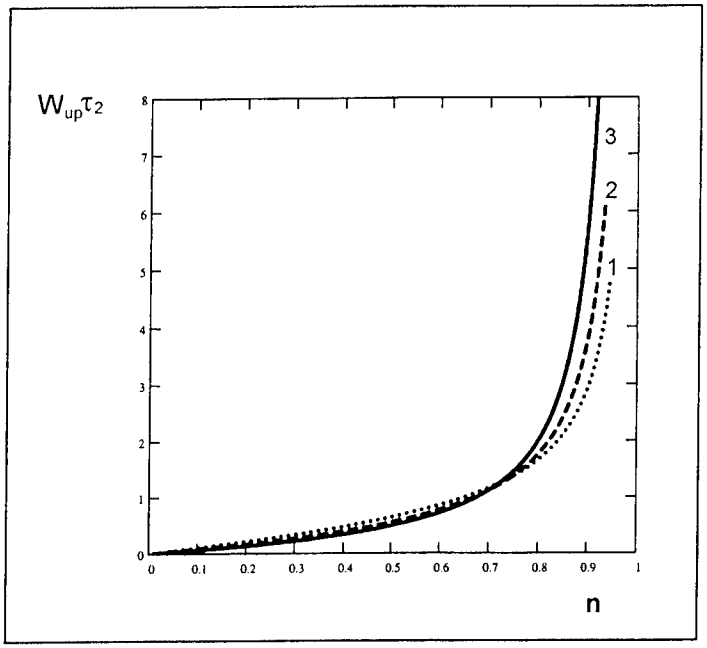

Fig1. *Upconversion rate* $\boldsymbol{W_{up}}$ *as function of population inversion* **n** *for different values of fractal dimension* **D**.
D=3 (1), **D**=2.5 (2), **D**=3 (3)
$\boldsymbol{R_{up}}$=10.5 Å, r=60, $c_{Er}=8.6\times10^{25}$ ions/m^3
τ_2 - liftime of the metastable level
n - population inversion of the metastable level

From (7) and (8) we also find an analytic expression for the upconversion rate in the limit $n\to0$:

$$W_{up}^{CW}=\frac{k^{6/D}n}{\Gamma(1+6/D)}\left(\frac{r}{2}\right)^{(1-D/6)(6/D-1)} \tag{9}$$

Eq. 9 could be used for determining an average fractal dimension of erbium clusters.

3. DISCUSSION

The presented model describes behavior of the upconversion process in the presence of Er clusters. The main results can be interpreted as follows:

1) For high population inversion the effect of migration is weak and it cannot efficiently smooth out the excitation distribution. Each of the excited ions sees different surrounding of other excited ions, hence the rate of upconversion is not proportional to the population inversion (Fig.1).

2) The more nonuniform ion distribution (i. e. the lower fractal dimension) the larger percentage of the excited ions have closely located excited neighbors. Therefore, for high population inversion the enhancement of the upconversion becomes larger with decreasing fractal dimension (compare the curves: 1, 2, 3 in Fig.1).

3) For low population inversion the migration is very fast and can efficiently equalize the distribution of the excited ions. As a result the rate of upconversion becomes proportional to the population inversion (Fig.1, Eq. 9).

4) It can also be seen from Fig.1 and Eq. 9 that at low population inversions the upconversion is weaker for lower fractal dimensions. This is because the distance between the ions outside the clusters becomes larger and the migration slower refills holes that the upconversion "burned" in the excitation distribution within the clusters.

The concentration dependence of the upconversion rate for small population inversion can be used for calculation of the fractal dimension of the erbium cluster.

4. REFERENCES

[1] *R*.S.Quimby, W.J.Miniscalo and B.Thompson, "Clustering in erbium-doped silica glass fibers analyzed using 980 nm excited-state absorption", *J.Appl. Phys.*, Vol. 76, No. 8, pp. 4472-4478 (1994)

[2] J. Nilsson, P. Blixt, B. Jaskorzynska and J. Babonas, "Evaluation of parasitic upconversion mechanisms Er^{3+}-doped silica glass fibers by analysis of fluorescence at 980 nm", *J. Lightwave Technol.* Vol.13, pp.341-349 (1995)

[3] B.J.Ainslie, "A reveiw of the fabrication and properties of erbium-doped fibers for optical amplifies", *J. Lightwave Technol.*, Vol. 9, No. 2, pp. 220-227 (1991)

[4] A.I. Slobodyanyuk , "Short wavelength luminescence of complex molecules in solutions under two photon excitation", PhD thesis, Department of Physics, Belarusian State University, Minsk (1988)

[5] V.A. Gaisenok and A.I. Slobodyanyuk, "Effect of energy cumulation of singlet-excited molecules on luminescence of dye solutions," *Opt.Spektrosk.*, Vol. 65, No. 1, pp. 39-41 (1988)

[6] J.L.Philipsen, A.Bjarklev, "Monte Carlo simulation of homogeneous upconversion in erbium-doped silica glasses" *IEEE J. Quant.Electron.*, Vol. 33, No. 5, pp.845-854 (1997)

[7] Marcin Swillo, Dan Bremberg, Bozena Jaskorzynska, Sten Helmfrid, and Jacob L. Philipsen, "Method for characterization of clustering and homogeneous upconversion in Er-doped waveguides", in Integrated Photonic Research, OSA Technical Digest (Optical Society of America, Washington DC, 1999), pp.73-75

[8] J. Philipsen, J. Broeng, A. Bjarklev, S. Helmfrid, D. Bremberg, B. Jaskorzynska, and B. Palsdottir, " Observation of Strongly Nonquadratic Homogeneous Upconversion in Er3+-Doped Silica Fibers and Reevaluation of the Degree of Clustering", *IEEE J. Quantum Electron.*, Vol 35, No. 11, pp.1741- 1749 (1999)

[9] D. Bremberg, S. Helmfrid, B. Jaskorzynska, M. Swillo, J. L. Philipsen, and B. Pálsdóttir, "Observation of energy-distribution-dependent homogeneous upconversion in erbium-doped silica glass fibers", *Electron. Lett.*, Vol 14, pp.1189-1191 (1999)

[10] S.V.Sergeyev, and B.Jaskorzynska ,"Analytical model for homogeneous upconversion in Er^{3+}-doped waveguides", accepted for CLEO Europe 2000, S.V.Sergeyev, and B.Jaskorzynska ,"Theory for concentration dependent homogeneous upconversion in Er^{3+}-doped glasses", prepared for publication (2000)

[11] E.N.Bodunov, "Approximate methods in the theory of nonradiative energy transfer of localized excitations in disordered media: A review," *Opt. Spektrosc.*, Vol. 74, No. 3, pp. 311-327 (1993)

[12] M.Hemstead, J.E.Roman, C.Ye, J.S.Wilkinson, P.Camy, P.Laborde, and C.Lerminiaux, "Anomalously high uniform upconversion in an erbium-doped waveguide amplifier" Proc. 7th Eur. Conf. Integrated Optics (ECIO'95), pp. 233-236 (1995)

[13] J.E.Roman, M.Hemstead, C. Ye, and S.Nouh, P. Camy, P. Laborde, and C. Lerminiaux, "1.7 μm excited state absorption measurement in erbium-doped glasses," *Appl. Phys. Lett*,. Vol 67, No. 4, pp. 470-472 (1995)

[14] J.F. Gouyet ,"Physics and Fractal Structures", Springer, pp. 130-146 (1996)

[15] M.W.Sckerl, S.Guldberg-Kjaer, M.Rysholt Poulsen, P.Shi and J.Chevallier, "Precipitate coarsening and self organization in erbium-doped silica," *Phys. Rev. B*, Vol. 59, No. 21, PP. 13494-13497 (1999)

[16] J.Klafter, A.Blumen, "Fractal behavior in trapping and reaction," *J. Chem. Phys.*, Vol. 80, No. 2, pp. 875-877 (1984)

[17] Ö. Peksan, "Inverted Klafter-Blumen equation for fractal analysis with interpenetrating network morphology," *Chem. Phys. Lett.*, Vol.198, No. 1,2, pp. 20-24 (1992)

[18] M.N. Berberan-Santos, E.N.Bodunov, J.M.M.Martinho, "Luminescence quenching in fractal media accelerated by migration," *Opt. Spectrosc.*, Vol. 81, No.2, pp. 217-221 (1996)

Actively mode-locked Er-doped fiber laser incorporating Bragg gratings written in polarization-maintaining fiber

O. Deparis*, R. Kiyan, P. Mégret, M. Blondel
Advanced Research in Optics group, Electromagnetism & Telecommunications Department,
Faculté Polytechnique de Mons, 31 blvd Dolez, B-7000 Mons, Belgium

S.A. Vasiliev, O.I. Medvedkov
Fibre Optics Research Center at General Physics Institute, 38 Vavilov Street, 117756 Moscow, Russia

ABSTRACT

Bragg gratings were written in H_2-loaded polarization-maintaining fiber (PM-FBGs) and inserted in an actively mode-locked Er-doped fiber laser. The use of PM-FBG in sigma laser cavity allows to effectively build all polarization-maintaining fiber laser. Long term stabilization of the laser was ensured by a feedback loop that controlled the cavity length. Peak wavelengths, reflection bandwidths and reflectivity values of the gratings were equal to 1545.5 nm and 1540.5 nm, 1.6-nm and 0.8-nm, of 99% and 90%, respectively. At a 3-GHz repetition rate, pulses of 9.4-ps and 27.9-ps duration were generated with first and second gratings, respectively. By inserting additional long piece of dispersion-shifted fiber in the cavity, nonlinear pulse shortening was observed due to formation of average soliton inside the cavity. In this case, pulses of 7.8-ps and 22.7-ps duration were generated with first and second gratings, respectively. With the first grating, generated pulses were close to transform limit for hyperbolic secant pulse shape. Longer pulse duration obtained with second grating is attributed to narrower bandwidth and residual chirp of the grating.

Keywords: Fiber lasers, active mode locking, fiber Bragg gratings, polarization-maintaining fibers

1. INTRODUCTION

Actively mode-locked Er-doped fiber lasers are stable sources of short optical pulse trains at repetition rates in the GHz range.[1] In order to select the lasing wavelength, tunable bandpass filters having bandwidths of several nanometers are commonly used. On the other hand, it has been soon recognized that fiber Bragg gratings (FBG) offer great flexibility for controlling the wavelength and bandwidth of the pulses generated from actively mode-locked Er-doped fiber lasers.[2] Moreover, several gratings can be combined in the laser cavity in order to obtain multiple-wavelength mode-locked pulses.[3] By incorporating two wide-bandwidth nonchirped fiber Bragg gratings in an actively mode-locked Er-doped fiber laser, we recently demonstrated transform-limited dual-wavelength pulses of 16-ps and 13-ps durations at 1547 nm and 1562 nm respectively, at a repetition rate of 3 GHz only limited by the bandwidth of the modulator.[4] To date, only Bragg gratings written in H_2-loaded standard fiber or photosensitive Ge-doped fiber have been used in actively mode-locked Er-doped fiber lasers. On the other hand, it is well known that single-polarization operation of fiber lasers reduces considerably their sensitivity to environmental perturbations. For this purpose polarization-maintaining (PM) laser configurations are often preferred. Because they preserve single-polarization operation of the laser, polarization-maintaining fiber Bragg gratings (PM-FBG) appear to be ideal candidates for wavelength selection in actively mode-locked Er-doped fiber lasers. In addition, they offer cheap, flexible and low-loss alternative to expensive fiber-pigtailed bulk optics components. For generation of short optical pulses through active mode locking, the intracavity filter should have a bell-shaped spectrum with sufficiently wide bandwidth to accommodate the pulse spectrum (duration of 10 ps corresponds to spectral width of 0.25 nm for transform-limited $sech^2$ pulses). In addition, the filter should not impart chirp on the pulse. All these requirements can be met with a proper design of the fiber Bragg grating.

In this paper, we present for the first time an actively mode-locked Er-doped fiber laser incorporating Bragg gratings written in polarization-maintaining fiber. Two PM-FBGs were fabricated especially for the experiments in H_2-loaded

* Correspondence : O. Deparis, Faculté Polytechnique de Mons, Electromagn. & Telecom. Dept., 31 blvd Dolez, B-7000 Mons, Telephone : + 32 65 37 41 94; Fax : +32 65 37 41 99, Deparis@telecom.fpms.ac.be;

Laser Optics 2000: Semiconductor Lasers and Optical Communication, Serguei A. Gurevich, Nikolay N. Rosanov, Editors, Proceedings of SPIE Vol. 4354 (2001) © 2001 SPIE · 0277-786X/01/$15.00

polarization-maintaining PANDA fiber. Pulses generated from the laser in different cavity configurations were characterized in time and frequency domains in order to assess the influence of grating parameters on pulse characteristics.

2. EXPERIMENTAL SET-UP

2.1 LASER CAVITY CONFIGURATIONS

For experiments, we used an actively-mode-locked Er-doped fiber laser in sigma configuration (Figure 1). The laser and its stabilization feedback loop have been described elsewhere.[5] Basically, it consists of a polarization-maintaining ring and a double-pass single-mode section ended by Faraday rotation mirror. The PM-FBG is connected to the ring through a single polarization circulator. Functionally, such a configuration is equivalent to polarization-maintaining unidirectional ring. Laser output is extracted from a 50:50 PM coupler (only PM coupler available at that time in the lab). Because the circulator acts itself as isolator, the PM isolator is not strictly necessary in the ring. However, it becomes necessary if circulator is removed and replaced by another type of filter in the cavity.

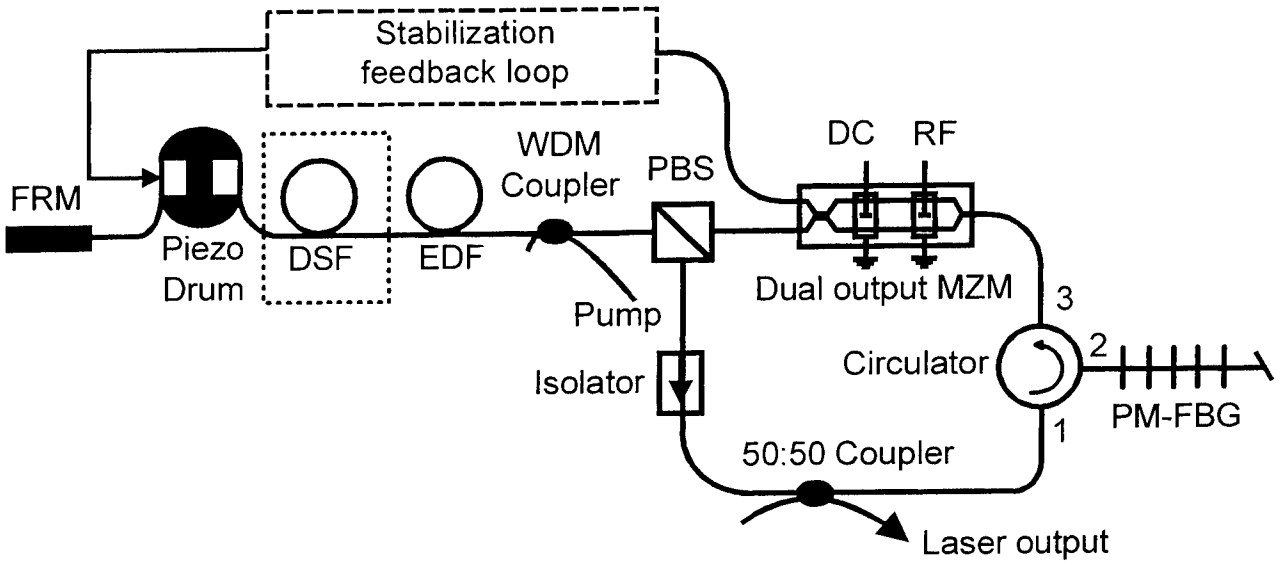

Figure 1. Actively mode-locked Er-doped fiber laser: FRM – Faraday rotation mirror, DSF – dispersion-shifted fiber (removed in basic laser cavity configuration), EDF – erbium-doped fiber, PBS – polarization beam splitter, MZM : Mach-Zehnder modulator, PM-FBG : polarization-maintaining fiber Bragg grating. All other elements in the laser ring are polarization-maintaining type. Feedback loop performs active stabilization of laser cavity length. Feedback signal is applied to piezoelectric drum on which a piece of single-mode fiber is wound.

Amplifying medium is 9.7-m Er-doped fiber (Lucent MP980) pumped by 980-nm laser diode (90 mW max. power). Active mode locking is achieved through dual-output Mach-Zehnder electro-optic modulator (3 GHz bandwidth). Light emerging from second output of modulator is detected and used by feedback loop for active stabilization of cavity length. When modulation frequency is perfectly tuned, average output power at second output is minimal.[5]

In order to observe nonlinear pulse shortening, piece of $L \approx 200$ m of dispersion-shifted fiber (DSF) was inserted in the double-pass section (effective length $2 \times L$). Dispersion parameter D and slope of DSF were ≈ 1 ps/(nm×km) at 1550 nm and ≈ 0.071 ps/(nm²×km) respectively. In the following, what is called 'long' ('basic') cavity is the cavity that does (not) contain additional piece of DSF. Cavity lengths (534 m and 127 m respectively) were determined from measurements of free spectral range (387 kHz and 1.63 MHz respectively).

2.2. POLARIZATION-MAINTAINING FIBER BRAGG GRATINGS

From theoretical point of view, UV-induced refractive index modulation in a high-birefringence fiber gives rise to dual peak Bragg resonance at wavelengths defined by $\lambda_{Bragg,s(f)} = 2n_{eff,s(f)}\Lambda$, were $n_{eff,s(f)}$ is the effective refractive index along the slow (fast) axis of the high-birefringence fiber and Λ is the grating pitch. When measuring spectral responses of Bragg gratings written in high-birefringence fiber, it is therefore necessary to specify if linearly polarized light is launched along either the slow or fast axis of the fiber.

For experiment, two different PM-FBGs were tested: the first (#FORC1) was fabricated at Fibre Optics Research Center, Russia and the second (#HW1) was supplied by Highwave Optical Technologies, France. Both gratings were written by exposing high-birefringence fiber (PANDA type) to CW 244-nm radiation from frequency-doubled Ar-ion laser using interferometer technique. Prior inscription, fibers were loaded with H_2 in order to increase their otherwise low photosensitivity. For inscription of FORC1 grating, fiber was first loaded at 125 bars (100 °C) during 16 hours and then irradiated at power density of about 80 W/cm² during 20 min. In both cases, gratings were written with constant pitch (i.e. no chirp) and without apodization. High reflectivity (> 90 %) of gratings was required for low insertion loss in cavity.

Reflection and transmission spectra of FORC1 and HW1 are shown in Figure 2 and Figure 3 respectively (polarization of the light aligned along the slow axis). Characteristics of the gratings are listed in Table 1. Both gratings have similar characteristics except that FORC1 has a FWHM bandwidth (determined from reflection spectrum measurement) which is about twice larger than that of HW1.

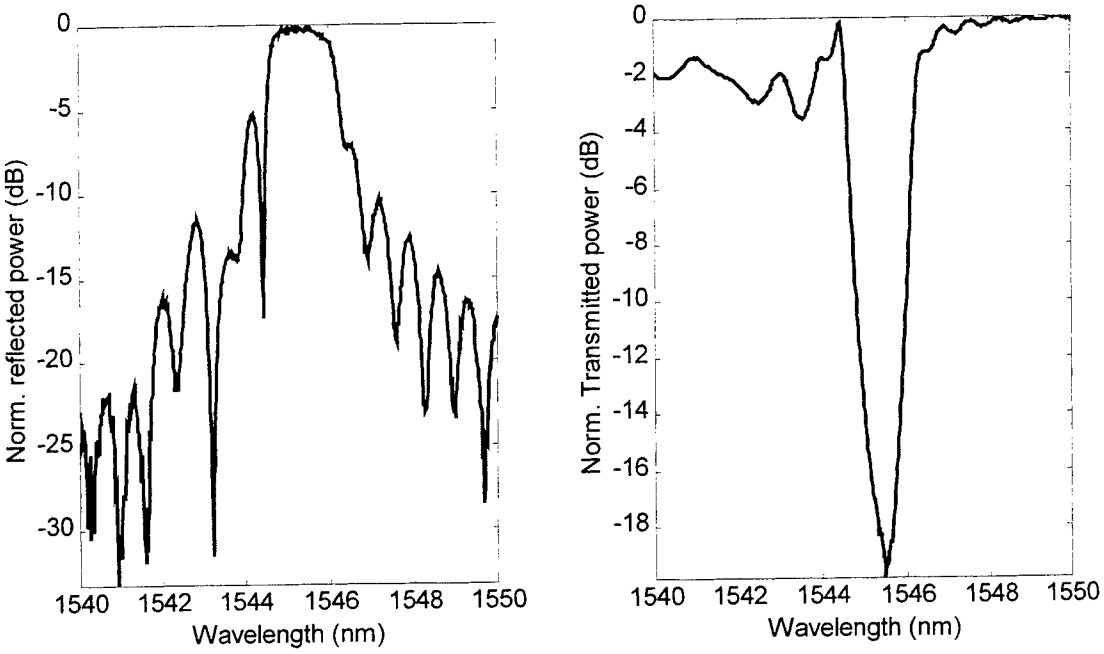

Figure 2. Normalized reflection spectrum (left) and transmission spectrum (right) of polarization-maintaining fiber Bragg grating FORC1. For measurements, linearly polarized light was launched along the slow axis of the fiber.

Table 1. Characteristics of PM-FBGs (measured using polarized light aligned along the slow axis) : R – reflectivity, T- transmission dip, FWHM - full width at half maximum.

PM-FBG	Peak wavelength (nm)	R = 1-T (%)	FWHM reflection bandwidth (nm)
FORC1	1545.5	99	1.6
HW1	1540.5	90	0.8

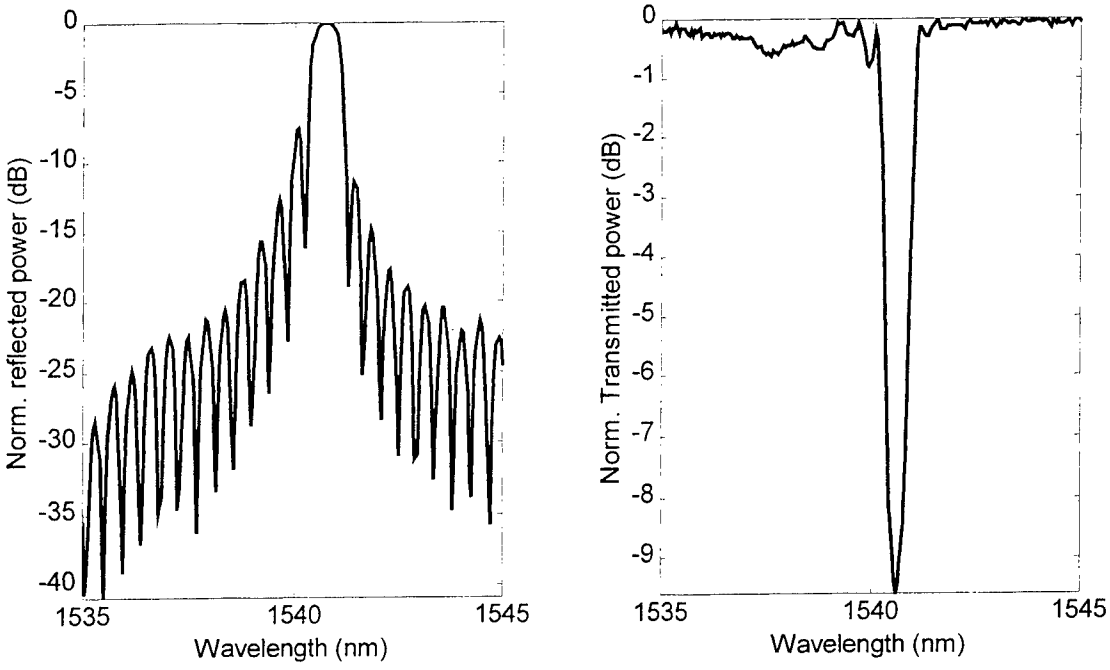

Figure 3. Normalized reflection spectrum (left) and transmission spectrum (right) of polarization-maintaining fiber Bragg grating HW1. For measurements, linearly polarized light was launched along the slow axis of the fiber.

3. RESULTS

Two sets of measurements were carried on with each PM-FBG : the first set with PM-FBG inserted in basic laser cavity and the second set with PM-FBG inserted in long laser cavity (i.e. with additional piece of DSF). For each experiment, pulse spectrum and autocorrelation were measured using optical spectrum analyzer (0.1 nm resolution) and second harmonic generation (SHG) autocorrelator, respectively. Temporal waveform and electrical spectrum of pulse train (detected by 20 GHz photodiode) were also recorded using digital sampling oscilloscope (rise time 50 ps) and electrical spectrum analyzer (22 GHz bandwidth), respectively. In all experiments, modulation frequency was tuned precisely around 3 GHz for harmonic mode locking and feedback loop was turned on for long-term stable operation.

Optical spectra (normalized to peak) and autocorrelation traces obtained with FORC1 and HW1 gratings inserted in basic cavity are shown in Figure 4 and Figure 5, respectively. Corresponding data obtained in long cavity are shown in Figure 6 and Figure 7, respectively. Together with pulse spectra are shown grating reflection spectra (normalized to peak). Autocorrelation traces were fitted using $sech^2$ function. Pulse duration (FWHM) is given by $\tau = \tau_{ac}/1.543$, where τ_{ac} is FWHM width of autocorrelation trace. Radio-frequency (RF) spectra, which contain information on noises affecting the pulse train, are shown in Figure 8 and Figure 9 for basic and long cavities respectively. Peak wavelength, spectral width, duration and time-bandwidth product of the pulses are listed in Table 2.

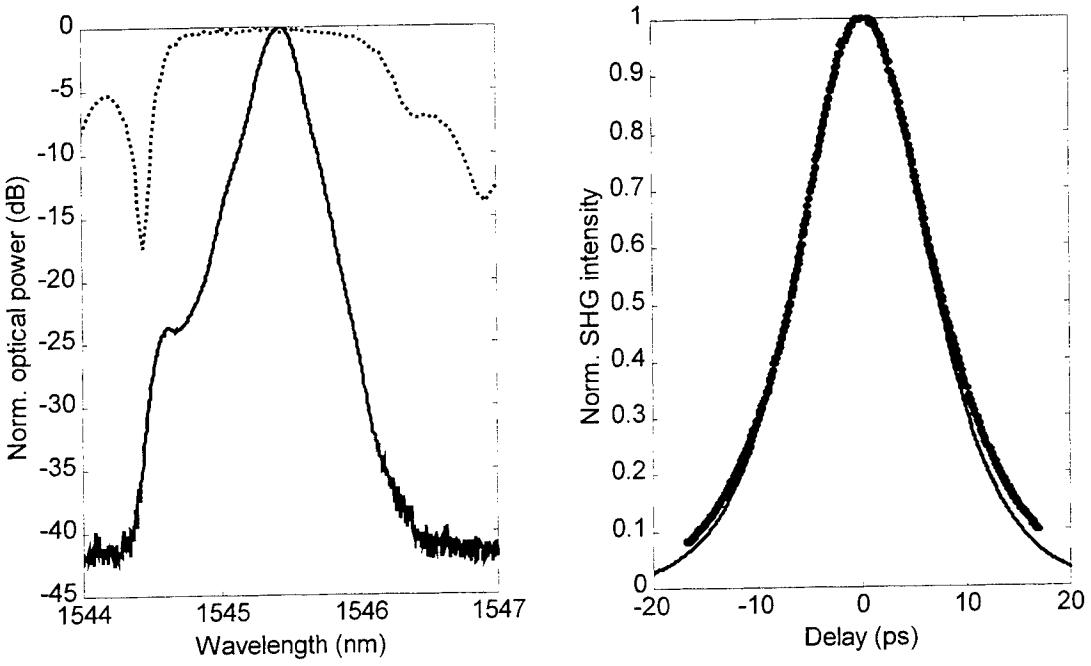

Figure 4. Normalized pulse spectrum (left) and pulse autocorrelation (right) obtained when FORC1 fiber Bragg grating was inserted in basic laser cavity. Normalized reflection spectrum of FORC1 fiber Bragg grating (dashed line) is shown together with pulse spectrum (left). Measured autocorrelation trace (dots) is fitted using $sech^2$ function (line). SHG : second harmonic generation.

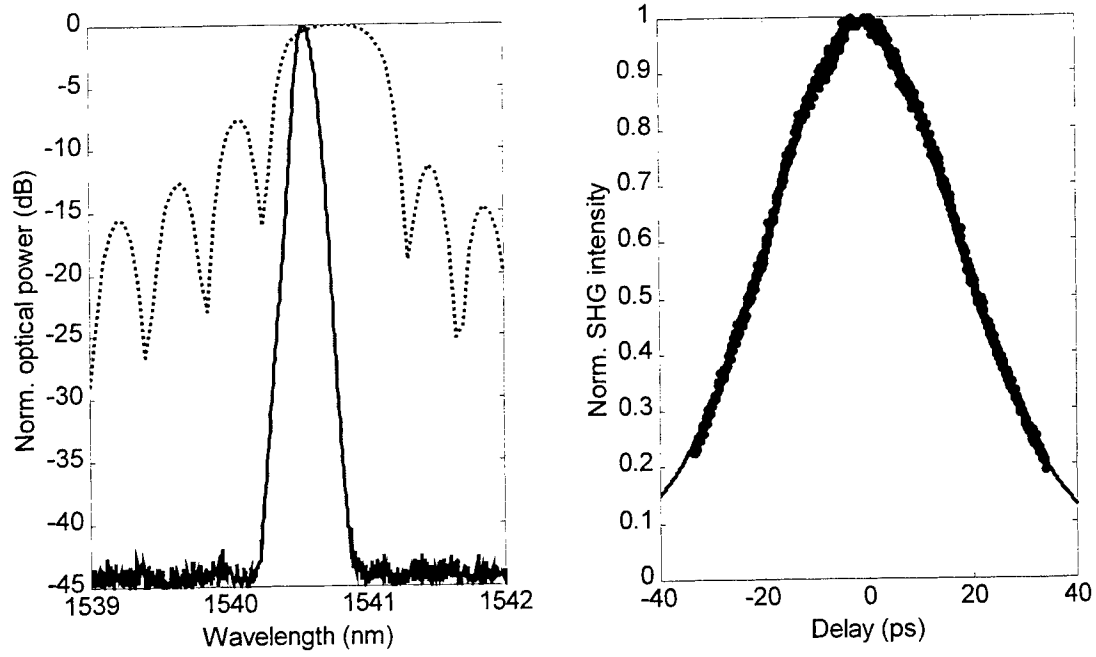

Figure 5. Normalized pulse spectrum (left) and pulse autocorrelation (right) obtained when HW1 fiber Bragg grating was inserted in basic laser cavity. Normalized reflection spectrum of HW1 fiber Bragg grating (dashed line) is shown together with pulse spectrum (left). Measured autocorrelation trace (dots) is fitted using $sech^2$ function (line). SHG : second harmonic generation.

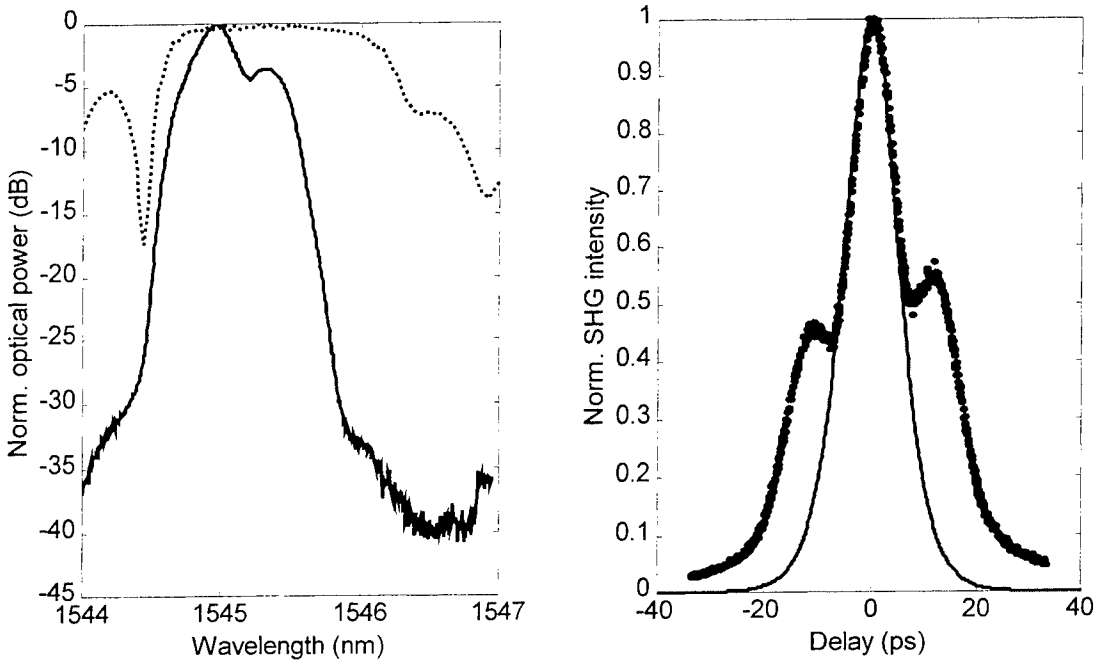

Figure 6. Normalized pulse spectrum (left) and pulse autocorrelation (right) obtained when HW1 fiber Bragg grating was inserted in laser long cavity. Normalized reflection spectrum of HW1 fiber Bragg grating (dashed line) is shown together with pulse spectrum (left). Measured autocorrelation trace (dots) is fitted using *sech²* function (line). SHG : second harmonic generation.

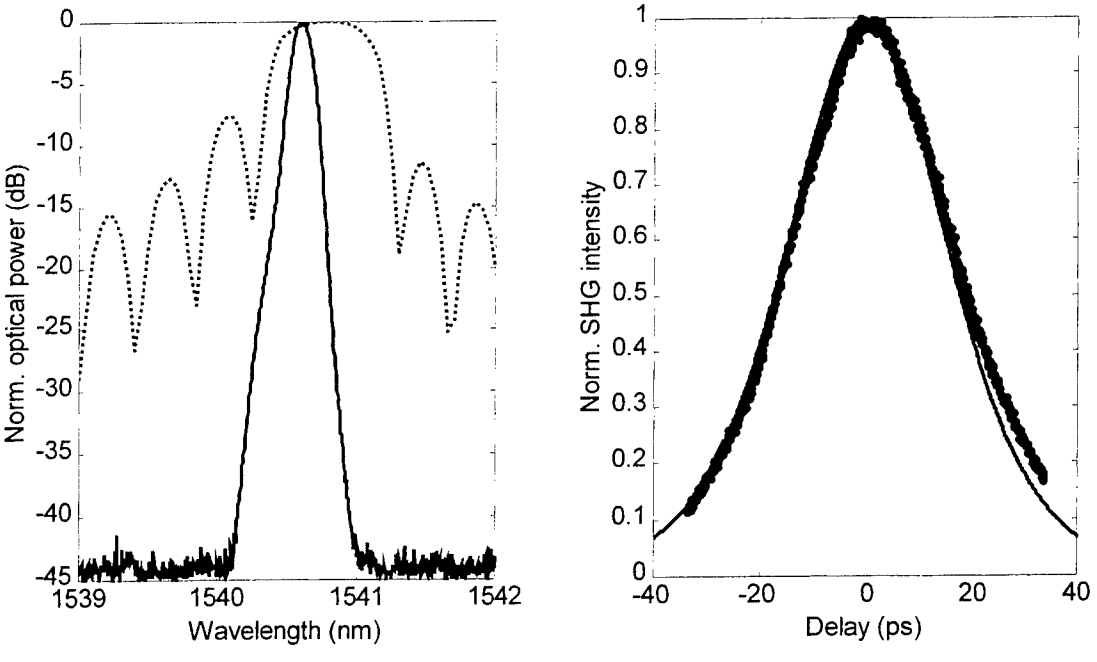

Figure 7. Normalized pulse spectrum (left) and pulse autocorrelation (right) obtained when HW1 fiber Bragg grating was inserted in long laser cavity. Normalized reflection spectrum of HW1 fiber Bragg grating (dashed line) is shown together with pulse spectrum (left). Measured autocorrelation trace (dots) is fitted using *sech²* function (line). SHG : second harmonic generation.

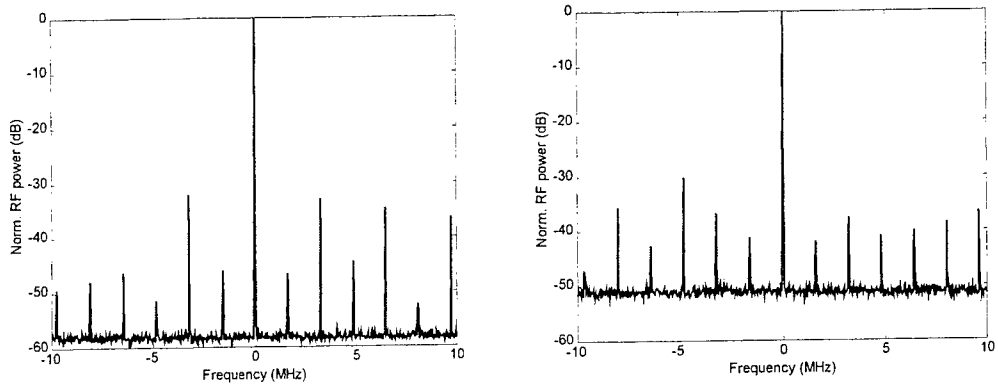

Figure 8. Normalized RF power spectrum of detected pulse train when FORC1 (left) or HW1 (right) was inserted in basic laser cavity. Center frequency corresponds to repetition rate of pulse train (left : f_m=3.000251046 GHz, right : f_m=3.000025481 GHz). Resolution is 3 kHz. Free spectral range of laser cavity is ≈ 1.63 MHz.

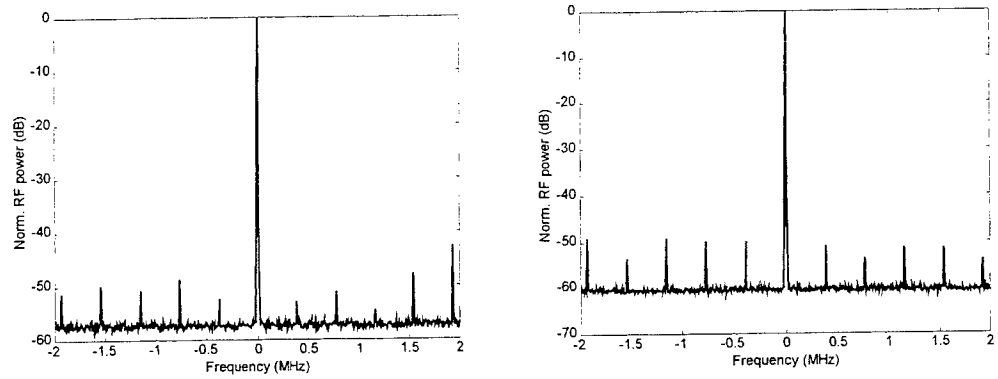

Figure 9. Normalized RF power spectrum of detected pulse train when FORC1 (left) or HW1 (right) was inserted in long laser cavity. Center frequency corresponds to repetition rate of pulse train (left : f_m=3.000312313 GHz, right : f_m=3.000663193 GHz). Resolution is 3 kHz. Free spectral range of laser cavity is ≈ 387 kHz.

For both gratings, pulses generated from the long cavity are shorter than those from the basic cavity (7.8 ps versus 9.4 ps with FORC1 and 22.7 ps versus 27.9 ps with HW1). This result is attributed to enhanced nonlinear pulse shortening in the long cavity. As discussed in next paragraph, pulse peak power is well above threshold of fundamental soliton, which is about three times lower in long cavity than in basic cavity. On the other hand it is clear that pulses circulating in the cavity are affected by grating reflection spectrum. In both cavity configurations, pulses generated with FORC1 grating are about three times shorter than those generated with HW1 grating. With FORC1 grating, pulses are near transform limit for *sech*^{2} pulses (time-bandwidth product is 0.32-0.34) while they are chirped with HW1 (0.44-0.46), possibly due to unwanted chirp imparted during grating inscription. Longer pulse duration obtained with HW1 grating is attributed to its narrower reflection bandwidth and residual chirp.

Table 2. Summary of measured pulse characteristics.

PM-FBG	$\lambda_{pulse,peak}$ (nm)	FWHM pulse bandwidth (nm)	FWHM pulse duration (ps)	Time-bandwidth product	Cavity configuration
FORC1	1545.4	0.27	9.4	0.32	Basic
HW1	1540.5	0.12	27.9	0.44	Basic
FORC1	1545.0	0.34	7.8	0.34	Long
HW1	1540.6	0.16	22.7	0.46	Long

4. DISCUSSION

Comparison of pulse autocorrelation and spectra obtained from basic cavity on one hand (Figure 4 & Figure 5), and from long cavity on the other hand (Figure 6 & Figure 7), shows that, for both gratings, pulses are shorter in the latter configuration. This shortening is attributed to average soliton effect inside the cavity. To verify this, it is interesting to calculate the peak power P_1 required to support fundamental soliton inside the cavity [6]:

$$P_1 = \frac{3.11}{n_2 c(2\pi)^2}\frac{D\lambda^3 A_{eff}}{\tau^2},$$

where D : average intracavity dispersion parameter, τ : FWHM duration of soliton, λ : wavelength, $n_2 = 3.2\ 10^{-16}$ cm²/W, nonlinear Kerr index, c : light velocity, A_{eff} : effective core area (typical value $A_{eff} = 57\ \mu m^2$ is used in calculation).

Total intracavity dispersion (ps/nm) was measured for both cavity configurations and divided by cavity length to obtain average intracavity dispersion parameter. At λ = 1545 nm, D = 9.2 ps/(nm×km) for basic cavity (127 m) and D = 2.9 ps/(nm×km) for long cavity (534 m). For a soliton duration τ = 10 ps, we find P_1 = 158.3 mW and P_1 = 50.4 mW in basic and long cavities, respectively. Note that the soliton period [6], $Z_0 = 0.322 \times \left(\pi^2 c\tau^2 / \lambda^2 D\right)$, is ≈ 4.3 km and ≈ 13.7 km in basic and long cavities, respectively. Insertion of DSF in cavity reduces threshold for fundamental soliton by a factor ≈3. Average power $P_{1,av}$ that would correspond to a train of 10-ps solitons with peak power equal to P_1 at repetition rate τ_R^{-1} can be calculated from :

$$P_{1,av} = 1.136 \times P_1 \frac{\tau}{\tau_R}.$$

At repetition rate τ_R^{-1} = 3 GHz, we find $P_{1,av}$ = 5.4 mW and $P_{1,av}$ = 1.7 mW in basic and long cavities, respectively. We can now compare these values with average intracavity power, P_{cav}. We estimate P_{cav} at some reference point in longest section of cavity (loss between reference point and output is noted Γ_{out}) using $P_{cav} = (G_S \Gamma_{out})^{-1} P_{out}$ where P_{out} is average output power, Γ is total cavity loss and $G_S = \Gamma^{-1/2}$ is single-pass gain. In present experimental conditions (G_S = 3.5, Γ_{out} = 0.4), P_{out} was measured to be ≈ 8 mW, which leads P_{cav} = 5.7 mW. According to this estimation, threshold for formation of fundamental soliton is well reached in long cavity ($P_{cav} \approx 3.35 \times P_{1,av}$) while it is just reached in basic cavity ($P_{cav} \approx 1.05 \times P_{1,av}$). Pedestals that are observed in autocorrelation trace of Figure 6 are attributed to nonlinear regime well above soliton threshold. Actually, when we decreased pump power, pedestals disappeared. Further experiments are needed to confirm this dependence on pump power.

Comparison of RF spectra obtained from basic and long cavities (Figure 8 and Figure 9, respectively), shows that supermode beat noise is strongly reduced in the latter configuration (same result was obtained with HW1 grating too). Reduction of the supermode beat noise is a known effect of the interplay between self phase modulation (SPM) and spectral filtering.[7] Observation of supermode noise reduction confirms that nonlinear pulse propagation does occur in long cavity.

5. CONCLUSION

Two Bragg gratings (1545.5 nm and 1540.5 nm, 1.6-nm and 0.8-nm reflection bandwidths, 99% and 90%, reflectivity) were written in H_2-loaded polarization-maintaining fiber and inserted in an actively-mode-locked Er-doped fiber laser. At a 3-GHz repetition rate, pulses of 9.4-ps and 27.9-ps duration were generated with first and second gratings, respectively. By inserting additional long piece of dispersion-shifted fiber in the cavity, nonlinear pulse shortening was observed due to formation of average soliton inside the cavity. Pulses of 7.8-ps and 22.7-ps duration were generated with first and second gratings in this case. With the first grating, generated pulses were close to transform limit for hyperbolic secant pulse shape. Longer pulse duration obtained with second grating is attributed to narrower bandwidth and residual chirp of the grating.

ACKNOWLEDGMENTS

This research was supported by Interuniversity Attraction Pole program (IAP IV 07) of the Belgian Government (SSTC). We are grateful to David Pureur (Highwave Optical Technologies, France) for giving us the opportunity to design and fabricate HW1 fiber grating. We are also grateful to Thibaut Sylvestre (Université libre de Bruxelles) for fruitful discussions about this work in the frame of IAP IV 07.

REFERENCES

1. D. Foursa, P. Emplit, R. Leners, L. Meuleman, IEE Electron. Lett. **33**, 486 (1997).
2. R. P. Davey, R. P. E. Fleming, K. Smith, R. Kashyap, J. R. Armitage, IEE Electron. Lett. **27**, 2087 (1991).
3. S. Li, K. T. Chan, IEEE Photon. Techn. Lett. **11**, 179 (1999).
4. O. Deparis, R. Kiyan, E. Salik, D. Starodubov, J. Feinberg, O. Pottiez, P. Mégret, M. Blondel, IEEE Photon. Techn. Lett. **11**, 1238 (1999).
5. R. Kiyan, O. Deparis, O. Pottiez, P. Mégret, M. Blondel, IEE Electron. Lett. **34**, 2410 (1998).
6. G. P. Agrawal, *Nonlinear Fiber Optics*, 1st Ed., Academic Press, 1989.
7. M. Nakazawa, K. Tamura, E. Yoshida, IEE Electron. Lett. **32**, 461 (1996).

Properties of the pulse train generated by an actively mode-locked Er-doped fiber laser in the rational-harmonic repetition-rate-doubling regime

R. Kiyan[1], O. Deparis, O. Pottiez, P. Mégret, M. Blondel

Advanced Research in Optics, Electromagn. & Telecom. Dept., Faculté Polytechnique de Mons, 31 Boulevard Dolez, B-7000, Mons, Belgium

ABSTRACT

We demonstrate for the first time that pulse-to-pulse amplitude fluctuations occurring in the rational-harmonic repetition-rate-doubling regime of actively mode-locked fiber laser are eliminated when modulation frequency is properly tuned. Irregularity of the pulse position in the train is found to be the only drawback of this technique. The irregularity can be reduced to value acceptable for applications by a proper laser design.

Keywords: Fiber lasers, active mode locking

1. INTRODUCTION

Actively mode-locked Er-doped fiber lasers in rational harmonic mode locking (RHML) regime [1] are potentially attractive sources for applications in high-speed fiber optic communication. An optical pulse train with repetition rate of $(np \pm 1) f_{FSR}$ can be produced by rational harmonic mode-locked fiber laser when the modulation frequency is equal to $(n \pm 1/p) f_{FSR}$, where n and p are integer, f_{FSR} is the free spectral range of the laser cavity. An important advantage of the RHML technique is its ability to generate a pulse train with a repetition rate significantly higher than the modulation frequency. Repetition rate multiplication up to factor 22 was successfully demonstrated [2]. Unfortunately, an inherent drawback of the rational harmonic mode locking with multiplication factor $p \geq 3$ is the strong pulse-to-pulse amplitude fluctuation caused by unmatched harmonics of the modulation frequency [3]. Such a fluctuation can be eliminated only by special pulse amplitude equalization techniques [4, 5] that involve optical nonlinearities and, therefore, are rather complicated and/or intrinsically set a limit to the maximal repetition rate through available pump power. On the other hand, repetition-rate-doubling $(p = 2)$ by rational harmonic mode locking does not suffer from this drawback and, for this reason, is the most attractive for applications. Although the repetition rate of the pulse train is increased only twofold with respect to the modulation frequency f_M in repetition-rate-doubling rational-harmonic mode-locking (RRD-RHML) regime, better quality of the pulse train is obtained in comparison with multiplication by a factor higher than two. Indeed, in RRD-RHML regime, about 35 dB suppression of an unmatched component at the modulation frequency f_M in the radio-frequency (RF) spectrum of the pulse train was observed experimentally [6] when the modulation frequency detuning, $\delta f_M = f_M / f_{FSR} - n - 1/2$, was equal to zero. However, the nature of the f_M - component is not completely elucidated and ultimate limitations on the parameters of the pulse train in RRD-RHML regime are not determined.

It is a commonly held idea that, in RHML regime, pulse passes through the modulator at its maximum transmission every p round trips. In the case of RRD-RHML it was assumed that optical pulse circulating in the laser cavity passes through the modulator at its maximum transmission every second round trips and at every other second round trips the pulse passes through the modulator at its minimum transmission. According to this model, the unwanted component at f_M in RF spectrum of the laser output in RRD-RHML regime is attributed to pulse-to-pulse amplitude fluctuations. Furthermore, pulse-to-pulse amplitude fluctuations are thought to be unavoidable, which is in contradiction with experimental observations [6]. Theoretical and experimental results presented in this paper will show that simplified explanation of RHML must be reconsidered. In this paper, a detailed experimental and theoretical investigation of the parameters of the pulse train in RRD-RHML regime of Er-doped fiber lasers is presented for the first time. For the reason of clarity we

[1] Correspondence : R. Kiyan. Faculté Polytechnique de Mons. Electromagn. & Telecom. Dept., 31 blvd Dolez, B-7000 Mons, Telephone : + 32 65 37 41 94; Fax : +32 65 37 41 99. E-mail: Kiyan@telecom.fpms.ac.be

Laser Optics 2000: Semiconductor Lasers and Optical Communication, Serguei A. Gurevich, Nikolay N. Rosanov, Editors, Proceedings of SPIE Vol. 4354 (2001) © 2001 SPIE · 0277-786X/01/$15.00

consider the case of a dispersion compensated laser cavity and we do not take into account Kerr nonlinearity in the optical fiber. Although Kerr nonlinearity is of importance in fiber lasers, we believe that the results presented here are significant because they demonstrate some properties of Er-doped fiber lasers in RRD-RHML regime that were not previously noticed. In the experiment, the relative temporal position of the pulse circulating in the laser cavity (with respect to cavity loss modulation), pulse-to-pulse amplitude fluctuations and pulse width were measured. The theoretical model is based on the self-consistency of the pulse after two round-trips in the laser cavity and analytical solution is obtained for dispersion-compensated Er-doped fiber laser in RRD-RHML regime. Unlike previously reported models [1, 7] we do not made any assumption on the pulse train parameters, including the pulse timing in the cavity. All pulse parameters are derived from the self-consistency condition.

2. THEORY

For theoretical analysis we consider an actively mode-locked fiber laser in unidirectional ring configuration shown in Fig. 1. The laser cavity is formed by Mach-Zehnder modulator (MZM) followed by output coupler, Fabry-Perot filter (FPF) and Er-doped fiber as amplification medium. All elements are connected by optical fiber to form a ring. It can be shown that only the total cavity dispersion influences the parameters of the generated pulse train rather than dispersion of each individual piece of optical fiber. As mentioned above, we consider the case of a dispersion-compensated cavity. The saturated gain of the Er-doped fiber is assumed to be equal to intracavity loss, spectrally flat within the FPF's transmission bandwidth and time independent. The transfer function of the FPF is $F(\nu) = 2 F_0 F_1 \left(F_0 + F_1 - \left(F_0 - F_1\right) \exp\left(-2\pi i \left(\nu - \nu_0\right)/\nu_{FSR}\right)\right)^{-1}$ where ν is optical frequency, ν_0 is optical frequency at maximal transmission of the FPF, ν_{FSR} is FPF's free spectral range, F_0 and F_1 are FPF's maximal and minimal transmissions, respectively. Finesse of the FPF is $k_F = \nu_{FSR}/\Delta\nu$, where $\Delta\nu$ is FPF's FWHM bandwidth. The time dependent transfer function of the MZM is $M(t) = M_0 \sin\left(\psi_0 + \pi R \sin(\theta)\right)$, where $\theta = 2\pi f_M t$ is normalized time, M_0 is MZM's maximal transmission, ψ_0 is the phase factor, $R = V_M/V_\pi$, V_π is π–voltage of the MZM, V_M is amplitude of the modulation voltage. For RRD-RHML, two conditions must be satisfied: $0 \le \psi_0 \le \pi/2$ and $0 \le \pi R \le \min\left(\psi_0;\ \pi/2 - \psi_0\right)$.

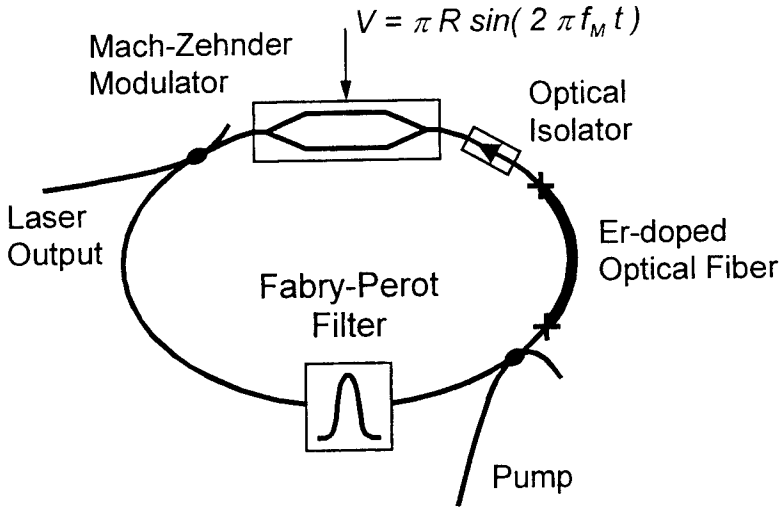

Figure 1. Schematic drawing of the actively mode-locked Er-doped fiber laser used for theoretical model.

For analysis of RRD-RHML, Kuizenga and Siegman's theory [8] is applied, assuming a Gaussian pulse circulating inside the laser cavity. Both MZM's transmission in time and FPF's transmission in frequency are approximated by Gaussian functions using quadratic expansions. A self-consistent steady-state solution is obtained after two complete cavity round-

trips. For two sequential cavity round-trips, electrical field of the optical pulse at MZM's output is expressed in the following form:

$$E_m(t) = E_{0m} \exp\left(2\pi i \nu_0 \left(t - t_m\right)\right) \exp\left(-2\ln 2 \left(t - t_m\right)^2 / \tau_m^2\right) \tag{1}$$

where $m = 1, 2$ corresponds to the first and the second cavity round-trips, E_{0m} is complex amplitude of the pulse, t_m is temporal position of the pulse peak and τ_m is FWHM pulse width. Normalized time $\theta_0 = \pi\left(\left(t_2 + t_1\right)/T_M - n - 1/2\right)$ is introduced that represents temporal position of the middle point between pulse positions at first and second round trips. Temporal shift of the pulse from this middle point is described by dimensionless parameter $\Delta\theta = \pi\left(\left(t_2 - t_1\right)/T_M - n - 1/2\right)$. Pulse-to-pulse amplitude fluctuation is characterized by parameter $\delta I = \left(\left|E_{02}\right|^2 - \left|E_{01}\right|^2\right) / \left(\left|E_{02}\right|^2 + \left|E_{01}\right|^2\right)$. Simple analytical expressions can be obtained in first order on small parameter $k = f_M / \Delta\nu$ for pulse train parameters at the MZM output, namely:

$$\Delta\theta = -\frac{\pi k}{k_S} \frac{R \sin(2\psi_0) \cos(\theta_0)}{2a\sqrt{\alpha_{M12}}} \tag{2}$$

$$\delta I = -ctg(\psi_0)\, tg\left(\pi R \sin(\theta_0)\right) \left(1 - \frac{k}{k_S} \frac{\pi^2 R^2 \cos^2(\theta_0)}{a\sqrt{\alpha_{M12}}}\right) \tag{3}$$

$$\tau_m = \frac{1}{\pi} \sqrt{\frac{2\ln 2}{k_S f_M \Delta\nu \sqrt{\alpha_{M12}}}} \left(1 - \frac{k}{k_S} \frac{\alpha_{Mm}}{\sqrt{\alpha_{M12}}}\right) \tag{4}$$

where $k_S = \sin(\pi k_F/2)/(\pi k_F/2)$, $a = M(\theta_0) M(\theta_0 + \pi) / M_0^2$, $\alpha_{M12} = \alpha_{M1} + \alpha_{M2}$, $\alpha_{M1} = \alpha_M(\theta_0)$, $\alpha_{M2} = \alpha_M(\theta_0 + \pi)$, $\alpha_M = -(1/2)\left(d^2 \ln(M(\theta))/d\theta^2\right)$. Temporal parameter θ_0 can be calculated from the following transcendental equation:

$$\frac{k_S}{k} \delta f_M = \frac{R \cos(\theta_0) \sin\left(2\pi R \sin(\theta_0)\right)}{2a\sqrt{\alpha_{M12}}} \tag{5}$$

It is easy to show from the eq. (5) that temporal parameter θ_0 is equal to zero for zero modulation frequency detuning. It means that optical pulse circulating in the cavity passes through the MZM at the instants of about half of its maximal transmission for both first and second roundtrips as it shown in Fig. 2, a. For variable definitions used in this paper, pulse passes through the MZM at the first and second cavity round trips when MZM's transmission is rising and falling, respectively. At both roundtrips pulse experiences the same loss when it passes through the MZM. As a consequence, there are no pulse-to-pulse amplitude fluctuations if $\delta f_M = 0$. Eq. (3) supports this conclusion. Pulse timing in the cavity is changed if modulation frequency detuning is differ from zero as it is shown in Fig. 2 b, c for negative and positive detuning, respectively. In these cases, losses caused by MZM are different at the first and second round trips, that causes pulse-to-pulse amplitude fluctuations. The temporal parameter $\Delta\theta$ is always negative and it is minimal when $\delta f_M = 0$. However, it is never equal to zero. Nonzero parameter $\Delta\theta$ cause pulse timing irregularity illustrated in Fig. 2.

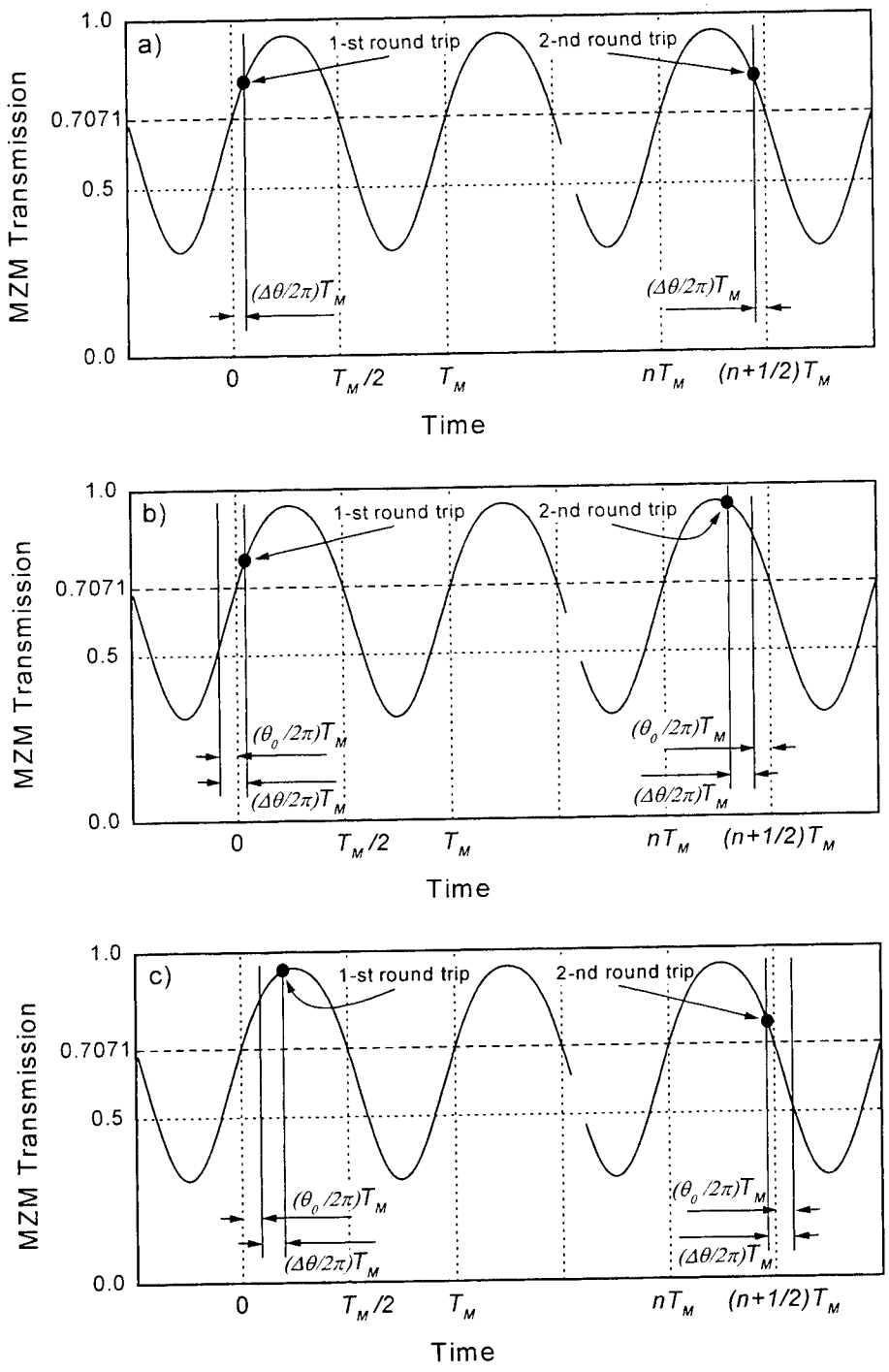

Figure 2. Pulse timing in respect to time-dependent transmission of the MZM with no modulation frequency detuning (a), with negative (b) and positive (b) detuning. Pulse position is marked by solid circle. The MZM transmission for electrical field is shown by solid line.

3. EXPERIMENT

For experimental investigation of the RRD-RHML regime, we used an actively mode-locked Er-doped fiber laser in sigma configuration as shown in Fig. 3. 9.7 m-long Er-doped fibre is placed in the single-mode (SM) part of the sigma-laser and pumped by a pigtailed 980 nm laser diode (~ 90 mW maximum output power). The mode locker is a lithium-niobate dual output intensity Mach-Zehnder modulator with an insertion loss of ~ 3 dB and a 3 dB bandwidth of ~ 3 GHz. The MZM is optically biased in such a way that input optical radiation is about equally divided between optical outputs 1 and 2 for zero voltage at its DC input and no signal at its RF input. There was no DC bias voltage applied to MZM so that it operated in the linear part of its modulation characteristic. The phase factor ψ_0 was measured to be about 0.19π for the MZM output 1. The tunable optical filter (TOF) installed in SM part of the laser, was tuned to run the laser at ~1545 nm. All measurements were carried out at 1545 nm. The tunable optical filter was not a Fabry-Perot filter. Optical transmission of the actual filter was fitted by function $|F(\nu)|^2$ to obtain filter parameters that are compatible with the presented theory. Fitting of filter's transmission spectrum led to FWHM bandwidth $\Delta\nu = 2.2$ nm and $k_S = 1$. To be consistent with the theoretical model, intracavity dispersion was compensated by inserting a 6.3-m piece of dispersion compensating fiber (DCF dispersion of ~ - 80 ps/km/nm at 1550 nm) into the single-mode part of the cavity. The total intracavity dispersion was estimated to be about (0.01±0.01) ps/nm at 1545 nm by measurement of the dependence of mode-locking frequency on operational wavelength. Free spectral range of the laser cavity was about 1.567443 MHz. In present experiment, value of the small parameter was $k = 0.065$.

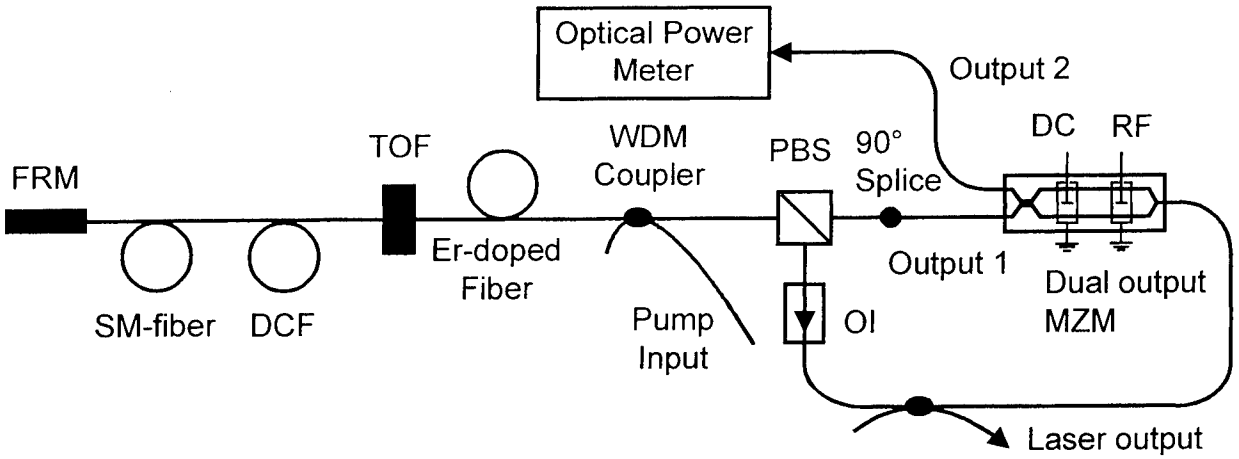

Figure 3. Actively mode-locked Er-doped fiber sigma-laser. DCF - dispersion compensating fiber; OI - Optical Isolator; PBS - Polarization Beam Splitter; FRM - Faraday Rotation Mirror; TOF - tunable optical filter.

Laser output was detected by photo-receiver with 25-GHz bandwidth and monitored by a 20-GHz sampling oscilloscope HP54120B. Oscilloscope was triggered by the modulating signal applied to the MZM. In order to allow measurement of the pulse timing in the cavity with respect to cavity loss modulation. additional time delay was introduced for triggering signal. This additional delay was tuned to equalize total delay of measured signal (optical delay plus electrical delay after photo-receiver) and delay of triggering signal. In order to determine the instant corresponding to maximal transmission of the MZM, modulation frequency was tuned for harmonic mode locking (HML) at $f_M \approx 2.699614627$ GHz. For optimally tuned HML, pulses circulating in the cavity are synchronized with instants of the MZM's maximal transmission, providing with reference points in oscilloscope trace. In the presented theoretical model, these instants correspond to $\theta = \pi/2 + 2\pi l$ where l is integer. Then modulation frequency was detuned by half of the laser cavity's FSR to achieve RRD-RHML regime. For both HML and RRD-RHML the average optical power at the second MZM output was monitored to determine modulation frequency corresponding to optimal tuning for HML [9] and $\delta f_M = 0$ for RRD-RHML [6]. Oscilloscope traces recorded for optimally tuned HML and RRD-RHML with no detuning $(\delta f_M = 0)$ are shown in

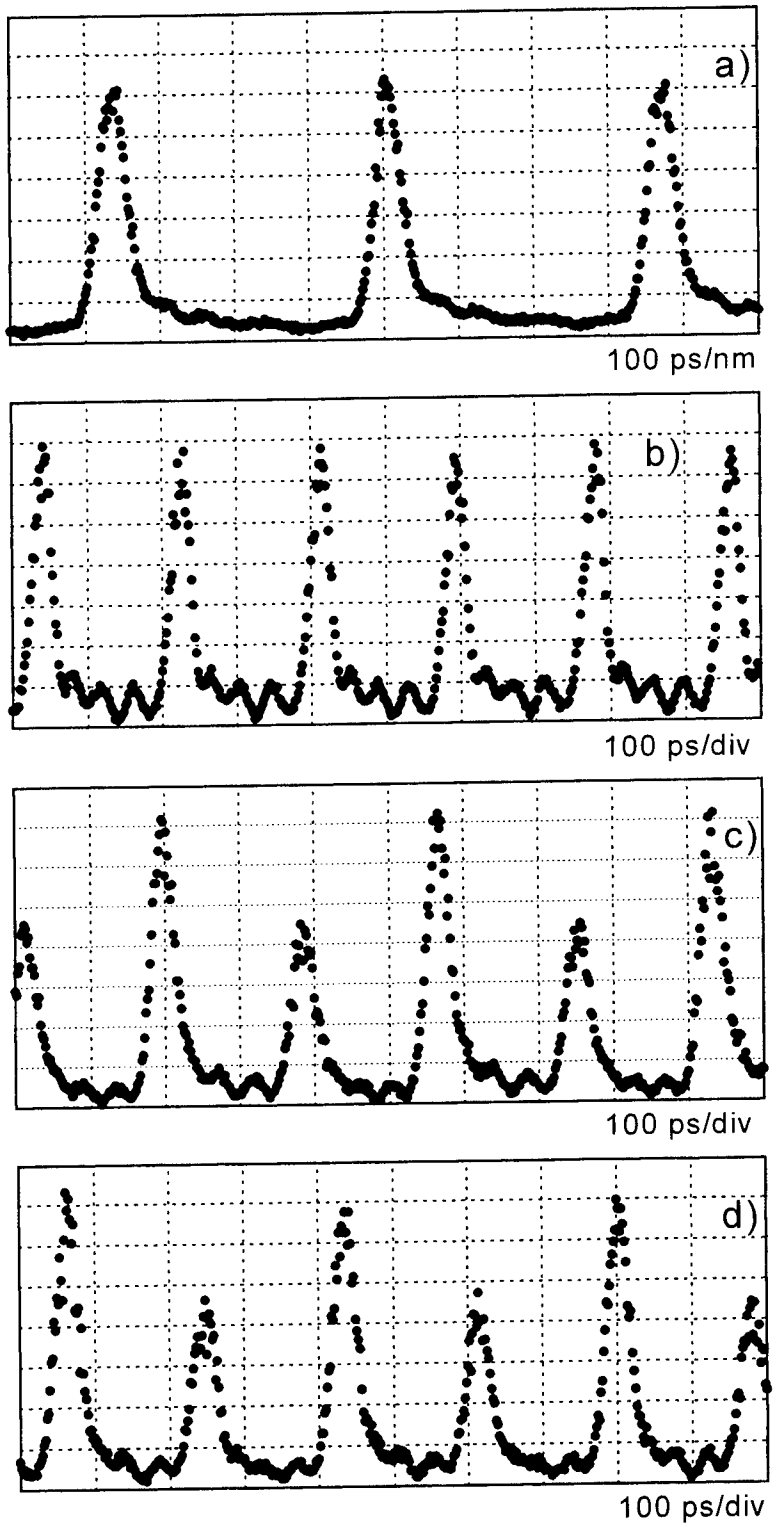

Figure 4. Oscilloscope traces recorded at the laser output for normalized modulation amplitude $R = 0.14$. a) - HML regime; b) - RRD-RHML regime with no modulation frequency detuning, c) - negative modulation frequency detuning $k_S \, \delta f_M / k = -0.39$; d) - positive modulation frequency detuning $k_S \, \delta f_M / k = 0.39$.

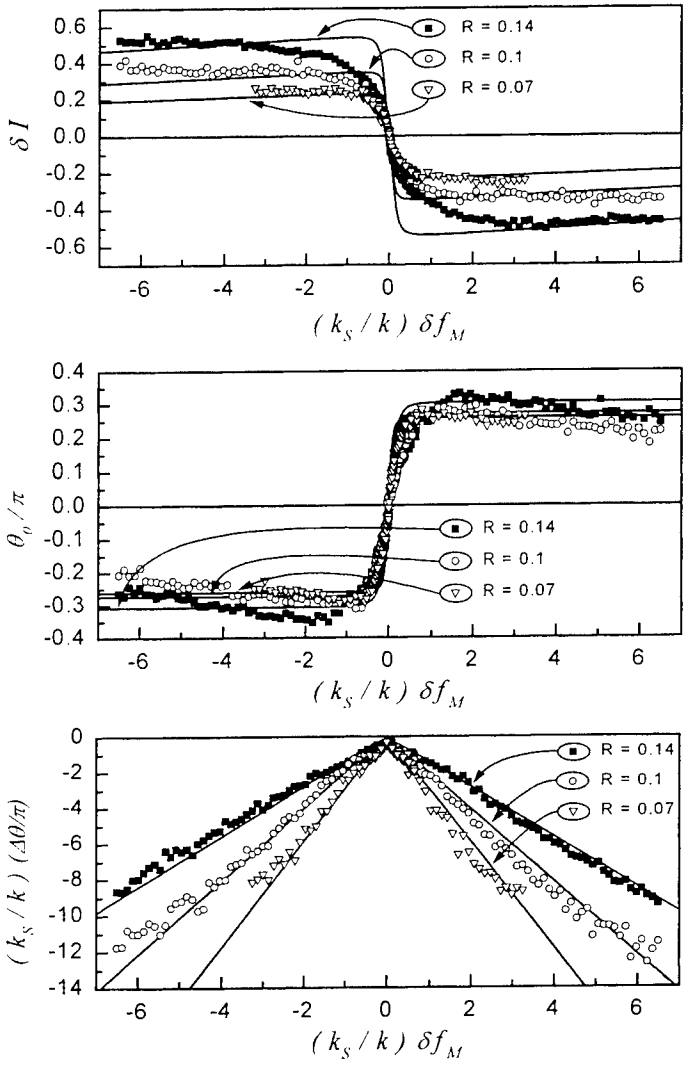

Figure 5. Experimental and theoretical dependencies of the temporal parameters θ_0, $\Delta\theta$ and the pulse-to-pulse fluctuations δI on the normalised modulation frequency detuning.

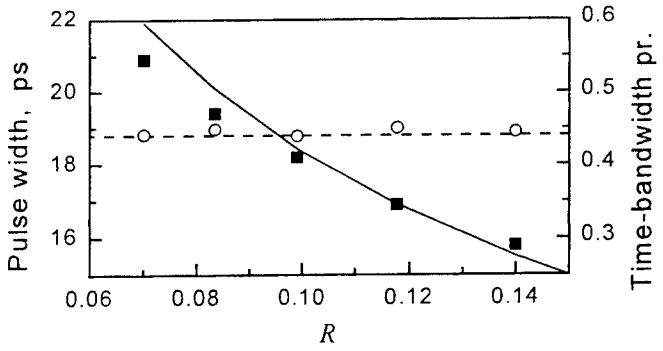

Figure 6. Experimental and theoretical dependencies of the pulse width (solid squares and solid line) and time-bandwidth product (open circles and dash line) on the normalised modulation amplitude for $\delta f_M = 0$.

Fig. 4 a, b. Oscilloscope traces for RRD-RHML with positive and negative detuning are shown in the same figure (Fig. 4 c, d). These experimental results demonstrate that optical pulses do not pass through MZM when its transmission minimal or maximal. For RRD-RHML with no detuning, pulses circulating in the cavity are timed in such a way that they pass through modulator at about middle between instants of the minimal and maximal transmissions of the MZM. In this case there are no pulse-to-pulse amplitude fluctuations (Fig. 4 b). Modulation frequency detunig causes shifts of the pulses from the middle positions. Furthermore, shifts are different for every first and second round trips. In another words pulse position irregularity appears in the pulse train. In addition, strong pulse-to-pulse amplitude fluctuations appear due to modulation frequency detuning. Oscilloscope traces are in qualitative agreement with pulse timing shown in Fig. 2.

For quantitative comparison between theoretical and experimental pulse train parameters oscilloscope traces were recorded for different values of the modulation frequency detuning δf_M. Pulse-to-pulse amplitude fluctuation δI and temporal parameters θ_0, $\Delta\theta$ were measured from the oscilloscope traces. Resulting experimental dependencies are shown in Fig. 5 for normalized modulation amplitudes $R = 0.07,\ 0.10,\ 0.14$. The theoretical dependencies calculated for actual laser parameters are shown in the same figures. Experimental and theoretical dependencies of the pulse duration (averaged on two round-trips) and time-bandwidth product on normalized modulation amplitude for $\delta f_M = 0$ are shown in Fig. 6. Quite good agreement between experimental results and theoretical model is observed. Some discrepancy is due to increasing error of the theoretical model with increasing modulation frequency detuning. On the other hand, generated pulse train became unstable and noisy for large modulation frequency detuning, that increased experimental error for large values of the detuning. However, only small values of the detuning are interesting for applications.

4. DISCUSSIONS

Main properties of the pulse train in RRD-RHML regime are summarized in the following. According to our approach and as it is experimentally confirmed the pulse train results from the superposition of two temporally shifted pulse trains both at the same repetition rate f_M (Fig. 7). The temporal shift between these pulse trains is about half of modulation period $T_M = 1/f_M$. Therefore, the repetition rate of the resulting pulse train is $2f_M$. A component at f_M appears in the RF spectrum if any of the pulse parameters is different at the first and the second round-trips or if the temporal shift between the two superposed trains is different from the ideal value $T_M/2$.

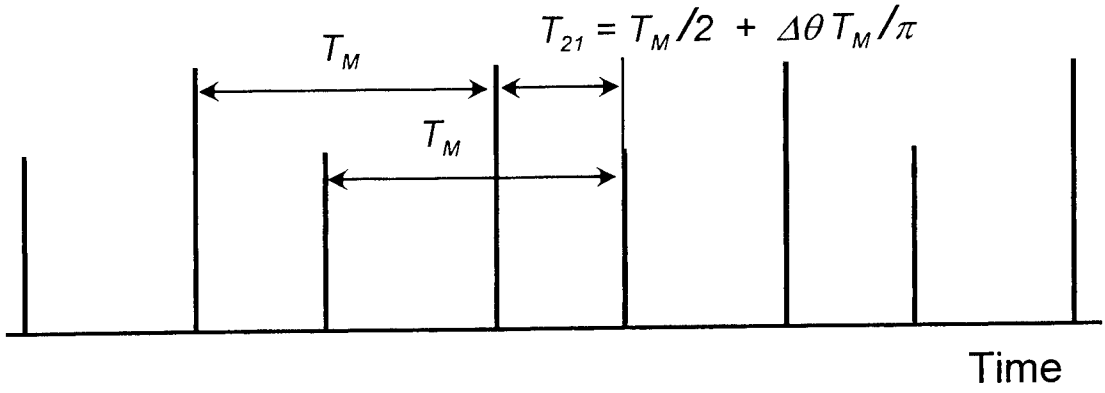

Figure 7. Schematic drawing of the pulse train at the laser output in RRD-RHML regime.

The instants at which the circulating pulse passes through the modulator at the first and the second round-trips depend on δf_M as shown in Fig. 5. For any value of δf_M, however, the pulse never passes through the modulator when its transmission is maximal or minimal, as it was assumed in ref. [1]. In case of $\delta f_M = 0$, at both the first and the second round-trips, the pulse passes through the modulator when its transmission is about at the middle between minimum and maximum (i.e. $\theta_0 = 0$ when $\delta f_M = 0$ as shown in Fig 5). The temporal shift between the two superposed pulse trains,

$T_{21} = t_2 - t_1 - n T_M$, is always different from its optimal value $T_M/2$. The higher the value of δf_M the higher the difference $\Delta T = T_{21} - T_M/2 = T_M \Delta\theta/\pi$ (Fig. 5). When $\delta f_M = 0$, the difference ΔT is minimal and $\Delta T = -\cos(\psi_0)/(\pi k_S \Delta\nu)$. The resulting pulse train suffers from irregularity of the relative temporal position of the pulses in the train. This irregularity is strongly reduced when $\delta f_M = 0$, although it can not be completely eliminated. Nevertheless, this irregularity may be reduced by increasing the optical filter bandwidth which in turns also reduces pulse duration.

The pulse amplitudes at the first and the second round-trips depend on δf_M as shown in Fig. 5 and, in general, are not equal. However, they are strictly equal when $\delta f_M = 0$. It means that pulse-to-pulse amplitude fluctuations are completely suppressed when $\delta f_M = 0$. This result is important and contrasts with general belief that pulse-to-pulse amplitude fluctuations are unavoidable in RHML.

5. CONCLUSION

In conclusion, we have demonstrated for the first time experimentally and theoretically that pulse-to-pulse amplitude fluctuations occurring in the repetition-rate-doubling rational-harmonic regime of actively mode-locked fiber lasers are eliminated if the modulation frequency is properly tuned. However, a component at modulation frequency is still present in the RF spectrum due to the irregularity of the pulse's temporal position in the train. This irregularity can be reduced to value acceptable for applications, but it can not be completely eliminated.

6. ACKNOWLEDGEMENT

This work is funded by the Inter-University Attraction Pole program (IAPIV/07) of the Belgian government (SSTC).

7. REFERENCES

1. Z. Ahmed, N. Onodera, "High repetition rate optical pulse generation by frequency multiplication in actively modelocked fibre ring lasers", Electron. Lett., 32, pp. 455-457, 1996.
2. C. Wu, N.K. Dutta, "High-repetition-rate optical pulse generation using a rational harmonic mode-locked fiber laser", IEEE J. of Quantum Electron., 36, pp. 145-150, 2000.
3. E. Yoshida, M. Nakazawa, "80~200 GHz erbium doped fibre laser using a rational harmonic mode-locking technique", Electron. Lett., 32, pp. 1370-1372, 1996.
4. M.-Y. Jeon, H.K. Lee, J.T. Ahn, K.H. Kim, D.S. Lim, E.-H. Lee, "Pulse-amplitude-equalized output from a rational harmonic mode-locked fiber laser", Opt. Lett., 23, pp. 855-857, 1998.
5. S. Li, C. Lou, K.T. Chan, "Rational harmonic active and passive modelocking in figure-of-eight fibre laser", Electron. Lett., 34, pp. 375-376, 1998.
6. R. Kiyan, O. Deparis, O. Pottiez, P. Mégret, M. Blondel, "Stabilization of actively mode-locked Er-doped fiber lasers in the rational-harmonic frequency-doubling mode-locking regime", Opt. Lett., 24, pp. 1029-1031, 1999.
7. N. Onodera, A.J. Lowery, L. Zhai, Z. Ahmed, R.S. Tucker, "Frequency multiplication in actively mode-locked semiconductor lasers", Appl. Phys. Lett., 62, pp. 1329-1331, 1993.
8. D. J. Kuizenga, A. E. Siegman, "FM and AM mode locking of the homogeneous laser – Part I: Theory", IEEE J. of Quantum Electron., 6, pp. 694-708, 1970.
9. R. Kiyan, O. Deparis, O. Pottiez, P. Mégret, M. Blondel, "Stabilization of actively mode-locked Er-doped fiber laser by minimising interpulse noise power", Electron. Lett., 34, pp. 2410-2411, 1998.

Guiding-center solitons of the first order, associated with the complex cubic Landau-Ginzburg equation

Alexandre S. Shcherbakov[1,2], Eduardo Tepichin Rodriguez[1], and Alexey Yu. Kosarsky[2]

1) National Institute for Astrophysics, Optics & Electronics, A.P.51 y 216, 72000, Puebla, Pue., Mexico
2) Radiophysics Department, Saint-Petersburg State Technical University, 195251, St.Petersburg, Russia

Abstract

The initial field amplitude a_0, normalized to the amplitude of a fundamental soliton, and the ratio Γ of the dispersion distance to the loss distance are successfully used to classify the areas of originating the "light" solitary waves of the first order in optical systems belonging to Landau-Ginzburg type. We analyze the model, described by the complex cubic Landau-Ginzburg equation in a reduced form, and demonstrate for the first time that the guiding-center solitons, associated usually with the interval of $a_0 \in [1.0;1.5]$, $\Gamma \geq 1$, can exist even if $\Gamma \leq 1$. The application of peculiarities inherent in picosecond optical guiding –center solitons of the first order to the problem of creating a fiber network for a precise synchronization is proposed and discussed.

Key words: guiding-center soliton, complex Landau-Ginzburg equation, picosecond optical solitons in single-mode fiber, optical fiber network for synchronization

1. Introduction

Modern theoretical study of solitary waves in the media with weak cubic-law nonlinearity has its origin in the well-known exact solution to the cubic Schroedinger equation, found by V.E.Zakharov and A.B.Shabat [1]. This basic result forms the foundation for nonlinear optics in fibers, where the cubic Schroedinger equation plays a key role. Applying that solution, the fundamental optical solitons [2], the asymptotic solitons [3], and the adiabatically perturbed fundamental solitons [4] in optical fibers were distinguished and investigated in succession. The "light" guiding-center solitons were associated initially with one of generalizations to the cubic Schroedinger equation, taking into account linear losses in a medium. In fact, such a form of generalization to this equation leads to considering the complex cubic Landau-Ginzburg equation, reduced in a special manner. For the first time, the guiding-center solitons had studied by A.Hasegawa and Y.Kodama [5,6]. Originally the area of existence for such solitary waves was estimated by the condition $\Gamma >> 1$, where Γ is the ratio of the dispersion distance to the loss distance. Then, A.S.Shcherbakov and E.I.Andreeva [7,8] had discovered both theoretically and experimentally that originating and developing the guiding-center solitons is possible when $\Gamma \geq 1$. The subject of the paper under presentation is the substantiation of sufficiently enlarged area where the guiding-center solitons, inherent in the systems described by the complex cubic Landau-Ginzburg equation, can be shaped. Actually, we are making an attempt to show that the area of their existence can be enlarged in the region $\Gamma \leq 1$. For this purpose a clear criterion for extracting the guiding-center solitons from a family of "light" solitary waves is put into operation. In our opinion, the formulation of such a problem is urgent, because now the guiding-center solitons are under consideration as ultrashort carriers of binary encoded signals in lengthy span optical fiber transmission systems. However, this area of exploitation is, evidently, not alone in applying similar soliton-like optical pulses. In particular, we consider an opportunity of using the peculiarities intrinsic in picosecond optical guiding–center solitons of the first order to the problem of creating a fiber network for a precise synchronization. For this purpose, two types of soliton-like pulses, being potentially suitable to be the sync-signal carriers in a medium-base fiber network, are distinguished and compared with each other. It is shown that the guiding-center soliton offers the advantage of less energetic sync-signal carrier over another soliton-like pulses.

Laser Optics 2000: Semiconductor Lasers and Optical Communication, Serguei A. Gurevich, Nikolay N. Rosanov, Editors, Proceedings of SPIE Vol. 4354 (2001) © 2001 SPIE · 0277-786X/01/$15.00

2. General consideration and computer simulations

Evolution of "light" solitary waves in the media with a weakly focusing cubic-law nonlinearity, anomalous dispersion of the group velocity, and the losses γ is described by the complex cubic Landau-Ginzburg equation in the reduced form

$$i\frac{\partial A}{\partial z} - \frac{1}{2}\frac{\partial^2 A}{\partial \tau^2} - |A|^2 A + i\Gamma A = 0. \qquad (1)$$

Here A is the field amplitude normalized to the amplitude of a fundamental soliton in the case of $\gamma = 0$. The normalized independent variables z and τ are connected with the propagation distance x and the retarded time t in tracking coordinate system as $z = xZ_D^{-1}$ and $\tau = t\tau_0^{-1}$; where $Z_D = \tau_0^2|k_2|^{-1}$ is the dispersion distance, k_2 is the dispersion coefficient ($k_2 < 0$ in the anomalous dispersion region), and τ_0 is the initial width of solitary wave, determined by the level of $sech\ 1 = 0.65$. Because of the losses, the dynamics of developing the "light" pulse is conditioned by the factor $\Gamma = \gamma Z_D$. The reduction of the complex cubic Landau-Ginzburg equation to Eq.(1) lies in the fact that both the spectral filtering and the nonlinear absorption processes are neglected, so the coefficients in the second and third terms are real-valued in Eq.(1). We assume that initially the solitary waves do not have the frequency chirp b and satisfy the following boundary conditions

$$A(z = 0, \tau) = a_0\ sech\ \tau; \qquad b(z = 0, \tau) = 0. \qquad (2)$$

Here the normalized initial amplitude a_0 determines an initial excess of the pulse amplitude over the magnitude of A_0 for corresponding fundamental soliton. Having in mind the only solitary waves of the first order, we restrict ourselves to considering the interval $1.0 \le a_0 \le 1.5$ [3]. Using a pair of perfectly measured values a_0 and Γ as the parameters, one can create the diagram, see Fig.1, displaying the areas where various types of the first order "light" solitary waves inherent in the complex cubic Landau-Ginzburg equation in the form of Eq.(1) exist under the limitation of $a_0 \in [1.0; 1.5]$ with the boundary conditions, pointed by Eq.(2).

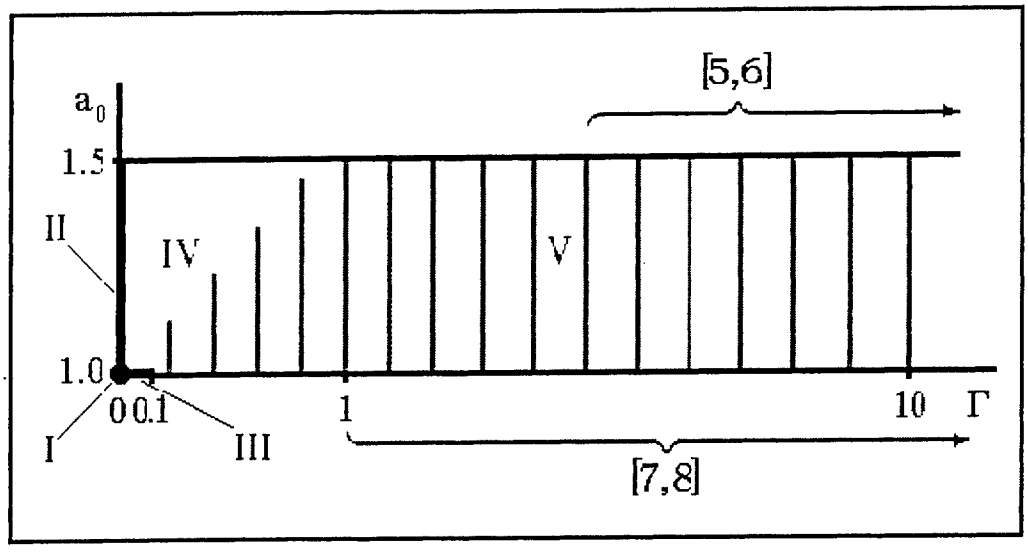

Fig.1 The areas of existence for the first order solutions, having the form of "light" solitary waves, to the complex cubic Landau-Ginzburg equation reduced to Eq.(1)

Applying the computer simulations we succeeded in finding that at least five zones, reflecting the difference in behavior of evolving the "light" solitary waves, can be marked out, see Fig.2. Besides the zones I - III, illustrating the areas of existence for the fundamental solitons and the asymptotic solitons in the absence of losses as well as the fundamental solitons adiabatically perturbed by low losses, respectively, one can separate still two another zones in this diagram. The zone IV corresponds to originating a set of solutions to Eq.(1), oscillating in a complicated manner, while the zone V, determined by the boundary curve $\Gamma = \Gamma_0(a_0)$, meets an area of shaping the guiding-center solitons in a medium with losses.

During the computer simulations, our main concern was with the evolution of such basic parameters as the amplitude, width, frequency chirp, and the shape of envelope for "light" solitary waves, belonging to the zones IV and V. The findings of our simulations make it possible to conclude that the conventional boundary between the zones IV and V may be defined as a function of the normalized amplitude a_0, and this function increases as a_0 increases. Some results of the calculations, reflecting the development of the peak amplitude $A_P = A(z, \tau = 0)$, the pulse width $\tau_p(z)$ at half a maximum, and the frequency chirp $b(z, \tau = 0)$ for $a_0 = 1.4$ and various values of the factor Γ are presented in Figs.3a – 3c. It is clearly seen from Figs.3a - 3c that as pulses are passing through a dissipative medium their peak amplitudes exhibit a natural tendency for decreasing while initially spectrally pure wave packets acquire the frequency chirp.

The case $\Gamma = 0.005$ corresponds to the oscillating solutions from deep within the zone IV, see the curves 1 in Figs.3a-3c. In this case the normalized pulse width stops short of reaching its own initial value and then exhibits spatial oscillations, as it is shown in Fig.3b. The peak amplitude and the frequency chirp also oscillate in a complicated manner. The curve 2 (with $\Gamma = 0.03$) in Fig.3b reaches in its peak the value of the initial pulse width and in doing so it represents the transition stage between the zones IV and V. The spatial dependences for both the amplitude and the chirp show an evident tendency for smoothing, see Figs.3a and 3c. Finally, the curves 3, 4, and 5 conform to the guiding-center solitons. These curves illustrate the main properties of the guiding-center solitons, primarily the effect of returning the pulse width to its own initial value after a passage of the distance $z = L_R$, see Fig.3b. In all the cases of $\Gamma = 0.2$, 0.4 or 0.8 the spatial dependences for the peak amplitude becomes to be monotone, while the spatial dependences for the frequency chirp demonstrate the quest for stabilization. Figure 3d illustrate the root-mean-square deviation Δ of the shape of envelope for a guiding-center soliton at the point $z = L_R$, where the pulse width reaches its own initial value, from the hyperbolic-secant envelope at the point $z = 0$ versus the factor Γ. It is seen from Fig.3d that the deviation Δ is quickly approaching to zero as the factor Γ is increasing. However, even if $\Gamma \geq 0.1$, the envelope of a guiding-center soliton is different from the initial one to only a small extent, because therewith $\Delta \leq 0.1$. This contention is supported by the upper insert at the right of the illustration, displaying the normalized amplitude profiles for one and the same guiding-center soliton at three different distances: $z = 0$, $z = L_{min}$, and $z = L_R$ in case, the "worst" of considered, when $a_0 = 1.4$ and $\Gamma = 0.4$. The presented profiles give an indication of the behavior of envelope that may be interpreted as the interference between the central portion of a pulse, having the envelope of an ideal fundamental soliton, and the oscillating portion of the same pulse, reflecting the nonstationarity in evolving a pulse on the interval $z \in [0, L_R]$. Depending on the current value of phase inherent in the oscillating portion of a field, the imposition of this field portion on the soliton center leads to deforming the pulse envelope and to compressing this pulse, peaking at the distance $z = L_{min}$. It is displayed in the insert at Fig.3d that the deviation Δ at the distance $z = L_R$ is accompanied by originating the only a moderate, up to 10% in magnitude of the amplitude, wings, which are placed exterior to the temporal interval of $3\tau_0$. Moreover, this insert at Fig.3d provides reason enough for a conclusion that even the pointed-above small deformations have a symmetrical manner, so both the maximum in amplitude distribution and the energetic center of the guiding-center soliton are placed at the same temporal position $\tau = 0$ in the accompanying coordinate system during all the process of passing and reshaping the pulse.

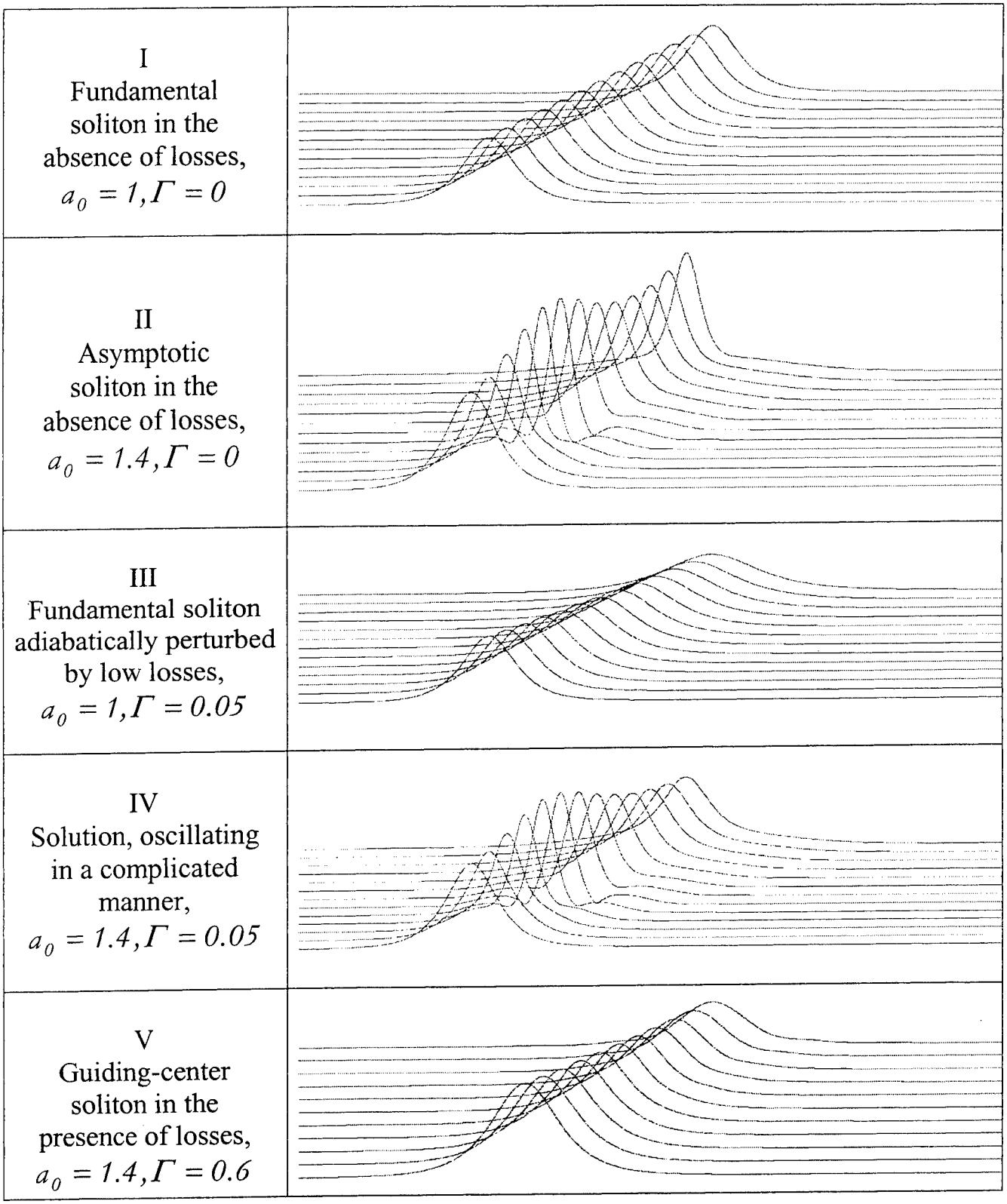

Fig.2. Developing "light" solitary waves of the first order, associated with Eq.(1)

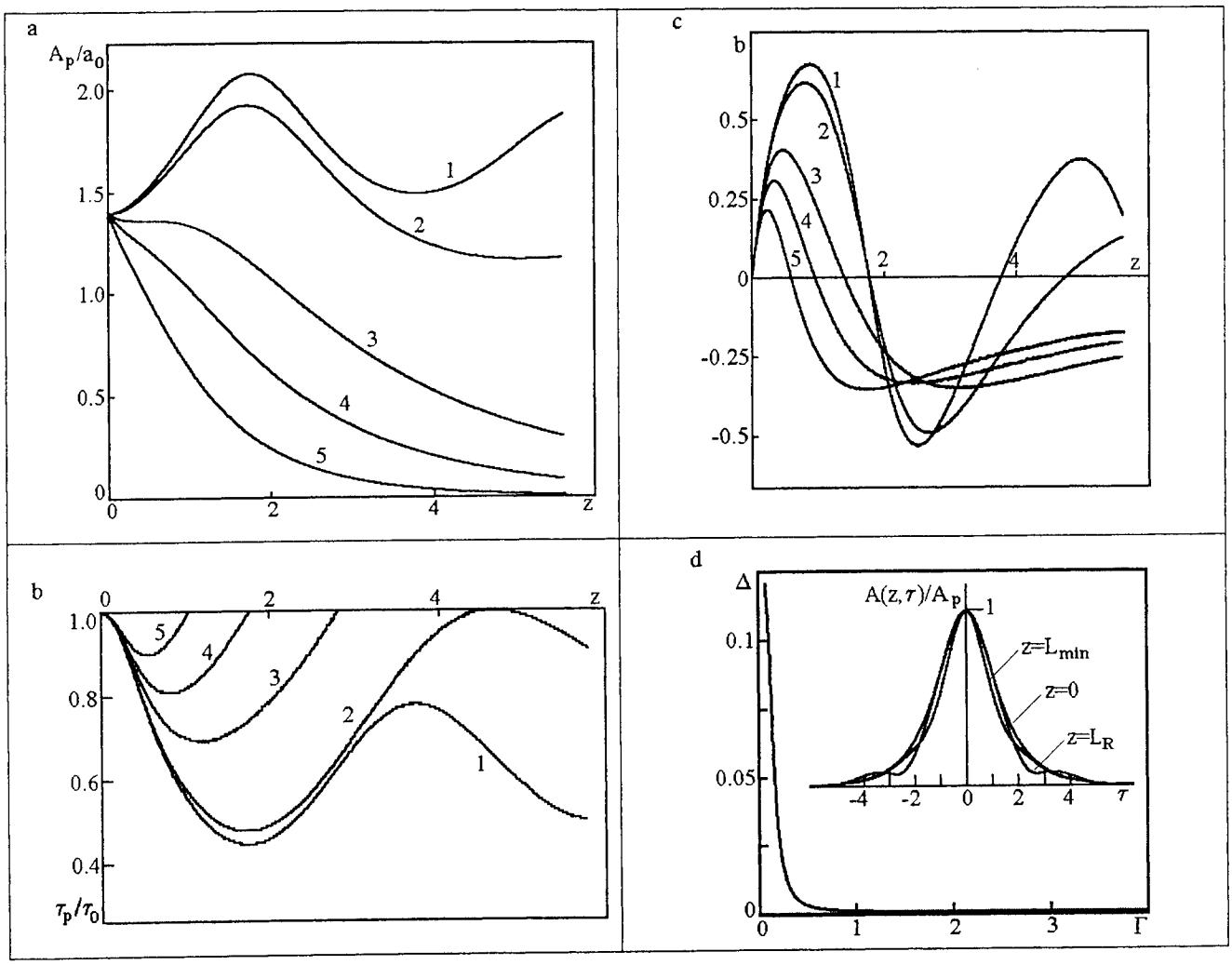

Fig.3 Developing the parameters of "light" solitary waves with $a_0 = 1.4$, belonging to the zones IV and V: (a) spatial dependencies of the normalized amplitude A_P / a_0; (b) spatial dependencies of the normalized pulse width τ_P / τ_0; (c) spatial dependencies of the frequency chirp b; (d) root-mean-square deviation of the shape of envelope for a guiding-center soliton from the sech-like envelope versus the factor Γ at the point $z = L_R$. The length of propagation is normalized to the dispersion distance Z_D. The curves from 1 to 5 correspond to Γ = 0.005, 0.03, 0.2, 0.4, and 0.8, respectively.

3. A new area of the application for guiding-center solitons

Usually, the guiding-center solitons are associated with transmitting the digital data [5,9]. This paragraph is connected with the application of guiding-center solitons to the problem of creating lengthy fiber networks for a precise synchronization. As an example let us consider an antenna complex, consisting of the central post and as low as two antennas, for the sake of simplicity, see Fig.4. Such is indeed the case that is the most frequent, for instance, in radio-astronomy. In order for operating an antenna complex to be provided, the mutual synchronization of individual antennas, comprising the complex, should be called on. Naturally, the delta-function pulse is an ideal sync-signal, but in practice, it can be realized rather approximately. That is why some general requirements to the sync-signals have to be satisfied in the synchronously operating complex of antennas with an arbitrary arrangement.

These signals should be precisely determined in the time scale compared with a temporal interval, corresponding to the cut-off frequency in data flow, or to the jitter time conditioned by any internal instability as well as external perturbations. Consequently, the requirements to both the duration and the repetition period of sync-signals increase by growing the informative capacity and processing accuracy. A selection of these problems may be resolved by looking at the technique based on the application of ultrashort optical pulses, which are able to play the part of delta-function-like pulses under certain conditions. The objective in designing a consideration under our proposal is to work out a radically new precise sync-network for synchronizing a medium-base complex of antennas. Therefore, we consider some aspects of implementing an optical fiber sync-network using ultrashort optical pulses as the sync-signal carriers. We take the simplest case when identical optical sync-signals are one-directionally distributed from the central processing unit all over the complex, see Fig.4. These signals are concurrently directed to both the antennas by different fiber channels, being just those fiber channels, which are used for transmission of data signals. Later, after a passage over the antennas, these sync-signals come back at the central processor. The principal measurable value is the clock skew between the energetic centers of ultrashort optical sync-pulses passed in parallel through different fiber channels. However, this brings up the problem of estimating picosecond temporal intervals, suggesting that one is in a need of accomplishing ultrafast photon-to-electron conversion. Nevertheless, this difficulty can be successfully got over if the repetition period inherent in the sync-pulse sequence is sufficiently short. To keep picosecond accuracy in electronic post-processing we rely on measuring the train-average clock skew [10].

Evidently, the preference should be given to the sync-signal carriers in the form of picosecond solitons being capable of passing through single-mode low-loss fibers at a short repetition period. As this takes place, the accuracy of synchronization is ultimately restricted by an error in determining the energetic center of a sync-pulse. In its turn, such an error is no more than the sync-pulse width, so the application of soliton regime to transmitting the sync-signals through single-mode fibers is an essential prerequisite to create a complex of antennas with a picosecond accuracy of synchronization.

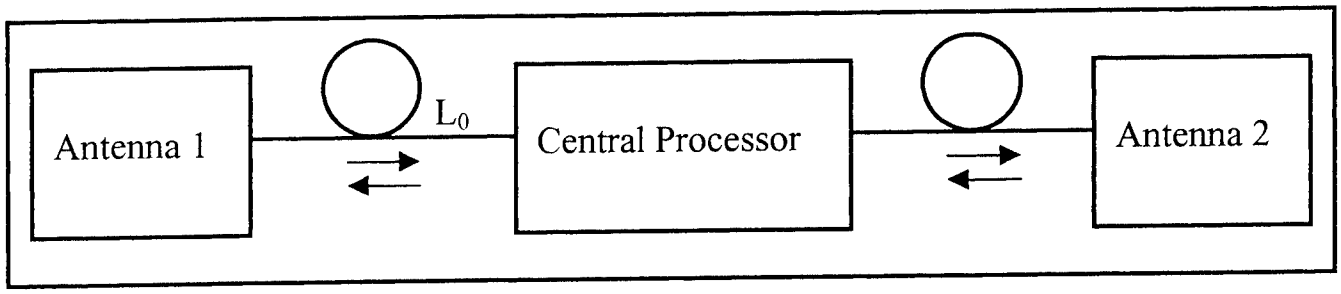

Fig.4. The schematic arrangement of an optical fiber network for a precise synchronization

The phenomenon of the self-phase modulation is capable of compensating a dispersive broadening of ultrashort pulse in the anomalous dispersion region of single-mode fiber and thereby of shaping a stable carrier in the form of "light" picosecond optical soliton. Unfortunately, the evolution of optical soliton in a fiber is also conditioned by the optical losses whose action is defined by the factor Γ, which represents the ratio of the dispersion distance Z_D to the loss distance γ^{-1}. As it was pointed above, if the factor $\Gamma = 0$, the initial balance between dispersion and nonlinearity gives rise to the fundamental soliton when the initial energy of such a pulse is $E_f = 2k_2(\sigma\tau_0)^{-1}$, where σ = 2.7 rad/W/km in standard single-mode silica fiber. When $\Gamma << 1$, a fundamental soliton cannot exist in an ideal sense, because the optical losses induce adiabatical perturbation due to broadening on the soliton pulse as $\tau(x) = \tau_0 \exp(2\gamma x)$, see Fig.2. In the case of $\Gamma \leq 1$ or $\Gamma > 1$, to realize the soliton-like regime of pulse propagation in a lossy fiber the initial energy of a pulse should be made larger than the energy of a fundamental soliton in the same but lossless fiber. Thus, we arrive at the application of optical guiding-center solitons in single-

mode fiber. The initial energy of optical guiding-center soliton is determined as $E_g = a_0^2 E_f$, where a_0^2 describes the above-mentioned excess of the optical pulse energy over the energy of an ideal fundamental soliton with the same initial width τ_0. During its propagation, the guiding-center soliton exhibits self-compression up to the distance L_{min} and return of its own width to the initial value followed by broadening a pulse.

From the viewpoint of the maximal accuracy of synchronization, associated with the minimal magnitude of the width τ_S of sync-pulse arriving at the central processor, see Fig.4, the potential designer of an antenna complex has two scopes for doing. The first scope is in using adiabatically perturbed fundamental soliton whose initial width is determined as $\tau_0 = \tau_S \exp(-4\gamma L_0)$, where L_0 is the arm length. The feasibility of creating an optical fiber sync-network, based on the adiabatically perturbed fundamental solitons, had been considered previously in Ref.10. The second one is in exploiting the guiding-center soliton with $\tau_0 = \tau_S$ as a sync-signal carrier. The relation between the initial energies E_f and E_g is the governing factor in deciding between adiabatically perturbed fundamental soliton and guiding-center soliton whose width are the same at the distance associated with twiced arm length $2L_0$, see Fig.5. The guiding-center soliton is initially less energetic than fundamental soliton, i.e. $E_g < E_f$, when the condition $2L_0 > L_A = \gamma^{-1} \ln a_0$ is true. For typical magnitudes a_0 = 1.4 and γ = 0.5 dB/km one can obtain L_A = 5.84 km. In this case $2L_0 = L_R$ = 18.3 km, and the potential designer can use either the adiabatically perturbed fundamental soliton with the initial width $\tau_1(x=0)$ = 1 ps and the initial energy E_f = 1.42 pJ or the guiding-center soliton with $\tau_2(x=0)$ = 8 ps and E_g = 0.34 pJ to obtain the same sync-pulse with τ_S = 8 ps at the central processor, that leads to the accuracy of synchronization at the range of 16 ps. As this takes place, the initial energy of a sync-pulse in the guiding-center soliton regime turns out to be more than 4 times less than the energy of a sync-pulse using the adiabatically perturbed fundamental soliton regime. Thus, the guiding-center soliton is energetically the best-suited carrier for a complex of antennas under consideration. Consequently, we may conclude that the exploitation of guiding-center solitons as sync-pulses has an advantage in creating a medium-base fiber networks for a precise synchronization.

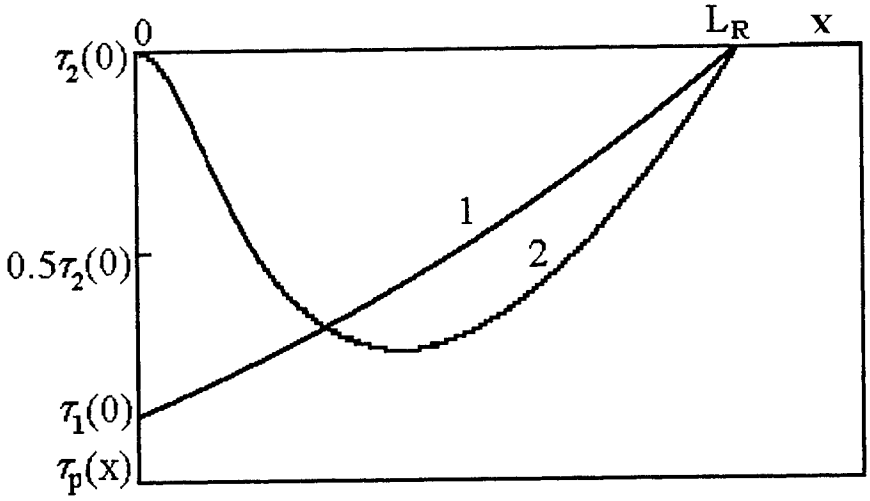

Fig.5. The peculiarities inherent in developing the width for two types of soliton-like of the first order as the carrier of sync-signal: 1 is the fundamental soliton, being adiabatically perturbed by low optical losses; 2 is the guiding-center soliton in the presence of optical losses in a fiber.

Technically well-grounded parameters of both the sync-signal carrier and the single-mode fiber arm can be chosen using spatial dependencies of the amplitude and width for guiding-center solitons, presented in Figs.3a, 3b, and 3c. It is clearly seen from Figs.3a and 3b, that the primary self-compression stage is accompanied by the increase in the amplitude only when the factor Γ is small. In the other cases the monotonous lowering of the amplitude is observed. The insert at Fig.3d shows that the energetic center of guiding-center soliton sync-pulse has no temporal shift while a pulse is passing through a fiber arm. The above-considered return of pulse width to the initial value is also clearly seen in Fig.5.

4. Conclusion

We have analyzed the conditions of existence for the guiding-center solitons inherent in the complex cubic Landau-Ginzburg equation. It has been shown that the area of their originating can be enlarged in the region $\Gamma \leq 1$. The property of a guiding-center soliton to return of its own width to the initial value has been put into operation as a criterion for extracting this class of soliton-like pulses from a family of "light" solitary waves. Key aspects of implementing a novel all-optical synchronization technique, based on picosecond guiding-center solitons as the ultrashort optical carriers of sync-signals, passing through silica single-mode fibers and being suitable for a medium-base complex of antennas, have been considered. Two types of soliton-like pulses, being potentially suitable to be the sync-signal carriers, have been compared with each other. The analysis of the relation between the initial energies of these pulses has shown that the guiding-center soliton has an advantage over the adiabatically perturbed fundamental soliton as the sync-signal carrier in a medium-base fiber network.

5. References

1. V.E.Zakharov and A.B.Shabat. "On the exact theory of two-dimensional self-focusing." *Sov. Phys. JETP*, **23**, 62-68 (1971).
2. A.Hasegawa and F.Tappert. "Transmission of stationary nonlinear optical pulses in dispersive dielectric fibers. I - Anomalous dispersion." *Appl. Phys. Lett.*, **23**, no.3, 142-144 (1973).
3. J.Satsuma and N.Yajima. "Solitons and the inverse scattering transform." *Prog. Theor. Phys., Supplement.*, **55**, 284-306 (1974).
4. A.Hasegawa and Y.Kodama. "Signal transmission by optical solitons in monomode fibers." *Proc. IEEE*, **69**, no.9, 1145-1150 (1981).
5. A.Hasegawa and Y.Kodama. "Guiding-center soliton in optical fibers." *Opt. Lett.*, **15**, no.24, 1443-1445 (1990).
6. A.Hasegawa and Y.Kodama. "Guiding-center solitons." *Phys. Rev. Lett.*, **66**, no.2, 161-164 (1991).
7. A.S.Shcherbakov and E.I.Andreeva. "Observation of picosecond optical pulses with a guiding-center soliton in a single-mode fiber-optic waveguide." *Tech. Phys. Lett.*, **20**, no.11, 873-875 (1994).
8. A.S.Shcherbakov and E.I.Andreeva. "Optical storage of binary data using the guiding-center solitons in a fiber loop." *Proc. SPIE*, **2429**, 227-234 (1994).
9. A.S.Shcherbakov and E.I.Andreeva. "Performance data of lengthy span soliton transmission system." *Optical Fiber Technology*, **2**, no.2, 127-133 (1996).
10. A.S.Shcherbakov. "Application of picosecond solitons in fibers for precise synchronization of a radio-interferometer" *Proc. SPIE*, **3733**, 306-315 (1999).

Free-space laser communication systems: internationally and in Russia

Nicolay P. Garaymovich, Vladimir N. Grigoriev, Alexander P. Huppenen,
Michael A. Sadovnikov Victor D. Shargorodsky, Victor V. Sumerin*

Research Institute for Precision Instruments
53, Aviamotornaya, 111250 Moscow, Russia

ABSTRACT

This paper presents a brief review of developments in modern wireless communication technology — free-space laser communication — both for intersatellite and terrestrial applications, including some Russian designs. The character of the Russian intersatellite terminal is its modular design and excluding of almost all opto-electronic instruments out of optical module, with duplex transfer of optical signals between components through fiber-optic cables. Such a design reduces the weight of stirring parts significantly and facilitates alignment. As for terrestrial lasercom, several commercial systems are listed, and results of link availability calculations (for Moscow region weather conditions) are presented.

Keywords: lasercom, intersatellite, terrestrial, terminal, link availability, Russian.

1. INTRODUCTION

The new technology of wireless communication — free-space lasercom systems — had appeared at the telecommunication market several years ago. Wide application of fiber-optic systems all over the world stimulated improvement of laser sources and photodetectors technology. As a result, comparatively cheap, highly reliable and efficient semiconductor laser diodes and sensitive detectors were developed — they made the basis for elaboration of commercial wireless lasercom systems. In the USA, Western Europe, Japan and Russia, lasercom systems rapidly develop in two trends: intersatellite lasercom systems (ILS) and terrestrial lasercom systems (TLS).

2. INTERSATELLITE LASERCOM SYSTEMS

In a few years, the practical use of ILS in spatial systems will take place both for real-time downloading of information (for example, from observation satellites) and as the components of relay systems based on satellite constellations or GEO satellites. More intensively ILS should be introduced during creation of global information networks in space. The most impressive project *Internet in the Sky*, which consists of 288 satellites, is being elaborated by a number of companies with share holding (Motorola, Teledesic, Boeing, Matra Marconi Space). In this project, all satellites are supposed to be linked together through high data rate cross-links in order to form a unified system.

There was the National Space Agency of Japan who held the first tentation of data transfer with relatively high rate from a satellite. In 1994, the satellite (*ETS-VI*), supposed to be in a geosynchronous orbit, was launched.[1] In spite of some problems with the satellite, demonstration of simplex link operation at data rate of 1 Mbps from the satellite to the ground station was conducted, so that the feasibility of such procedure was proved. Results of this experiment permitted to the National Space Agency of Japan to start elaboration of LEO terminal for *OISETS*[**], which is supposed to be got to take part in SILEX[***]

* Correspondence: Email: L-device@dialup.ru
** Optical Inter-orbit Communications Engineering Test Satellite

Laser Optics 2000: Semiconductor Lasers and Optical Communication, Serguei A. Gurevich,
Nikolay N. Rosanov, Editors, Proceedings of SPIE Vol. 4354 (2001) © 2001 SPIE · 0277-786X/01/$15.00

project (the European Space Agency).[2] France, Great Britain, Germany, Italy, Belgium, Spain and Netherlands are involved in SILEX project. The leading company is *Matra Marconi Space*. The project includes the creation of relay terminal at GEO satellite (*ARTEMIS*) which must cooperate with a similar terminal at LEO satellite (*SPOT-4*). In March 1998, SPOT-4 was launched, and for last two years it runs the trials. *ARTEMIS* launch is planned by the end of 2000 — this will the beginning of the full-scale flight test. The main purpose of this experiment is transmission of video images from *SPOT-4* to *ARTEMIS* and then to the ground station in Toulouse (France) at data rate of 50 Mbps. The weight of the SILEX terminal is 150 kg. In 1998, *Matra Marconi Space* had reported the development of the new generation of laser terminals with a mass less than 25 kg, optimized for transmission of vast multimedia information (see Table 1). Similar researches are held in the USA. The main purpose of these researches is to show — to the potential users — the availability and validity of laser communication technology for solving any communication problems in space, which emerge in modern society. In American projects, such companies as TermoTrex, Astroterra, Bell Aerospace, etc. take part.

The main problem for ILS is requirement of extremely precise alignment for two partner terminals that use narrow laser beams. Beacon lasers with relatively wide beam illuminating uncertainty area are used for acquisition. During data transfer the direction to partner satellite is maintained by beacon signals with error less than beam divergence. So, in the conditions of mutual motions and vibration of spacecraft, error should be no more than some tenths of arc second. This is the central problem for designers.

Some well-known ILS designs are shown in Table 1. The last developments of *Matra Marconi Space* — *SOUT*[****] and *OMINS*[*****] — have the best parameters.

In Russia, the works on ILS designing are held in the Research Institute for Precision Instruments (RIPI). Parameters of terminals worked out in RIPI are also shown in Table 1. The specific feature of terminal construction is that electronic components are placed outside mechano-optical unit. There are only optical components and pointing system sensors at the moving part of the unit. Lasers, photodetectors and other electronic components of power supply and control systems are in separate electronic unit. Duplex transfer of optical signals between mechano-optical unit and electronic unit goes through fiber-optic cables. It gave the possibility to considerably decrease the weight of the moving part of equipment and so to facilitate alignment. RIPI has designed the unified ILS terminal as well, and with the help of its main modules it is possible to assemble different types of cross-links with range up to 70000 km and with transmission speed up to 2 Gbps. Single-mode Al-Ga-As lasers with power about 100 mW are used as light sources.

3. TERRESTRIAL LASERCOM SYSTEMS

TLS gain rapidly telecommunication marketplace worldwide. The reason is that such systems offer a number of advantages over traditional ones.

First, TLS are capable of much higher data rates than other wireless communication technologies. Potentially, TLS can provide data rate at least as high as fiber optics do. For example, the systems that support data rate up to 2.5 Gbps at distances up to 2 km are already put on the market by *Lucent Technologies Co.*[3]

Second, there is no need to obtain frequency spectrum licenses when using TLS. Not only because the optical spectrum is not still included into regulations (and will not included next years, perhaps), but also because two adjacent laser links do not interfere with each other when the angle between their lines of sight exceeds beam divergence (the latter is less than 30 arc minutes, for up-to-date transmitters).

Installation and alignment of TLS can be performed very quickly (for a few hours). Running power and communication cables to the lasers usually require the most time. At any rate, this allows to use TLS for temporary installations efficiently.

Narrow beamwidth makes the laser link secure with no additional encrypting.

[***] Semiconductor Inter-satellite Link EXperiment
[****] Small Optical User Terminal
[*****] Optical terminal for Multimedia Network In Space

But one has to pay for anything! Achilles' heel of TLS is high dependence of its availability on weather conditions. Meanwhile, research work showed possibility to overcome many problems.

3.1. Atmospheric effects

Atmospheric effects on laser beam propagation can be broken out into two categories:

- Fluctuations of laser power due to laser beam deformation as result of small-scale dynamic changes in the index of refraction of the atmosphere,
- Scattering of the laser light photons by the aerosols.

3.1.1. Refraction

The power profile, as the beam travels through the atmosphere, becomes 'speckled' (on the target, this is seen as chaotic set of bright and dark spots which size and scintillation frequency — from tens herzs to some kiloherzs — mainly depend on atmospheric turbulence, i.e. weather conditions).

The simplest way to decrease influence of scintillation on link performance is increasing of receive aperture which leads to averaging of fluctuations.

Another way is non-coherent addition of powers from the lasers that are spaced out. If spaces between transmitters are greater than atmospheric turbulence correlation radius, the fluctuations on receive aperture from each transmitter are also non-coherent, and total fluctuation decrease.

3.1.2. Scattering

Absorption and scattering of the light photons by the different aerosols and gaseous molecules cause the attenuation of laser power in the atmosphere. This attenuation is described by Buger's law:

$$\tau\ \lambda\ = \text{H}\ \text{S}[-\alpha\ \lambda) \cdot L@ \tag{1}$$

where:

$\tau(\lambda)$ — transmittance at wavelength λ
$\alpha(\lambda)$ — attenuation coefficient
L — distance

The attenuation coefficient is made up of four parts: molecular absorption coefficient, aerosol absorption coefficient, molecular scattering coefficient, and aerosol scattering coefficient. For near-infrared laser wavelengths, typical for TLS, molecular and aerosol absorption as well as molecular scattering are negligible.

Aerosols include finely dispersed solid and liquid particles, such as water droplets, ice, and dust. Since size of particles is much greater than laser wavelength, the attenuation coefficient has small dependence on wavelength. Practically, the attenuation coefficient is equal to the aerosol scattering coefficient.

The relation between the main parameters of TLS link may be described as:

$$(P_t \cdot \beta_t^{-2}) \cdot (D_r \cdot P_r^{-1}) \cdot \tau_0 = L^2 \cdot exp(k \cdot L \cdot S_m^{-1}) \cdot [ln(BER^{-1}) \cdot C]^{1/2} \tag{2}$$

where:

P_t — laser source power,

β_t — transmit beam divergence,

D_r — receive antenna diameter,

P_r — power on the detector,

τ_o — antenna throughput coefficient,

L — link range,

C — data rate,

k — scale factor (2.5-3), depending on kind of aerosols.

As seen from (2), the left part of the equation mainly depends on the link range and on visibility; dependence on data rate and on BER in much weaker. This means that it is easy to increase data rate, but not the range of the link. The most part of TLS products available on the market (see Table 3) has limited range (no more than 1.5 km); at the same time, almost all manufacturers offer systems with data rate from 2 to 155 Mbps. To make TLS available at typical weather for given region, the system must have corresponding link budget margin. In fact, this margin determines maximum L/S_m value for which the link is still available. For example, if L/S_m is equal to 3, link margin must be of 30 dB from power level needed for operation in clear weather.

S_m has random nature and strongly depends on season and climatic zone. As any random value, it has a distribution of probabilities. Knowledge of the function of this distribution allows calculating availability of the link. Results of calculation (using statistics on long-term measurements in the Moscow region) are shown in Table 2, where F is probability of $S_m<S_{m1}$. Please note that the best weather occurs in June, the worst — in December.

Above-mentioned TLS with budget margin of 30 dB will have availability 0.999 at distance 1.5 km, 0.99 — at distance about 6 km, and 0.98 — up to 9 km.

In many countries, TLS operate successfully within telephone and computer networks and in other communication systems. For instance, British *PAV Data Systems Ltd.* (from this year having activities also in Russian market) has installed more than 3000 free-space laser links for last half decade (data rate up to 155 Mbps, range up to 6 km). *PAV Data System's* equipment is certified for use in Russia. Main parameters of some other TLS with atmospheric links are presented in Table 3.

In Russia, the development and field tests of specimens of TLS (AOLT****** type) with range to 10 km for telephone signals transmission at rate up to 155 Mbps are completed. There are also interface units for the computer protocols and TV signals. Such devices can successfully solve "Last Mile" problem. The main characteristics of these systems and special features of their operation are presented in Table 3. The availability of AOLT links with range up to 2 km is at least 0.99, and with range 5-6 km — 0.98, in any weather.

4. CONCLUSION

The European Space Agency (in the person of *Matra Marconi Space* and its partners) attained in new communication technology, namely intersatellite lasercom with range of 45000 km (SILEX project, and the others). On such a background, the Russian design of a generic terminal with range up to 70000 km and data rate of 2 Gbps (RIPI, Moscow) is worthy of regard.

Russian terrestrial terminals for horizontal atmospheric links with data rate up to 155 Mbps (RIPI, Moscow) worked through. Field tests showed link availability of 0.99 for 2 km distance (0.98 for 5-6 km) in any weather.

****** The transliteration of the Russian abbreviation. Approximately: *Atmospheric Open Link for Telephony*

Customer	Creator	Project / terminal	Link direction	Data rate, Mbps		Link distance, Thousand km	Weight, kg	Power, W
Science and Tech. Agency of Japan	Communication Recearch Lab., Japan	OICETS	LEO-GEO (*OICETS—ARTEMIS*)	LEO-GEO Up to 50	GEO-LEO 2.048	45	100	140
ESA	Matra Marconi Space	SILEX	LEO-GEO (*SPOT-4—ARTEMIS*)	LEO-GEO 50	GEO-LEO 2.048	45	150	130
ESA	Matra Marconi Space	SOUT	LEO-GEO	LEO-GEO From 2 to 1244 (2 x 622)		45	25	40
ESA	Matra Marconi Space	OMNIS	LEO-LEO	4 x 622 (2.488 Gbps)		7.5	20	60
BMDO, USA	Astroterra, USA	Astrolink-1000 (*STRV-2*)	LEO-LEO LEO-ground station	155 (2x500 in test mode)		1.6	13	94
'Energy' Space-Rocket Company, Russia	*RIPI, Russia*		*LEO-LEO LEO-ground station*	*LEO-LEO 34*	*LEO-ground station 128*	*6*	*35*	*150*
Aviation and Space Agency, Russia	*RIPI, Russia*		*LEO-GEO*	*LEO-GEO Up to 512*	*GEO-LEO 2.5*	*43*	*50*	*210-300*

Table 1. Comparison characteristics of ILS

	During the year		*In December*		*In June*	
Visibility, km	**F**	**t, hours**	**F**	**t, hours**	**F**	**t, hours**
0,5	0,0008	7,06	0,0011	0,85	0,0002	0,18
1,0	0,0024	21,4	0,0039	2,88	0,0008	0,56
1,4	0,0042	37,1	0,0071	5,25	0,0013	0,97
2,0	0,0077	67,2	0,0135	10,04	0,0025	1,76
2,8	0,0137	119,8	0,0252	18,79	0,0044	3,16

Table 2. Results of link availability calculations (Moscow region)

Manufacturer	**Model**	**Data rate, Mbps**	**Range, km**	**Size, cm**	**Weight, kg**	**Availability, %**
PAV Data Systems, GB	SkyNet	Ethernet,10 Token Ring,1-16 Fast Ethernet,100 FDDI, 100 ATM, 155	0,2—6 0,2—2 0,2—4 0,2—4 0,2—4	34x18x55 34x18x55 34x18x55 34x18x55 34x18x55	13—18 13 13—18 13—18 13—18	99.1 99.9
	SkyCom	G703/E1(E2),2	0,2—6	34x18x55	13—18	
LightPointe Communications Inc.	Compact Linc Light Station	Ethernet, 10 10 155	≤ 0,35 ≤ 0,6 ≤ 4	22.5x20x42 13,5x16,5x5 0 29x29x47	4 4,5 12	90
AirOptics	UWIN904 UWIN3303 PHL811/IM	Ethernet,10 E3,T3, FDDI, FastEthernet, ATM T1/E1, 1,5/2	1,1 0,65 0,78	71,3x36,4x4 8 41x27x15,5 41x27x15,5	10 7,5 7,5	
PROTEON	FreeSpace Fibre FreeSpace Turbo	Ethernet,10, TokenRing,4/16 Ethernet,45, Ethernet,100, ATM,155, FDDI	0,3 0,3	42x16x18 42x16x18	3,4+ 3,4 3,4+ 3,4	
Eagle Optoelectronics, Germany	MultiLink 20/4000 155/2000	Ethernet,10, 100 ATM,155, FDDI, TokenRing, 4/16	≤ 4	30x30x65	13,5	
Russia	*BOKS-10M* *BOKS-E1* *BOKS-E2* *BOKS-E3*	*Ethernet,10* *E1, 2,048* *E2, 8,448* *E3, 34,368*	*0,5* *1,5* *1,5* *1,0*	 *50x12x22* *100x24x44* *50x12x22*	 *16* *8* *8*	
RIPI, Russia	*AOLT*	*E1, 2,048,* *E2, 8,448,* *E3, 34,368,* *E4, 139,264*				

Table 3. Main parameters of some free-space terrestrial lasercom systems

ACKNOWLEDGMENTS

The authors would like to thank the colleagues in the Institute of Laser Physics (St.-Petersburg, Russia), as well as some other participants of the *10th Conference on Laser Optics 2000,* — for fruitful discussion on the matter of this paper.

REFERENCES

[1] K.E. Wilson, J.R. Lesh, K. Araki, Y. Arimoto, "Overview of the Ground-to-Orbit Lasercom Demonstration", SPIE Vol. 2990, pp. 23-30.
[2] G. Oppenhauser, "Silex program status — a major milestone is reached", SPIE Vol. 2990, pp.2-9.
[3] P.F.Szajowski et al., "Key Elements of High-Speed WDM Terrestrial Free-Space Optical Communications Systems", SPIE Vol. 3932, pp.2-14.

Author Index